Numéro d'ordre: 2013-ISAL-0004 Année 2013

THÈSE

présentée devant

L'Institut National des Sciences Appliquées de Lyon

pour obtenir

LE GRADE DE DOCTEUR

ÉCOLE DOCTORALE: ÉLECTRONIQUE, ÉLECTROTECHNIQUE, AUTOMATIQUE
FORMATION DOCTORALE : SCIENCES DE L'INFORMATION, DES DISPOSITIFS ET DES SYSTÈMES

par

WANG Lihui

Modélisation et Simulation de l'IRM de Diffusion des Fibres Myocardiques

Soutenue le 21 Janvier 2013

Jury :

Rachid DERICHE	Directeur de recherche INRIA	Rapporteur
Cyril POUPON	Chercheur CEA	Rapporteur
Jean-Philippe THIRAN	Professeur d'EPFL	Examinateur
Leon AXEL	Professeur de NYU	Examinateur
Pierre CROISILLE	Professeur, Praticien Hospitalier CHU St-Etienne	Examinateur
Wan-Yu LIU	Professeur de HIT	Examinateur
Isabelle E. MAGNIN	Directeur de recherche INSERM	Directeur de thèse
Yue-Min ZHU	Directeur de recherche CNRS	Codirecteur de thèse

Lihui WANG
Thèse en traitement de l'image medicale / 2012
Institut national des sciences appliquées de Lyon

INSA Direction de la Recherche - Écoles Doctorales – Quinquennal 2011-2015

SIGLE	ECOLE DOCTORALE	NOM ET COORDONNEES DU RESPONSABLE
CHIMIE	**CHIMIE DE LYON** **http://www.edchimie-lyon.fr** Insa : R. GOURDON	M. Jean Marc LANCELIN Université de Lyon – Collège Doctoral Bât ESCPE 43 bd du 11 novembre 1918 69622 VILLEURBANNE Cedex Tél : 04.72.43 13 95 directeur@edchimie-lyon.fr
E.E.A.	**ELECTRONIQUE, ELECTROTECHNIQUE, AUTOMATIQUE** **http://edeea.ec-lyon.fr** Secrétariat : M.C. HAVGOUDOUKIAN eea@ec-lyon.fr	M. Gérard SCORLETTI Ecole Centrale de Lyon 36 avenue Guy de Collongue 69134 ECULLY Tél : 04.72.18 60 97 Fax : 04 78 43 37 17 Gerard.scorletti@ec-lyon.fr
E2M2	**EVOLUTION, ECOSYSTEME, MICROBIOLOGIE, MODELISATION** **http://e2m2.universite-lyon.fr** Insa : H. CHARLES	Mme Gudrun BORNETTE CNRS UMR 5023 LEHNA Université Claude Bernard Lyon 1 Bât Forel 43 bd du 11 novembre 1918 69622 VILLEURBANNE Cédex Tél : 04.72.43.12.94 e2m2@biomserv.univ-lyon1.fr
EDISS	**INTERDISCIPLINAIRE SCIENCES-SANTE** **http://ww2.ibcp.fr/ediss** Sec : Safia AIT CHALAL Insa : M. LAGARDE	M. Didier REVEL Hôpital Louis Pradel Bâtiment Central 28 Avenue Doyen Lépine 69677 BRON Tél : 04.72.68 49 09 Fax : 04 72 35 49 16 Didier.revel@creatis.uni-lyon1.fr
INFOMATHS	**INFORMATIQUE ET MATHEMATIQUES** **http://infomaths.univ-lyon1.fr**	M. Johannes KELLENDONK Université Claude Bernard Lyon 1 INFOMATHS Bâtiment Braconnier 43 bd du 11 novembre 1918 69622 VILLEURBANNE Cedex Tél : 04.72. 44.82.94 Fax 04 72 43 16 87 infomaths@univ-lyon1.fr
Matériaux	**MATERIAUX DE LYON** Secrétariat : M. LABOUNE PM : 71.70 –Fax : 87.12 Bat. Saint Exupéry **Ed.materiaux@insa-lyon.fr**	M. Jean-Yves BUFFIERE INSA de Lyon MATEIS Bâtiment Saint Exupéry 7 avenue Jean Capelle 69621 VILLEURBANNE Cédex Tél : 04.72.43 83 18 Fax 04 72 43 85 28 Jean-yves.buffiere@insa-lyon.fr
MEGA	**MECANIQUE, ENERGETIQUE, GENIE CIVIL, ACOUSTIQUE** Secrétariat : M. LABOUNE PM : 71.70 –Fax : 87.12 Bat. Saint Exupéry **mega@insa-lyon.fr**	M. Philippe BOISSE INSA de Lyon Laboratoire LAMCOS Bâtiment Jacquard 25 bis avenue Jean Capelle 69621 VILLEURBANNE Cedex Tél :04.72.43.71.70 Fax : 04 72 43 72 37 Philippe.boisse@insa-lyon.fr
ScSo	**ScSo*** M. OBADIA Lionel Sec : Viviane POLSINELLI Insa : J.Y. TOUSSAINT	M. OBADIA Lionel Université Lyon 2 86 rue Pasteur 69365 LYON Cedex 07 Tél : 04.78.69.72.76 Fax : 04.37.28.04.48 Lionel.Obadia@univ-lyon2.fr

Lihui WANG

Thèse en traitement de l'image medicale / 2012
Institut national des sciences appliquées de Lyon

Modeling and Simulation of Diffusion Magnetic Resonance Imaging for Cardiac Fibers

Abstract

Diffusion magnetic resonance imaging (dMRI) appears currently as the unique imaging modality to investigate noninvasively both *ex vivo* and *in vivo* three-dimensional fiber architectures of the human heart. However, it is difficult to know how well the diffusion characteristics calculated from diffusion images reflect the microstructure properties of the myocardium since there is no ground-truth information available and add to that the influence of various factors such as spatial resolution, noise and artifacts, etc. The main objective of this thesis is then to develop realistic model-based dMRI simulators to simulate diffusion-weighted images for both *ex vivo* and *in vivo* cardiac fibers by integrating different imaging modalities, and propose a generic tool for the evaluation of imaging quality and image processing algorithms.

To achieve this, the present work focuses on four parts. The first part concerns the formulation of basic dMRI simulation theory for diffusion image generation and subsequent applications on simple cardiac fiber models, and tries to elucidate the underlying relationship between the measured diffusion anisotropic properties and the cardiac fiber characteristics, including both physical and structural ones. The second part addresses the simulation of diffusion magnetic resonance images at multiple scales based on the polarized light imaging data of the human heart. Through both qualitative and quantitative comparison between diffusion properties at different simulation scales, the relationship between the microstructure variation and the diffusion properties observed at macroscopic scales is investigated. The third part deals with studying the influence of imaging parameters on diffusion image properties by means of the improved simulation theory. The last part puts the emphasis on the modeling of *in vivo* cardiac fiber structures and the simulation of the corresponding diffusion images by combining the cardiac fiber structure and the a priori known heart motion.

The proposed simulators provide us a generic tool for generating the simulated diffusion images that can be used for evaluating image processing algorithms, optimizing the choice of MRI parameters in both ex vivo and *in vivo* cardiac fiber imaging, and investigating the relationship between microscopic fiber structure and macroscopic diffusion properties.

Lihui WANG

Thèse en traitement de l'image médicale / 2012
Institut national des sciences appliquées de Lyon

Modélisation et Simulation de l’IRM de Diffusion des Fibres Myocardiques

Résumé

L’imagerie par résonance magnétique de diffusion (l’IRMd) est actuellement la seule technique non-invasive pour étudier l’architecture tridimensionnelle des fibres myocardiques du cœur humain à la fois *ex vivo* et *in vivo*. Cependant, il est difficile de savoir comment les caractéristiques de diffusion calculées à partir des images de diffusion reflètent les propriétés des microstructures du myocarde à cause de l’absence de la vérité-terrain sans parler de l’influence de divers facteurs tels que la résolution spatiale, le bruit et les artéfacts. L'objectif principal de cette thèse est donc de développer des simulateurs de l’IRM de diffusion basés sur des modèles réalistes afin de simuler, en intégrant différentes modalités d'imagerie, les images pondérées en diffusion des fibres myocardiques à la fois *ex vivo* et *in vivo*, et de proposer un outil générique permettant d’évaluer la qualité de l’imagerie et les algorithmes de traitement d’images.

Pour atteindre cet objectif, le présent travail se focalise sur quatre parties principales. La première partie concerne la formulation de la théorie de simulation IRMd pour la génération d’images de diffusion et pour les applications sur les modèles simples de fibres cardiaques chez l’homme, et essaie de comprendre la relation sous-jacente entre les propriétés mesurées de la diffusion et les caractéristiques à la fois physiques et structurelles des fibres cardiaques. La seconde partie porte sur la simulation des images de résonance magnétique de diffusion à différentes échelles en s’appuyant sur des données du cœur humain issues de l'imagerie par lumière polarisée. En comparant les propriétés de diffusion à différentes échelles, la relation entre la variation de la microstructure et les propriétés de diffusion observée à l'échelle macroscopique est étudiée. La troisième partie consacre à l’analyse de l'influence des paramètres d'imagerie sur les propriétés de diffusion en utilisant une théorie de simulation améliorée. La dernière partie a pour objectif de modéliser la structure des fibres cardiaques *in vivo* et de simuler les images de diffusion correspondantes en combinant la structure des fibres cardiaques et le mouvement cardiaque connu a priori.

Les simulateurs proposés nous fournissent un outil générique pour générer des images de diffusion simulées qui peuvent être utilisées pour évaluer les algorithmes de traitement d’images, pour optimiser le choix des paramètres d’IRM pour les fibres cardiaque aussi bien ex vivo que in vivo, et pour étudier la relation entre la structure de fibres microscopique et les propriétés de diffusion macroscopiques.

Remerciement

Je voudrais exprimer ma sincère gratitude à tous ceux qui m'ont aidé au cours de ma thèse.

Je tiens tout d'abord à remercier chaleureusement mes directeurs de thèse Isabelle Magnin, Yue-Min Zhu, et Wan-Yu Liu, sans qui cette thèse n'aurait jamais vu le jour.

Isabelle, avec sa riche expérience dans le domaine de l'imagerie médicale, sa capacité d'identifier les problèmes, ses précieuses suggestions quant à cette aventure qu'est la recherche, sa patience pour m'avoir guidée et ses efforts pour m'avoir expliquée les choses clairement et simplement, qui m'a aidée à finir finalement ce périple de recherche doctorale. J'apprécie vraiment ces contributions, le temps passé et ses idées sur ce travail. Je la remercie beaucoup de m'avoir introduite dans le monde de l'imagerie médicale et de m'avoir soutenue jusqu'ici.

Yue-Min, même s'il n'est pas mon codirecteur officiel de thèse, pendant ces trois ans et demi, il m'a guidé au jour le jour, m'a aidé à résoudre les problèmes en détail, m'a donné des conseils précieux sur tous les aspects de ce travail, m'a encouragée lorsque je manquais de motivation. Au-delà de son encadrement scientifique, il est comme un ami, partage avec nous sa joie et enthousiasme pour la recherche et la vie, ce qui m'a motivée durant ma thèse. Grâce à lui, j'ai passé un séjour agréable en France. Je tiens à le remercier du fond de mon cœur.

Wan-Yu, je lui exprime toute ma gratitude pour m'avoir recommandée auprès de Creatis, et ainsi, de m'avoir donnée l'occasion de travailler dans ce laboratoire. Je le remercie beaucoup pour son aide précieuse, ses conseils pertinents et pour toute la confiance qu'il m'a accordée pendant ces années.

J'exprime toute ma gratitude aux membres de mon jury de thèse, particulièrement aux rapporteurs, M. Rachid Deriche et M. Cyril Poupon, merci d'accepter d'être mes rapporteurs de thèse et de me donner plein d'idées pour la suite. Je voudrais remercier profondément M. Jean-Philippe Thiran, président du jury, pour ses conseils précieux au sujet de mes recherches et pour toute sa gentillesse avec moi. Merci également aux Dr. Pierre Croisille et professeur Leon Axel d'avoir accepté de faire partie de mon jury de thèse.

Je tiens aussi à remercier particulièrement ceux qui ont eu la gentillesse de m'aider pendant la thèse. Un grand merci à Sorina Camarasu-Pop et Tristan Glatard pour leur aide sur le calcul de grille, sans eux, mes travaux n'auraient pas pu être menés à terme aussi rapidement. Je leur suis très reconnaissante pour leurs réponses promptes, même sur des sujets qui, parfois, pouvaient sembler naïfs. Ils m'ont appris l'attitude à adopter dans la recherche scientifique. Merci beaucoup aussi à Dr. Pierre-Simon Jouks et M. Yves Ussons pour leur aide quant aux données utilisées dans le cadre de mes travaux et les discussions stimulantes et fructifiantes. En outre, je souhaite remercier aussi à M. Denis Grenier pour son aide et ses conseils sur les séquences de l'IRM au début de ma thèse. Merci à Eduardo Davila pour son aide en programmation. Merci aussi à Fabrice Bellet pour les instructions sur le cluster.

Merci à mes collègues de laboratoire, ils étaient toujours gentils et patients. Je pense plus particulièrement à Matthew Ozon, merci de m'avoir accompagnée pour faire la manipulation à l'ESRF et aussi pour sa gentillesse et son amitié, Xavier Lojacono, le petit garçon qui est toujours gentil avec les Chinois, François Varray et Christopher Casta, merci à vous d'avoir corrigé ma présentation française pendant le weekend, Pierre Ferrier, merci pour ton aide sur les logiciels et les petites affaires quotidiennes, Christiane Jeanguillaume, merci pour ton soutien et ta sollicitude et merci aussi pour ta compréhension quant à mes demandes de temps en temps.

Un grand merci à tous mes meilleurs amis présents et passés au cours de ces années, aujourd'hui, sans oublier ceux que j'ai rencontrés auparavant, Feng Yang, Fanglue Lin, Yue Zhao, Yan Wang, Xinxin Guo, Hongying Li, Hongjiang Wei, Pei Dong, Miao Liu, Rui Xu, Shengfu Li, Xuejiao Jiang, Hexiang Yan, Jikai Liu, et Jianping Huang. Vous êtes comme ma famille, merci pour votre aide et vos encouragements pendant ces années. Sans vous, la vie en France n'aurait pas été remplie de souvenir heureux et plein de joie.

Pour terminer, je voudrais remercier ma chère famille, pour son soutien, son écoute, ses encouragements, son aide et son amour, je suis très heureuse que vous soyez toujours là autour de moi. Surtout je tiens à remercier mon mari pour m'avoir attendu si longtemps.

Contents

Content of Figures

Introduction Générale

Les maladies cardiaques sont une des principales causes de mortalité dans le monde. Selon les estimations de 2011 de l'Organisation mondiale de la santé (OMS), 17,3 millions de personnes dans le monde sont mortes de maladies cardiaques en 2008, ce qui représente environ un tiers (27% en France) du nombre total de décès et les rend comme la principale cause du décès et du handicap dans le monde. Selon encore l'OMS, le nombre de décès causés par les maladies cardiaques devrait augmenter à plus de 20 millions par an d'ici à 2020 et à plus de 24 millions à 2030 [Allender *et al.*, 2008; Hoyert *et al.*, 2009; Roger *et al.*, 2011; Nichols *et al.*, 2012]. En raison de leur prolifération et de leur taux élevé de mortalité, les maladies cardiaques deviennent le groupe de pathologies le plus coûteux: elles représentaient 16% des dépenses totales de santé en 2008 [Roger, 2011]. Par conséquent, d’un point de vue de la santé et des perspectives économiques, il est fondamental et important de développer des techniques qui permettent une meilleure compréhension des structures et des fonctions cardiaques a priori avant l'insuffisance cardiaque.

La fonction myocardique est fondamentalement liée à son architecture fibre spécifique. Par exemple, la propagation de l'activité électrique est plus rapide le long de l’orientation des fibres et plus lente à travers les fibres [Jouk *et al.*, 2007], et au niveau cellulaire, la contraction se produit le long de la direction de l'axe longitudinal des faisceaux myocytes et conduit à l'épaississement transmural et raccourcissement de apex-base après les réarrangements grâce à des interactions avec la matrice extracellulaire de collagène. En outre, les fibres à travers les ventricules pourraient être un substrat pour les arythmies, y compris tachycardie ventriculaire et fibrillation, et la mort cardiaque subite, comme suggéré dans les études expérimentales et théoriques [Delon *et al.*, 2006; Collin *et al.*, 2006]. Tout cela témoigne de l'importance d’appréhender la relation entre les maladies cardiaques et l’architecture de fibres.

Notre première compréhension de l'architecture des fibres cardiaques est issue des mesures histologiques sur des régions du tissu sélectionnées [Ross *et al.*, 1979]. Ces techniques histologiques sont connues de souffrir de distorsion et de désalignement, et elles ne permettent pas la reconstruction tridimensionnelle (3D) des structures fibreuses. Afin de résoudre ces problèmes, l'imagerie en lumière polarisée (Polarized Light Imaging-PLI, en anglais) a été proposée pour obtenir les orientations des fibres dans des cœurs de fétus *ex vivo* [Jouk *et al.*, 1995; Jouk, 2007]. Cette technique fournit une carte d'orientation 3D des fibres myocardiques à haute résolution spatiale (0,1 mm x 0,1 mm x 0,5 mm). Par rapport aux méthodes de dissection et histologiques, il est plus objectif, car elle n'implique aucune opération humaine durant le processus de mesure. Cependant, les deux techniques histologiques et PLI sont *ex vivo* et ne peuvent pas être utilisées pour étudier l’architecture des fibres *in vivo* du cœur humain.

Plus récemment, l’imagerie par résonance magnétique de diffusion (IRMd) [Le Bihan *et al.*, 1985], qui comprend l’imagerie du tenseur de diffusion (DTI) [Kingsley, 2006a, 2006b, 2006c] et l’imagerie de diffusion en haute résolution angulaire (HARDI) [Tuch, 2002, 2004; V Wedeen *et al.*, 2005; Assemlal *et al.*, 2011; Descoteaux *et al.*, 2011], a émergé comme une technique nouvelle et prometteuse pour analyser la structure des fibres des tissues en 3D. Cette approche a été largement appliquée dans le cerveau humain [Tuch *et al.*, 2002; Beaulieu, 2002; Assaf *et al.*, 2005, 2008c; Tristán-Vega *et al.*, 2010; Douaud *et al.*, 2011]. Cependant, seules quelques études ont été réalisées sur le cœur et la plupart d'entre eux se concentraient sur l'imagerie ex vivo [Helm *et al.*, 2005; Healy *et al.*, 2011; Englund *et al.*, 2011]. Malgré quelques tentatives sur DTI cardiaque *in vivo* [Gamper *et al.*, 2007; Rapacchi *et al.*, 2009; Toussaint *et al.*, 2010; Nielles-Vallespin *et al.*, 2012; Mekkaoui *et al.*, 2012; Delattre *et al.*, 2012], il n'est actuellement pas possible d'obtenir l'architecture des fibres d'un cœur entier *in vivo* à cause des propriétés mêmes du tissu myocardique et de la sensibilité au mouvement. De plus, comme la vérité-terrain n'est pas disponible sur la structure des fibres myocardiques, il est difficile d'évaluer dans quelle mesure les caractéristiques de diffusion calculées à partir de l'IRM de diffusion reflètent les propriétés microscopiques réelles des fibres myocardiques.

Dans ce contexte, la simulation numérique de l'IRMd offre une approche alternative pour aborder le problème. Dans ce cadre, des modèles de simulation à l'aide des données synthétiques ont été développés. Les données synthétiques, contrairement aux données réelles, fournissent la réalité de terrain, ce qui nous permet d'évaluer et d'optimiser les méthodes utilisées. L'approche numérique la plus courante pour la synthèse des données d'IRMd est le modèle de Monte-Carlo (MC) [Cai *et al.*, 2005; Assaf *et al.*, 2008a; Fieremans *et al.*, 2010; Yeh *et al.*, 2011; Schmitt *et al.*, 2012]. Mais, en raison de la limite en ressource de calcul et de l'absence de connaissances sur la structure des fibres cardiaque, toutes les simulations de MC existantes ont été effectuées jusqu'à présent sur des objets de géométrie simple et utilisées la plupart du temps pour analyser le coefficient de diffusion. À notre connaissance, il n'existe pas encore des images de diffusion simulées avec la méthode MC pour les fibres cardiaques.

L'objectif principal de cette thèse est de simuler les images d'IRMd des fibres cardiaques à la fois *ex vivo* et *in vivo*, en utilisant la méthode de MC et en combinant plusieurs modalités d'imagerie. L'idée consiste à modéliser tout d'abord les structures virtuelles des fibres cardiaques (VCFS) 3D à partir des données de lumière polarisée, et à simuler le comportement de diffusion des molécules d'eau dans les VCFS avec la méthode de MC qui nous permet de calculer à la fin des images de diffusion. Comme ce type de simulations implique un très grand nombre de molécules d'eau, nous allons recourir à la grille de calcul pour faire face aux besoins d'énormes ressources de calcul. Le mémoire de cette thèse est organisé ci-dessous avec les contributions principales mises en caractères gras.

La première partie de cette thèse est consacrée à la présentation des fondements médicaux de l'imagerie cardiaque et à la méthodologie de notre travail:

Le chapitre 1 décrit les notions d'anatomie et de physiologie cardiaques et l'organisation architecturale du cœur humain en multi-échelles.

Le chapitre 2 expose en détail le principe de l'imagerie par résonance magnétique de diffusion et de l'imagerie par lumière polarisée.

Le chapitre 3 résume l'état de l'art sur les modélisations et les simulations de l'IRMd. Selon les moyens d'analyse, nous classons les méthodes en trois grandes catégories et comparons brièvement leurs avantages et inconvénients.

La seconde partie est dédiée aux contributions méthodologiques:

Les travaux présentés au chapitre 4 portent sur **la simulation de l'IRMd pour un simple modèle de fibres cardiaques virtuel en utilisant la méthode de Monte-Carlo et sur une première compréhension de la relation sous-jacente entre les propriétés de l’anisotropie de diffusion et les caractéristiques à la fois physiques et structurelles des fibres cardiaques.** Dans ce chapitre, nous présentons tout d'abord l'algorithme de simulation de l’IRMd, qui est une approche de Monte-Carlo sur la base de la marche aléatoire et le modèle de collision. Afin d'analyser l'influence des caractéristiques physiques et structurelles des fibres cardiaques sur les propriétés de diffusion, deux VCFS sont modélisées. Pour l'analyse des caractéristiques physiques, le myocyte cardiaque est représenté par la combinaison d'une série d'hexagones, qui nous permet de changer facilement la forme de l'espace intra- et extracellulaires. Pour l'analyse des caractéristiques structurelles, les myocytes sont modélisés par des cylindres qui nous permettent de varier aisément l’orientation et la disposition de fibres. Après l’étape de modélisation, les images pondérées en diffusion et le tenseur de diffusion sont simulés pour les deux VCFS différentes ci-dessus, à partir desquelles l'orientation des fibres et l'anisotropie fractionnelle sont estimées et les effets des propriétés physiques et structurelles sur la diffusion à différentes échelles sont analysés. Ce chapitre fournit une base théorique pour les chapitres suivants.

Pour mieux comprendre la relation entre les structures de fibres cardiaques réelles et les propriétés de diffusion mesurées en utilisant notre simulateur d’IRMd, dans le chapitre 5**, nous construisons un modèle réaliste de fibres cardiaques à partir des données provenant de PLI. Avec les données PLI, les images de diffusion des fibres cardiaques à différentes échelles sont simulées et la relation entre les différentes échelles est interprétée. Ainsi, en utilisant notre simulateur, nous analysons la variation des propriétés de diffusion pour différentes structures de fibres qui imitent de possibles pathologies.** Nous présentons d’abord brièvement le processus d’acquisition en PLI. Ensuite, à partir des données PLI, des modèles des fibres cardiaques à différentes échelles sont construits. Enfin, les images de diffusion pondérées correspondant aux différents modèles sont simulées. La comparaison des propriétés de diffusion à différentes échelles, comme FA and MD, nous permet de comprendre la relation entre la variation des microstructures et les propriétés de diffusion observées à l'échelle macroscopique. C’est la première fois que l’on intègre les deux modalités d’imageries pour interpréter l’architecture des fibres cardiaques du cœur humain en multi-échelle. En outre, en modifiant les paramètres du modèle de fibres, les images pondérées en diffusion et les indices de diffusion pour une architecture de fibres imitant de possibles pathologies peuvent être simulées, ce qui nous permettrait d’élaborer la corrélation entre la maladie cardiaque et les propriétés de diffusion.

Le chapitre 6 **se focalise sur l’étude de l’influence des paramètres d’imagerie sur FA, MD et l’orientation des fibres.** L’architecture des fibres cardiaques est généralement reconstruite à partir de l'orientation des fibres estimée à chaque voxel de l’image de diffusion en utilisant des algorithmes de tractographie de fibres, et la maladie cardiaque peut être généralement étudiée en termes d’indices de diffusion, tels que le coefficient apparent de diffusion (ADC), l'anisotropie fractionnelle (FA), et la fonction de distribution d’orientations (ODF-Orientation Distribution Function en anglais). La fiabilité de reconstruction des structures de fibres et de calcul des indices de diffusion dépend de la précision de l’estimation des orientations des fibres dans chaque voxel, qui à son tour dépend des méthodes d'estimation utilisées, des paramètres d'imagerie et de la qualité des images pondérées en diffusion. Afin d'obtenir une vision qualitative de l'influence des paramètres d'imagerie sur les propriétés de diffusion des fibres cardiaques, nous proposons dans ce chapitre d'étudier ces influences au moyen de notre simulateur d'IRMd. En fonction des propriétés des séquences d'impulsion d'imagerie, trois types de simulations et d'analyses sont effectués. Nous utilisons tout d'abord le gradient de diffusion parfait pour simuler les images pondérées en diffusion et pour analyser l'influence du temps de diffusion, de l'amplitude et de la durée du gradient de diffusion sur des indices de diffusion. Ensuite, en tenant compte des caractéristiques réelles de l'impulsion de gradient de diffusion, nous améliorons la théorie de la simulation et analysons l'influence du temps de diffusion, du temps de rampe et de la durée du gradient de diffusion sur des indices de diffusion. Enfin, les effets sur les propriétés de diffusion des gradients d'imagerie comprenant le gradient de sélection de coupe, le gradient de codage de phase et le gradient de lecture sont simulés.

Dans le chapitre 7, **nous proposons d'utiliser notre simulateur pour simuler les images de diffusion des fibres cardiaques *in vivo*.** L'IRMd *in vivo* pour les fibres cardiaques en 3D reste actuellement toujours un défi à cause de sa sensibilité aux variations de phase de spin, causées par le mouvement du cœur. De nombreuses approches sur l'acquisition ont été proposées pour obtenir des images de diffusion *in vivo*. Mais, en raison du mouvement rapide du cœur, ces techniques se limitent actuellement à une seule coupe en 2D, et il fallait utiliser un modèle d'extrapolation pour obtenir des volumes 3D *in vivo*. Afin de résoudre ce problème et de mieux comprendre la relation entre le mouvement cardiaque et les propriétés des images pondérées en diffusion, nous proposons de simuler les images de diffusion des fibres cardiaques *in vivo* à l'aide de notre simulateur d'IRMd. L'idée consiste à modéliser d'abord l'architecture des fibres cardiaques *in vivo* en utilisant une structure de fibres cardiaques référentielle et un champ de mouvement cardiaque bien connu, simuler ensuite les images de diffusion à les instants différentes, et étudier enfin la variation de l'intensité du signal pour une certaine position et l'influence du mouvement cardiaque sur les propriétés de l'architecture des fibres cardiaques telles que l'orientation des fibres, FA et MD.

La troisième partie résume les conclusions et les perspectives.

Part I

Medical and methodological background

Chapter 1

The multi-scales anatomical structure of the heart

Contents

Résumé en français

Afin de bien comprendre le contexte de cette thèse, dans ce chapitre nous introduisons les structures du cœur en multi-échelles et certaines caractéristiques des structures musculaires en cas de pathologie cardiaque.

Le cœur est composé par les cavités (*ventricule gauche, ventricule droit, oreillette gauche, et oreillette droite*), les valves (*la valve tricuspide, la valve mitrale, la valve pulmonaire, et la valve aortique.*) et la paroi (l'endocarde, le myocarde et l'épicarde). Sachant que la plupart des pathologies cardiaques concernent les structures de la paroi, en particulier l'architecture du myocarde. Ces structures de muscles cardiaques sont présentées en détailles à partir de deux échelles.

À l'échelle mescoscopique, on s'intéresse uniquement à l'arrangement des fibres cardiaques. De nombreux modèles décrivant la structure du myocarde existent, dans ce chapitre nous en présentons plusieurs.

- Le modèle de bande du myocarde

  Torrent-Guasp considère les parois ventriculaires comme une bande orientée dans l'espace suivant une hélice formée par des boucles basale et apicale, qui se replient pour former les cavités ventriculaires.

- Le modèle géodésique

  Streeter décrite le myocarde ventriculaire comme un continuum dans lequel l'orientation des myocytes varie doucement à travers la paroi ventriculaire de l'épicarde à l'endocarde, Sa conjecture sur l'architecture du cœur : les fibres du myocarde courent comme des géodésiques sur un ensemble imbriqué de corps torique de révolution.

- Le modèle pretzel

  Jouk, en quantifiant la direction des fibres sous forme de cartes d'angles d'azimut et d'élévation, propose le modèle des géodésiques imbriquées de pretzel pour l'architecture des fibres du cœur, et considère les fibres du myocarde comme des géodésiques sur un ensemble imbriqué de « pretzels » déformé. Ce modèle est une extension à toute la masse ventriculaire du modèle de Streeter, qui était limité au ventricule gauche.

- La modèle de feuilles laminaires

  Les modèles ci-dessus appartiennent à la classe des modèles continus qui supposent que les propriétés matérielles du myocarde ventriculaire sont transversalement isotropes par rapport à l'axe des myofibrilles, traduisant l'opinion selon laquelle les myocytes voisines sont couplées de manière uniforme. Cependant, LeGrice et ses collaborateurs ont démontré que le myocarde ventriculaire est structurellement orthotrope, avec les myocytes disposées en couches distinctes connues sous le nom de feuilles laminaires, d'environ quatre cellules d'épaisseur et séparées par un réseau de collagène extracellulaire.

À l'échelle microscopique, on présente la structure des myocytes cardiaques. Elles sont le composant principal du muscle cardiaque, représentant environ 70% de son volume. Les myocytes cardiaques d’environ 10-20 µm de large et 80-100 µm de long sont striées, binucléés, unies par des disques intercalaires. Elles sont entourées par l’espace extracellulaire.

Le groupe d'affections qui endommagent directement la paroi musculaire du cœur est connu sous le vocable de cardiomyopathie. En fonction de la nature de l’anomalie du muscle cardiaque et des changements structurels qui en résultent, il existe trois types de maladie non-ischémique du muscle cardiaque, Il s’agit des myocardiopathies dilatée congestive, hypertrophique et restrictive qui sont présentées brièvement dans ce chapitre.

1.1 Introduction

The heart is one of the most important organs in the human body, which pumps the blood, nutrition and oxygen to the other parts of the body by the powerful heart muscle contraction. Actually, this pump is a highly complex system, with intrinsic different cell type distributions, complex electro-mechanical properties and an organized activity sequences. Any change in this system may have significant effects on the cardiac function. Therefore, as any other pump, it can become clogged, break down and need repair. Each year heart diseases cause almost 25% deaths [Roger, 2011], thus it is very critical to learn about the heart structure and its functions for both understanding the heart disease symptoms and investigating the effective therapy means. In this chapter, we illustrate the heart structures from macroscopic scale to microscopic scale and introduce some cardiac diseases related to the cardiac muscle structure.

1.2 Heart structure observed at macroscopic scale

It is well known that the heart has the size of a fist and lies in the thoracic cavity. The base of the heart is the wide superior portion of the heart from which the great vessels emerge, and the apex of the heart is the inferior end pointing to the left. Generally, shown as in Fig. 1.1, the heart can be divided mainly into three different parts, chambers, valves and cardiac wall according to their physical properties and functions. In the following paragraphs, we explain them in details.

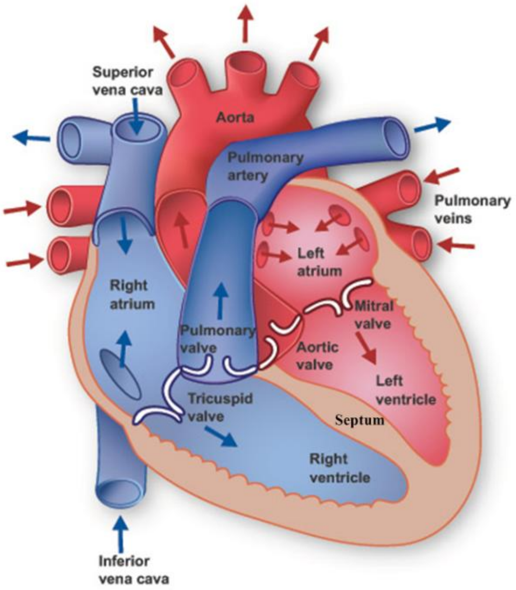

Fig. 1.1 Heart anatomical structure at macroscopic scale
http://www.texasheartinstitute.org/hic/anatomy/anatomy2.cfm

1.2.1 Chambers

The whole human heart has four chambers and is divided into right and left sides. Each side has an upper chamber called an atrium and a lower chamber called a ventricle. These four chambers constitute the blood circulation system of the body, where the chambers in the right side pump the deoxygenated blood and those in the left side pump the oxygenated blood.

Right atrium: It situates in the upper right section of the heart, receiving the de-oxygenated blood from the other parts of the body though two major veins, the superior vena cava and the inferior vena cava. The superior vena cava returns de-oxygenated blood mainly from the head, neck, arm and chest regions of the body to the right atrium. The inferior vena cava returns de-oxygenated blood from the lower body regions such as legs, back, abdomen and pelvis to the right atrium. The right atrium also pumps blood through the tricuspid valve into the right ventricle situated below.

Right ventricle: Located below the right atrium, this chamber has a form of triangle and extends from right atrium to near the apex of the heart. It receives blood from the right atrium and pumps it to the main pulmonary artery. The main pulmonary artery extends from the right ventricle and branches into left and right pulmonary arteries, which extend to the lungs, here oxygen-poor blood picks up oxygen and is returned to the heart via the pulmonary veins.

Left atrium: This chamber sits opposite to the right atrium. The blood went through the lung becomes oxygenated, it returns into the left atrium via the right and left pulmonary veins and then the left atrium pumps this oxygen-rich blood into the left ventricle through the bicuspid valve or mitral valve.

Left ventricle: It is the lower part of the heart in the left side. Compared with the right ventricle, it is much longer and looks like a cone. It receives oxygen-rich blood from the left atrium above it, and pumps it through the aortic valve to be distributed throughout the entire body via the aorta, including to the heart muscle itself through the coronary arteries.

The left side of the heart is thicker than the right one because of the requirement to pump blood from the left side throughout the body, as opposed to the right side pumping only through the lungs.

1.2.2 Valves

The blood circulating in the heart must flow in the right direction: this is guaranteed by the heart valves. Four main valves determine the pathway of blood flow and allow the chambers of the heart to carry out their functions efficiently. These four valves can be classified into two groups, one is the atrioventricular valves and the other is semilunar valves.

Atrioventricular valves

The valves that allow the blood to flow from the atria to the ventricles are called atrioventricular valves, which keep the blood from returning to the atrium. They are located between the atria and the ventricles. Named after the left and right side, atrioventricular valves can be divided into two types: tricuspid valve and mitral valve. The **tricuspid valve** is located between the right atrium and the right ventricle. The purpose of this valve is to open when the right atrium is in systole phase, thereby forcing any additional de-oxygenated blood into the ventricle. The **mitral valve** is located between the left atrium and the left ventricle. Similar to the tricuspid valve, during the atrium's systole phase, the valve is forced open to allow the oxygenated blood from the lungs to enter into the left ventricle.

Semilunar valves

There are two kinds of semilunar valves, one is **pulmonary valve**, which sits between the right ventricle and the pulmonary artery, the other is **aortic valve** which is located at the exit of the aorta and the left ventricle. Either of two valves opens and closes to allow the unidirectional flow of blood out of the heart, while preventing the blood flowing back into the ventricles.

1.2.3 Cardiac wall

Generally, the cardiac wall consists of three tissues layers: epicardium, myocardium and endocardium, shown as in Fig. 1.2. Each layer is specialized in its structure and function. Thus, all three layers function together to ensure proper functioning of the heart and to ensure that it pumps blood properly to all organs in the body. Given below are details about the structures and functions of these three layers.

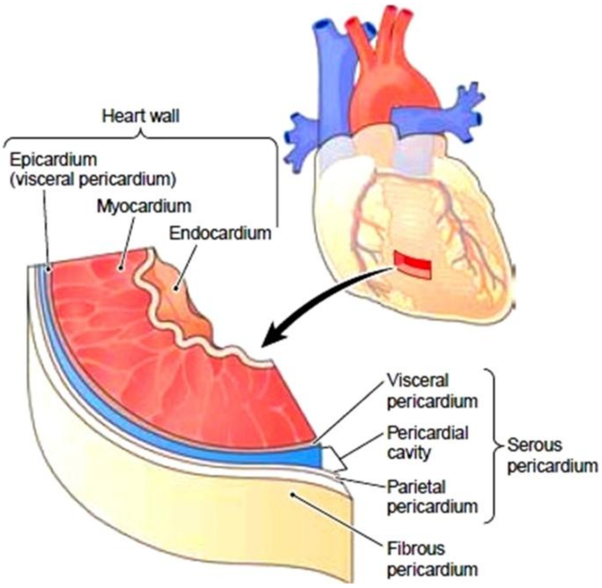

Fig. 1.2 Heart wall structure
http://encyclopedia.lubopitko-bg.com/Structure_of_the_Heart.html

Epicardium

Epicardium describes the outer layer of heart tissue, when considered as a part of pericardium, it is the inner layer and called visceral pericardium. It is composed of a single sheet of squamous epithelial cells overlying delicate connective tissue. Epicardium serves as a protection layer because it can produce a pericardial fluid, which lubricates motion between the inner and outer layer of pericardium

Myocardium

The myocardium is the basic muscle that makes up the heart. This muscle is involuntary and, this is striated in nature. The cardiac muscle structure consists of basic units of cardiac muscle cells known as myocyte. Coordinated contraction of the cardiac muscles is what makes the heart propel blood to various parts of the body. It is the function of the coronary arteries to supply blood and oxygen to the cardiac muscles. This is the thickest of all the layers. As is common knowledge, the cardiac muscle function is to ensure that the heart beats around 72 times per minute. Thus, the cardiac muscles cannot afford to rest even for a single second. Therefore, it is essential that these muscles get blood supply and nutrition continuously, as any kind of disruption in the blood and nutrition supply to these muscles can result in death of a part of the cardiac muscle, which is known as myocardial infarction or heart attack. This could in turn lead to a complete cessation of functioning of the heart muscles, known as cardiac arrest.

Endocardium

The endocardium is the innermost, thin and smooth layer of epithelial tissue that lines the inner surface of all the heart chambers and valves, which is responsible for prolonging myocardial contraction.

1.3 Myocardium structure at mesoscopic scale

In the three layers of the heart wall, the myocardium layer is the most important one for maintaining the heart normal functions. There are numerous models describing the structure of myocardium, here we present several well-known ones.

1.3.1 Myocardial band model

The helical ventricular myocardial band (HVMB) concept, proposed in 1972 by the Spanish scientist Francisco Torrent-Guasp [Torrent-Guasp, 1973], brings a new light on the architecture of ventricular myocardium. This idea is presented based on the helical rope model, which provides an elegant way to demonstrate the configuration of myocardium, shown in Fig. 1.3.

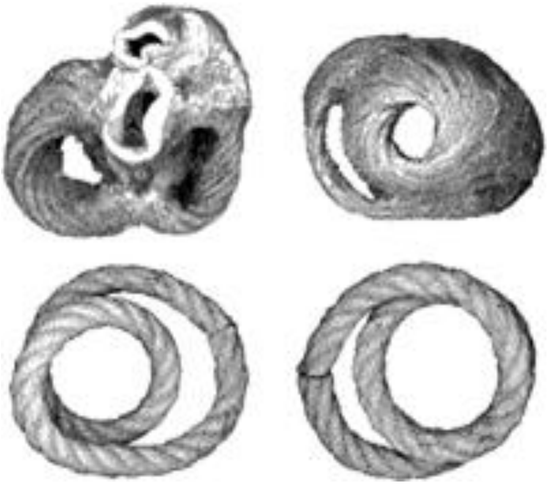

Fig. 1.3 Helical rope model of myocardium

This model describes the myocardium structure with a hierarchy of helical ropes whose length varies with the position in the base-apex direction. The rope orientation reveals the cross-sectional and two-dimensional relationships between LV and RV walls. However, the absence of the visible branching connections between rope bundles is the major weakness of this model. In order to deal with this problem, the HVMB model [Torrent-Guasp *et al.*, 2001a, 2001b; Corno *et al.*, 2006] was brought up. HVMB takes the myocardium as a muscular band twisted and curled in two helical loops: the basal loop (from the root of the pulmonary artery to the beginning of the central fold) and the apical loop (from the beginning of central fold to the root of aorta). Each of these two loops is further divided into two segments, where the basal loop is divided into the right segment (RS) which coincides with the RV wall and the left segment (LS) that coincides with the LV wall, the apical loop is divided into descendent (DS) and ascendant segments (AS), shown in Fig. 1.4.

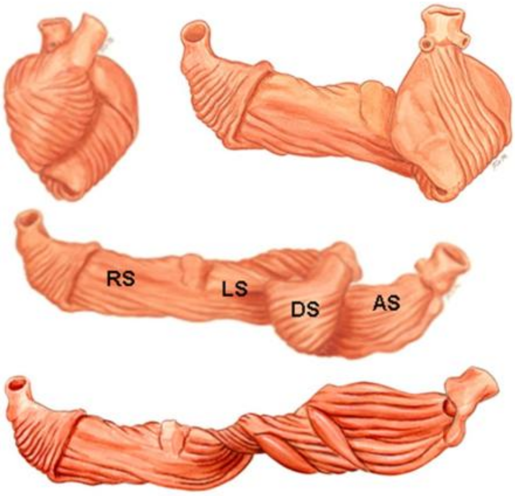

Fig. 1.4 Torrent-Guasp's myocardial band model

HVMB provides us a perceptual recognition about the myocardium muscular trajectories by the dissection means and gives some reasonable explanations about the heart electrical and mechanical properties and functions. It is very important for evaluating the other means for investigating the myocardium muscle orientations.

1.3.2 Geodesic model

Geodesic cardiac fiber model is firstly proposed by Streeter [Streeter, 1979], he stated that the myocardial fibers run like geodesics on a nested set of toroidal bodies of revolution. This mathematical expression is a little obscure for anatomist and cardiologist, therefore a few years ago, Jouk [Jouk, 2007] made a clear explanation about this model using the Fig. 1.5.

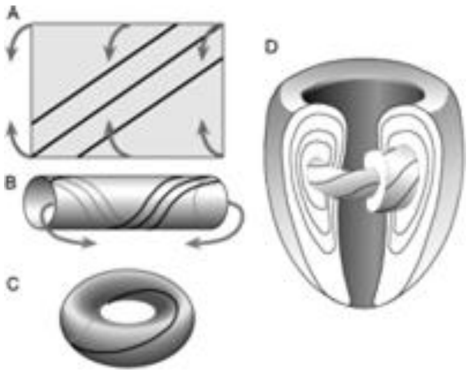

Fig. 1.5 Geodesic model

Firstly, take a piece of paper and draw three parallel lines, these lines could be considered as the geodesics of the plane surface. Secondly, roll the paper making the superior border against the inferior border and forms a cylinder, the drawn lines in the first step becomes the geodesics of the cylinder. Thirdly, bend the cylinder until the left reaches the right end, a torus will be generated and the lines are still geodesics. Finally, Streeter's conjecture supposed that from inner to outer the myocardial muscle nested by the elongated tori like Russian dolls, as shown in Fig. 1.5 D.

Streeter's model gives only the cardiac fiber map of LV. As an extension of Streeter's conjecture, Jouk proposed the pretzel model [Jouk, 2007] which describes the fiber architecture of the whole ventricular mass, illustrated in Fig. 1.6.

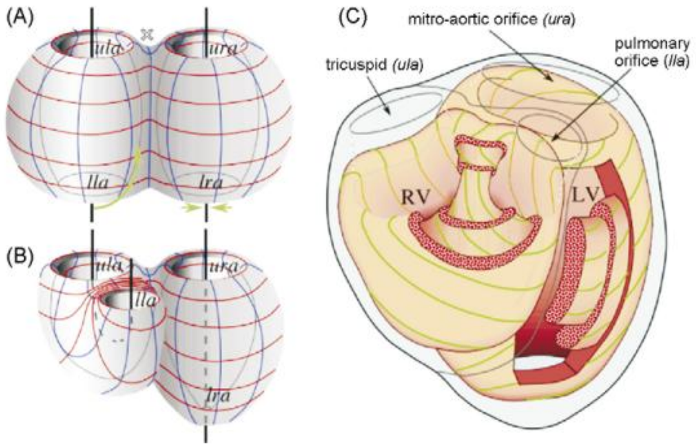

Fig. 1.6 An extension of geodesic model: pretzel model. Like the pretzel cookies, two joined torus form a pretzel in this model. For better understanding the further deformations, a lattice was drawn, where the lines in red are parallel to the surface of revolution, and those in blue are the meridians, as shown in subfigure (A). Four special positions are defined: lower left aperture (lla), lower right aperture (lra), upper left aperture (ula) and upper right aperture (ura). For mimicking the right ventricle structure, the torus on the left was bent in such a way that the lower aperture comes up to the upper aperture. However, for the left ventricle, it is mimicked by shrinking the lower right aperture into a point, as shown in subfigure (B). In subfigure (C), it explains how LV and RV could nest together and form a pretzel model, where the green lines represent the geodesic on the nested pretzels.

Compared to the Streeter's conjecture, this model gives not only the same description for the LV myocardial structure, but also provides a new recognition about the fiber arrangement of the RV. The upper left aperture would correspond to the tricuspid orifice and the lower left aperture to the pulmonary orifice. Between these apertures is the supraventricular crest. In this representation, it is given by the narrow part of the nested bent tori, while the wide part of the bent tori corresponds to the septal and lateral walls of the right ventricle. Up to now, this model still requires the mathematical and experimental validations.

1.3.3 Laminar structure model

The both two models above belong to continuum model which assumed that the material properties of ventricular myocardium are transversely isotropic with respect to the myofiber axis, reflecting the view that neighboring myocytes are uniformly coupled. However, LeGrice and coworkers [Legrice *et al.*, 1997] demonstrated that ventricular myocardium is structurally orthotropic, with myocytes arranged in layers that are typically four cells thick, as shown in Fig. 1.7. Adjacent layers are separated by cleavage planes that have a characteristic radial orientation in base-apex ventricular section and are significant in extent, particular in the LV mid-wall. Therefore, at any point within the ventricle, it is possible to define three structurally based material axes: (i) the fiber orientation, (ii) perpendicular to fiber orientation within a muscle layer, and (iii) normal to the muscle layer.

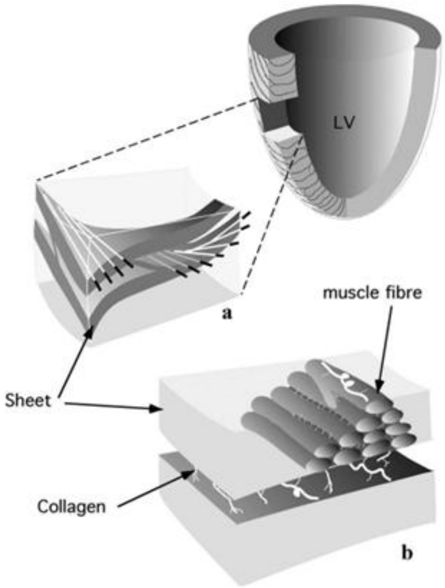

Fig. 1.7 Schematic of laminar structure model for cardiac fiber

Using these three axis representing the cardiac fiber orientation of dog and pig, the results conform to the anatomy structure, thus it has been proved the existence of lamina [Legrice *et al.*, 1995].

1.4 Cardiac myocyte structure at microscopic scale

The cardiac muscle cell or myocyte is the main structural component of myocardium, occupying around 70% of ventricular wall volume under normal circumstances [Villarreal, 2004]. Cardiac myocytes resemble ellipsoid cylinders with a major-axis dimension of 10 to 20 μm and a length of 80 to 100 μm [Severs, 2000]. Myocytes are brunched and connected end to end by the intercalated disk, besides they are also connected with extracellular matrix (ECM) to form a three dimensional network of cells, as shown in Fig. 1.8.

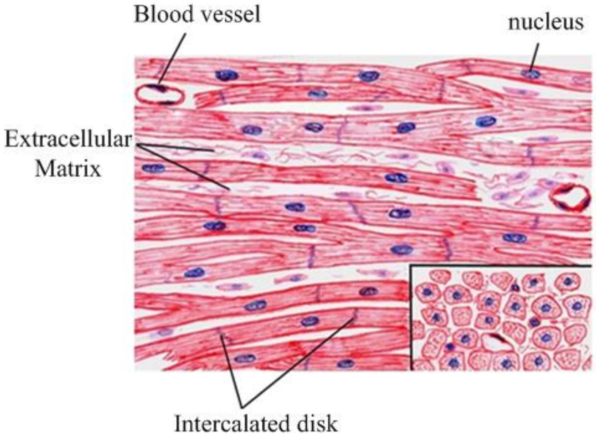

Fig. 1.8 Schematic of cardiac muscle structure
http://www.vetmed.vt.edu/education/curriculum/vm8054/labs/lab12a/lab12a.htm

For better understanding the myocyte structure and its arrangement, we will elaborate in details the myocyte components and the extracellular matrix.

1.4.1 Myocyte

From outside to inside, the myocyte structure can be divided into basement membrane, sarcolemma, sarcoplasmic reticulum, myofibrils and mitochondria. An illustration of this structural organization is shown in Fig. 1.9.

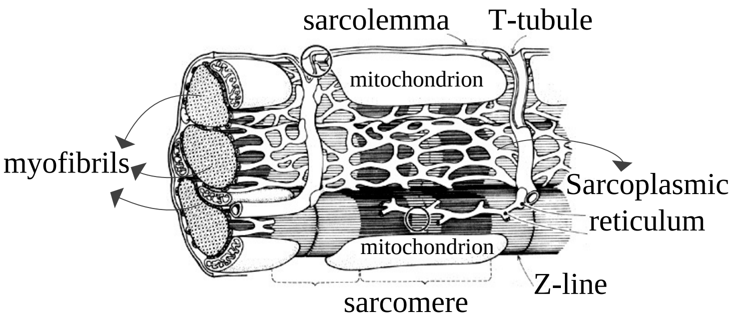

Fig. 1.9 Anatomic structure of cardiac myocyte [Walker *et al.*, 1999]

Basement Membrane

Basement membrane is the first layer that encountered when we isolated the myocyte from the extracellular space. It is composed primarily of type IV collagen, the glycoproteins laminin, fironectin and proteoglycans. The function of the basement membrane is to provide an initial barrier that will influence the exchange of macromolecules between the extracellular space and the myocyte, and it serves as an interface for guaranteeing the myocyte adhesion and continuity with the extracellular matrix.

Sarcolemma

Sarcolemma is a specialized structure of myocyte. It is a cellular membrane looks like the basement membrane to which it is attached. However, the difference between them is that the sarcolemmic membrane acts as a conductor for electrical stimuli passing through muscle cells. The sarcolemma is composed of a lipid bilayer, which contains hydrophilic heads and hydrophobic tails. This configuration allows the sarcolemma to interact with the intracellular and extracellular environment, but a hydrophobic core results in the sarcolemma being impermeable to charged molecules.

In the cardiac myocyte, sarcolemma forms 2 specialized regions named intercalated disks and the transverse tubular system (T-tubule). The intercalated disks make two myocytes connected end to end and they serve as a path of low resistance that allows for rapid conduction of the action potential between myocytes. T-tubule is invaginations of the sarcolemma into the myocyte, which form a barrier between the intracellular and extracellular space.

As most of lipid bilayers, the fundamental function of the sarcolemma is to provide a barrier for diffusion. The sarcolemma also contains membrane proteins, which include receptors, pumps, and channels. This is specialized feature of the sarcolemma and is essential to the contractile process of the myocyte.

Sarcoplasmic Reticulum

The sarcoplasmic reticulum, an endoplasmic membrane network, forms specialized structural regions of the myocyte in close opposite with the sarcolemma, particularly, the T-tubule. The sarcoplasmic reticulum is responsible for calcium transfer.

Myofibrils

Each myofibril is wrested by the T-tubule system, which contains many myofilaments. The myofibrils have distinct, repeating micro-anatomical units, termed sarcomeres, which represent the basic contractile units of the myocyte. The sarcomere is defined as the region of myofilament structures between two Z-lines. The distance between Z-lines (sarcomere length) ranges from about 1.6 to 2.2 μm in human hearts. The sarcomere is composed of thick and thin filaments – myosin and actin, respectively. Chemical and physical interactions between the actin and myosin cause the sarcomere length to shorten, and therefore the myocyte to contract during the process of excitation-contraction coupling.

Mitochondria

Mitochondria are specialized organelles directly responsible for several activities within cells, dealing with how nutrients cross the cellular membrane and are then synthesized and transformed into energy.

1.4.2 Extracellular Matrix

The myocardial ECM consists of macromolecules, primarily produced locally by fibroblasts, and includes a fibrillar collagen network, a basement membrane and proteoglycans [Polimeni, 1974; Kim *et al.*, 2000]. The fibrillar collagen network strengthens the matrix and ensures the structural integrity of adjoining myocytes. It provides the means allowing to translating the myocyte shortening into the overall ventricular pump function and contributing to myocardial diastolic stiffness. The basement membrane surrounds the myocyte is attached to the sarcolemma as well as to the fibrillar collagen network. It is postulated that myocyte adherence to basement membrane may be a major determinant in maintenance of cell shape and positional integrity within the ventricular wall. Proteoglycans are composed of a protein core to which polysaccharide chains called glycosaminoglycan are covalently bound.

The proteoglycan molecules in connective tissue thus form a highly hydrated, gel-like "ground substance" in which the fibrous proteins are embedded. The polysaccharide gel resists compressive forces on the matrix while permitting the rapid diffusion of nutrients, metabolites, and hormones between the blood and the tissue cells. Qualitatively, the composition of the ECM is similar in all tissues, however, it is unique, and reflects the physiology of that particular tissue.

1.5 Cardiac muscle diseases

Cardiac muscle diseases refer to a group of disorders that directly damage the muscle of the heart walls, also named cardiomyopathy. In these disorders, all chambers of the heart are affected. Depending on the nature of the injury of abnormality in the heart muscle and the resulting structural changes in the heart chambers, three types of non-ischemic heart muscle disease are described in this chapter, including dilated congestive, hypertrophic or restrictive.

1.5.1 Dilated congestive cardiomyopathy

This is the most common type of heart muscle disease. It is generally called either dilated or congestive cardiomyopathy. This type of disease damages the fibers of the heart muscle, weakening the walls of the heart's chambers [Jefferies *et al.*, 2010], as shown in Fig. 1.10. Usually, all chambers are affected, and depending on the severity of the injury, they lose some of their capacity to contract forcefully and pump blood through the circulatory system. To compensate for the muscle injury, the heart chambers enlarge or dilate. The dilation is often more pronounced in the left ventricle, the heart's main pumping chamber.

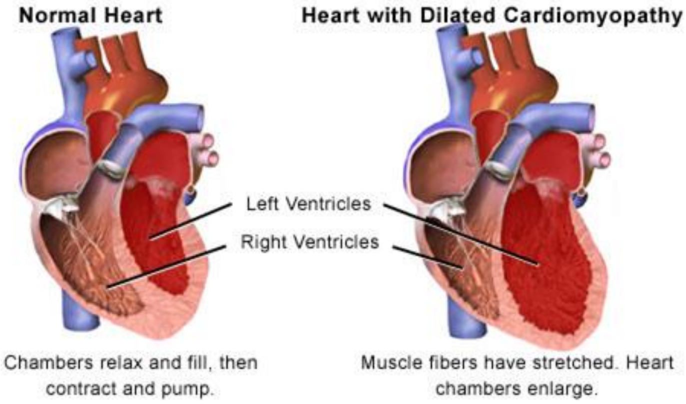

Fig. 1.10 Dilated Cardiomyopathy

http://www.allinahealth.org/mdex/ND0162G.HTM

1.5.2 Hypertrophic cardiomyopathy

This rare disease is the second most common type of cardiomyopathy. Hypertrophic cardiomyopathy [Maron, 1997] is also known as idiopathic hypertrophic subaortic stenosis (IHSS) or asymmetric septal hypertrophy (ASH). It is characterized by a disorderly growth of heart muscle fibers causing the heart chambers to become thick-walled and bulky, see Fig. 1.11.

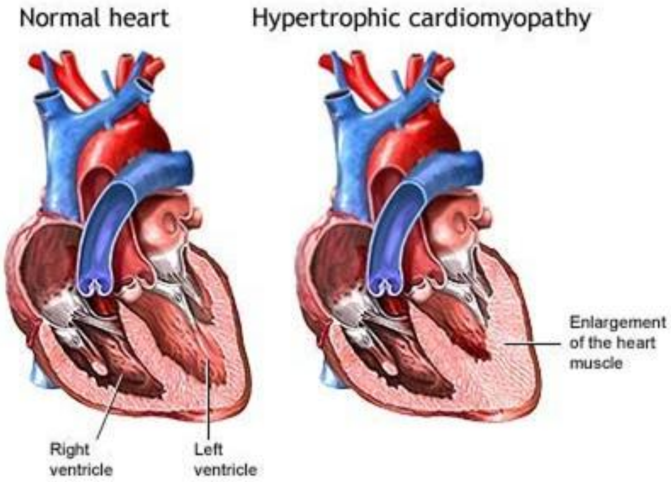

Fig. 1.11 Hypertrophic cardiomyopathy
http://www.umm.edu/imagepages/18141.htm

All the chambers are affected, but the thickening is generally most striking in the walls of the left ventricle. Most commonly, one of the walls, the septum, which separates the right and left ventricles, is asymmetrically enlarged. The distorted left ventricle contracts will cause the inadequate supply of blood to the brain and other vital organs. Mitral valve function is often disrupted by the structural abnormalities in the left ventricle with backward leakage of blood.

1.5.3 Restrictive cardiomyopathy

Restrictive cardiomyopathy is extremely rare. In this type of heart muscle disease, abnormal cells, proteins, or scar tissue infiltrate the muscle and structures of the heart, causing the chambers to become stiff and bulky [Kushwaha *et al.*, 1997] (Fig. 1.12). The heart may initially contract normally, but the rigid chambers restrict the return of blood to the heart. Consequently, high pressures are needed to fill the heart chambers, forcing the blood back into various tissues and organs—the lungs, abdomen, arms, and legs. Eventually, heart muscle is damaged and contractions impaired.

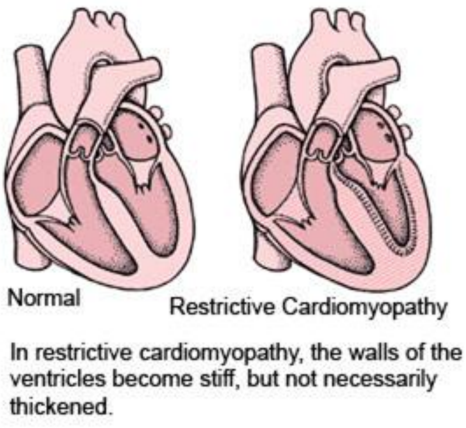

Fig. 1.12 Restrictive cardiomyopathy
http://trialx.com/curebyte/2011/08/28/photos-related-to-restrictive-cardiomyopathy

1.6 Conclusion

In this chapter, the heart structures from macroscopic scale to microscopic scale have been presented, especially, the architecture of heart wall and the cardiac fiber arrangement patterns have been described in details. It has been illustrated that most of cardiomyopathies affect the structure of ventricles, especially the left ventricle, thus investigating the cardiac fiber architecture in the left ventricle before and after heart disease becomes so significant for the clinical diagnosis and treatment.

Chapter 2

Imaging modalities

Contents

Résumé en français

Comme nous l'avons précisé dans le premier chapitre, analyser l'architecture des fibres cardiaques est l'un des plus importants moyens pour étudier la cardiomyopathie. Notre première compréhension de l'architecture des fibres cardiaques proviennent de l’histologie des tissus cardiaques dans une région sélectionnée. Ces techniques connues pour souffrir de distorsion et de désalignement, ne permettent pas la reconstruction en 3D des structures fibreuses. Pour résoudre ce problème, l'imagerie par lumière polarisée (PLI) a été proposée. Elle permet de détecter l’orientation des fibres du cœur *ex vivo*. Cette technique fournit une carte d'orientation des fibres myocardiques en 3D avec une haute résolution spatiale (0,1 mm x 0,1 mm x 0,5 mm). Par rapport aux méthodes de dissection et histologiques, l'imagerie par lumière polarisée est plus objective, car elle n'implique aucune opération humaine durant le processus de mesure. Cependant, les deux techniques histologiques et PLI sont *ex vivo* et ne peuvent pas être utilisées pour des études *in vivo* du cœur humain.

Plus récemment, l’imagerie par résonance magnétique de diffusion (IRMd), qui comprend l’imagerie du tenseur de diffusion (DTI) et l’imagerie de diffusion à haute résolution angulaire (HARDI), a été proposée comme une technique nouvelle et prometteuse pour analyser la structure des fibres *in vivo*. Mais la résolution spatiale de l’IRMd limitée par le système d’acquisition n'est pas assez fine pour observer les détails à des échelles très fines. Nous présentons en détail les méthodes d’imagerie PLI et IRMd dans ce chapitre, en soulignant leurs avantages et inconvénients pour les mesures *ex vivo* et *in vivo*.

- **L’imagerie par lumière polarisée (PLI)**

PLI produit des images dont le contraste est basé sur la dispersion de la lumière par l'ultrastructure d'un tissu, à savoir, des noyaux, des mitochondries, des membranes (un réticulum endoplasmique, d'autres organites) et des fibres comme le collagène ou l’actine-myosine. En général, le système de PLI se compose des éléments suivants : une source de lumière blanche, un premier filtre polarisant linéaire utilisé comme polariseur, un support pour maintenir le spécimen de tissu biréfringent à analyser, un autre filtre de polarisation linéaire qui agit comme analyseur et dont l’axe de polarisation est perpendiculaire à celui du polariseur et enfin une caméra CCD qui mesure la quantité de lumière transmise. Quand un échantillon biréfringent est positionné dans le trajet de la lumière polarisée, il interfère avec l'axe de polarisation de la lumière. Ainsi la quantité de lumière transmise est une fonction de la biréfringence de l'échantillon et de son orientation par rapport à la lumière.

- **L’imagerie par résonance magnétique de diffusion (IRMd)**

Dans ce chapitre nous introduisons d’abord le principe général de l’IRM, puis le phénomène de diffusion, et enfin la théorie de l’IRMd.

L’IRM mesure les propriétés magnétiques des tissus (principalement de l'eau et de la graisse) grâce à la différence des temps de relaxation et de densité de spins des protons ^{1}H suite à une excitation magnétique radio fréquence. Afin de bien comprendre les fondements physiques de l’IRM, nous introduisions brièvement les concepts de précession, de résonance et de relaxation. L’obtention d’une image à partir du signal magnétique de relaxation nécessite un codage spatial qui repose sur l’application successive de gradients de champ magnétique dans chaque direction spatiale, à savoir un gradient de sélection de coupe, le codage de phase, et le codage par la fréquence. Une séquence d’imagerie consiste en une série d’impulsions et de gradients. De nombreuses séquences d’acquisition d’IRM existent, mais nous nous limitons ici à la description des séquences d'écho de spin (SE) et d’écho de gradient (GE), qui sont les plus courantes.

Une fois le principe de l’IRM introduit, nous décrions les différents phénomènes de diffusion, à savoir la diffusion libre, la diffusion contrainte et la diffusion entravée. Le trajet parcouru par les molécules d’eau dans les tissus porte beaucoup d'informations sur l'architecture anatomique sous-jacente. L’imagerie par résonance magnétique pondérée en diffusion (en anglais, DWI) est utilisée pour détecter la façon dont l’eau diffuse dans les tissus afin de obtenir de précieuses information sur les structures sous-jacentes. La technique mesure la diffusion des molécules d'eau dans les tissus par l'atténuation du signal magnétique après déphasage et rephasage magnétique successifs dans des directions différentes (directions du gradient).

2.1 Introduction

As elaborated in the first chapter, one of the most important mean for investigating the cardiac diseases is to get information about the cardiac fiber architecture. Our first understanding of the cardiac fiber architecture comes from histological measurements of selected tissue regions [Ross, 1979]. Such techniques are known to suffer from distortion and misalignment, and they do not allow the 3D reconstruction of fiber structures. To cope with these problems, polarized light imaging (PLI) was proposed to detect fiber orientations in *ex vivo* human hearts [Jouk, 1995, 2007]. This technique provides a 3D orientation map of myocardial fibers with high spatial resolution (0.1mm x 0.1mm x 0.5mm). Compared with dissection and histological methods, it is more objective because it does not involve any human operation during the measurement process. However, both histological and PLI techniques are *ex vivo* and cannot be used for *in vivo* studies of the human heart.

More recently, Diffusion Magnetic Resonance Imaging (dMRI), which includes Diffusion Tensor Imaging (DTI) and High Angular Resolution Diffusion Imaging (HARDI), has emerged as a new and promising technique for analyzing the 3D fibrous structure of tissues. This approach has been extensively applied to the human brain. However, only a few studies have been performed on the heart [Hsu *et al.*, 2001; Helm, 2005; M-T Wu *et al.*, 2006; Toussaint, 2010]. dMRI is currently the unique potential method for noninvasively detecting the *in vivo* human cardiac fiber architecture, but due to the limitation of the MRI scanners, the spatial resolution of which is not good enough for observing the details. In this chapter we present mainly the PLI *ex vivo* imaging technique and the *in vivo* dMRI method with their respective advantages and limitations.

2.2 Polarized Light Imaging (PLI)

Polarized light imaging is a contrast-enhancing technique, well adapted to imaging birefringent materials. This technique is used in a broad range of disciplines, including medicine, biology, geology, materials science, and food industry etc. Recently, lot of works focus on fiber tracking. For instance, the white matter architecture was imaged by means of PLI [Larsen *et al.*, 2007; Palm *et al.*, 2010]. The 3D fiber structure of the brain with high spatial resolution using PLI was mapped [Axer *et al.*, 2011a, 2011b; Dammers *et al.*, 2012]. Reconstruction and signal enhancement methods for PLI used in fiber tracking were proposed [Dammers *et al.*, 2010; H Wang *et al.*, 2011]. An attempt to using PLI to investigate the cardiac fiber architecture was also raised [Jouk, 1995, 2007]. This section briefly introduces the PLI principle, its advantages, limitations, and the way it is used to measure 3D cardiac fiber orientations.

2.2.1 Polarization

Light is an electro-magnetic transverse wave, which propagates via the mutually perpendicular, fluctuating electric, and magnetic fields and vibrates in a direction perpendicular to the direction of propagation. Ordinarily a ray of light consists of a mixture of waves vibrating in all the directions perpendicular to its line of propagation. This kind of light is called “unpolarized” light. If for some reason the vibration remains constant in direction, the light is said to be “polarized”. There are varieties of methods for polarizing light and here we introduce three frequently used ones.

2.2.1.1 Polarization by use of a polaroid filter

The polaroid filter is made of a special material which has a long-chain molecules aligned in the same direction. The alignment makes the polaroid filter absorb light parallel to the direction of long-chain molecules, but transmits light perpendicular to it. As a result, the alignment of these molecules gives the filter a polarization axis, perpendicular to the alignment direction. This polarization axis only allows vibrations of the electromagnetic wave that are parallel to the axis to pass through, as shown in Fig. 2.1.

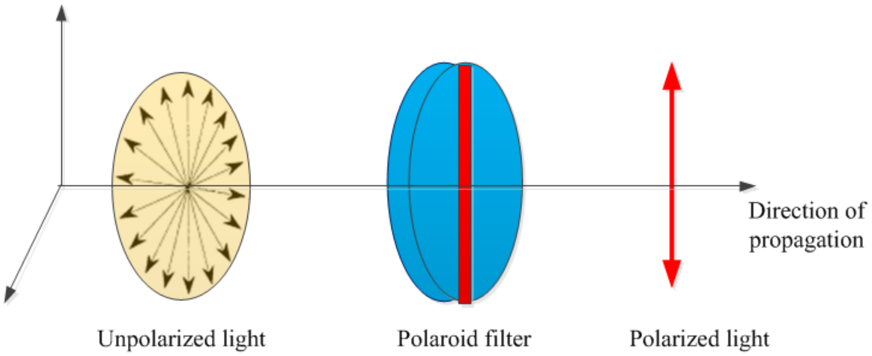

Fig. 2.1 Polarization by polaroid Filter

A polaroid filter often appears in pair in the polarized system, the first is used for generating the polarized light and the second serves as looking for the polarized direction. Slowly rotating the second filter until there is no light transmitted from it, at this moment, the polarization axes of these two polaroid filters are perpendicular to each other. If one sample is added between these two filters, sample will change the polarized direction of the light, and by rotating the second filter until the output light disappears again, the relative polarized direction of the sample to the first filter can be calculated.

2.2.1.2 Polarization by reflection

When unpolarized light encounters a boundary between two different media, some of it is usually reflected by the boundary and some of it is refracted. The fraction that is reflected is described by the Fresnel equations [Weisstein], and is dependent upon the incoming light’s polarization and angle of incidence. The Fresnel equations predict the light with p-polarization (with electric field direction parallel to the plane of incidence) will not be reflected, as shown in Fig. 2.2, if the incident angle satisfies:

$$\theta_B = \arctan(\frac{n_2}{n_1}) \tag{2.1}$$

where n_1 is the refractive index of the input medium1 and n_2 refractive index of medium2. Eq.(2.1) is known as Brewster’s law [Hecht, 1998], and the angle θ_B is defined as Brewster’s angle. The Brewster's angle is often referred to as the "polarizing angle", because the light reflected from the boundary at this angle is entirely polarized perpendicularly to the incident plane. A glass plate placed at Brewster's angle in a light beam can thus be used as a polarizer. This kind of polarizer is usually used for the sunglasses.

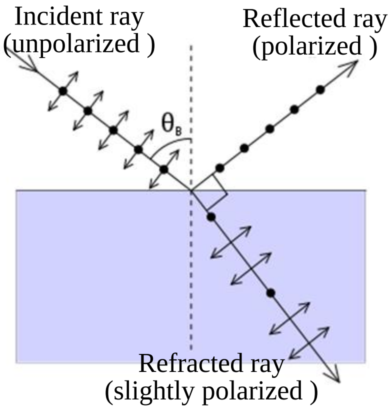

Fig. 2.2 Polarization by reflection
http://en.wikipedia.org/wiki/Brewste's angle

2.2.1.3 Polarization by double refraction

Double refraction, also called birefringence, is an optical property in which a single ray of unpolarized light entering an anisotropic medium is split into two rays, each one travelling in a different direction. One ray (extraordinary ray) is bent or refracted at an angle as it travels through the medium, the other ray (ordinary ray) passes through the medium unchanged. In double refraction, the ordinary and extraordinary rays are polarized in planes vibrating at right angles to each other, as shown in Fig. 2.3.

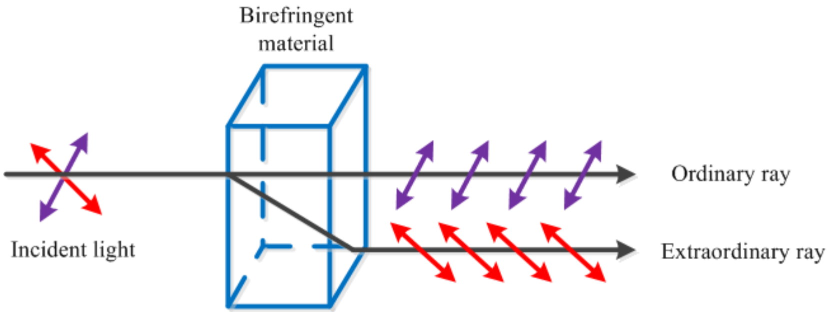

Fig. 2.3 Polarization by double refraction

This angle is determined by the incidence angle and the birefringence Δn :

$$\Delta n = n_e - n_o \tag{2.2}$$

where n_e is the refractive index of the extraordinary ray and n_o is that of the ordinary ray. The refractive index of the ordinary ray is constant in all directions, but the refractive index of the extraordinary ray varies according to the direction taken.

The polarized light generated by birefringent materials is usually used in the polarized light microscopy technique for detecting the properties of such materials. The detailed principle is given in section 2.2.2.

2.2.2 PLI system for cardiac fiber and its principle

2.2.2.1 PLI system

The principle of PLI is to use the polarization property of light to detect the birefringence of a material under study and consequently to infer its spatial structure. Generally, the PLI system is composed of the following elements: a white light source, a first linear polarizing filter served as the polarizer, a stage to hold the birefringent specimen, another linear polarizing filter acting as the analyzer whose vibration axis is perpendicular to that of the polarizer and finally a CCD camera that measures the amount of transmitted light, as shown in Fig. 2.4.

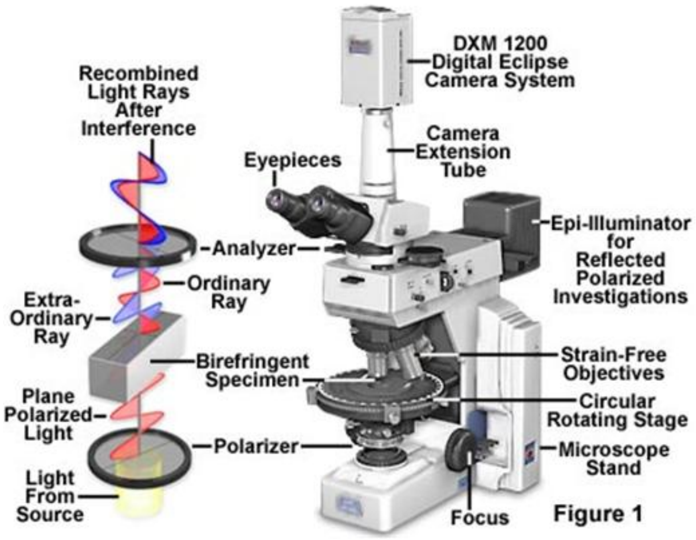

Fig. 2.4 The diagram of a PLI system configuration
http://www.microscopyu.com/articles/polarized/polarizedintro.html

In this setting, polarized light is not modified when an isotropic specimen or a birefringent sample with a main axis parallel to the light vibration axis is placed in the optical path. In such a case, light vibrates perpendicularly to the analyzer and no light comes out of it. On the contrary, when a birefringent sample is rotated in the polarized light, it interferes with the light vibration axis and some light is transmitted across the analyzer. Thus, the amount of transmitted light is a function of the birefringence that is related to the physic-chemical characteristics of the sample and its orientation with respect to the light.

2.2.2.2 Measuring cardiac fiber orientation using PLI

As illustrated in chapter 1, a cardiac fiber consists of myosin and collagen. Both of them exhibit optical birefringence, thus a cardiac fiber is a kind of anisotropic tissue and its structure can be measured by a PLI system. The birefringence of the myosin is positive and uniaxial, but that of collagen is negative, biaxial and highly variable according to its type. A PLI system is good at detecting the uniaxial birefringence but it is not elaborated enough to study biaxial birefringent material. The orientation of cardiac fiber being mainly determined by the uniaxial birefringence of myosin, it is necessary in a first step to eliminate the effects of the biaxial birefringence of collagen. This can be obtained by embedding the heart tissue in methyl methacrylate (MMA) [Jouk, 1995]. After removing the influence of the collagen, the birefringence of cardiac fiber can detected by PLI system, the principle is illustrated in Fig. 2.5.

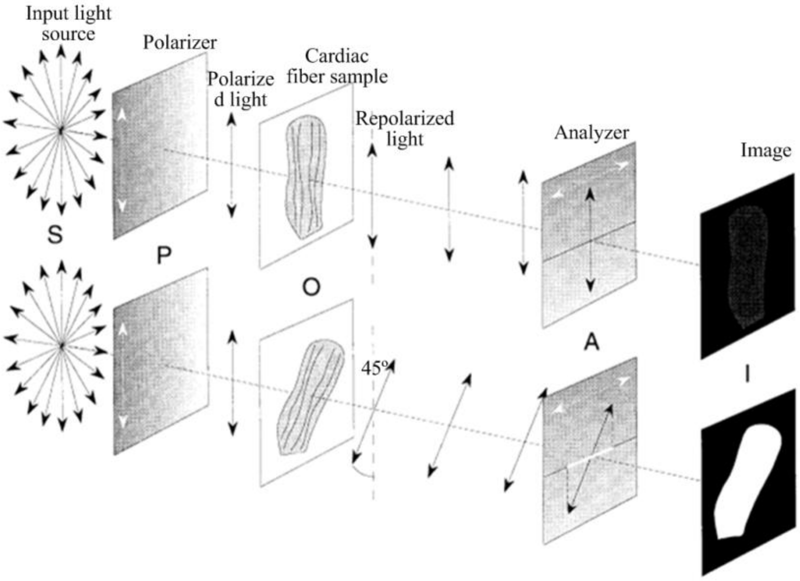

Fig. 2.5 Principle of PLI system for detecting the cardiac fiber orientation. From left to right along the optical path: S is the unpolarized input light source, when it passes through the polarizer P (one polarization filter with a vertical polarization axis), the unpolarized light becomes vertical polarized light, it goes through the object O under detection, here it represents cardiac fiber sample, the light is repolarized and is transmitted into the analyzer A (the other polarization filter with a polarization axis perpendicular to that of P), the light after A is received by the camera and finally forms one image I. At the top, because the orientation of the fiber is parallel to the polarization axis of P, the vibration axis of the repolarized light is not modified by the cardiac fiber, thus the light is totally blocked by A, and the image formed is black. At the bottom, conversely, the fiber orientation is 45º related to the polarizer axis, the light transmitted from the cardiac fiber is modified, the light transmits the analyzer and forms a bright image.

Because a cardiac fiber is uniaxial birefringent, thus the incident light is split into two rays after entering into the cardiac fiber, one is extraordinary (vibrates along the fiber axis with refractive index n_e) and the other one is ordinary (vibrates perpendicular to fiber axis with refractive index n_o). These two rays have different propagation velocities and accordingly the phase shift φ is induced. If the wavelength of the input light beam is λ, the cardiac fiber sample thickness is d, when the light propagates perpendicular to the fiber axis the phase shift between extraordinary and ordinary rays are :

$$\varphi = 2\pi d \Delta n / \lambda \tag{2.3}$$

where Δn is the birefringence of cardiac fiber defined as $\Delta n = n_e - n_o$. Defining the angle between the cardiac fiber direction and the propagation plane (x-y plane) of light wave as elevation angle α, the x-axis as the orientation of holding stage, the angle between the fiber projection on propagation plane and x-axis as azimuth angle β, and the angle between the polarization vibration axis and the x-axis as ρ, as illustrated in Fig. 2.6.

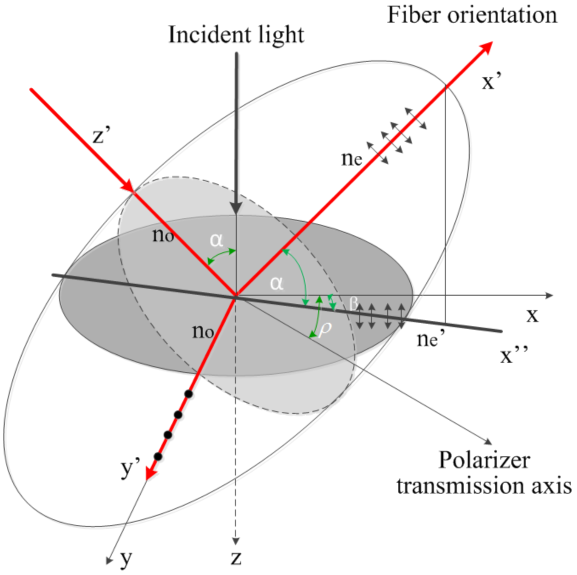

Fig. 2.6 Definition of fiber orientation with azimuth and elevation angle

From Fig. 2.6, it can be seen that, when the incident light propagates along the z direction, after entering the cardiac fiber, the extraordinary and ordinary rays propagates along y and x'' directions with refractive indices of n_o and $n_e^{'}$. According to the theory of refractive indices ellipsoid, $n_e^{'}$ is given by:

$$n_e^{'} = \left(\frac{n_o^2 n_e^2}{n_e^2 \sin^2(\alpha) + n_o^2 \cos^2(\alpha)}\right) \tag{2.4}$$

Subsequently, the phase shift induced by the cardiac fiber sample is:

$$\begin{aligned} \varphi &= 2\pi d (n_e^{'} - n_o) / \lambda \\ &= 2\pi d (n_e - n_o) \sin^2(\alpha) / \lambda \end{aligned} \tag{2.5}$$

According to the Jones Calculus [Jones 1941], the light intensity transmitted from the analyzer is

$$I = I_0 \sin^2(2\rho - 2\beta) \sin^2(\varphi / 2) \tag{2.6}$$

where I_0 describes the intensity of the incident light. In order to calculate the elevation and azimuth angle, the images are acquired separately with 4 different polarizer rotation angles ($\rho = 0°$, $\rho = 22.5°$, $\rho = 45°$ and $\rho = 67.5°$) and accordingly adjust the analyzer orientation to ensure that they are always orthogonal. The acquired intensities are $I_{\rho 0}, I_{\rho 22.5}, I_{\rho 45}, I_{\rho 67.5}$, from which the elevation and azimuth angles at each pixel of the image can be calculated by:

$$\begin{aligned} \beta &= \frac{1}{4}\mathrm{Arg}((I_{\rho_0} - I_{\rho_{45}}) + i(I_{\rho_{67.5}} - I_{\rho_{22.5}})) \\ \alpha &= \arccos\sqrt[4]{\frac{I_{\rho_{\max}}}{I_{\max}}} \end{aligned} \tag{2.7}$$

with $i^2 = -1$, Arg is the argument of the complex number . $I_{\rho\max}$ is the maximum value of $I_{\rho 0}, I_{\rho 22.5}, I_{\rho 45}, I_{\rho 67.5}$, $I_{\max}$ is the maximum intensity obtained when $\alpha = 0°$ and $\beta = 45°$. From the elevation and azimuth angles, the 3D cardiac fiber orientation can be mapped.

2.2.3 Advantages and limitations of PLI

Advantages:

1) A PLI system has an ultra-high spatial resolution. Generally, the spatial resolution in the cardiac fiber orientation detection experiments is chosen as 100µm × 100 µm × 500µm, however, when the thickness of the sample is 500 µm, the pixel size can range from 10 µm×10 µm to 500 µm×500 µm by changing the magnification degree of the objective lens.
2) The PLI method strongly depends on the nature of the molecule present in the material to be studied and orientation of which is well defined. Myosin is a major contractile protein involved in the myocyte, which is aligned with cardiac myocytes and gives cardiac myocyte a specific orientation. Thus, the characteristics of the cardiac fiber guarantee the reliability and robustness of PLI measurement.
3) PLI not only provides an average value of the directions of all the myosin filaments contained in each pixel of the cardiac fiber section, but also gives the orientation dispersion information. Both parameters are important for modeling the cardiac fiber structure and describing the cardiac fiber properties.

Limitations:

1) Up to now, due to the limitations of the PLI system setting, the detected elevation angle is reliable only for the range 20º~70º. For angles between 70º and 90º, it is difficult to calculate the elevation angle from the light intensity because there is not enough light transmitted through the analyzer. For angles between 0º and 20º, there is a systematic bias for the measurement of the angle of elevation, which is the consequence of the dispersion of the other orientations of the fibers around the average orientation and the incomplete coverage of the definition of elevation angle. When the average elevation is close to 0°, negative values are folded in positive and therefore the average elevation angle is greater than its actual value.

2) This PLI system is not able to measure the biaxial birefringent material (such as collagen), thus it is only suitable for the fetal heart not older than 3 months, because 3 months after the naissance, the collagen increases and the cardiac fibers are no longer uniaxial birefringent but biaxial.
3) In addition, the sample size is also limited. In the experiments, the cardiac fiber section thickness is 500 µm, which is optimal for the image analysis. So far, it is possible to reduce the thickness to 300 µm, but reducing the thickness of the sample decreases the signal to noise ratio (SNR), thus it is difficult to study the ventricles of length less than 1.5 cm, because in such case, the detailed geometrical variation of the inner ventricular wall is no longer negligible. On the other hand, the maximum size of the ventricles is also limited by the embedding and sectioning process. In fact, the polymerization of the acrylic resin is exothermic and the heat induced by the large samples' polymerization can change proteins' nature [Jouk, 1995], besides, during the sectioning process, it is difficult to obtain larger sections with a constant thickness. Thus in practice, the size of a heart that can be measured by this system should be smaller than 10 cm.
4) Besides, the PLI technique can only be used for the *ex vivo* hearts.

2.3 Diffusion Magnetic Resonance Imaging (dMRI)

dMRI is a way to perform Magnetic Resonance Imaging (MRI) which came into existence in the mid-1980s [Merboldt *et al.*, 1985; Le Bihan, 1985; Taylor *et al.*, 1985]. It allows inferring the microstructures of the *in vivo* biological tissues noninvasively by detecting the water molecules' diffusion. Its main clinical application has been neurological disorders, especially for the management of patients with acute stroke. More recently, dMRI is gradually used for mapping the cardiac fiber architecture, and diagnose the abnormality of cardiac muscles [Frindel *et al.*, 2010; Yang *et al.*, 2012].

A correct understanding of dMRI requires first a basic knowledge of MRI. Therefore, this section firstly explains the principles of MRI briefly and the basics of pulse sequence design. Secondly, we introduce the principle and concepts of self-diffusion and dMRI concisely.

2.3.1 Magnetic Resonance Imaging principles

MRI is an extraordinary and versatile technique because it is capable to produce various types of contrast in the images. For learning more in details, we can refer to the works [Goldman M, 2004; Westbrook *et al.*, 2011], which elaborated the MRI development history, physical phenomena, principles and applications.

2.3.1.1 Basic concepts involved in MRI

In order to understand the concept involved in MRI and to make clear how it works, we must firstly step into some interesting phenomena called precession, resonance and relaxation.

Precession

It is well known that our body tissues contains a lot of water and hence protons ^{1}H. This little positive electrical charged proton behaves like a little planet, such as earth, it is constantly turning around an axis, which is called spin as shown in Fig. 2.7 (a). The spinning of the protons will generate a lots tiny magnets, in our body these tiny bar magnets are ordered in such a way that the magnetic forces equalize. However, when we put these protons in a much stronger magnetic field B_0, some interesting things happen, all the protons align with the magnetic field, parallel or anti-parallel, meanwhile, they precess or wobble due to the magnetic momentum of the atom, as illustrated in Fig. 2.7 (b). The precession frequency is called Larmor frequency [Levitt, 2002] ω_0 which is determined by the strength of the magnetic field B_0 and the gyromagnetic ratio γ of proton ^{1}H .

$$\omega_0 = \gamma B_0 \tag{2.8}$$

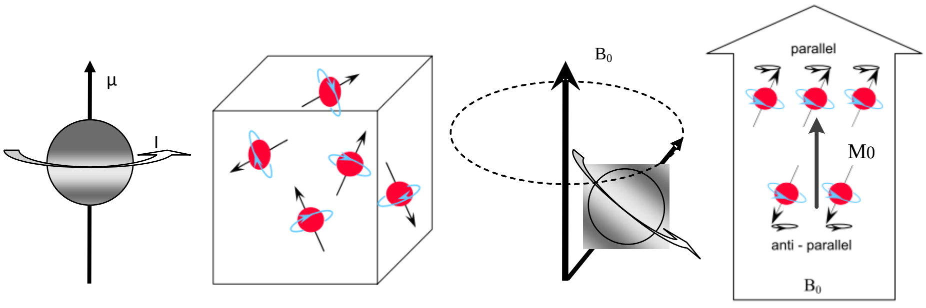

(a) spin

(b) precess

Fig. 2.7 Spin and precession of protons

In the end we see that the sum of all magnetic fields of each proton, which is called magnetization M_0, pointing in the same direction as the main magnetic field B_0. M_0 is related to the proton density which we are interested in, thus we intend to see what happens with M_0 during the MRI experiments. However, compared with B_0, M_0 is too small to be detected if they share the same direction, thus in order to observe the variation of M_0, the scientific community came up with a brilliant idea to separate them with resonance technique.

Resonance

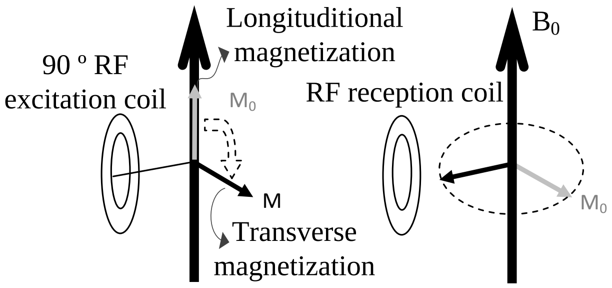

Fig. 2.8 RF excitation and reception

In a MRI system, resonance is generated by applying a Radio Frequency (RF) pulse with exactly Larmor frequency of hydrogen, this is called RF excitation. During the excitation, the protons are given sufficient energy to move out of alignment away from B_0. The angle to which the M_0 moves relative to B_0 is called flip angle. The magnitude of the flip angle depends on the amplitude and duration of the RF pulse. Usually the flip angle is 90° so that the longitudinal magnetization M_0 is completely transferred into the transverse magnetization M, as illustrated in Fig. 2.8.

Relaxation

As a result of resonance, the protons are processing in phase in the transverse plane. But this is just temporary, when the RF pulse is switched off, the magnetization in transverse plane is again influenced by B_0 and it tries to realign with it. In order to do so, the magnetization must lose the energy given to it by the RF pulse, this process is called relaxation, as shown in Fig. 2.9. During this period, the amount of magnetization in the longitudinal plane gradually increases, this is called *T_1 recovery*, the rate of recovery is an exponential process, with a recovery time constant called T_1, and at the same time but independently, the amount of magnetization in the transverse plane gradually decreases, this is called *T_2 decay*. It is caused by nuclei exchanging energy with their neighbors. The rate of decay is also an exponential process, so that the T_2 relaxation time of a tissue is its time constant to decay.

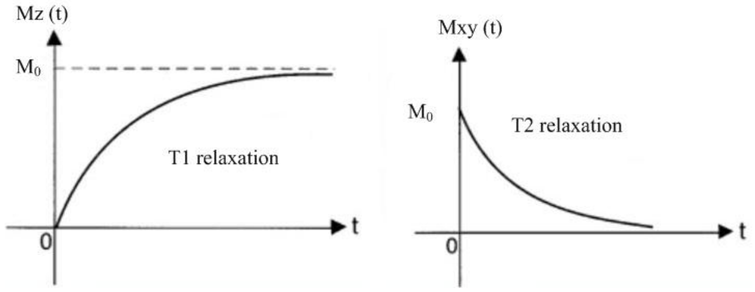

Fig. 2.9 Schema for T1 and T2 relaxation

If we place a receiver coil in the transverse plane, the variation of magnetization will produce magnetic field fluctuations inside the coil and consequently a voltage. This voltage constitutes the MR signal that relates to the three properties of a tissue, namely proton density, T1 and T2. The magnetization variation is calculated by Bloch equation [Bloch F, 1946].

$$\frac{d\vec{M}}{dt} = \gamma(\vec{M} \times \vec{B}_0) - \begin{pmatrix} \dfrac{M_x}{T_2} \\ \dfrac{M_y}{T_2} \\ \dfrac{M_z - M_0}{T_1} \end{pmatrix} \qquad (2.9)$$

where M_x, M_y, M_z are the component of $\overrightarrow{M}$ along the directions x, y, z.

2.3.1.2 K-space encoding

Now we know how MRI works and how to acquire MRI signals, for obtaining 3D images we should go a step further to learn about the most important MRI technique, K-space encoding. MRI signal measured by RF receive coils has its own amplitude, frequency and phase which result from the RF excitation and resonance. The amplitude of MR signal depends on the proton density in the voxel, the frequency and phase related to the RF pulse and the magnetic field strength. Using these properties, the MRI signal can be located spatially in three dimensions.

Slice selection

As the RF pulse is switched on, if the magnetic field is homogenous through the patient, all the protons fall in resonance with the same precession frequency and therefore make contribution to the MRI signal. If we desire to observe the MRI signal resulted from one selected part of the body, we have to choose the protons located in that part: this is called slice selection. Slice selection occurs when a RF pulse is turned on and simultaneously a magnetic gradient field ΔB is applied. As stated earlier, excitation of spins only happens when the RF pulse is applied at the Larmor frequency of those spins. In the presence of a gradient, the Larmor frequency ω_0 changes along the direction of the gradient, therefore only the spins located at a given slice perpendicular to the gradient direction can be in resonance, as shown in Fig. 2.10.

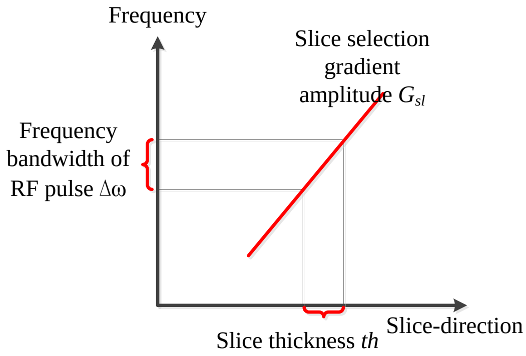

Fig. 2.10 Diagram for MRI slice selection

The slice location along that perpendicular direction may be translated by changing the frequency of the RF pulse. The slice thickness th depends both on the frequency bandwidth $\Delta\omega$ of the RF pulse and the strength of the gradient G_{sl}, which is expressed as:

$$th = \frac{\Delta\omega}{\gamma G_{sl}} \tag{2.10}$$

Phase encoding

Once a slice has been selected, the MRI signal coming from it must be located along both the axis of this slice. This is realized by phase and frequency encoding. Before the application of phase encoding gradient, all the spins in the slice precess with the same frequency and they are in phase. However, when the phase encoding gradient is switched on, the magnetic field strength and therefore the precessional frequency of spins along the axis of the phase gradient is altered. As the speed of precession of the spins changes, so does the accumulated phase of magnetic moments along their precession path, which is illustrated in Fig. 2.11.

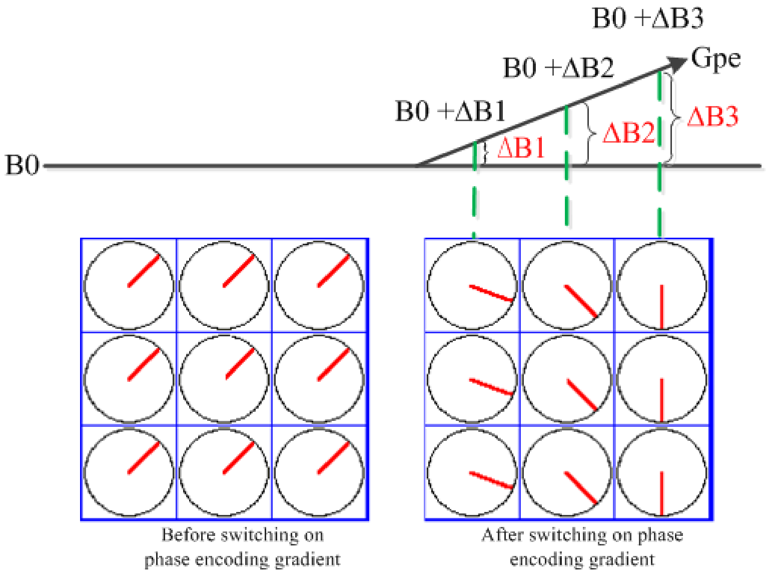

Fig. 2.11 Diagram for MRI phase encoding

As the phase encoding gradient is turned off, the magnetic field strength returns to the main field strength, and therefore the precessional frequency of all the spins returns to the Larmor frequency. However, the phase difference between the spins remains. Thus, at this moment, the spins precess with the same frequency but different phases. This difference in phase between the spins is used to encode the spins' position along the phase encoding direction.

The spatial resolution along the phase encoding res_{pe} direction is determined by the field of view (FOV_{pe}) along this direction, the phase encoding steps number n_{pe} , the encoding gradient strength changes ΔG_{pe} between two steps and the gradient duration δ_{Gpe}, which is expressed as [Larsson, 2008]

$$res_{pe} = \frac{FOV_{pe}}{n_{pe}} = \frac{1}{\gamma \Delta G_{pe} \delta_{Gpe} n_{pe}} \tag{2.11}$$

Frequency encoding

Signal must be now located along the remaining axis of the slice, and this is done by frequency encoding. With the same principle of phase encoding, when the frequency encoding gradient is switched on, the magnetic field strength is altered and so does the precessional frequency of spins. Therefore, the frequency difference between the spins is produced, and the signal can be identified according to its frequency along the gradient direction (Fig. 2.12).

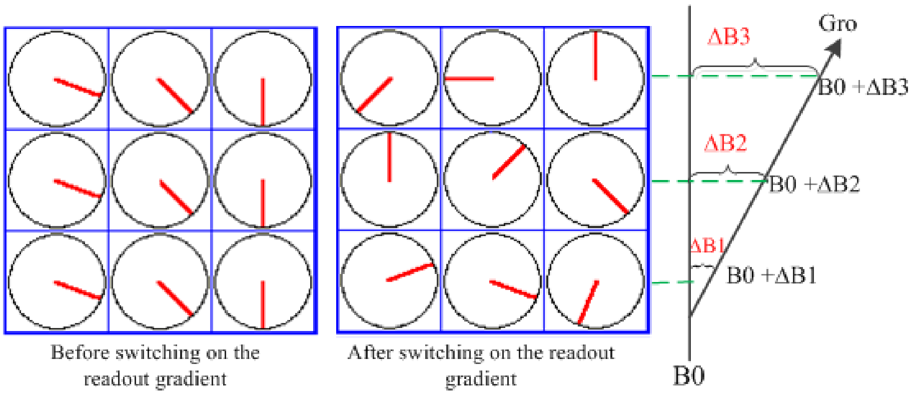

Fig. 2.12 Diagram for frequency encoding

Frequency encoding gradient is usually turned on when the signal is received and is also called the readout gradient. The steepness of the slope of the frequency encoding gradient determines the size of field of view (FOV_{ro}) and also the spatial resolution res_{ro} in this direction [Westbrook, 2011].

$$res_{ro} = \frac{FOV_{ro}}{n_{ro}} = \frac{BW}{\gamma G_{ro} n_{ro}} \tag{2.12}$$

where BW is the bandwidth of the receive digitizer, G_{ro} is the strength of the frequency encoding gradient, and n_{ro} is the acquisition number.

Once the MRI signal is encoded, it will be organized in a coordinate system known as k-space [Moratal *et al.*, 2008]. Performing the multiple acquisitions enables the filling of the k-space. Through the Fourier transform, the raw MR imaging data from k-space will become a position-encoded visual image. The process of filling the k-space is determined by specific MRI sequences which combine the RF pulse and encoding gradients in a given order.

2.3.1.3 MRI pulse sequences

MRI pulse sequences enable us to control the way in which the system applies pulses and gradients. In this way, the image contrast type and quality is determined. There are many different MRI sequences available, and each is designed for a specific purpose [Bernstein *et al.*, 2004]. This subsection discusses two very commonly used pulse sequences: spin echo and gradient echo.

Spin echo sequence

The spin echo (SE) sequence is frequently used in MRI experiments because of its versatile styles and good imaging qualities. It uses a 90° excitation RF pulse followed by one or a series of 180° rephasing RF pulses to generate a spin echo. Fig. 2.13 Shows a SE sequence. After the 90° excitation pulse, the magnetization is flipped into the transverse plane, it immediately starts to dephase due to T2 relaxation, some spins slow down and others speed up. A 180º pulse is then applied to flip the spin vectors so that the previously slower vectors are effectively precessing ahead of the previously faster ones. After a further time delay (equal to TE/2), a spin echo is formed.

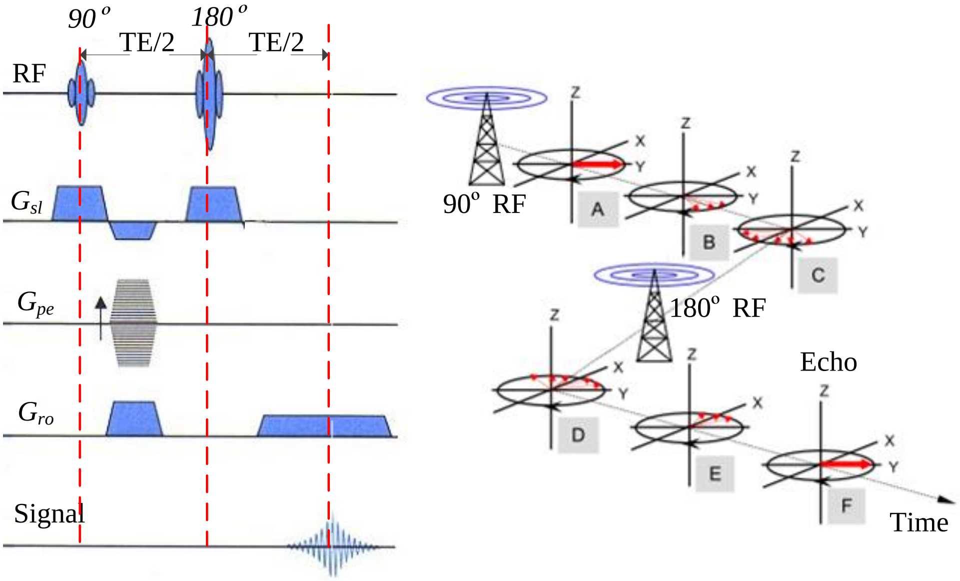

Fig. 2.13 Diagram of SE sequence and its principle.

In most MRI sequences, followed by the slice selection gradient there is often a gradient with half amplitude strength of G_{sl} , which is used to compensate the dephasing effects caused by the inhomogeneity of the gradient. With the same reason, before 180 RF pulse, a gradient is applied along the reading out direction.

Due to the spatial encoding with the gradients, the intensity of each voxel in the image only depends on the proton density, T1 and T2 values. Changing the sequence parameters lead to the images with different weighting contrast. The SE sequence has a high SNR and few artifacts, it is the best one to obtain T2 contrast image, but it needs long acquisition time.

Gradient echo sequence

The gradient echo sequence (GE) is similar to the SE sequence with the exception that it forms the echo using a gradient polarity reversal, see

Fig. 2.14. It starts with an excitation RF pulse with flip angle of αº, depending on which more or less magnetization is flipped into the transverse plane, because of T2 relaxation, spins are dephasing. Dephasing lasts until the polarity of the G_{ro} is changed, after that the spins begin to rephrase until it is in phase again.

GE sequence does not compensate the inhomogeneity of the magnetic field , therefore there is an increased sensitivity to T2* decay caused by the lack of a 180º refocusing pulse, but this saves the acquisition time which is useful when fast scan is required.

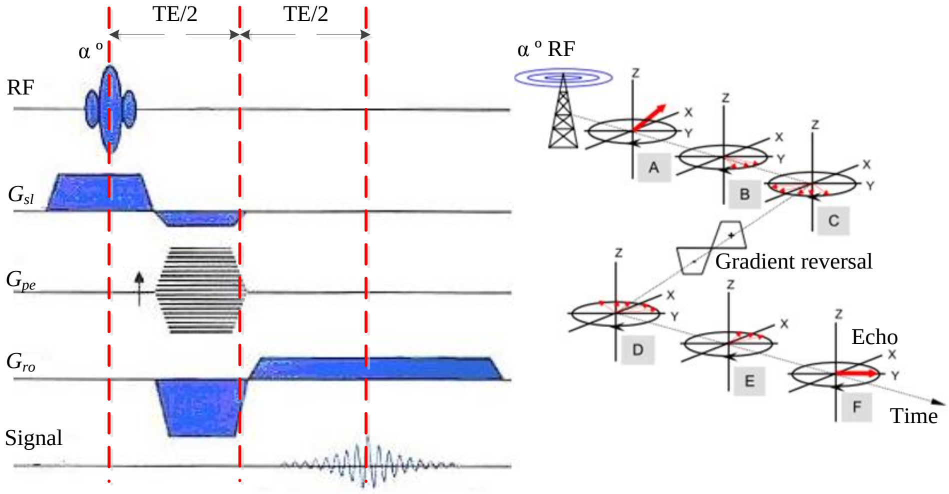

Fig. 2.14 Gradient echo sequence and its principle

2.3.2 Diffusion physics

2.3.2.1 *Brownian motion*

"Diffusion" in biological tissues usually means "molecular diffusion", also called Brownian motion [Brown, 1866], which refers to the random motion of water molecules when they are agitated by thermal energy. The Brownian motion is usually described by the random walk model [Goel *et al.*, 1974], which not only gives the trajectory of molecular diffusion, but also the diffusion displacement during a given time interval, as shown in Fig. 2.15.

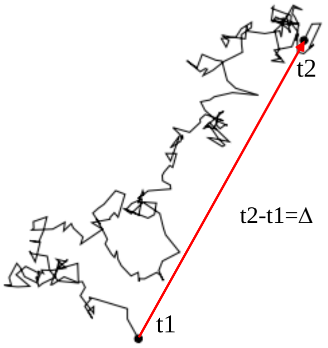

Fig. 2.15 The diagram shows the molecular diffusion trajectory of a single water molecule.

The red vector represents the molecular displacement during the diffusion time interval Δ, between t1 and t2. The displacement experienced by one molecule is determined by the diffusion time interval Δ, the diffusion coefficient D of the medium, and the diffusion types: free, hindered, or restricted. Diffusion is considered as a random process, so one molecule beginning from the same position and diffusing the same time would probably end at the different locations. Therefore, for better describing the diffusion phenomenon, the concept of diffusion displacement distribution, also called displacement *probability density function* (PDF) was introduced [P Callaghan, 1994]. In this thesis, PDF is written as $P(\vec{p}_\Delta | \vec{p}_0, \Delta)$, which describes the probability of a water molecule located at position $\vec{p}_0$ moving to the position $\vec{p}_\Delta$ after the time interval Δ.

In case of isotropic diffusion in a homogeneous medium, following the central limit theorem, the distribution of PDF is Gaussian, for a three-dimensional system it can be expressed as:

$$P(\vec{p},\Delta) = \frac{1}{\sqrt{|D|(4\pi\Delta)^3}} \exp\left(-\frac{(\vec{p}^{\,\mathrm{T}} D^{-1} \vec{p})2}{4\Delta}\right) \tag{2.13}$$

with $\vec{p} = \vec{p}_\Delta - \vec{p}_0$. The variance of $\vec{p}$ is proportional to the diffusion time Δ:

$$< |\vec{p}|^2 >= 6D\Delta \tag{2.14}$$

The Eq.(2.14) is the famous Einstein equation [Einstein, 1956].

However, in the biological tissues, the diffusion of water molecules is no longer isotropic and it is usually restricted or hindered by the tissue boundaries. We called this kind of diffusion as “hindered” and “restricted” diffusion.

2.3.2.2 *Hindered diffusion*

Hindered diffusion usually happens in heterogeneous media and it is often anisotropic. Fig. 2.16 illustrates the water diffusion in the medium with the circle obstacles.

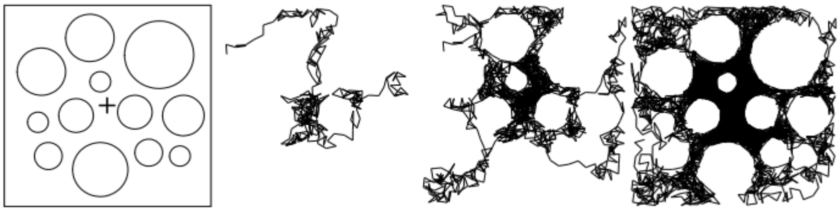

a b c d

Fig. 2.16 Illustration of hindered diffusion. Subfigure a shows the diffusion hindered environment, the diffusion process of the particles is simulated by a random walk method. The total number of random walk steps is 150. The diffusion trajectories of the particles are shown in subfigures b, c and d. The number of particles involved the simulation in subfigure *b*, *c* and *d* is respectively 3, 12 and 48. It can be seen that the trajectories of the particles can provide the structure of the environment. That is why imaging the diffusion process of water molecules in the biological tissues can reflect the microstructure of the tissues.

2.3.2.3 *Restricted diffusion*

Relatively to “hindered” diffusion, in biological tissues, “restricted” diffusion usually means the intracellular diffusion in which water is not allowed to diffuse toward the extracellular space. Fig. 2.17 shows the difference between the “hindered” and “restricted” diffusion. It also illustrates the water molecules exchange between both diffusion processes.

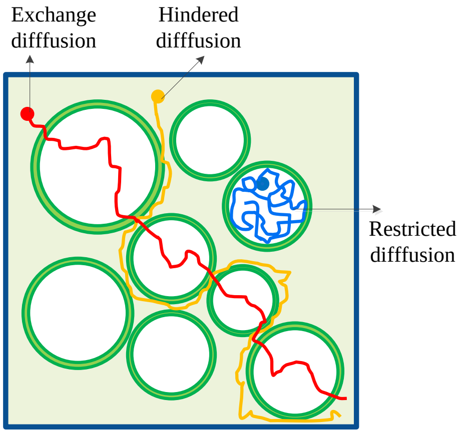

Fig. 2.17 Illustration of the difference between restricted and hindered diffusion

Restricted diffusion is a time dependent process. It behaves as free diffusion when the diffusion time is too short so that the molecules cannot reach the boundary of the cells. But for long diffusion time, the restricted diffusion has the same capability as the hindered diffusion for sensing the structure of the cells.

The PDF of restricted and hindered diffusion is complicated. It depends on the diffusion time, the diffusion coefficient of medium, and most importantly the diffusion environment structures. Thus, the variation of the PDF can reveal the tissues structure and the physical properties changes. This last point may be very useful for disease diagnosis.

2.3.2.4 Water diffusion in cardiac fiber

As we illustrated in the first chapter, the cardiac fiber is a highly heterogeneous medium for the water molecular diffusion. Because the length of a cardiac myocyte is about five times its diameter [Severs, 2000], water molecules diffuse much faster along the fiber orientation than in the transverse direction. Such a diffusion directional preference can be described by a parameter called “diffusion anisotropy”. The exact micro structural features underlying the measured anisotropy remains matter of debate until now. Postulated sources of anisotropy include both intracellular and extracellular structures: myocyte dimensions and extracellular spaces.

The diffusion in the intracellular space has been assumed restricted, during a certain time interval there is no water molecules permeate the membrane to enter the extracellular space. The diffusion in the extracellular space is considered to be hindered because the myocytes form obstacles for the molecules. For long diffusion times, exchanges between the intra- and extra-cellular spaces may change the diffusion profile as well.

The “apparent diffusion coefficient” (ADC) in cardiac fiber as measured with MR ranges between 1×10^{-3} mm^2/s and 2.2×10^{-3} mm^2/s [Chen *et al.*, 2003] which is smaller than the diffusion coefficient of free water at 37° which is 3.28×10^{-3} mm^2/s [Liu *et al.*, 2001]. The overall low diffusivity of water in cells could not be fully explained by restriction and the combination of restricted and hindered diffusion. The exact influence of the cardiac fiber structure on diffusion is still elusive. The correct assignment of water diffusion patterns to the underlying tissue microstructure thus remains a challenging task.

2.3.3 Diffusion Weighted Magnetic Resonance Imaging (DW-MRI)

The effects of diffusion on the MRI signal was first noticed by Hahn in 1950 [Hahn, 1950]. Few years later, Torrey [Torrey, 1956] presented a generalized version of the Bloch equations which incorporated the elements of molecular diffusion. He pointed out that in the presence of molecular diffusion, the transverse magnetization variation is

$$\frac{d\vec{M}}{dt} = \gamma \vec{M} \times \vec{B}_0 + \begin{pmatrix} \dfrac{M_x}{T_2} \\ \dfrac{M_y}{T_2} \\ \dfrac{M_0 - M_z}{T_1} \end{pmatrix} + D\nabla^2 \vec{M} \tag{2.15}$$

where ∇^2 signifies the Laplace operator, the first two terms of Eq.(2.15) come from the original Bloch equation as described in section 2.3.1.1, the third term accounting for molecular diffusion. The complete equation is called Bloch-Torrey equation. In order to detect the molecular diffusion information, the original MRI pulse sequence was altered and produced another imaging modality, which is called diffusion weighted magnetic resonance imaging (DW-MRI) [Mori *et al.*, 1999].

2.3.3.1 Principles for detecting the diffusion using DW-MRI

All MRI pulse sequences are to some extent sensitive to molecular motion and diffusion, however, a specific diffusion measurement sequence was developed by Stejskal and Tanner in order to extract the diffusion information [Stejskal *et al.*, 1965]. This sequence is designed based on a SE sequence, one symmetric pair of diffusion-weighted gradients is added to either side of the refocusing 180° RF pulse in each encoding directions (slice selection, phase and frequency encoding), illustrated in Fig. 2.18.

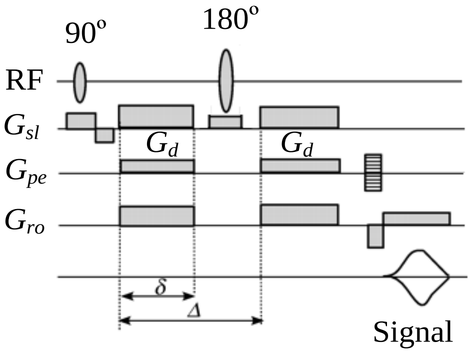

Fig. 2.18 Stejskal-Tanner diffusion magnetic resonance imaging sequence

The different magnitudes of the diffusion-weighted gradients in the three encoding directions will provide a specific diffusion-weighted direction corresponding to the encoding coordinate system. The first of these gradients offsets the phase of the spins by an amount that depends on their location, the second will provide equal and opposite (due to 180° pulse) rephasing if the spins have not moved during the diffusion time Δ, which is the time between the application of the two gradients. As the spins move randomly due to diffusion, the rephasing effects of 180° will disappear. The further the spins have diffused during the diffusion time, the less perfect the rephasing and the smaller the amplitude of the final signal will be. More diffusion is thus indicated by a more attenuated signal.

The diffusion signal detected by this sequence is:

$$S(b) = M_0 \exp(-\frac{t}{T_2}) \exp(-bD) \tag{2.16}$$

where b is given by

$$b = \gamma^2 \int_0^{TE} (\int_0^t G_d(t')dt')^2 dt \tag{2.17}$$

For the sequence in Fig. 2.18, b-value is:

$$b = \gamma^2 \delta^2 (\Delta - \delta / 3) G_d^2 \tag{2.18}$$

b-value is known as the diffusion-weighting factor which incorporates the relevant characteristics of the diffusion gradient, including the diffusion gradient amplitude G_d , the duration δ and the time interval Δ between two diffusion gradients. In the absence of diffusion gradients, the b-value is 0 and the signal detected by MRI scanner is:

$$S_0 = M_0 \exp(\frac{-t}{T_2}) \tag{2.19}$$

Thus Eq.(2.16) becomes :

$$S(b) = S_0 \exp(-bD) \tag{2.20}$$

Then the diffusion coefficient along the direction of the applied diffusion gradients can be measured by comparing the MRI signal with and without diffusion-weighted gradients. But Eq.(2.20) is derived by assuming that the diffusion has a Gaussian profile, it is only valid under the assumption of $\delta << \Delta$ such that the effect of diffusion during the application of the diffusion gradients is negligible. It also is supposed that the dephasing due to the application of the imaging gradients can be neglected.

The diffusion process in biological tissues is no longer free, but hindered and modulated by many mechanisms, such as the restriction due to the cell membrane, tortuosity around the obstacles, the influence of perfusion caused by the blood flow, etc. [Köpf *et al.*, 1996; Beaulieu, 2002]. Thus the diffusion coefficient detected by dMRI is usually smaller than that of free diffusion, and Le Bihan proposed to call it apparent diffusion coefficient (ADC) [LeBihan *et al.*, 1986]. ADC is a global parameter reflecting the diffusion properties of a tissue, which depends on the direction, diffusion time and gradient amplitude. The D in the Eq.(2.20) represents ADC.

2.3.3.2 Advantages and limitations of dMRI

Advantages

1) dMRI provides information that differs from other imaging modalities. Its major technological advantage is that it can characterize and discriminate the tissues using their physical and biochemical properties (dimension size, proton density, T_1 and T_2 relaxation time).
2) dMRI acquisition does not use ionizing radiation, thus it is noninvasive for *in vivo* imaging.
3) dMRI acquisitions can be programmed to encode various physiological phenomena and to satisfy some specific requirement.

Limitations

1) The spatial resolution of dMRI used for human beings is about 6 mm^3 (1.5T or 3T MRI devices). For improving the spatial resolution, the hardware with strong gradient pulses is required, which may cause artifacts in the image.
2) The nonlinearity of the gradients used in MRI sequence will also bring eddy current effects that influence the image quality.
3) dMRI is exquisitely sensitive to motion, thus for *in vivo* imaging, there is often an image ghost caused by the patient motion or breathing.

2.4 Conclusion

In this chapter, we mainly introduced two kinds of cardiac fiber imaging modalities: PLI and dMRI, the former is for *ex vivo* and the latter is for *in vivo* imaging. For a better understanding of the main work of this thesis, the basic concepts and principles of PLI and dMRI were explained.

For PLI, we showed the setup of devices for obtaining the cardiac fiber images and introduced the technique using the polarization properties of the light to detect the cardiac fiber orientation. We also pointed out the pearls and the pitfalls of this imaging technique.

As to dMRI, the basic concepts involved in the magnetization process of ^1H, including precession, excitation and relaxation, were illustrated. Then following the introduction of spatial encoding technique, some commonly used MRI sequences were explained. All of these make it clear how MRI works. Next, the physical process of molecular diffusion was presented, including free diffusion and the diffusion process in the cardiac fiber. Finally, combining the principles of MRI and process of diffusion, the principle of dMRI was elaborated.

Chapter 3

State of the art of dMRI modeling and simulation

Contents

Résumé en français

Comme nous l'avons montré dans le chapitre précèdent, l'IRMd permet d'examiner les propriétés de diffusion des molécules d'eau dans les tissus biologiques et donc d'inférer la microstructure sous-jacente.

Suite à leurs succès dans les applications cliniques, certaines méthodes avancées d'IRMd ont été proposées pour analyser la diffusion dans les tissues plus complexes. Ces méthodes peuvent être essentiellement divisées en trois catégories: la première catégorie se concentre sur le post-traitement des signaux de l'IRMd, ce qui signifie que, après l'acquisition, le signal de diffusion est reconstruit et les propriétés de diffusion sont extraites et décrites par certains outils mathématiques. Dans cette thèse, nous avons appelé ces méthodes « modèles mathématiques de l'IRMd ». Il existe de nombreux types de modèles dans ce groupe. Nous avons limité notre analyses à l'imagerie par résonance magnétique du tenseur de diffusion (DTI), l'imagerie du spectre de diffusion (DSI), l'imagerie Q-ball (QBI) et l'imagerie de tenseurs multiples (MTI). La deuxième catégorie de méthodes, contrairement à la première, est basée sur la physique du processus de diffusion de l'eau dans les différents tissus et connue les méthodes de numérique utilisée pour générer des images de diffusion pondérées dans les tissus. Nous les avons regroupées sous la dénomination: « modèles de simulation numérique ». Il s'agit des approches par éléments finis (FE) et de Monte-Carlo (MC). La troisième catégorie regroupe les méthodes par simuler le processus entier de l'imagerie de diffusion, y compris la conception de séquence, les propriétés de l'objet virtuel analysé, et la reconstruction du signal. Nous l'appelons « Modèles basés sur l'équation de Bloch-Torrey ». Ce chapitre, présenté l'état de l'art de ces trois classes de méthodes avec leur principe, leurs mérites comparés et leurs inconvénients.

À partir de l'état de l'art concernant ces trois types de méthodes de modélisation et de simulation en IRMd, nous pouvons constater que, chaque méthode présente ses avantages et ses inconvénients. Les modèles mathématiques destinés à fournir des paramètres qui décrivent les propriétés de diffusion des molécules d'eau qui se déplacent dans les tissus biologiques, tels que MD, FA, PDF, ODF, et les directions principales de diffusion sont très utiles pour interpréter la microstructure des tissus. Toutefois, en l'absence de vérité terrain, la microstructure déduite de ce type de modèle est difficile à évaluer. Les « méthodes de simulation numérique », présente un avantage évident de fournir une parfaite vérité-terrain pour évaluer les résultats de la simulation. Néanmoins, la simulation numérique nécessite souvent de temps de calcul très longs, les simulations ont jusqu'à présente été limitées à des structures simples.

Enfin, le modèle de simulation à partir de l'équation de Bloch-Torrey appartient aussi aux méthodes de simulation numérique, mais avec une spécificité qui justifié que nous l'ayons présenté séparément. Cette méthode simule le processus de l'imagerie de diffusion, y compris l'impulsion RF d'excitation, le codage spatial, la pondération de diffusion et l'échantillonnage du signal. Elle est donc capable de fournir des images de diffusion plus réalistes. Cependant, contrairement aux simulateurs IRM, qui ont déjà été largement développés, la simulation IRMd en utilisant l'équation de Bloch-Torrey est une nouvelle proposition. Toutefois, celle-ci ne peut que simuler la diffusion isotrope. Des recherches plus approfondies sont donc nécessaires pour étendre ce type d'approche au cas de la diffusion anisotrope et complexe.

En résumé, le défi à ce stade est donc de trouver un modèle de simulation de l'IRMd capable d'interpréter la diffusion anisotrope dans les tissus biologiques complexe, et en même temps, capable de fournir une vérité terrain pour évaluer ce modèle. Ce point est précisément l'objet de cette thèse, détaillé dans les prochains chapitres.

3.1 Introduction

As we illustrated in chapter 2, dMRI allows examining the diffusion properties of water molecules in biological tissues and therefore inferring the microstructure of the diffusion environment. Followed by the success of DW-MRI in clinical applications, some advanced dMRI modalities sprung up for satisfying the requirements of analyzing more complicated diffusion processes. These methods can mainly be divided into three categories: the first category focuses on the post-processing of the dMRI signals, which means that after the acquisition, the diffusion signal is reconstructed and the diffusion properties are extracted and described by some mathematical tools. In this thesis, we called such methods “mathematical models of dMRI”. Various types of models exist, here we will focus on the Diffusion Tensor Imaging (DTI), Diffusion Spectrum Imaging (DSI), Q-Ball Imaging (QBI) and Multi-Tensor Imaging (MTI). The second category of methods, in contrast with the first one, is grounded on the physics of the diffusion process in different media. Here computer simulation is used to provide the corresponding diffusion weighted images. We name this kind of models “numerical simulation models”. It includes finite element (FE) and Mont-Carlo (MC) approaches. The third category of methods simulates the whole process of diffusion imaging, including sequence design, virtual object properties assignment, and signal reconstruction, we consider here the “Bloch-Torrey equation simulation model”. In this chapter, we introduce the state of the art of these models, present briefly their principles and compare their merits and pitfalls.

3.2 Mathematical models of dMRI

The mathematical models used to analyze the diffusion signal and its related properties can be divided into two groups according to the angular resolution: low-angular resolution diffusion imaging and High-Angular Resolution Diffusion Imaging (HARDI). The angular resolution, in other words, the angular sampling of space during acquisition determines different diffusion directions within one voxel. Low-angular resolution diffusion imaging includes DW-MRI, apparent diffusion coefficient weighting imaging [Moseley *et al.*, 1990], and DTI [Kingsley, 2006a, 2006b, 2006c]. HARDI includes a large number of models, such as mixture models [Y-C Wu *et al.*, 2007], QBI [Tuch, 2004], DSI [V Wedeen, 2005], Diffusion Orientation Transformation (DOT) [Ozarslan *et al.*, 2006], and Diffusion Propagator Imaging (DPI) [Descoteaux *et al.*, 2009] etc. Here we introduce the commonly used models and some typical ones.

3.2.1 Diffusion Tensor Imaging (DTI)

In the traditional DW-MRI, the diffusion process is simply described by a single scalar parameter, the Apparent Diffusion Coefficient (ADC). However in presence of diffusion anisotropy, diffusion can no longer be characterized by a single ADC, but requires other parameters able to fully describe the molecular diffusion along each spatial direction. Thus the concept of diffusion tensor $\underline{D}$ was introduced into dMRI [Basser *et al.*, 1994b] and leading to DTI.

3.2.1.1 *DTI model description*

In DTI, the diffusion magnetic resonance signal is expressed by [Le Bihan *et al.*, 2001]

$$E(b) = S_0 \exp(-b\underline{D}) \tag{3.1}$$

where b characterizes the gradient pulses used in the MRI sequence, including the gradient amplitude G, the gradient impulse duration δ and the diffusion time Δ. In the spin echo sequence [Stejskal, 1965], the b value is calculated by:

$$b = \left(\gamma \vec{G} \delta\right)^2 (\Delta - \delta / 3) \tag{3.2}$$

with γ designating the gyromagnetic ratio of ^{1}H proton, S_0 the magnetic resonance signal intensity when $b = 0$ and $\underline{D}$ the diffusion tensor given by

$$\underline{D} = \begin{pmatrix} D_{xx} & D_{xy} & D_{xz} \\ D_{yx} & D_{yy} & D_{yz} \\ D_{zx} & D_{zy} & D_{zz} \end{pmatrix} \tag{3.3}$$

According to the thermodynamic laws [Groot *et al.*, 1962], the diffusion tensor of water molecules is thought to be symmetrical ($D_{ij} = D_{ij}$, with $i, j = x, y, z$).

3.2.1.2 *Estimation of the tensor from data acquisition*

Because the diffusion tensor $\underline{D}$ is symmetrical, the diffusion signal in Eq. (3.1) becomes:

$$E = S_0 \exp(-b_{xx}D_{xx} - b_{yy}D_{yy} - b_{zz}D_{zz} - 2b_{xy}D_{xy} - 2b_{xz}D_{xz} - 2b_{yz}D_{yz}) \tag{3.4}$$

The logarithm of the diffusion signal E is

$$\ln(E) = \ln(S_0) - b_{xx}D_{xx} - b_{yy}D_{yy} - b_{zz}D_{zz} - 2b_{xy}D_{xy} - 2b_{xz}D_{xz} - 2b_{yz}D_{yz} \tag{3.5}$$

For convenience, the right-hand side of Eq.(3.5) can be written as

$$\ln(E) = BX \tag{3.6}$$

where

$$B = (-b_{xx}, -b_{yy}, -b_{zz}, -2b_{xy}, -2b_{xz}, -2b_{yz}, 1) \tag{3.7}$$

$$X = [D_{xx}, D_{yy}, D_{zz}, D_{xy}, D_{xz}, D_{yz}, \ln(S_0)]^{\mathrm{T}} \tag{3.8}$$

In order to obtain the six components of the diffusion tensor, the diffusion signal should be measured in at least six different diffusion angles (projections) corresponding to six different gradient directions.

$$\ln(E_i) = B_i X \tag{3.9}$$

where $i = 1, \ldots, M$, with $M \geq 6$. When $M = 6$, The diffusion tensor can be calculated directly through the following equation.

$$X = B_i^{-1}\ln(E_i) \tag{3.10}$$

When the number of acquisition directions is more than six, there is no true inverse B_i^{-1}, but Eq.(3.9) can still be solved by calculating a pseudo inverse matrix B^{ψ} [Langlet, 2006]

$$B^{\psi} = (B^{\mathrm{T}}B)^{-1}B^{\mathrm{T}} \tag{3.11}$$

Consequently, the components of the diffusion tensor are computed from:

$$X = (B_i^{\mathrm{T}}B_i)^{-1}B_i^{\mathrm{T}}\ln(E_i) \tag{3.12}$$

3.2.1.3 Diffusion characteristics extraction

Once the diffusion tensor is calculated, some diffusion characteristics should be extracted for explaining the structures of the diffusion environment. Generally, concerning diffusion in biological tissues, especially in the cardiac fibers, we mostly care about the main direction of diffusion, the local mean diffusivity and the diffusion anisotropy.

Main direction of the diffusion

dMRI, especially DTI, is often used to detect the privileged orientations within tissues. Mathematically, a tensor is often represented by an ellipsoid [Basser, 1995] with its three main axes called eigenvectors. Each eigenvector corresponds to one eigenvalue, expressed by λ. It is assumed that the direction of the eigenvector associated with the largest eigenvalue of the tensor corresponds to the local orientation of the tissue. The diffusion orientation extracted from DTI is commonly used for doing fiber tracking in the brain [Mori *et al.*, 2002; Le Bihan, 2003; Hüppi *et al.*, 2006; Assaf *et al.*, 2008b], sometimes in the heart muscle[Zhukov *et al.*, 2003; Sosnovik *et al.*, 2009a; Zhang *et al.*, 2010] and some other tissues. Up to now, it is the unique method to observe the "*in vivo*" cerebral connectivity non-invasively.

Mean Diffusivity (MD)

Mean diffusivity is often used in diffusion tensor imaging. It represents the overall mean-squared displacement of the water molecules and gives information about the overall presence or not of obstacles to the diffusion in one voxel or one region. It is defined by the average of the three ADCs respectively measured along the three axes of the tensor. Assuming that the tensor axes along x, y and z, then the MD is written as:

$$MD = (ADC_x + ADC_y + ADC_z)/3 \tag{3.13}$$

From the mathematical point of view, the MD can also be calculated from the eigenvalues of the tensor

$$MD = (\lambda_1 + \lambda_2 + \lambda_3)/3 \tag{3.14}$$

Fractional Anisotropy (FA)

The fractional anisotropy describes the spatial heterogeneity of the water molecules displacements that is related to the presence of orientated structures[Pierpaoli *et al.*, 1996], it is defined as

$$FA=\sqrt{\frac{3}{2}}\sqrt{\frac{(\lambda_1-MD)^2+(\lambda_2-MD)^2+(\lambda_3-MD)^2}{(\lambda_1^2+\lambda_2^2+\lambda_3^2)}} \tag{3.15}$$

3.2.1.4 Advantages and limitations

Advantages

1) The diffusion tensor can be theoretically reconstructed from only six acquisition directions (projections), allowing a short acquisition time compatible with clinical applications. The patient will not feel uncomfortable to keep immobile during the examination.
2) DTI is a relatively mature diffusion imaging technique, which is often used in clinics. It has a good measurement accuracy for the voxels which experience only one principal orientation [Lin *et al.*, 2001].

Limitations

DTI makes a Gaussian assumption for the diffusion profile, thus it is unable to reflect the diffusion properties of a tissue when the voxels acquired contain two or more privileged directions of diffusion [Le Bihan *et al.*, 2006; Savadjiev *et al.*, 2008].

3.2.2 Diffusion Spectrum Imaging (DSI)

Diffusion Spectrum Imaging (DSI) [Tuch, 2002; V Wedeen, 2005; Lenglet *et al.*, 2009; Descoteaux, 2011] is the most generalized model for describing the diffusion properties in a tissue. It is the practical implementation of the dMRI theory, which attempts to accurately derive the probability density function (PDF) of the number of water molecules in each voxel from sufficiently dense acquisitions. Unlike DTI, DSI can reveal the diffusion properties in one voxel even in the case of complex geometries. Before introducing the DSI model, a new definition in dMRI must be presented: it is called the Q-Space.

3.2.2.1 Q-space definition

Q-space is a concept analogous to the K-space used in conventional MRI. It was introduced in the works [Stejskal, 1965; Cory *et al.*, 1990; PT Callaghan *et al.*, 1999] and is defined as a space used to depict the directions and strengths of diffusion weighting. This is usually expressed by a $\vec{q}$ vector, defined as:

$$\vec{q}=\gamma\int_0^t \vec{G}dt \tag{3.16}$$

For a Single Echo pulsed gradient sequence, $\vec{q}$ is given by:

$$\vec{q}=\gamma\vec{G}\delta \tag{3.17}$$

where $\vec{G}$ means applying a diffusion weighted gradient with strength G in a specific direction (angle), δ is the duration of this gradient. Repeated applications of the diffusion gradients that vary in strength and direction (angle) (with variations of $\vec{q}$) allow data acquisition throughout q-space. More precisely, each single $\vec{q}$ produces one image with a given diffusion weighting.

Like processing the data from the conventional MRI, where we apply a Fourier transform on the k-space data, for the q-space acquisition, we also perform the Fourier transform, which results in one Fourier transform pair: the diffusion distribution PDF VS the q-space acquired data in each voxel.

For describing the parameters applied in sampling q-space, the term "b-value" is also used. The *b-value* is proportional to the product of the diffusion time interval Δ and the square of the strength of the diffusion gradient. For a SE sequence, the relationship between the b-value and $\vec{q}$ is [Johansen-Berg *et al.*, 2009]:

$$b = \vec{q}^{\,2}(\Delta - \frac{\delta}{3}) \tag{3.18}$$

Since the acquisition of diffusion signal can be carried out almost throughout the entire q-space (DSI), no assumption about the diffusion process is necessary. Therefore there is no need to use any model for estimating the diffusion.

3.2.2.2 Diffusion characteristics extraction

Diffusion Probability Density Function (PDF)

As mentioned above, the diffusion distribution PDF $P(\vec{q})$ is the three-dimensional Fourier transform of the diffusion signal $E(\vec{q})$.Thus in DSI, the PDF is the most important diffusion characteristic extracted from the image.

$$P(\vec{q}) = \int_{\vec{q}\in\Omega_q} E(\vec{q})\exp(-i2\pi\vec{q}^{\mathrm{T}}\vec{p})d\vec{q} \tag{3.19}$$

where Ω_q represents the q-space and $\vec{p}$ the average diffusion displacement of all the molecules in one voxel.

Orientation Density Function (ODF)

The diffusion orientation density function (ODF), compared with PDF, is defined as the radial projection of the PDF $P(\vec{q})$ on a unit sphere [Goh *et al.*, 2009]. In other words, the integral of the data acquired with the same diffusion weighted gradient strength along the different directions. For a point k on the sphere, the ODF is expressed by:

$$ODF(\vec{k}) = \int_{\vec{q}\perp\vec{k}} P(\vec{q})d\vec{q} \tag{3.20}$$

Main diffusion direction

Compared with the DTI, the extraction of the diffusion principal direction using DSI is a bit more complicated. It is realized by discretizing the q-space to look for the maxima of the ODF. This step requires significant computing time and the precision of the measure depends on the quality of the spatial sampling and quantification [Tournier *et al.*, 2004; Aganj *et al.*, 2009; Tristán-Vega *et al.*, 2009; Kezele *et al.*, 2010]. Once the ODF maxima are extracted, the main diffusion direction corresponds to the orientation located at the ODF maxima. The ODF overcomes the limits of the DTI by its ability to distinguish the intra-voxel fiber crossing and the fiber kissing, two crucial primary steps for fiber tracking.

3.2.2.3 Advantages and limitations

Advantages

Because DSI does not make any assumption about the diffusion profile of the water molecules in the tissues, it is potentially capable to estimate the PDF and reveal the tissues' microstructure accurately.

Limitations

Although the DSI is one of the most accurate methods for analyzing the diffusion profile from diffusion images, two limitations make it inappropriate for clinical applications:

1) The DSI requires a very long acquisition time for the entire q-space to be sampled with sufficient angular resolution, at least hundreds of acquisitions [VJ Wedeen *et al.*, 2008].
2) The DSI requires relative high magnetic gradients to explore the entire q-space, therefore limiting its use for clinical applications.

3.2.3 Q-Ball Imaging (QBI)

In order to acquire accurate diffusion distribution profiles, while reducing the acquisition time, a new technique called "Q-ball" imaging was proposed by Tuch in 2004 [Tuch, 2004]. The idea is to primarily extract the ODF by acquiring the diffusion signal along a few selected directions and then to post-process the sparse ODF with interpolation. At the beginning, the interpolation was performed using a Funk-Radon transform with a Gaussian kernel [Cho *et al.*, 2008; Tristán-Vega, 2010], with about two hundreds acquisition directions. Later works suggest that the use of Spherical Harmonics (SH) basis lowering the required acquisition angular sampling [Hess *et al.*, 2006; Canales-Rodríguez *et al.*, 2009]. The diffusion signal acquired on a sphere of radius q' with a SH basis in the q-space is expressed as:

$$E(\vec{u}) = \sum_{l=0}^{L} \sum_{m=-l}^{l} c_{lm} Y_l^m(\vec{u}) \tag{3.21}$$

where $\vec{u}$ is the unit vector of $\vec{q}$. In this case, the magnitude of $\vec{q}$ is q'. The coefficient c_{lm} represents the diffusion signal under the basis Y_l^m (l is the order of the SH basis and m is the phase range from $-l$ to l). Several recent researches suggest the use of other basis such as spherical ridgelets [Michailovich *et al.*, 2010a, 2010b] , spherical wavelets [Kezele, 2010], and compressed sensing [Michailovich *et al.*, 2010c; Cheng *et al.*, 2011] etc. arguing their potential to lower the acquisition sampling rate, but at the expense of strong assumptions about the diffusion signals.

3.2.3.1 QBI model description

As talked above, the QBI technique requires only a few set of acquisitions. In order to accurately reveal the diffusion distribution within the tissue, the method requires to process the acquired diffusion signal with appropriate interpolation methods. With the SH basis, the interpolated diffusion signals can be approximated by the coefficient c_{lm} defined as:

$$c_{lm} = \int_{\vec{u}\in S^2} E(\vec{u}) Y_l^m(\vec{u}) d\vec{u} \tag{3.22}$$

where Y_l^m is the SH basis given by:

$$Y_l^m(\vec{u}) = Y_l^m(\theta,\phi) = \sqrt{\frac{(2l+1)(l-m)!}{4\pi(l+m)!}} p_l^m(\cos(\theta))\exp(im\phi) \tag{3.23}$$

with p_l^m the associated Legendre polynomial, and θ and ϕ determined by the direction of $\vec{u}$. $E(\vec{u})$ is the diffusion signal acquired along the direction $\vec{u}$. Eq.(3.22) illustrates the fact that projecting onto the SH basis the diffusion signal acquired from each diffusion direction respectively and summing these projections generates the needed coefficient c_l^m.

3.2.3.2 Diffusion characteristics extraction

Orientation density function (ODF)

From QBI the ODF of the diffusion can not only be extracted as from DSI, but also be calculated by a simpler approximation [Descoteaux *et al.*, 2007]:

$$ODF(\vec{k}) = \sum_{l=0}^{L} \sum_{m=-l}^{l} 2\pi P_l(0) clm Y_l^m(\vec{k}) \tag{3.24}$$

Besides ODF, the other diffusion characteristics mentioned in DTI, such as the diffusivity, diffusion anisotropy, and the principal diffusion orientation etc. could also be extracted from QBI.

3.2.3.3 Advantages and limitations

Advantages

1) As DSI, QBI does not make any assumption about the diffusion profile during the signal analysis.
2) Compared to DSI, it requires less acquisition directions (about 60 directions are sufficient) and the lower diffusion weighted gradients.
3) The linear estimation algorithm of the ODF based on the SH basis is very convenient and fast.

Limitations

1) This method is unable to reveal the real diffusion PDF because it allows calculating the diffusion characteristics for only one unit sphere.
2) Because the signal is acquired from only one sphere, thus the ODF estimated from such data is not exact.

3.2.4 Multi-Tensor Imaging (MTI)

A variety of models [Yassine *et al.*, 2006; Pasternak *et al.*, 2008; Assaf, 2008c] in the literature assume that the diffusion signal can be described as a weighted sum of several diffusion tensor models. This is called “Multi-Tensor Imaging”.

3.2.4.1 MTI model description

Assuming that the number of main diffusion directions in each voxel is n, and each one can be represented by a diffusion tensor $\underline{D}_i$, $i = 1,2,3...n$, then the diffusion signal in each voxel can be modeled by:

$$E(\vec{q}) = \sum_{i=1}^{n} f_i \exp(-4\pi^2 t \vec{q}^{\mathrm{T}} \underline{D}_i \vec{q}) \tag{3.25}$$

where f_i is the weight of the i^{th} main diffusion direction.

The estimation of this model requires various prior knowledge, such as the number of possible components number n and a criterion to define the weighting constant f_i [Tuch, 2002; Yassine, 2006]. The choice of the number n of components is usually arbitrarily set or is selected by a statistical criterion. The estimation of other parameters is carried out by a non-linear iterative numerical process such as the gradient descent [Tuch, 2002], a Gauss-Newton scheme [Deriche *et al.*, 2004], or an unscented Kalman filter [Malcolm *et al.*, 2010]. Once these parameters have been estimated, the diffusion characteristics can be clearly described.

3.2.4.2 Advantages and limits

Advantages

1) MTI allows analyzing fiber crossings contrary to traditional DTI, because it does not make any Gaussian assumption about the angular distribution of diffusion.
2) The extraction of diffusion characteristics does not require any post-processing once the reconstruction is finished.
3) The number of acquisitions is reasonable. (Typically, 64 directions on a sphere are enough).

Limitations

1) The estimation of the parameters in the model is based on empirical hypothesis under a specific context. This limits the generality of the model in other conditions.
2) The stability and the accuracy of this model depend on the initial parameters selected during the non-linear estimation process.

3) An error on the choice of the number of the component directly degrades the results.

3.3 Numerical simulation models

We presented in subsection 3.2 the most common mathematical models used in dMRI analysis. All these techniques aim to extract the various diffusion characteristics using different mathematical tools. They provide useful means for estimating the specific microstructure properties of biological tissues. However, one question remains. How well these diffusion characteristics calculated from diffusion MRI reflect the actual tissue microstructure properties since there is no ground-truth information available?

In this context, the numerical simulation models for dMRI using synthetic data were developed. Synthetic data, unlike real data, provides ground-truth, thereby allowing us to evaluate and optimize the methods in a given environment. The most common numerical methods for synthesizing diffusion MRI data are either determinist as the finite-difference (FD) approaches or stochastic as Mont-Carlo (MC) methods [Grebenkov, 2007]. We briefly introduce these two numerical approaches in the following paragraphs.

3.3.1 Finite difference simulations

The finite difference method is the most common determinist method to solve partial differential equations (PDE) on a spatial grid over a series of time steps. A diffusion equation being a typical PDE, various models of FD were developed to get the solution with the objective to increase the computation efficiency and improve the stability of the models. To simulate dMRI using a FD technique was firstly proposed by Hwang [Hwang *et al.*, 2003], he used an image-based finite difference method to illustrate the temporal evolution of the magnetization of each point in the image. Few years after, this model was modified by Xu [Xu *et al.*, 2007], which calculated the magnetization variations using a matrix and parallel computing methods, so reducing the simulation time. We introduce how FD can simulate the dMRI.

3.3.1.1 Principle

For simplicity, we illustrate the FD principle for simulating the magnetization changes in only one-dimension with three discretized points, see Fig. 3.1.

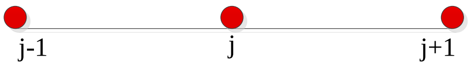

Fig. 3.1 Finite element points

At point j, the transverse magnetization is expressed as:

$$M_j^{n+1} = \exp\left(\frac{-t_n}{T_{2j}}\right)\exp(-i\gamma g_n x_j t_n)M'^{n+1}_j \tag{3.26}$$

$$M'^{n+1}_j = \left(1-2\frac{D_j t_n}{(\Delta x)^2}\right)M_j^n + \frac{D_j t_n}{(\Delta x)^2}M_{j+1}^n + \frac{D_j t_n}{(\Delta x)^2}M_{j-1}^n \tag{3.27}$$

The subscript of n represents the time step indices, g_n means diffusion gradient applied at the time t_n. The subscript j indicates the spatial index, D_j and T_{2j} are respectively the diffusion coefficient and transverse relaxation time at point j, Δx is the displacement experienced by the molecules during the each time step. Thus Eq. (3.26) describes the transverse relaxation and the phase accumulation during the application of the diffusion weighted gradients and Eq. (3.27) illustrates the diffusion process itself.

In biological tissues, the diffusion is not isotropic, thus the diffusion of water molecules is described by the jump probability in FD [Layton, 2006], defined as the probability of a spin to start at one grid point and to migrate to another point after a time interval of ($t_n - t_{n-1}$). Thus, Eq. (3.27) can be rewritten as:

$$M_j^{'n+1} = (1 - p_{j\to j-1} - p_{j\to j+1})M_j^n + p_{j-1\to j}M_{j-1}^n + p_{j+1\to j}M_{j+1}^n \tag{3.28}$$

where $p_{j\to j-1}$ is the jump probability from point j to point $j-1$. If there are totally N points in the image, then we will obtain N equations that have the same form as Eq. (3.28). From the equations and combining the initial conditions the jump probability can be estimated, and therefore the diffusion coefficient in each point is inferred [Xu, 2007].

3.3.1.2 Advantages and limitations

Advantages

1) The FD technique is able to deal with the diffusion process in complex geometries with various initial conditions.
2) It is proficient in handling heterogeneous materials where every element in the model can be assigned a different set of properties.
3) This method provides a ground-truth to evaluate the simulation results because the structure of the diffusion environment is well known a priori.

Limitations

1) The choice of the boundary conditions for the diffusion equations directly determines the FD simulation results. If the boundary conditions are not appropriate, edge effect artifacts will arise, that will have to be reduced by additional computation not to become a source of significant error.
2) The FD is sensitive to user-introduced modeling errors, such as inadequate geometrical models.
3) The computing efficiency remains poor.

3.3.2 Monte-Carlo simulations

Monte-Carlo (MC) methods simulate the Brownian motion of spins within a given geometrical model and accordingly calculate the diffusion signal based on the diffusion displacement in the different directions. The authors [Duh *et al.*, 2001] simulate diffusion signal distributions for one-dimensional restricted geometries, so providing a theoretical basis for later studies. [Cai, 2005] calculate the diffusion propagator in the case of restricted diffusion with different diffusion sequences, so offering a convenient, intuitive and precise method for the study of the diffusion behaviour in complex tissues. [Assaf, 2008a] model the diffusion signal in a cylinder using a random walk method and compare the simulation with experimental results. This model successfully predicts the dependence of diffusion signals on gradient pulse duration and gradient strength as well as the tube cylinder diameter. [Fieremans *et al.*, 2008] simulate the diffusion coefficient in 3D geometries of fiber phantoms with varying packing densities and validate the simulation results with real experiments, which shows that the MC simulation can be useful for the quantitative validation of diffusion imaging on clinical MRI devices. For better understanding, the MC simulation process is briefly introduced.

3.3.2.1 Principle

There is not a single principle describing Mont-Carlo methods. Instead, MC methods include a large class of stochastic simulation approaches. In dMRI, according to the diffusion environment, the diffusion laws of the water molecules are not identical, but the basic simulation steps of MC are similar:

1) Generate the initial spatial distribution of water molecules according to the properties of the tissues.
2) Assign the diffusion coefficient to the different components of the tissues according to some statistical criteria.
3) Give a certain diffusion time interval, using the random walk model to simulate the diffusion process. The random walk step length and direction of water molecules must conform to a given distribution determined by the diffusion environment.
4) Calculate the diffusion signal and the diffusion properties from the obtained diffusion displacement of the water molecules.

3.3.2.2 Advantage and limitations

Advantages

1) As FD methods, the MC method provides a ground-truth to evaluate the simulation results because the structure of diffusion environment is well known a priori.
2) Simulation accuracy can be controlled by choosing the number of molecule involved in the simulation process.

Limitations

A lot of confrontation is required to obtain an accurate estimator.

3.4 Bloch-Torrey equation simulation model

Inspired by the successful simulation of MRI using the Bloch equations [Benoit-Cattin *et al.*, 2005; Balac *et al.*, 2008; Latta *et al.*, 2010], several researchers began to apply the analytical model to investigate dMRI by changing the Bloch-Torrey equation to adapt it to various diffusion situations. [Rhomer *et al.*, 2006] presented a Bloch-Torrey equation expressed in general curvilinear coordinates in order to describe the diffusion phenomenon in deforming media. [Awojoyogbe *et al.*, 2009] introduced a time-dependent Bloch diffusion equation using the Boubaker polynomials expansion scheme, and provided a new expression form for the spin magnetization. [Jochimsen *et al.*, 2006] simulated the diffusion-weighted image of the brain based on calculating the partial derivatives of the magnetization in Bloch-Torrey equation. As a supplement to MRI experiments, the simulation of the MRI sequence and the imaging process based on the solution of Bloch-Torrey equation provides a valuable tool for developing, optimizing and assessing the new imaging parameters.

3.4.1 Principle

According to the Bloch-Torrey equation, the magnetization vector is:

$$\frac{d\vec{M}_t}{dt} = \gamma(\vec{M}_t \times \vec{B}) - \begin{pmatrix} \dfrac{m_t^x}{T_2} \\ \dfrac{m_t^y}{T_2} \\ \dfrac{m_t^z - m_0^z}{T_1} \end{pmatrix} + \begin{pmatrix} \nabla \cdot \underline{D} \nabla m_t^x \\ \nabla \cdot \underline{D} \nabla m_t^y \\ \nabla \cdot \underline{D} \nabla m_t^z \end{pmatrix} \tag{3.29}$$

where $\vec{M}_t = (m_t^x, m_t^y, m_t^z)$ is the spin magnetization at time t , m_t^x, m_t^y, m_t^z are its three components. If assuming that the main magnetic field is applied along z direction, m_0^z represents the initial equilibrium value of magnetization which depends on the proton density ρ . T_1, T_2 are the relaxation constants, $\vec{B}$ is the magnetic field which consists of the main magnetic field and the gradient field. $\underline{D}$ is the diffusion tensor and in the case of isotropic diffusion $\underline{D}$ becomes a constant. Using the iterative simulation the Eq. (3.29) can be solved by [Jochimsen, 2006]:

$$M_{t+1} = EA_D R_{RF} R_z M_t + E_0 \tag{3.30}$$

with initial condition $M_0 = (0, 0, m_0^z)^T$.

The relaxation part is expressed by:

$$E = \begin{bmatrix} \exp(\frac{-t}{T_2}) & 0 & 0 \\ 0 & \exp(\frac{-t}{T_2}) & 0 \\ 0 & 0 & \exp(\frac{-t}{T_1}) \end{bmatrix} \tag{3.31}$$

$$E_0 = \begin{pmatrix} 0 & 0 & m_0^z(1 - \exp(\frac{-t}{T_1})) \end{pmatrix}^T \tag{3.32}$$

The self-diffusion of molecules will introduce the attenuation of the magnetization, which is expressed by the parameter A_D :

$$A_D = \begin{bmatrix} \exp(-a_1 D) & 0 & 0 \\ 0 & \exp(-a_2 D) & 0 \\ 0 & 0 & \exp(-a_3 D) \end{bmatrix} \quad (3.33)$$

Here we just illustrate the isotropic diffusion, thus D in Eq.(3.33) represents the diffusion coefficient, a_1, a_2, a_3 are the factors related to the gradients. The detailed calculation process refers to [Jochimsen, 2006]. The rotation matrix caused by the RF pulses is:

$$R_{RF} = Rot_z(\phi) Rot_x(\alpha) Rot_z(-\phi) \quad (3.34)$$

ϕ is the phase angle of the RF pulse and α is the flip angle. Rot_z and Rot_x are respectively the rotation matrix about the z axis and x axis.

$$\phi = \gamma B t \quad (3.35)$$

Finally, off-resonance effects due to the local field inhomogeneity, chemical shift or externally applied gradient fields are taken into account by the rotation matrix R_z .

$$R_z = \begin{pmatrix} \cos\theta_z & \sin\theta_z & 0 \\ -\sin\theta_z & \cos\theta_z & 0 \\ 0 & 0 & 1 \end{pmatrix} \quad (3.36)$$

Combining the equations from (3.30) to (3.36), at each time, the local magnetization can be calculated.

3.4.2 Advantages and limitations

Advantages

1) This method obtains the diffusion images by simulating the image generating process, which includes the simulation of the MRI sequences, by modeling the object properties, and by analyzing the influence of noise and artifacts etc.. Thus, it provides a valuable tool for evaluating and optimizing the imaging conditions.
2) It provides a ground-truth for assessing the simulation result because the virtual imaging object is perfectly known in advance.

Limitations

1) The simulation is easy to realize for isotropic diffusion. However, for anisotropic diffusion, molecular diffusion cannot be described simply by the diffusion coefficient instead of the diffusion tensor or other parameters, this will increases the complexity of the iteration steps.

2) The iteration process should be executed through every voxel of the image for generating the diffusion-weighted image. This requires a long computing time.

3.5 Conclusion

From the state of the art of three kinds of dMRI modeling and simulation methods, it can be seen that, up to now, each method has its own merits and drawbacks. The mathematical models are able to provide versatile parameters to describe the diffusion properties of water molecules moving within the biological tissues, such as MD, FA, PDF, ODF, and main diffusion directions. These parameters are very useful for inferring the microstructure of tissues. However, in the absence of ground-truth, the microstructure inferred from this kind of model is difficult to assess.

The second kind of models, “numerical simulation methods”, has an obvious advantage in that it provides a perfect ground-truth for evaluating the simulation results. Nevertheless, because numerical simulation often requires a long computing time, only simulations in simple structures was validated until now.

The Bloch-Torrey simulation model also belongs to the numerical simulation methods, but has some specificity that justify that we presented it separately. It simulates the process of diffusion imaging, including RF pulse excitation, spatial encoding, diffusion weighting, and signal sampling. It is therefore capable of providing more realistic diffusion images. However, contrary to MRI simulators, which have already been largely developed, the dMRI simulation using the Bloch-Torrey equation is a new proposal. It can only simulate isotropic diffusion. Further research is needed to extend it into complex anisotropic diffusion case.

In summary, finding a dMRI simulation model able to reveal the complex anisotropic diffusion in biological tissues, and meanwhile, able to provide a ground-truth for evaluating this model is a new challenge.

PART II

Contributions

Chapter 4

Simulating dMRI for simple structures using a Monte-Carlo method

Contents

Résumé en français

Comme il a été précisé dans les chapitres précédents, la structure des fibres du myocarde joue un rôle important en assurant les fonctions normales mécaniques et électriques du cœur. Il est donc intéressant d'étudier la différence de structure entre les états normaux et pathologiques. Jusqu'à présent, la plupart des recherches sur la structure des fibres du myocarde se focalise sur l'orientation des fibres, qui peut être fournie par de nombreuses modalités d'IRMd, telles que le DTI, QSI et QBI que nous avons mentionnées dans le chapitre précédent.

Ces différentes modalités d'imagerie fournissent des connaissances plus ou moins précises sur la distribution des orientations des fibres. En générale, à partir de la distribution des orientations des fibres et des propriétés de la diffusion telles que FA et MD, on espère pouvoir prédire les maladies cardiaques. Cependant, pour l'IRMd typique, la taille du voxel d'une image volumique est de l'ordre d'environ 10 mm^3. Pour les applications cardiaques, cela signifie qu'un tel voxel contient des milliers de myocytes cardiaques et d'autres tissus extracellulaires. Par conséquent, de nombreux facteurs peuvent influencer l'orientation et l'anisotropie de la diffusion mesurée, tels que le changement de structure des myocytes cardiaques, la variation de l'arrangement des myocytes, l'échange de l'eau entre les espaces intra et extracellulaire, etc. Dans ces conditions, il serait difficile de savoir exactement l'origine des changements de l'anisotropie de diffusion et d'orientation, et par conséquent impossible de les corréler avec les causes de la maladie.

Pour attaquer ce problème, nous proposons dans ce chapitre de simuler l'IRMd pour un simple modèle de structure virtuelle des fibres cardiaques, à l'aide de la méthode de Monte-Carlo. La relation entre l'anisotropie de diffusion mesurée et les caractéristiques des fibres cardiaques, y compris les effets physiques et structurels, est étudiée.

Nous décrivons tout d'abord l'algorithme de simulation de l'IRMd. Ensuite, la relation entre l'anisotropie de diffusion et les propriétés physiques des fibres cardiaques est analysée. Enfin, l'influence des caractéristiques structurelles des fibres cardiaques sur l'anisotropie de diffusion est étudiée.

Les résultats montrent que:

- L'augmentation du contenu de l'eau dans l'espace intracellulaire produit une grande valeur d'anisotropie fractionnelle (FA).
- La diminution de la perméabilité de la membrane augmente la valeur de FA.
- FA est influencé principalement par la taille des myocytes.
- FA change doucement avec la variation de l'arrangement de myocytes.

Ces résultats démontrent que le simulateur proposé dans ce chapitre nous permet de comprendre la relation entre la structure microscopique et les propriétés de diffusion mesurées. Ils fournissent une base théorique pour les travaux décrits dans les chapitres suivants.

4.1 Objectives

As detailed in the preceding chapters, the myocardial fiber structure plays an important role in ensuring normal mechanical and electrical properties of the heart. It is therefore interesting to investigate the difference of structure between its normal and pathological states. Up to now, most research on myocardial fiber structure focuses on fiber orientation that can be provided by various dMRI modalities, such as DTI, QSI and QBI that we mentioned in the preceding chapter. These imaging modalities provide more or less accurate knowledge about the orientation distribution of fibers. Generally, from the orientation distribution and the corresponding diffusion anisotropic properties such as FA and MD, one expects to predict cardiac diseases. However, for typical dMRI, the size of an image voxel is of the order of about 10 mm^3. For cardiac applications, it means that such voxel contains thousands of cardiac myocytes and other extracellular tissues. As a result, there are many factors which may influence the measured orientation and diffusion anisotropy, such as the cardiac myocyte structure change, the variation of myocyte arrangement patterns, the water exchange between intra- and extra-cellular spaces, etc. In this condition, it would be difficult to know exactly the origin that leads to the change of diffusion anisotropy and orientation, and consequently impossible to correlate it with disease causes.

In order to deal with this problem, we propose in this chapter to simulate the dMRI for a simple virtual cardiac fiber architecture model using Monte-Carlo method and attempt to understand the underlying relationship between the measured diffusion anisotropic properties and the cardiac fiber characteristics, including both physical and structural ones.

This chapter is organized as follows. The dMRI simulation algorithm is first presented in section 4.2. Then, the relationship between diffusion anisotropy and physical properties of cardiac fiber is studied in section 4.3. Finally, in section 4.3.3, the effect of structural characteristics of cardiac fibers on diffusion anisotropy is investigated, followed by a conclusion in section 4.5.

4.2 dMRI simulation algorithm

The principle of dMRI is to detect the MR signal attenuation caused by the diffusion of water molecules in the tissues. Molecular diffusion is a kind of Brownian motion resulted from the thermal energy. During the diffusion, the molecules collide with each other, which results in the change in motion direction of each molecule. Thus, the overall diffusion process could be well described by a sequence of tiny random walks of water molecules, although the real diffusion process is more complex. In order to simplify the simulation process in a first attempt, in the present work, the diffusion process is simulated by a random walk using Monte-Carlo method.

In a free medium, during a given time interval, molecular displacement can be expressed by Einstein diffusion law [Einstein, 1956], which is well described by the diffusion coefficient of water molecules in this medium. Thus, in our simulation, the distance s during one random walking time interval τ is given by:

$$s = \sqrt{2mD\tau} \tag{4.1}$$

where D is the free diffusion coefficient of water molecules in the cardiac muscle at 37ºC, and m is the diffusion dimension.

In the biological tissues, the walking displacement distribution of water molecules is determined by the structure of tissues. In our simulation, this distribution is split into two items. One is the distribution of diffusion distances $P(s)$ during one walk step, which is simulated by a Monte-Carlo method. The other is about the diffusion directions that conform to uniform distribution in our case.

When the molecules diffuse in the tissues, besides the collision that takes place among the molecules, the collision between the molecules and the tissue boundaries should be considered. In this work, the interaction between molecules and tissue boundaries is described by a collision and reflection model, in which the molecules do not lose any energy after collision and just change the direction for going on walking. No matter how many times that molecule collides with boundaries, the total length of walking trajectory during one walking step always keeps the same.

Since the molecule position randomly varies with time, at the end of each walking step, the displacement $\overrightarrow{r_i^j}$ of each molecule i for the j^{th} walking step is different, which is expressed by

$$\overrightarrow{r_i^j} = sP(s) \tag{4.2}$$

In order to measure this displacement, a pair of magnetic field gradient pulses in the different directions are simulated, whose duration is δ, diffusion time is Δ and gradient strength vector is $\vec{G}$. These parameters determine the simulated $\vec{q}$ value and $\vec{b}$ factor for calculating diffusion signal:

$$\vec{q} = \frac{\gamma}{2\pi}\vec{G}\delta \tag{4.3}$$

$$\vec{b} = 4\pi^2 \vec{q}^{\,2}(\Delta - \delta/3) \tag{4.4}$$

where γ is the gyromagnetic ratio of ^{1}H with a constant value of 42.5657 MHz/T. According to the basic theory of dMRI, the phase shift induced by the displacement of molecule i during the j^{th} walking step is:

$$\phi_i^j = 2\pi\vec{q}\cdot\overrightarrow{r_i^j} \tag{4.5}$$

The total number of random walks k is:

$$k = \Delta/\tau \tag{4.6}$$

Thus at the end of the diffusion gradient pulse, the phase shift caused by one molecule is:

$$\phi_i = \sum_{j=1}^{k}\phi_i^j = 2\pi\sum_{j=1}^{k}\vec{q}\cdot\overrightarrow{r_i^j} \tag{4.7}$$

Accordingly, the diffusion signal caused by the diffusion of n molecules is numerically approximated by:

$$E = \frac{1}{n}\sqrt{(\sum_{i=1}^{n}\cos(\phi_i))^2 + (\sum_{i=1}^{n}\sin(\phi_i))^2} \tag{4.8}$$

The key point of this simulation is to find accurately the collision point between the molecules and the complex tissue structures at different diffusion moments. It determines whether the simulated diffusion images are capable of interpreting the microstructures for a given model. The flow diagram in Fig. 4.1 illustrates the simulation process.

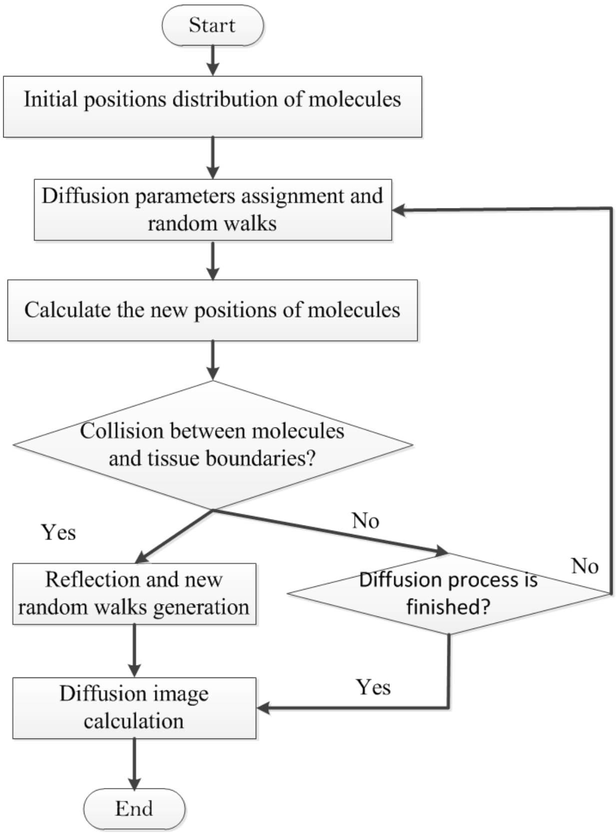

Fig. 4.1 Flow diagram of the proposed simulation.

In order to choose an appropriate distribution $P(s)$ of random walking step lengths, we compared two situations with respectively Gaussian and uniform distributions, which are often used in diffusion simulations [Farnell *et al.*, 2004; Fieremans, 2008; Hall *et al.*, 2009]. We assume that water molecules diffuse in two infinite parallel plates separated by a distance of $2a$. If the diffusion gradient is applied along the direction normal to the plates, the thus resulting diffusion corresponds to the restricted one. However, if the gradient is added in the direction parallel to the plates, it then concerns free diffusion of the water molecules in this direction. For the restricted diffusion and the free diffusion, the corresponding analytical diffusion signals are given respectively in the works of [Price, 1997; Price *et al.*, 1998]:

$$E_{\text{retrict}} = \sin^2(\pi qa)/(\pi qa)^2 \tag{4.9}$$

$$E_{\text{free}} = \exp(-bD_0) \tag{4.10}$$

Using Monte-Carlo method, we simulate the diffusion of water molecules between two plates and calculate the diffusion signal for both free and restricted diffusion. By comparing the simulation results obtained with different distributions and the analytical results, we can choose the appropriate one. In all the simulations, the number of molecules is set to 2×10^8 in order to obtain the results with high accuracy. At the beginning, the molecules are uniformly distributed in space. Then, they walk randomly with either uniform or Gaussian distribution of walk step lengths, but with the same distribution of directions. After a given time, according to Eq. (4.8) the diffusion signals in the directions both normal and parallel to the plate are calculated. All simulations were performed on a PC machine cluster and the computation time was about 16 hours. The simulation results with the corresponding parameters are illustrated in Fig. 4.2.

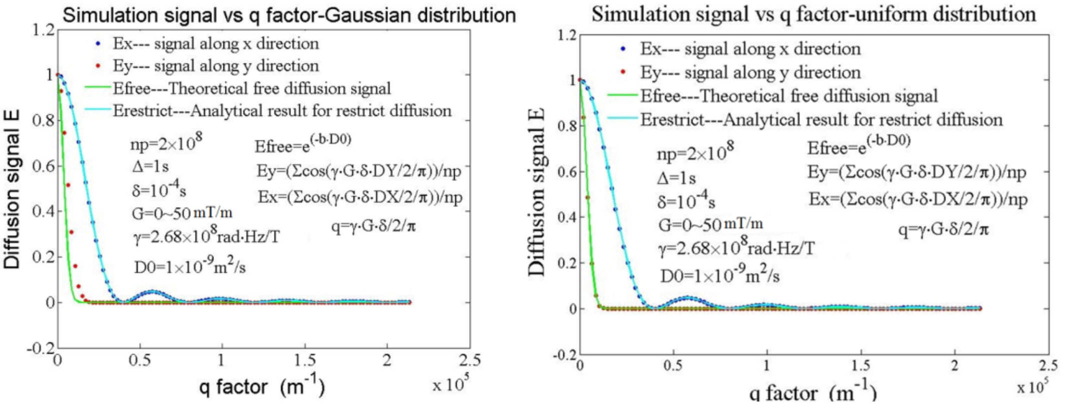

(a) (b)

Fig. 4.2 dMRI signal for diffusion between two plates. (a) The comparison between the simulation results obtained with Gaussian distribution of walk step lengths and the analytical results. (b) The comparison between the simulation results obtained with uniform distribution of walk step lengths and the analytical results. The curves drawn in line are the analytical results and those drawn in point are the simulation result.

It can be seen that the simulation with the uniform distribution conforms better to the theoretical results. For this reason, in the following works of this thesis, all the diffusion processes will be simulated using the uniformly distributed walking step lengths.

4.3 Diffusion anisotropy VS physical characteristics of cardiac fiber

As we illustrated in chapter 1, a cardiac fiber consists mainly of cardiac myocytes and extra-cellular matrix that includes various types of collagens. This complex structure impedes definitely the displacement of water molecules in certain directions and therefore introduces the diffusion anisotropy. However, the exact mechanisms underlying the relationship between diffusion anisotropy and tissue properties remain unknown. Some proposals suggested that the high viscosity and restriction effects of intra-cellular space for the water diffusion determine the diffusion anisotropy, but the others believed that the tortuosity effects for the water diffusion in the extra-cellular space is the main cause for the diffusion anisotropy [Pfeuffer *et al.*, 2000; Beaulieu, 2002; Zheng, 2009]. It is therefore important to evaluate respective contributions of intra- and extra-cellular compartments in the diffusion characteristics of cardiac fibers. To this end, the diffusion weighted and diffusion tensor images are simulated for a simple virtual cardiac fiber structure model, and then the influence of physical properties, including the water content in intra- and extra-cellular spaces and the membrane permeability, upon diffusion anisotropy is investigated in what follows.

4.3.1 Simple cardiac fiber structure modeling

In order to mimic the realistic structure of myocytes as well as that of myocardial fibers, and to find an easy way to describe some of known variations in the tissue structure, such as the shape and the location of the myocytes, we model the virtual cardiac fibers as a three-dimensional matrix of realistically shaped myocytes which are connected with intercalated disk and collagen network. In order to reduce computation consuming resources, the spatial resolution of the model was selected as 5 μm. The model consists in the mixture of two regions, the intracellular cytoplasm and the extracellular collagen. Each myocyte in the model has a size of about 15×25×90 μm^3 and all the myocytes share the same direction along the long axis but they are arranged differently in space, which means that, from a macroscopic viewpoint, the anisotropy is uniform, but from a microscopic view, it is not.

In order to approximate the actual structure of myocytes, we represent it by random hexagons combination. In the transverse plane, the myocyte location is randomly distributed on the surface. Based on the voronoi theory, a myocyte is formed by combining the nearest neighbor hexagons. Fig. 4.3 provides the histological image (in the transverse section) of the myocytes and its corresponding simulation model. It can be seen that our model is fairly realistic, and that it can generate myocytes with certain regular organization but varying shapes.

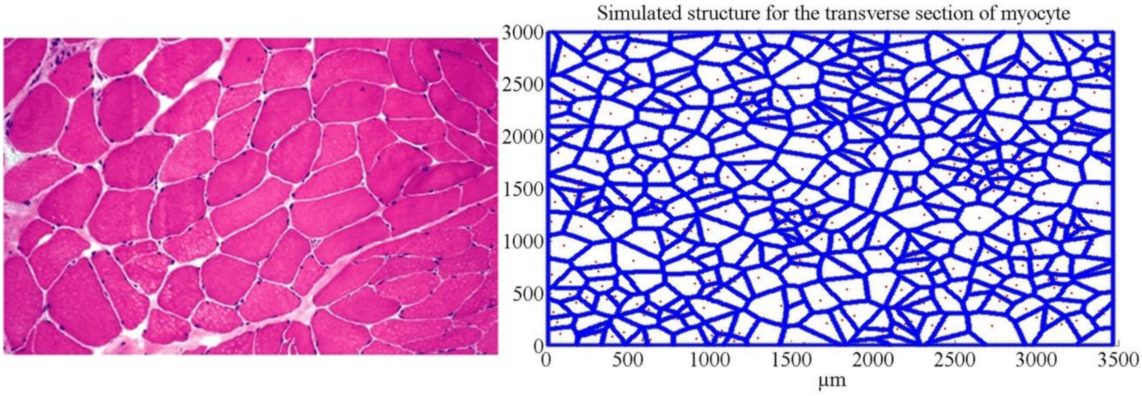

(a) (b)

Fig. 4.3 Simulated and histological images for cardiac fiber model. (a) Histological image for the transverse section of myocytes; (b) The virtual cardiac fiber transverse model

From this transverse slice, a three-dimensional myocyte is constructed by changing the length of the myocytes. By choosing the hexagon as the basic modeling element, we can control various parameters of diffusion simulation such as the boundary condition for the random walk, the simulation spatial resolution, the computation complexity, etc. In the present study, the hexagon edge length is chosen as 5µm.

4.3.2 Influence of water content on diffusion anisotropy

In the work of [Le Bihan, 2007], it was considered that water molecules diffuse quickly in the intra and extra spaces, but diffuse slowly near and in the membrane. The dimension of the membrane of cardiac myocytes being about 7.5 nm [Iaizzo, 2009], it is so small in comparison with that of cytoplasm and collagen that it is ignored in the present simulation. The diffusion coefficient in the cytoplasm and the collagen is selected as the same, which is $D_0 = 1000\ \mu m^2/s$, because both of them belong to the quick diffusion region. Moreover, the dimension of water molecules is about 3.2Å, and in the cytoplasm the water content is 78% and of which 92% of the water is immobilized [Iaizzo, 2009]. Thus, for our voxel (5x5x5 μm^3), there are about 3×10^{11} water molecules. In practice, it is almost impossible to simulate with such number of water molecules. A trade-off between computing time and simulation accuracy should then be performed. We selected 1000 molecules for one voxel. For the diffusion gradient, the amplitude was chosen as 2000 mT/m (note however that in real imaging, it ranges from 45 t0 87 mT/m) and pulse duration is 0.2 ms, the diffusion time as 50 ms, and the number of random walks during this period is 300. These parameters will generate a b-value of 578 s/mm^2 and q-value of 17 mm^{-1}.

Since water content in intra- and extra-cellular spaces is an important index to reflect the cardiac diseases such as the ischemia [Schaefer *et al.*, 2003], it is necessary to simulate the effects of the ratio of water content on diffusion anisotropy.

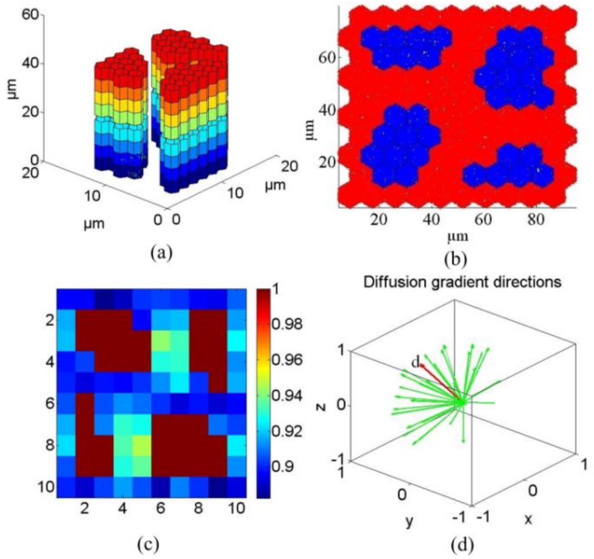

Fig. 4.4 Simulated myocyte structure and diffusion image. (a) A simulated 3D structure of myocytes; (b) A transverse slice of myocyte structure (red represents the extracellular space and blue is the intracellular space); (c) Simulated DWI for the slice (b) in the direction d shown in subfigure (d) (red one); (d) Diffusion gradient directions.

Fig. 4.4 shows a simulated structure and its corresponding diffusion image in one direction (red color). For this illustrated situation, water was distributed only in the extra-cellular space in order to distinguish it from the structure information. To investigate the influence of water content in different compartments, the ratio of water content in cytoplasm and extracellular was chosen respectively as 1/6, 1/5, 1/4, 1/3, 1/2, 1, 2, 3, 4, 5 and 6. The simulation results are given in Fig. 4.5.

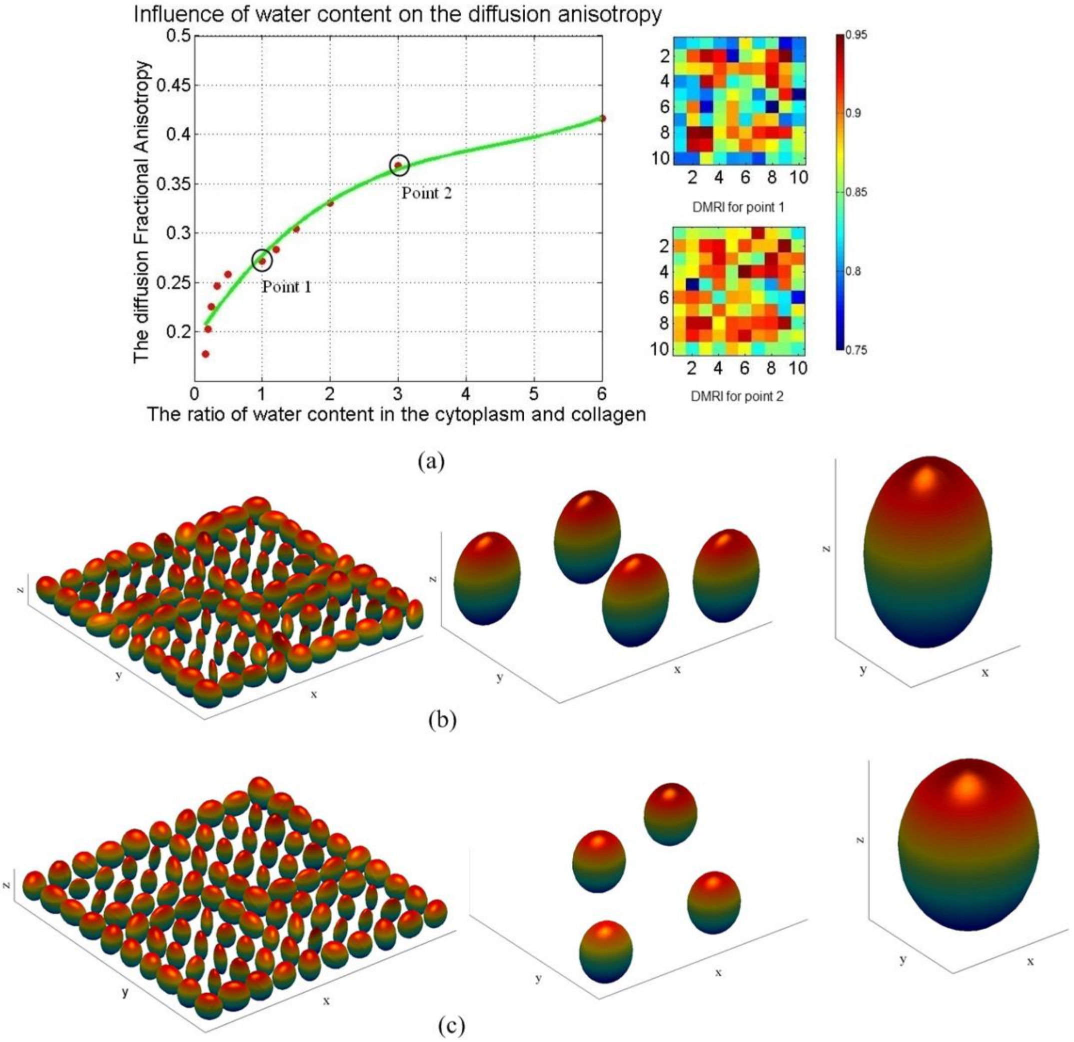

(a)

(b)

(c)

Fig. 4.5 Influence of water content on FA. (a) Influence of water content on FA and DW images in one direction for two different water content ratios. (b) Diffusion tensors of one hexagon, one myocyte and four myocytes for Point2. (c) Diffusion tensors of one hexagon, one myocyte and four myocytes for Point1.

Comparing the diffusion tensors in the first image of subfigure (b) and that of subfigure (c), it can be seen that at the scale of one voxel, the water content ratio change does not influence greatly the anisotropy. However, for a larger scale of single myocyte or several myocytes as shown in the second and the third tensor images in subfigure (b) and (c), the diffusion FA increases if the water content in the myocyte is bigger than that in the extracellular space. With increment of the water content ratio of intra- to extra- cellular space, the anisotropic diffusion becomes more obviously as illustrated in subfigure (a). This phenomenon is caused by the combination effects of diffusion in different compartments in the large-scale measurement. All these imply that for modeling MRI diffusion signal with DTI in large scales, the water content influence should be taken into account.

4.3.3 Influence of permeability on diffusion anisotropy

Besides the influence of water content, the water exchange between intra- and extra-cellular spaces also affects the diffusion anisotropy. Since the diffusional water exchange across the cell membrane is a fundamental process in metabolism system, it is an important indicator about cell functions. Analyzing the influence of membrane permeability on diffusion anisotropy can provide a useful mean to investigate the water exchange phenomenon using dMRI [Sehy *et al.*, 2002; Sukstanskii *et al.*, 2004; Imae *et al.*, 2009].

According to the research of [Ogura *et al.*, 2002], the permeability in the human tissues ranges from 0 to 100 μm/s. During their random walk process, water molecules will pass through the membrane with a certain probability p, which is determined by the permeability p_t, the diffusion coefficient D_0 and the random walk step length s. Their relationship is given by:

$$p = \frac{p_t \times s}{D_0} \tag{4.11}$$

Thus in our Monte-Carlo simulation, when water molecules collide with myocyte boundaries, a permeation probability for the molecules is randomly generated. When the latter is bigger than the value of p, the molecule in question will transverse the membrane. We simulated the DW images with permeability of 0, 10, 20, 30, 50, 70, 80, 90 and 100 μm/s respectively, from which the diffusion tensor images and FA were calculated. The variation of FA as a function of permeability is shown in Fig. 4.6.

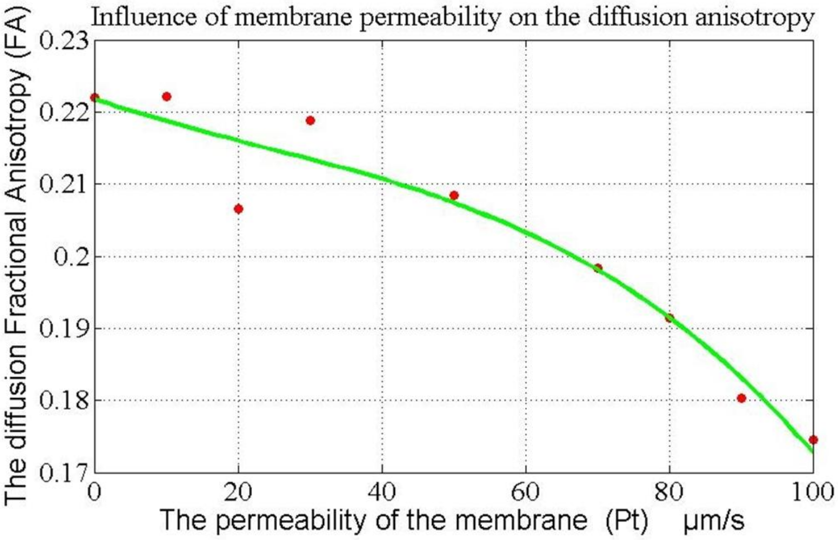

Fig. 4.6 Influence of membrane permeability on FA.

The results show that the diffusion anisotropy decreases when the membrane permeability is raised. In the present work, walk step length is 1µm that corresponds to a diffusion time of 1/6 ms for one step. In this condition, when the membrane permeability is smaller than 50µm/s, its influence can be ignored. In practice, diffusion time in dMRI ranges from several milliseconds to several seconds. As a result, for such long diffusion process, the contribution of permeability to FA should be considered accordingly.

4.4 Diffusion anisotropy VS structural characteristics of cardiac fibers

We have analyzed above the effects of physical properties of cardiac fibers, including water content and membrane permeability, on diffusion anisotropy. However, apart from the physical properties, cardiac fiber structural characteristics, such as the cardiac morphological heterogeneity and the myocyte arrangement patterns, also influence greatly the estimation of diffusion properties including fiber orientation and diffusion anisotropy [Stylianopoulos *et al.*, 2010; Shemesh *et al.*, 2012]. Therefore, in this section, we will investigate, in a multi-scale manner, the effects of cardiac fiber structural characteristics.

4.4.1 Modeling cardiac myocyte distribution in one voxel

In order to easily vary fiber orientations during virtual cardiac fiber modeling, the cardiac myocyte in the model is represented by a cylinder instead of the hexagons. According to histological parameters, the myocytes are modeled by a series of cylinders whose diameters range from 5 to 25µm and lengths from 50 to 100µm [Severs, 2000]. Since the spatial resolution of conventional MR images is about 2mm, and the myocyte density is about 0.2×10^{8} cells/cm^3 [Milica *et al.*, 2005], there are, in one voxel of an MR image, about 50000 myocytes. These myocytes have in general different orientations whose variance depends on the myocyte location. This means that, at the apex, the divergence of myocyte orientations can be up to 90 degrees, whereas in the middle wall it is less than 10 degrees [Severs, 2000]. Meanwhile, the arrangement pattern of myocytes is always a debatable issue. In the present study, both cardiac sheet and cardiac random patterns are simulated. All the above elements (shapes, arrangement pattern, and orientation divergence) constitute the cardiac myocyte structure heterogeneity in one voxel. In order to analyze their respective influence, the VCFS model is divided into three groups:

1) Myocytes are arranged randomly.
2) Myocytes are arranged in a cardiac tissue sheet manner.
3) Myocytes bear the same orientation but with various sizes.

The orientation of the myocytes is described by both the elevation and azimuth angles. The elevation angle is randomly selected between -π/2 and π/2, and the azimuth from 0 to 2π. In Fig. 4.7 is illustrated the VCFS model formed of a volume of 20x20x20 myocytes which have the same size (diameter 20µm, and length 100µm), and their arrangement pattern is random and independent of their orientation. In Fig. 4.8, the myocytes are arranged according to an orientation similarity, which allows simulating the laminar structure of cardiac fiber proposed by [Legrice, 1997]. In order to analyze the influence of size variation on fiber orientation measurements, the VCFS model with different myocyte sizes (length and diameter) but the same arrangement pattern as in Fig. 4.7 is considered, as illustrated in Fig. 4.9. The myocytes in these three models are taken as ground-truths for the following simulation.

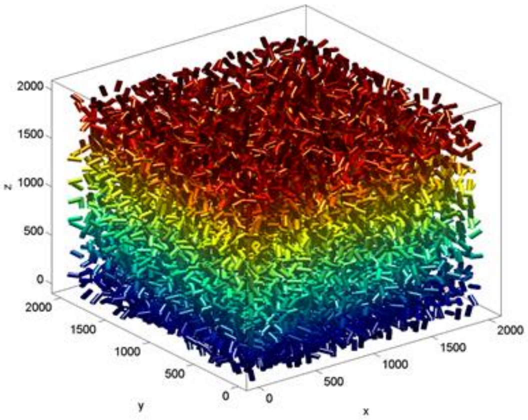

Fig. 4.7 Model 1: simulation of a 2mm×2mm×2mm voxel containing 20×20×20 myocytes having the same size but arranged randomly (uniform distribution).

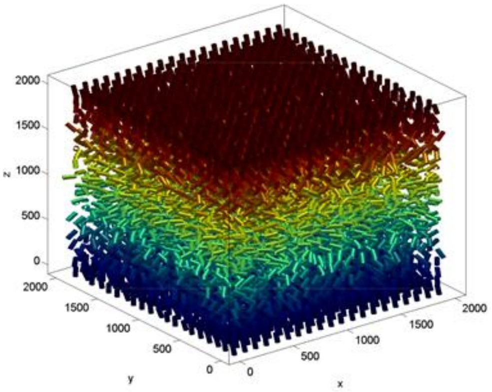

Fig. 4.8 Model 2: simulation of a 2mm×2mm×2mm voxel containing 20×20×20 myocytes having the same size and arranged regularly, which represents the laminar model of cardiac fiber.

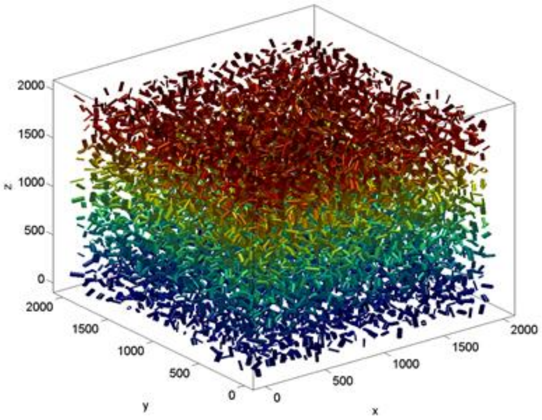

Fig. 4.9 Model 3: simulation of a 2mm×2mm×2mm voxel containing 20×20×20 myocytes having random sizes and arranged randomly (the arrange pattern is the same with Model 1).

4.4.2 Effects of observation scales on fiber orientation estimation

As stated in the previous section, dMRI data can be simulated by applying diffusion gradients along different directions. In this work, the number of diffusion directions defined by icosahedrons is 162, and the diffusion gradient magnitude is 3000 $\mathrm{mT/m}$ with pulse duration of 0.2 ms, which generates a q-value of 25.5 mm^{-1}. The number of water molecules in each myocyte is 5000, the diffusion time is 60 ms, and accordingly the b-value is 1543 $\mathrm{s/mm}^2$.

Because of the orientation distribution heterogeneity, the fiber orientation observed at different scales will not be the same. In order to investigate the influence of observation scales on the measurement of diffusion orientations, the diffusion tensor images corresponding to one slice (axial slice 3) in the model of cardiac fiber sheet structure (Fig. 4.7) are calculated at different scales. According to Eq.(4.8), for different gradient directions, we calculate different diffusion signals, from which are derived the diffusion tensors. The primary eigenvector of the tensor is taken as the measured diffusion orientation, as shown by the red color vectors in Fig. 4.10.

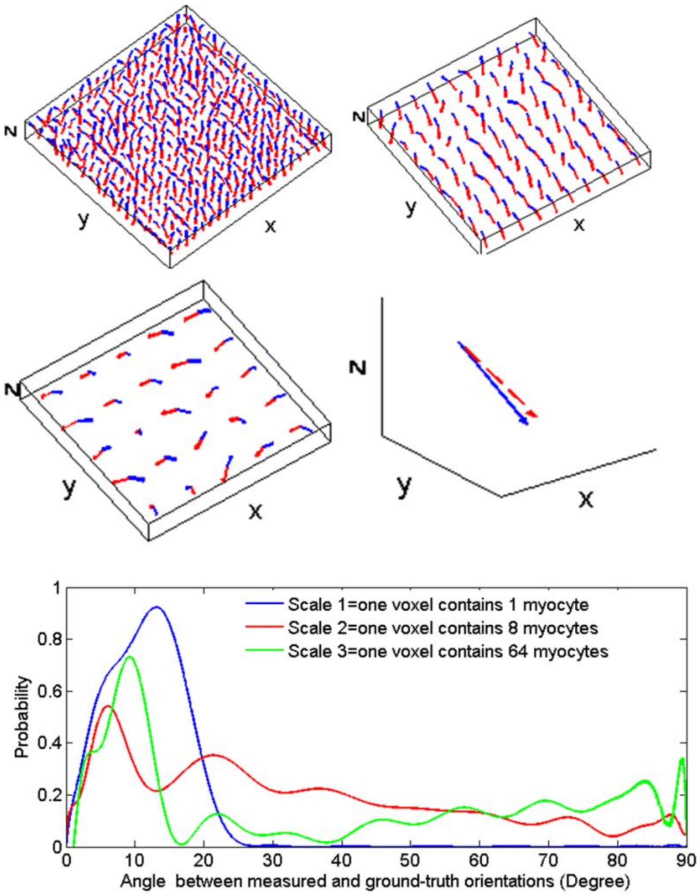

Fig. 4.10 Results of measurement of fiber orientations and probability distribution of fiber orientation deviations as a function of voxel size (observation scales). Measured (red) and ground-truth (blue) orientations at scale 1=one voxel contains 1 myocyte (a), at scale 2=one voxel contains 8 myocytes (b), at scale 3=one voxel contains 64 myocytes (c), and at scale of 20×20×20=8000 myocytes (d). (e) Comparison of probability distributions of fiber orientation deviations between measured and ground-truth at different scales.

Subfigure (a) is the result observed at a microscopic scale, where in each voxel there is only one myocyte. The subfigure (b) and subfigure (c) give the results observed at mesoscopic scales, with 8 and 64 myocytes respectively in each voxel. Subfigure (d) shows the result observed at a macroscopic scale that corresponds to clinical MRI spatial resolutions, in which 8000 myocytes were included. At the micro-scale, the orientation of the cylinder in the VCFS models is taken as the reference or ground-truth. At the meso- and macro-scales, the ground-truth orientation is based on the previous micro-scale reference, and is given by the average orientation of the cylinders inside the voxel corresponding to the given scale. In Fig. 4.10, the ground-truth orientation is indicated by blue color vectors.

From the probability distribution curves in Fig. 4.10(e), it can be seen that, from microscopic to macroscopic scales, the measured diffusion orientation deviates more and more from the ground-truth. At micro-scale (scale 1), the distribution of angles between the measured and ground-truth orientations is located mainly in the interval [0°, 25°]. However, at meso- (scale 2) and macro- (scale 3) scales, the angle distribution spreads almost over the entire interval [0°, 90°], which implies that, with conventional dMRI, the measured fiber orientations might greatly deviate from the actual ones.

4.4.3 Effects of arrangement patterns and size variations on diffusion properties

As we illustrated above, at the macroscopic scale, the fiber orientation and the diffusion properties estimated from diffusion images may not be able to reveal the actual cardiac fiber orientation distribution. This estimation error is probably caused by the myocyte arrangement patterns and the size of myocytes. Therefore, investigating their influences on diffusion properties may provide reasonable explanation about cardiac disease characteristics.

In order to do this, we simulated the diffusion images of these three models in a macroscopic scale. From the DW images, the fiber orientation and the FA values were derived (Fig. 4.11).

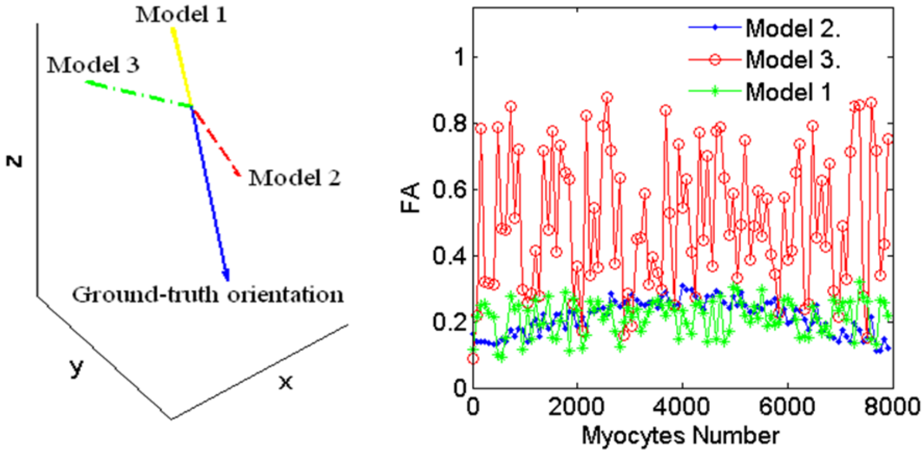

Fig. 4.11 Measured fiber orientations and FA values for the three models: Model 1 (Fig. 4.7), Model 2 (Fig. 4.8), and Model 3 (Fig. 4.9).

As mentioned in section 4.4.1, Model1 and Model2 have the same orientation distribution and myocyte size but with different arrangement patterns. Model1 and Model3 have the same orientation distribution and arrangement patterns but with various myocyte sizes. We remark that different myocyte sizes and arrangement patterns lead to different measured fiber orientations, and that it is the myocyte size (ratio of length to diameter) causes the most important changes both in FA and in orientation variation.

The above measurement results with the same scale or different scales demonstrate that the variation of arrangement patterns and myocyte sizes influences the macroscopically measured fiber orientation and FA. This means that we can generate various simulation configurations with different microscopic arrangements and myocyte sizes to understand the relationship between microscopy and macroscopy, and predict microstructure information from macroscopic measurements.

4.4.4 Noise influence on the choice of optimal observation scales

According to our research, we can infer that for correctly mapping the cardiac fiber orientation distribution, the observation scale should be small. However, taking into account practical imaging conditions, a smaller observation scale means a strong imaging gradient and therefore introduces more signal attenuation. In this case, the influence of noise should no longer be ignored, and a compromise between observation scales and signal-to-noise ratio (SNR) is required. To investigate the choice of optimal voxel sizes, we simulated the DW images with different noise levels at two different scales (scales 1 and 2). In the present work, we considered only the displacement noise with Gaussian distribution (mean value is 0), and the SNR defined by

$$SNR = 20\times\log(\frac{\max(\text{molecule displacements})}{\sigma}) \tag{4.12}$$

with σ designating the variance of the noise. According to the fiber orientation deviation from the ground-truth, the optimal observation scale is selected.

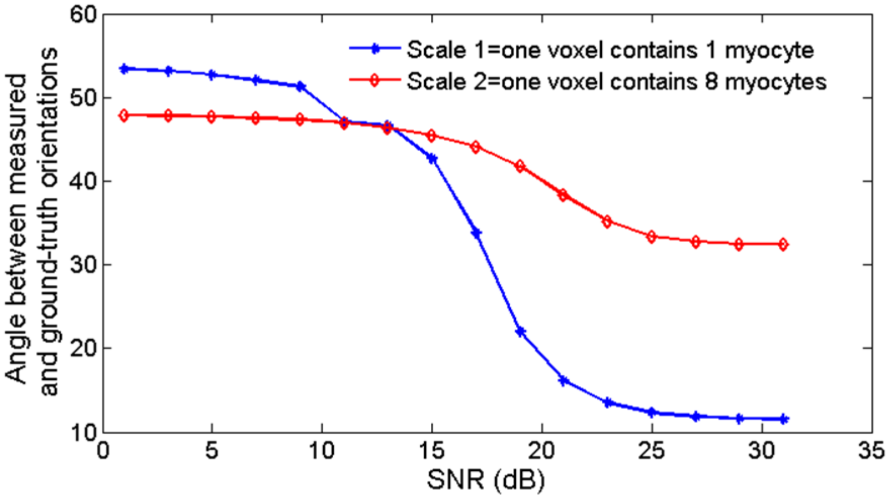

Fig. 4.12 Noise influence on the choice of optimal voxel sizes. SNR ranges from 1 to 31dB, accordingly the displacement variance is calculated based on Eq. (4.12).

Fig. 4.12 represents the variation of angles between the measured and ground-truth fiber orientation as a function of SNRs for two different scales. We observe that the orientation deviation is much more sensitive to noise at smaller voxel sizes as expected (scale 1) than at bigger voxel sizes (scale 2). Meanwhile, when the SNR is lower than 15 dB, the simulation at larger scales gives better results than at smaller scales, which means that, for lower SNRs, the optimal voxel size should be bigger.

4.5 Conclusion

In this chapter, we have firstly presented a basic dMRI simulation algorithm, the Monte-Carlo approach based on random walking and collision model. In order to analyze the influence of physical and structural characteristics of cardiac myocytes on diffusion properties, the corresponding VCFS was modeled. In the physical characteristics analysis, the cardiac myocyte was modeled by the combination of a series of hexagons, which enables us to change readily the shape of intra- and extra-cellular space, whereas in the structural properties analysis, myocytes were modeled by the cylinders that allow us to vary the orientation and arrangement patterns easily. After modeling, the DW images and diffusion tensor images were simulated for the above two different VCFS, from which the fiber orientation and fractional anisotropy were estimated and the effects of the physical properties including water content and membrane permeability, and the structural characteristics including arrangement pattern, observation scales and myocyte size were analyzed. The obtained results showed that the increase of water content in the intra-cellular space and the decrease of the membrane permeability lead to a high diffusion FA. Moreover, the FA changes dramatically with the variation of myocyte size but smoothly with that of arrangement patterns. The results suggest that using the proposed multi-scale modeling and simulation, the relationship between microscopic structure heterogeneity and macroscopic measurements can be established to predict microscopic tissue structure and explain macroscopic behaviors.

In the present chapter, all the simulations were performed by means of simple structures, which do not represent real cardiac fiber structures. In order to obtain the simulated DW images of an entire human heart, we will, in the following chapter, model the VCFS using the polarized light imaging data, and simulate the realistic DW images of the human heart at multi-scales.

Chapter 5

Multi-scale dMRI simulation for myocardium based on PLI data

Contents

Résumé en français

Comme nous l'avons élaboré dans le dernier chapitre, pour mieux comprendre la structure des fibres cardiaques et de ses propriétés de diffusion microscopique, il est indispensable que notre simulateur d'IRMd s'appuie sur un modèle de fibres cardiaques réalistes. Pour ce faire nous avons construit notre modèle de fibres en nous appuyant sur la vérité terrain fournie par les données acquises en lumière polarisée (PLI). Cette technique permettra également d'évaluer notre approche de simulation multi-échelle.

Pour atteindre ces objectifs, nous décrivons dans ce chapitre, le processus d'acquisition des données en lumière polarisée (PLI). Nous montrons ensuite l'orientation des fibres cardiaques ainsi obtenues. À partir de ces données PLI, les modèles de fibres cardiaques en mono- et multi- échelles sont construits. Ensuite, nous simulons les images de diffusion d l'eau à travers ces fibres cardiaques virtuelles en multi-échelles. L'influence de l'échelle d'observation sur les propriétés de diffusion mesurées a alors été analysée. On étudie les paramètres d'orientation des fibres cardiaques, FA et MD qui sont les caractéristiques les plus importantes utilisées en clinique pour distinguer un cœur normal d'un cœur pathologique. Nous avons aussi simulée les images de diffusion obtenues pour différentes pathologies virtuelles. Sachant qu'une anomalie peut être induite par l'endommagement des fibres cardiaques, nous avons testé différentes configurations en modifiant l'arrangement des myocytes, leur taille, la variation des espaces extracellulaires, etc. Dans ce chapitre, les pathologies sont représentées respectivement par l'hétérogénéité de l'orientation des fibres, la variation du rapport de longueur sur diamètre des myocytes, les changements d'épaisseur du disque intercalaire et la distance radiale entre les myocytes. L'influence de ces changements sur FA et MD est ensuite analysée.

Les résultats de la simulation démontrent que :

- L'orientation des fibres est observée en échelles différents. Avec la croissance des échelles d'observation, on remarque que l'angle d'élévation augmente mais que l'azimut ne change quasiment pas.
- FA diminue mais MD augmente avec la croissance des échelles d'observation.
- Les changements de la taille du disque intercalaire et la distance radiale entre les myocytes cardiaques n'ont pas d'influence notable sur FA et MD. On note que ces paramètres dégradent la qualité des images de diffusion quand ils augment.
- La croissance de l'hétérogénéité de l'angle d'élévation dans un voxel augmente à la fois FA et MD en raison de l'augmentation de la diffusivité le long de la direction des myocytes.
- Les variations de taille des myocytes sont le paramètre principal responsable des changements des indices de diffusion. Pour un temps de diffusion fixé, la croissance du rapport longueur sur rayon des myocytes se conduit à un FA plus grand un MD plus petit. Lorsque le rayon des myocytes devient plus petit, cette tendance au changement devient plus évidente.

FA et MD sont des paramètres liés au temps de diffusion, c'est pourquoi toutes les études ci-dessus ont été réalisées à un temps de diffusion fixé. Lors des changements de paramètres d'imagerie de diffusion, tels que le temps de diffusion et la durée des gradients de diffusion, leur influence sur les propriétés de diffusion doit alors être considérée. Ainsi, dans le chapitre suivant, pour une structure de fibre cardiaque fixé, les effets des paramètres d'imagerie sur les indices de diffusion seront analysés en détail.

Compte tenu des besoins inconcevables en ressources de calcul de notre simulateur de l'IRMd, toutes les simulations présentées dans ce chapitre sont effectuées avec la grille EGEE.

5.1 Objectives

The aim of the dMRI simulator is to provide a better understanding of the cardiac fiber structure and of its microscopic diffusion properties. To reach this objective, the cardiac fiber model must be constructed using realistic data. We previously mentioned that PLI is able to provide 3D cardiac fiber orientation information with high spatial resolution. Therefore, we consider the PLI data as a ground-truth and use them to validate and to evaluate our multi-scales dMRI simulation approach. In this chapter, we firstly describe the PLI data acquisition process and give the resulting cardiac fiber orientation. Then, based on PLI data, the single-scale and multi-scales cardiac fiber models are constructed. The dMRI simulation process is subsequently performed for both single and multi-scales virtual cardiac fibers. Through a fair comparison of diffusion properties derived from DWI at different simulation scales, the relationship between the microstructure variations and the diffusion properties observed at the macroscopic scale is interpreted.

Cardiac fiber orientation, FA and MD are the most important characteristics that distinguish normal from pathological hearts in the dMRI clinical applications. As illustrated in chapter 1, some cardiac muscle diseases can result from the damage of cardiac fibers, such as arrangement disorder, changes of cardiac myocytes size, variation of extracellular spaces, etc. Thus using our dMRI simulator, we are able to simulate cardiac DW images related to several possible abnormal tissues. The pathological changes are respectively introduced by the distribution heterogeneity of the elevation angle, the variations of the myocyte length to diameter ratio, the changes of intercalated disk thickness and the radial distance between the cardiac myocytes. The influence of these features changes on the FA and MD measurements are finally analyzed.

Taking into account the huge computing resource requirements of our dMRI simulator, all the simulations in this chapter are performed using the EGEE grid.

5.2 Polarized light imaging (PLI) data acquisition

We explained the basic principle of PLI for measuring the cardiac fibers orientations in the chapter 2. In this section, to avoid the redundancy, we just illustrate the preparation process of the experimental samples and interpret the corresponding measurement results.

5.2.1 Sample preparation

The experimental sample is a 40 weeks old human fetus heart. In chapter 2 we stated that for removing the influence of the collagen on the cardiac fiber uni-axial birefringence, the cardiac muscle sample must be processed with following specific steps according to the work of Jouk [Jouk, 2007]:

1) The heart was immerged in a solution of 10% neutral buffered formalin for one week;
2) Infiltrated at room temperature with 2 solutions of glycol methacrylate (GMA) for one week;

3) Infiltrated again for another one week in a series of mixtures of GMA and MMA (methyl methacrylate), in which the concentration of MMA was gradually increased until reaching 100% MMA;
4) Embedded by polymerization of MMA at a temperature of 32ºC;
5) Drill 4 holes in the embedding resin for providing a 3D anatomical reference used in the further fiber orientation analysis;
6) Cut 43 heart sections of thickness 500 µm with a rotary microtome (1600, Leica).The rate of penetration of the rotatory saw is set to a low speed (15 min per section) in order to avoid mechanical stress and distortions.

5.2.2 The PLI acquisition result

The heart sample is placed in the optical path. Rotating the polarizer results in the different light intensity received by CCD and then forms an image. Using obtained images for different polarizer rotation angles, it is possible to calculate the azimuth and elevation angles of each cardiac fiber (Eq. (2.7)). The elevation angle represents the obliquity of the fiber with respect to the plan of the section. The azimuth angle corresponds to the angle between the projection of the fiber orientation onto the section and the axis orientation of the stage. The detection results are given in the form of selected maps of the elevation and azimuth angles of the myocardial muscles, as illustrated in Fig. 5.1.

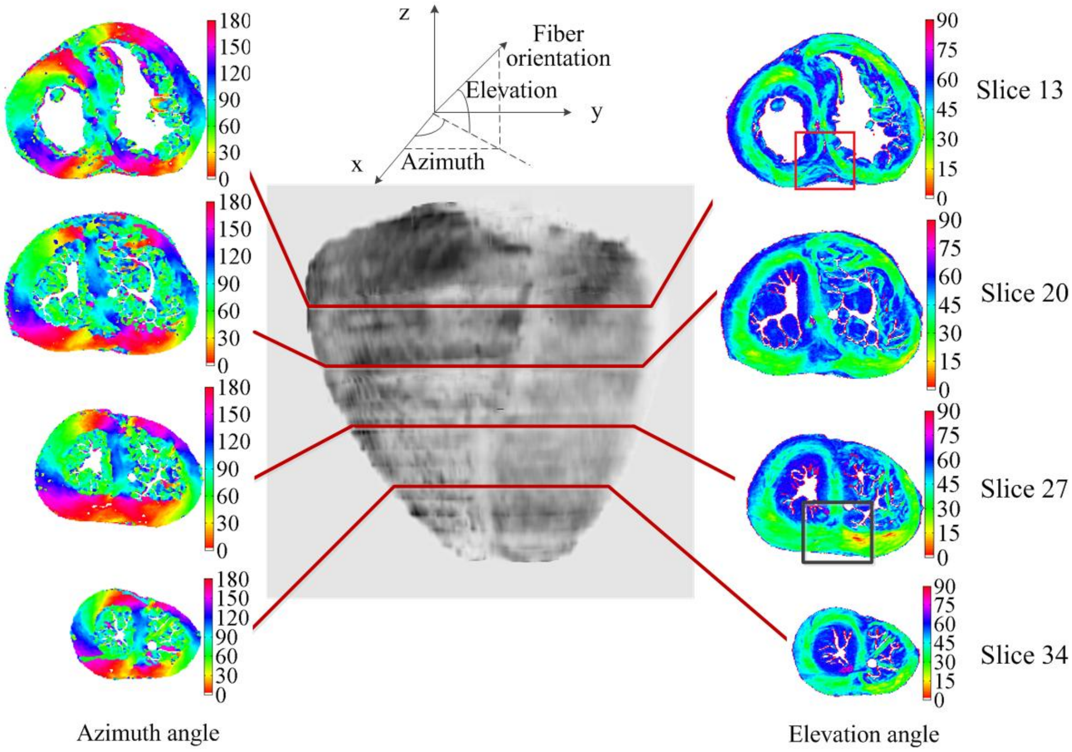

Fig. 5.1 The fiber orientation expressed by the azimuth and elevation angles detected by PLI with a spatial resolution of 0.1 × 0.1 × 0.5 mm^3. The whole ventricle is sectioned into 43 slices. The azimuth and elevation angle maps for slices 13, 20, 27 and 34 are shown. The azimuth angle is coded in false color from 0º to 180º and elevation from 0º to 90º.

It can be observed that, the fiber at the diaphragmatic face of the heart has a 0º azimuth angle (red), and at the interventricular septum and lateral wall of the ventricles has an about 90º (blue) azimuth angle. The values of the azimuth angle vary in sympathy with the curvature of the left ventricular wall. While turning around the left ventricle the azimuth is rotating with a smooth progression from one color to the other. This means that the fibers are circumferential. A spiral anticlockwise arrangement is visible toward the apex, while the basal map shows a spiral arrangement with an inverse sense of rotation. As to the elevation angle, according to the slice location, two different fiber separate patterns between the left and right ventricles can be observed. For explaining, we make a comparison between the slices 13 and 27. The red square in the elevation angle map of slice 13 highlights the inferior part of the ventricular septum, where the medial circumferential fibers (green) of left and right ventricles converge into the circumferential medial part of the interventricular septum. However, for the same part of slice 27 highlighted with a black square, the circumferential fibers of left and right ventricles are in either continuity or converging toward the interventricular septum.

For validating the cardiac fiber orientation detection results, in the work of Jouk [Jouk, 2007], a quantitative comparison between the fiber orientation distribution measured by PLI and the presently most discussed models was detailed. It has been proved that the cardiac fiber structure derived from PLI technique conforms to the Steeter's conjecture that we elaborated in chapter 2. But during the fetus period, it is not found the helical structure described in the Torrent-Guasp's model. This may be caused by the fetus structure itself. It may also possible come from the insufficient elevation angle definition during the PLI detection steps. Normally the elevation should range from -90º to 90º, but in the PLI experiments, the measured data was interpreted at a quarter of sphere which restricts the elevation angle range to 0º - 90º, so making difficult to verify and explore the Torrent Guasp's conjecture using fiber tracking with our data. At present, our collaboration partner, the laboratory of TIMC is working on a tilting microscopic stage that will extend the definition range of elevation angle to 180º and thus track the ambiguity of fiber tracking. It will allow a fair comparison between PLI data and the helical structure.

Although the elevation angle is not completely defined, it will not influence our simulation results for validating our simulation method and analyzing the effects of the cardiac fiber structures on the diffusion properties observed at multi-scales.

5.3 Cardiac fiber modeling based on PLI data

In chapter 4 we have introduced two kinds of methods for modeling a cardiac myocyte, the first one consists to represent the cardiac myocyte as a series of hexahedral, and the second one is to use an orientated cylinder to express each myocyte. To model the virtual cardiac fiber structure using PLI data, we modeled the cardiac fiber structures using cylinders with single-scale or multi-scales according to the different purposes.

5.3.1 Single scale modeling

In order to validate our simulation method aiming at mimicking the real cardiac fiber architecture imaging, we assumed that there is only one cardiac myocyte in each voxel of the simulated diffusion image whose spatial resolution is considered to be the same as PLI (0.1 × 0.1×0.5 mm^3). If our simulation algorithm is appropriate, the simulated diffusion signal and the corresponding diffusion tensor images can completely reveal the local cardiac fiber orientation and its diffusion properties. To achieve this, the modeling module is illustrated in Fig. 5.2. From the PLI data, we can calculate the cardiac fiber position, orientation, and the image spatial resolution, which are transferred into the structure information. The cardiac fibers are then arranged in a 3D space according to the location and orientations. After the arrangement, each fiber is given a specific radius and length, the minimum and maximum values of which are respectively determined by *RadiusMin*, *RadiusMax*, *LengthMin* and *LengthMax*. In our simulation, according to histological knowledge, we choose the *RadiusMin* equal to10 μm, the *RadiusMax* to 20 μm, the *LengthMin* to 50 μm and *LengthMax* to 100 μm. The output of the modeling module gives a 3D cardiac fiber structure image in which each voxel is filled with an orientated cylinder with radius r and length h .

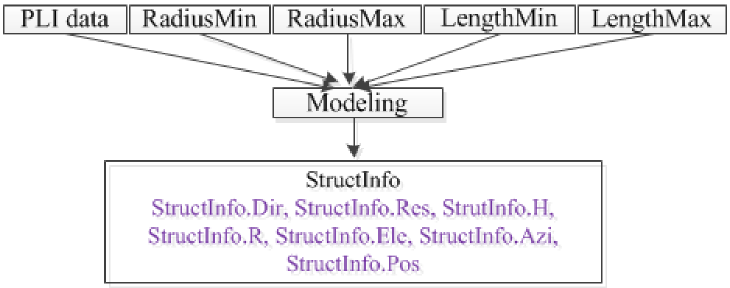

Fig. 5.2 Single scale cardiac fiber modeling module. Input: the PLI data, the radius and length of the cardiac myocyte for each voxel. Output: a structure of the modeling results including the cardiac fiber orientation (StructInfo.Dir), the spatial image resolution (StructInfo.Res), the length of the cardiac fiber in that voxel (StructInfo.H), the cardiac fiber radius (StructInfo.R), the elevation and azimuth angles of the fibers derived from PLI data (StructInfo.Ele and StructInfo.Azi) and the cardiac fiber position (StructInfo.Pos).

5.3.2 Multi-scale modeling

Actually, in a PLI voxel with size of 0.1 × 0.1 × 0.5 mm^3, there is not only one myocyte. In order to obtain a realistic myocardium model composed of the cardiac muscle cells, we construct a new modeling module, shown in Fig. 5.3. Besides the input parameters for single-scale modeling, the parameters used to describe the structural correlation between each myocyte are also considered. They include the *DiskRatio* representing the ratio of intercalated disk thickness to myocyte radius and the *DistanceRatio* indicating the ratio of radial distance between two myocyte neighbors to the myocyte radius. The input parameters *spcx*, *spcy* and *spcz* correspond to the spatial sampling of PLI original data. All the above parameters determine the number of myocytes in a PLI voxel. In this modeling module, there are two parameters called *infoNum* and *modeling seed*, the former is used for changing the cardiac fiber arrangements and the latter is for parallelizing the simulation in grid. Generally, the *infoNum* provided by PLI data is five. These five parameters include cardiac fiber position *posx*, *posy*, and *posz* and the fiber orientation expressed by both *elevation* and *azimuth* angles. In our simulation model, we introduce another parameter into the PLI data information, which is called *heterogeneity*. It describes the fiber orientation variations inside of PLI voxel, if the value of *infoNum* is 5, all the myocytes in one PLI voxel will share the same orientation. If the value of *infoNum* is 6, the *heterogeneity* will be generated for each voxel and accordingly the myocyte orientation varies.

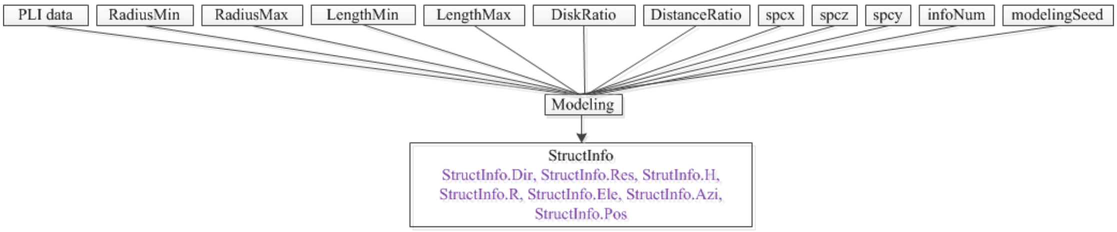

Fig. 5.3 Multi-scale cardiac fiber structure modeling module. Input parameters include the PLI data, the maximum and minimum value for myocyte radius and length, the intercalated disk and extracellular space dimension expressed by DiskRatio and DistanceRatio, the PLI imaging spacing *spcx*, *spcy* and *spcz* used to calculate the number of myocyte involved in each voxel, the infoNum useful for changing the model properties. The modeling seed allows the simulation using parallel computing.

Using these modeling parameters, the detailed reconstruction process of the multi-scale myocardium structure is shown as follows:

Step 1: In each voxel of PLI data, there is a given fiber orientation with the location is known a priori. Taking the fiber location as the center point, the PLI image spacing spcx, spcy, and spcz as the side length, a small volume of cardiac myocardium is separated. Passing through the center point and along the fiber orientation, we place a cardiac fiber in this volume, which is shown in Fig. 5.4 (a).

Step 2: The laminar cardiac fiber structure proposed by LeGrice [Legrice, 1997], supposes that the cardiac myocytes are arranged in layers. Thus in our models the extracellular space is modeled based on the cardiac myocyte arrangements. In the light of the cardiac fiber orientation *dir*, we create a new coordinate system *u*, *v* and *dir*, as shown in Fig. 5.4 (b). The cardiac fibers are laid out respectively along the directions of u and v, and the distance between the cardiac fibers is set up by the parameter *DistanceRatio*. The length of the cardiac fiber is determined by the voxel size.

Step 3: We have already arranged the cardiac fibers in one voxel. However, actually, a cardiac fiber is not continuous: it is composed of the cardiac myocytes connected by the intercalated disks. Thus we divided each cardiac fiber modeled in the step 2 into several myocytes. The length of the cardiac fiber and the length range of myocytes determine the division number. In Fig. 5.4 (b), the blue line represents the intercalated disk. Its thickness is given by the input parameter *DiskRatio*.

Step 4: We can observe that all the myocytes in one PLI voxel share the same orientation. In fact, the orientations between the neighboring myocytes are slightly different. In our model, this kind of difference is described by the heterogeneity of the elevation angle. As the elevation angle changes, the fiber orientation and the myocyte orientation vary accordingly, as shown in Fig. 5.4 (d). For simplicity, here we just illustrate the orientation variations of the cardiac fiber. Similarly, the myocyte orientation can also be varied by introducing the elevation heterogeneity.

The modeling of myocardium structure from the viewpoint of cardiac cells is completed through the four steps above. The output of this modeling module includes the myocytes position *StructInfo.Pos*, orientation *StructInfo.Dir*, length *StructInfo.H* and radius *StructInfo.R*. The output parameters of the modeling module will be used as the input of the dMRI simulation.

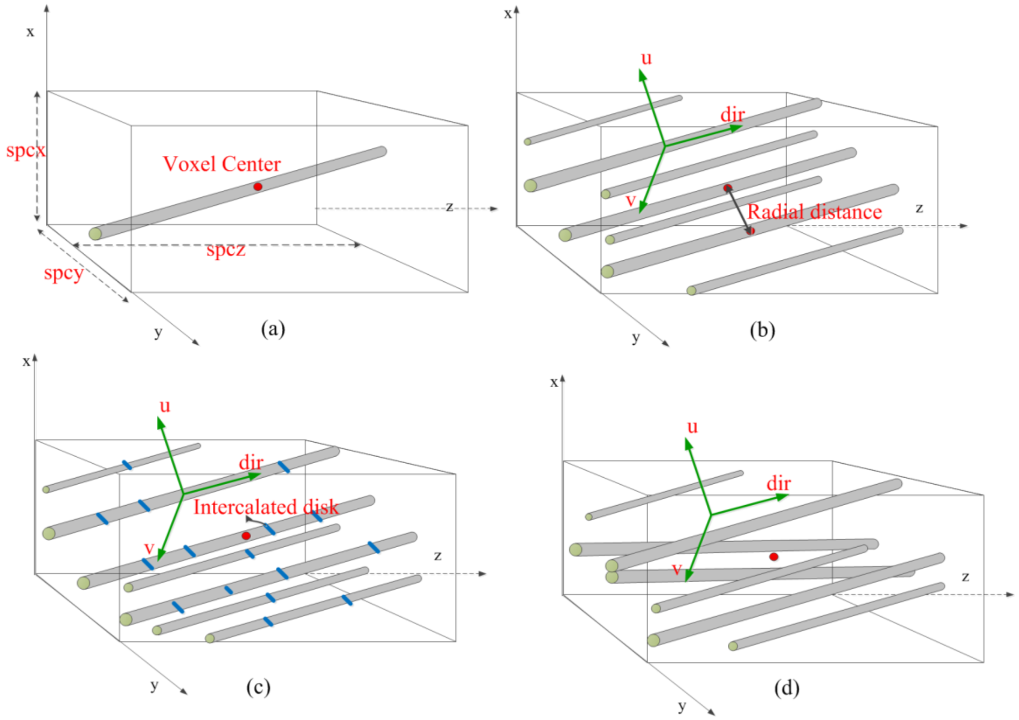

Fig. 5.4 Diagram for multi-scale cardiac fiber modeling steps. (a) Construct one cardiac fiber through the voxel center point and calculate its maximum length. (b) Arrange the cardiac fiber along the direction perpendicular to the fiber orientation, the distance between the fiber neighbors is determined by the input parameter *DistanceRatio*. (c) Divide each cardiac fiber into several myocytes by introducing the intercalated disk, the thickness of which depends on the input parameter *DiskRatio*. (d) Change the myocyte orientation according to the heterogeneity of the elevation angle provided by the PLI data.

5.4 Single-scale simulation result and validation

In order to verify our simulation method, the dMRI simulation is firstly performed with the single scale model, in which each voxel contains only one cardiac fiber.

5.4.1 Simulation parameters selection

The Siemens MRI systems with 3 Tesla magnetic field used to acquire the dMRI data has a maximal gradient intensity of 400mT m^{-1} with slow slew rate and 45mT m^{-1} with fast slew rate (200 T/m/s). The diffusion gradient strength is set to 40 mTm^{-1} in our dMRI simulation. According to the work of [Bar-Shir *et al.*, 2008], extracting the structure information from MR experiments needs a long enough time for diffusion. Namely, the diffusion time Δ should satisfy $\Delta >> l^2/2D$, where l is the size of the tissues in which the molecules diffuse and D is the diffusion coefficient. Here, the diffusion coefficient is selected as $10^{-3}\text{mm}^2/\text{s}$, the diameter of the myocyte is chosen to be 20 μm and the length 100 μm. In order to distinguish the smallest structure, the diffusion time should be longer than 200 ms. The diffusion time used in this work is therefore fixed as 200 ms and accordingly the diffusion gradient duration to 10 ms, which results in a q-value of 17 mm^{-1} and b-value of 2281 s/mm^{2}.

Since Monte-Carlo simulation is a statistical method, the number of water molecules involved in the simulation directly determines the result accuracy. The larger the molecules number, the more accurate the simulation results. However, the simulation with a large number of water molecules requires huge computing resources. In order to choose the appropriate water molecule number and to make a reasonable compromise between simulation accuracy and computing resources, we first simulate the diffusion signal along one of the radial directions of the myocyte with different molecules numbers for a given diffusion time. The diffusion signal along this direction corresponds to the restricted diffusion case. The results are shown in Fig. 5.5.

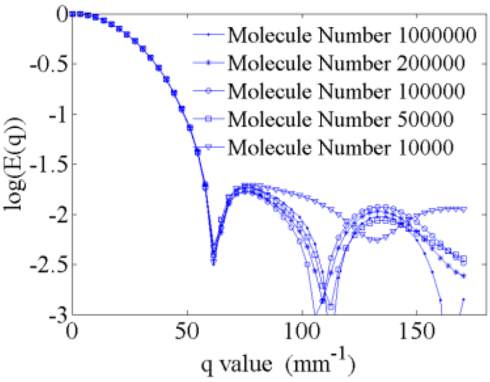

Fig. 5.5 Influence of Molecule numbers on the simulation accuracy. The restricted diffusion signal was simulated individually with 10000, 50000, 100000, 200000, and 1000000 molecules for a diffusion time of 200 ms.

It can be noted that, when the q-value is less than 50 mm^{-1}, for a diffusion time of 200 ms, the simulation results with a number of molecules of 10000, 50000, 10000, 200000, and 1000000 are almost the same. Thus for gaining time, the number of water molecules in each myocyte involved in the simulation is chosen as 10000 for $q < 50\ \mathrm{mm}^{-1}$. When q is larger than 50 mm^{-1}, the diffusion signal has great fluctuations when the number of molecules is smaller than 100000. Thus to guarantee the simulation accuracy and stability, the number of molecules is chosen equal to 200000.

5.4.2 DWI and DTI simulation results obtained using cardiac fiber model

The Monte-Carlo simulation gives the displacement of the water molecules in the different directions allowing the dMRI signal to be simulated according to the diffusion MRI theory by applying diffusion gradients along different directions, as illustrated in chapter 4. In this simulation, there are 162 diffusion directions, defined by icosahedrons. As illustrated in the above paragraph, when q is less than 50 mm^{-1} (for b = 1000 s/mm^{2}, the real range of q value is about 17 mm^{-1}), 10000 water molecules in each myocyte for the simulation are enough and thus here for guaranteeing the simulation accuracy we use 24000 molecules in each cardiac fiber. The number of cardiac fibers provided by PLI is 706472. The simulation based on the same number of cardiac fibers involves about 16 billion of water molecules. The estimated computing time using a personal PC reaches several years cannot be accepted. This is why the simulation is executed using the Grid. The so obtained simulated DW images for the whole heart along one direction and those for one slice along 12 diffusion directions are given in Fig. 5.6. The 3D reference space system used here is the one used in the PLI experiments. These 12 directions are given in Fig. 5.7.

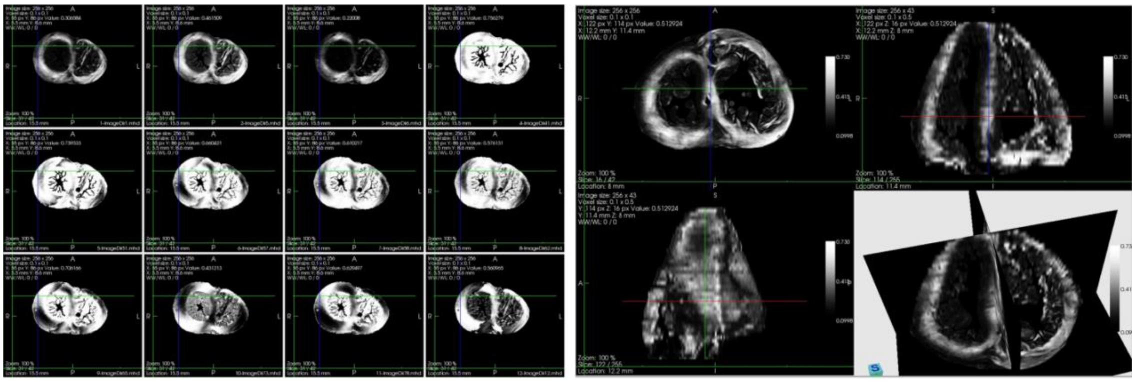

(a) (b)

Fig. 5.6 Simulated DW images of an *ex vivo* fetus heart. (a) DW image of one slice along 12 directions. (b) DW image for the whole heart along one diffusion direction *Dir1*.

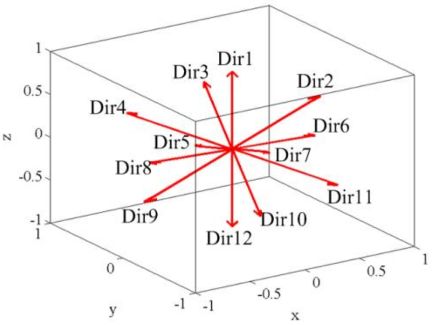

Fig. 5.7 Diffusion gradient directions

The simulated DW images present a “clean” aspect because they are noise-free and without artifacts compared to the physical DW images acquired with a clinical MRI systems. They also have a very high spatial resolution of $0.1 \times 0.1 \times 0.5$ mm^3 compared to the real one ($2 \times 2 \times 2$ mm^3 about) which allows to reveal finer details about the cardiac fiber architecture. Up to now, high spatial resolution can only be achieved in the imaging for small animal heart. For example, using 9.4 T MRI system, the resolution of DW image of a mouse heart with size 6.7 mm × 1.5 mm (base-apex length × LV wall thickness) can reach 0.1 mm [Healy, 2011]. For a rabbit heart with size 19.5 mm × 3.5 mm, the resolution comes to 0.25 mm with a 7.1T MRI systems, and for a sheep heart with dimensions of 77 mm × 12.5 mm, the resolution reaches about 0.78 mm using a 2 T MRI scanner. This implies that an increment of the sample size and of the field of view (FOV) leads to a decreasing of the spatial resolution. In our case, we consider a 40 weeks old fetus heart whose size is about 33 mm × 19 mm × 22 mm, with a base-apex length equal to 33 mm and a LV wall thickness of about 5 mm. Up to now, obtaining real DW images of this heart with a spatial resolution of 0.1 mm is not easy. We demonstrate that however our simulated dMRI model, based on PLI data, makes it possible. Besides the high spatial resolution, the dMRI simulator proposed here is able to provide DW images along a large number of diffusion directions. This point is required when a q-ball imaging technique is used. It is particular useful to analyze the diffusion heterogeneities, and the fiber crossing.

Based on the above diffusion images simulated in 162 directions, we calculated the diffusion tensor images using a least square method [Kingsley, 2006a, 2006b, 2006c], as shown in Fig. 5.8.

The local fiber orientation, the MD and the FA can be estimated from the diffusion tensor. In this simulation, we choose a free diffusion coefficient equal to 10^{-3} mm^2/s. As a result, the simulated MD ranges from 4×10^{-4} mm^2/s to 7×10^{-4} mm^2/s, and the FA varies from 0.31 to 0.96. By combining PLI and simulated dMRI data, it is possible to provide the fiber orientation distribution, also the FA and the MD information. This approach takes advantage of the merit of the high spatial resolution of PLI aiming at compensating the insufficiency in terms of spatial resolution of experimental dMRI.

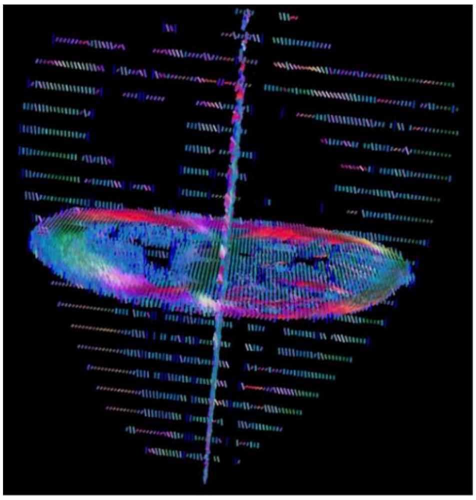

(a) Diffusion tensor

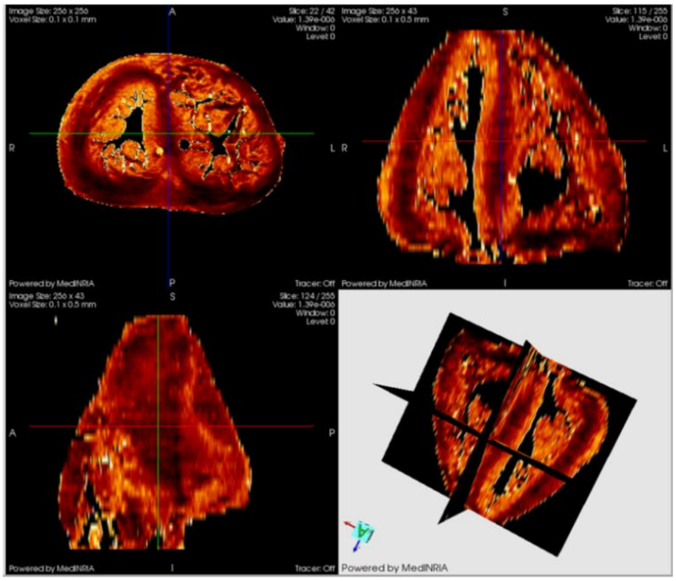

(b) MD

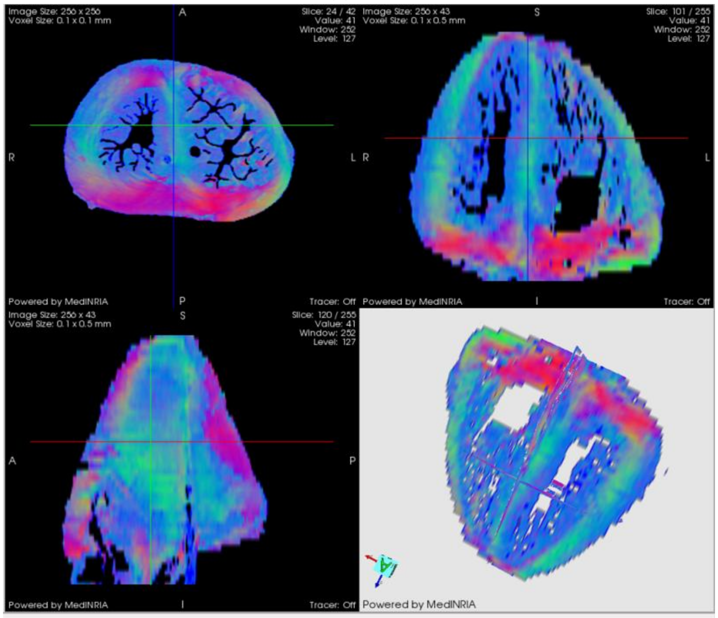

(c) FA

Fig. 5.8 Diffusion tensor, MD and FA images for the whole heart.

5.4.3 Validation

For validating our dMRI simulation approach, we compare the simulated fiber orientation, elevation and azimuth angle with the ground-truth provided by PLI. For sake of clarity, we illustrate the comparison on one slice. Fig. 5.9 shows the fiber orientations derived from the simulated DW images for slice 13. The original diffusion tensor image is displayed on the left, and on the right the sampled tensors, from which we can observe the cardiac fiber's circumferential distribution.

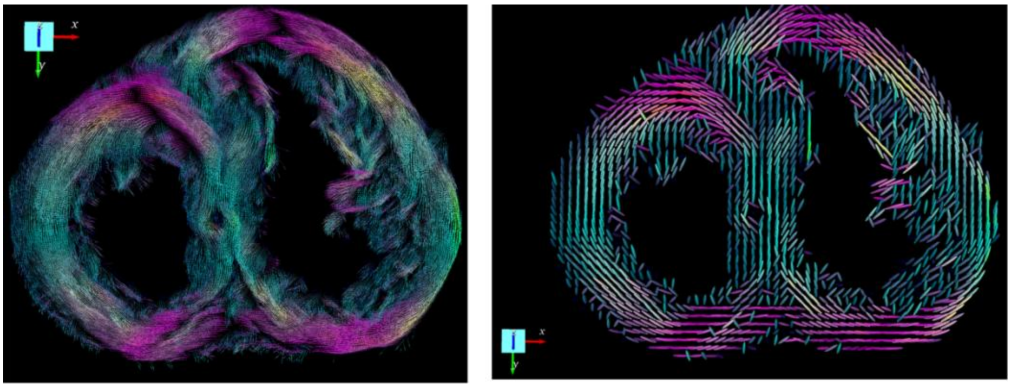

Fig. 5.9 Diffusion tensor field represented by arrows and ellipsoid. The left image is the diffusion tensor of the entire slice 13. In order to enhance the orientation of the cardiac fibers, the tensor image (left) is sampled with a ratio of 4 to1, and shown on the right.

The fiber orientation, the elevation and the azimuth angles have been calculated from the diffusion tensors. We estimated the accuracy of the simulation by comparing the simulated data with PLI data (Fig. 5.10).

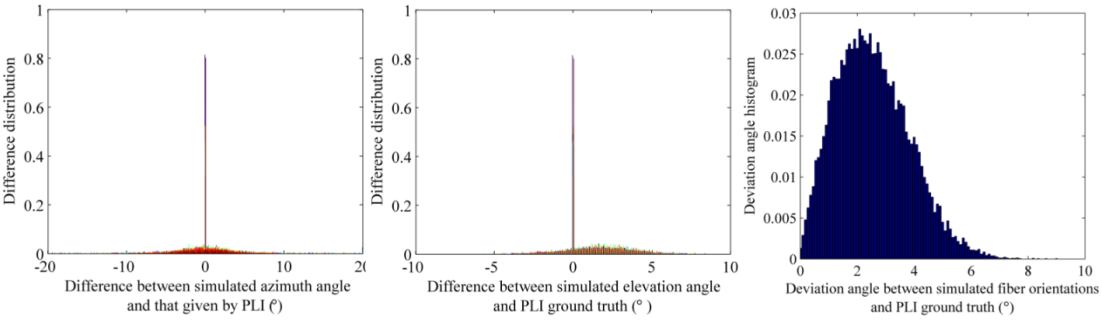

Fig. 5.10 Simulation and PLI comparison of the cardiac fiber orientation, azimuth and elevation angles. (a) Azimuth angle deviation between simulated data and PLI ground-truth. The maximum difference is 10º. (b) Elevation angle deviation between simulated data and PLI ground-truth. The maximum difference is about 5º. (c) Fiber orientation deviation between simulated data and PLI ground-truth.

We note from Fig. 5.10 that there is no significant difference between the Mont-Carlo simulation and the PLI experiment results, which validates the principle of our simulation method for analyzing the structure of cardiac fiber. The simulation error of the azimuth angle ranges roughly between -10º and 10º and that of the elevation angle varies between -5º and 5º.

5.5 Multi-scale simulation results and analysis

We have shown the validation of our simulation method with the single scale structure assessing that one cardiac fiber is present in each voxel. However, in practice, a PLI voxel with a size of 0.1 × 0.1 × 0.5 mm^3 contains hundreds of myocytes that constitute together the local cardiac fiber, so if we image them at various scales, we will obtain different results. In this subsection, we use the multi-scale cardiac fiber model detailed in section 5.3.2 to simulate the corresponding DW images and to analyze the variations of the diffusion image properties with the observation scales.

To avoid the effects of cardiac fiber orientation heterogeneity, in this simulation the cardiac myocyte heterogeneity in each PLI voxel is set to zero, which means all the myocytes in one PLI voxel share the same orientation. This is done to avoid side effects that could come from the local heterogeneity of the cardiac fibers orientation. Table 5-1 displays the values of the input parameters used in the multi-scale modeling module.

TABLE 5-1 VALUE OF INPUT PARAMETERS FOR MULTI-SCALE MODELING MODULE

RadiusMin	RadiusMax	LengthMin	LengthMax	Spcx	Spcy
0.005 mm	0.01 mm	0.05 mm	0.1mm	0.1mm	0.1mm
Spcz	InfoNum	diskRatio	distanceRatio	Modeling seed	PLI data
0.5 mm	5	0.1	0.1	1	C9232_Slice31

Once the realistic cardiac fiber model is constructed, the corresponding DW images at three different observation scales are simulated with the following realistic parameters: diffusion time Δ of 200 ms, gradient duration δ of 2 ms, gradient strength of 148.1 mT/m, which results in a q-value of 12.6 mm^{-1} and a b-value of 1268 s/mm^2. Here the chosen observation scales correspond to a size of voxel equal to 0.1 × 0.1 × 0.5 mm^3, 0.5 × 0.5 × 0.5 mm^3 and 1 × 1 × 1 mm^3 respectively. The number of diffusion gradient directions is 42.

DW images

Fig. 5.11 illustrates the simulated DW images and the corresponding intensity histogram along one diffusion gradient direction at different observation scales. Subfigure (a) is the simulated DW image with a spatial resolution of 0.1 × 0.1 × 0.5 mm^3 for the multi-scale cardiac fiber model, in which several myocytes are present in one voxel. Subfigure (b) and subfigure (c) are the DW images for multi-scale cardiac fiber structure simulated with a spatial resolution of 0.5 × 0.5 × 0.5 mm^3 and 1 × 1 × 1 mm^3 respectively. We note that increasing the observation scales decreases the DW image intensity contrast. This implies that as the observation scale increases, more myocytes with different orientations are involved in one image voxel, therefore, this multiple orientations decrease the diffusion preference, which means the water molecules have almost the same probability to diffuse along any directions. This leads to the decreasing of diffusion image contrast.

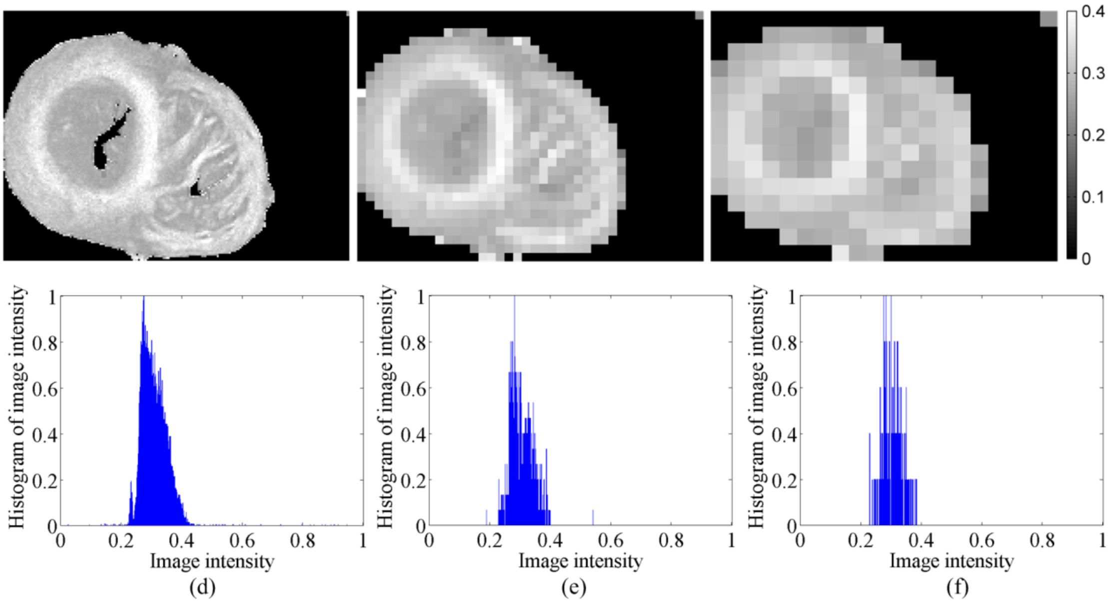

Fig. 5.11 DW images along one direction simulated at different scales. (a) DW image for the multi-scale fiber model with a spatial resolution of 0.1 × 0.1 × 0.5 mm^3, in (e) is the corresponding image intensity histogram. (c) DW image for the multi-scale fiber model with a spatial resolution of 0.5 × 0.5 × 0.5 mm^3, (e) corresponds to the image intensity histogram. (d) DW images for the multi-scale fiber model with a spatial resolution of 1 × 1 × 1 mm^3. (f) gives the image intensity histogram of (d).

Fiber orientation: elevation and azimuth angle

We now analyze the effects of the observation scales on the fiber orientation and diffusion properties. We compute the diffusion tensor images based on the simulated DW images along 42 diffusion gradient directions, we can then derive the cardiac fiber orientation, the FA and MD values from the so obtained diffusion tensor images. For keeping consistence with the PLI description, we describe the fiber orientation by the elevation and azimuth angles. Fig.

5.12 shows the azimuth angle image and its distribution histogram for different observation scales. As mentioned in the previous sections, the cardiac fibers are circumferential in the axial plane. This is reflected by the azimuth angle distribution. Increasing the observation scales leads to a no longer smooth progress of the azimuth angle, as shown in subfigures (d), (e) and (f). This makes the circumferential distribution of the cardiac fibers somewhat unperceivable.

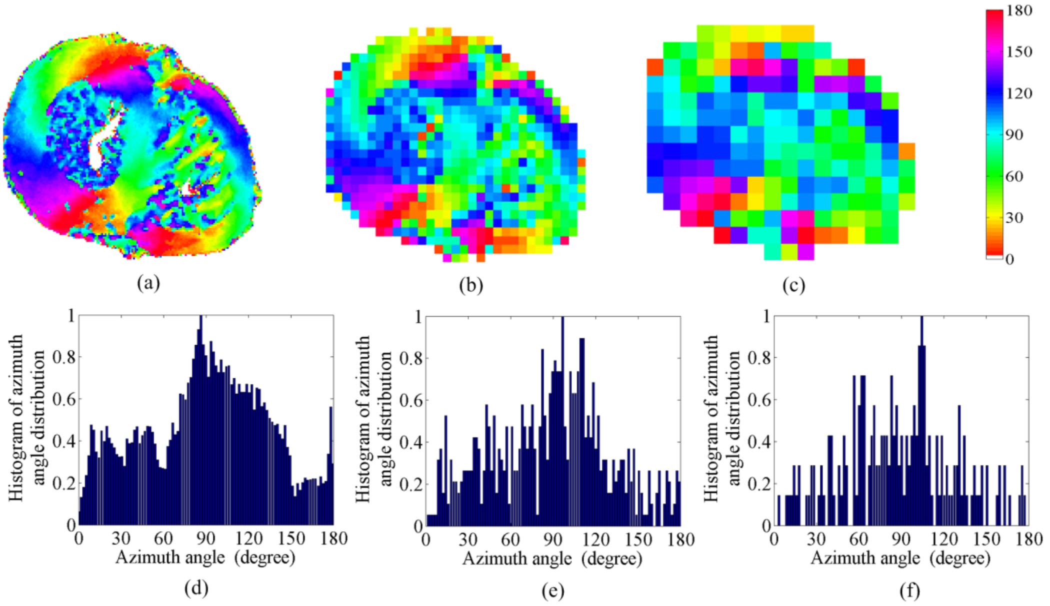

Fig. 5.12 Extracted azimuth angles and the corresponding distribution histograms simulated at different scales. (a) shows the azimuth angle for multi-scale fiber model with a spatial resolution of $0.1 \times 0.1 \times 0.5$ mm^3, its distribution histogram is shown in (d). (b) demonstrates the azimuth angle for multi-scale fiber model with a spatial resolution of $0.5 \times 0.5 \times 0.5$ mm^3, subfigure (e) corresponds to its distribution histogram. (c) illustrates the azimuth angle for multi-scale fiber model with a spatial resolution of $1 \times 1 \times 1$ mm^3 and in (f) is its distribution histogram.

In Fig. 5.13 the elevation angles and the related distribution histograms obtained at different observation scales are given. Unlike the azimuth angle that is not influenced greatly by the observation scales, the measured elevation angle increases with the raise of observation scales. (a), (b) and (c) illustrate the elevation angle obtained with different spatial resolutions but the same cardiac fiber structure, it can be seen that when the observation scale increases, the measured elevation angle becomes larger and larger but its variation range becomes narrower and narrower. This implies that the image spatial resolution must absolutely be considered when describing the distribution range of the cardiac fiber elevation angle.

The measured cardiac fiber orientation is determined by both the elevation and azimuth angles. Our simulation results illustrate the fact that if the cardiac myocyte orientation heterogeneity is not taken into account, the observation scale does not influence the azimuth angle but greatly affects the elevation angle. Therefore, the variation of the cardiac fiber orientation observed at different scales is mainly determined by the change of elevation angles.

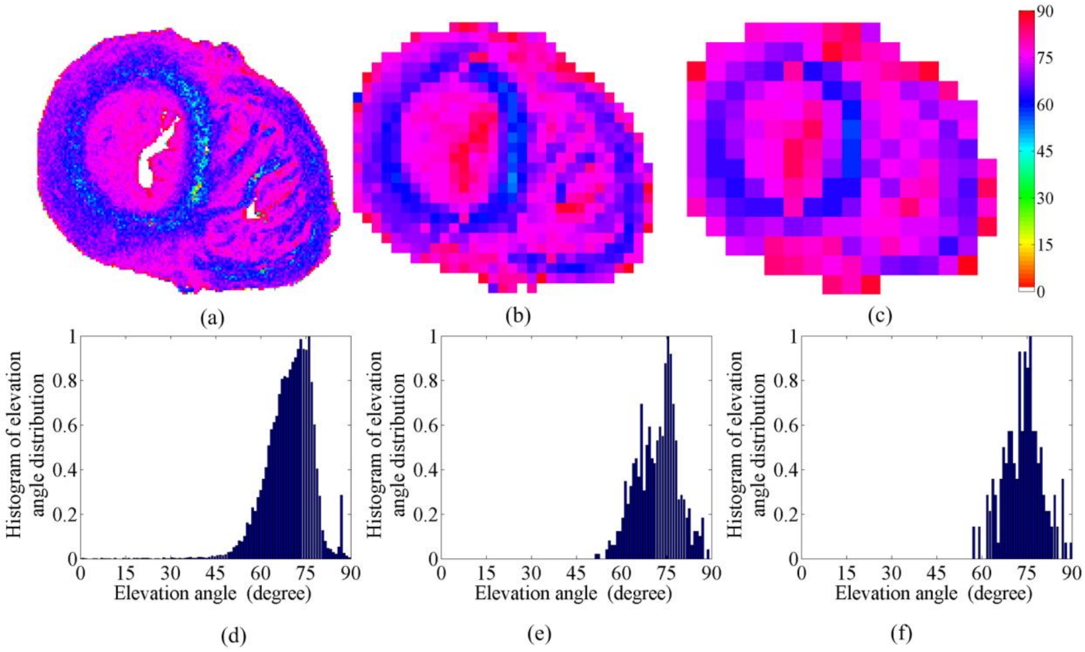

(a) (b) (c)

(d) (e) (f)

Fig. 5.13 Elevation angles and their related distribution histograms obtained at different observation scales displayed for one slice. (a) shows the spatial distribution and (d) the corresponding histogram of the elevation angle for the multi-scale cardiac fiber model with a spatial resolution of 0.1 × 0.1 × 0.5 mm^3. (b) and (e) correspond to the elevation angle for the multi-scale cardiac fiber model with a spatial resolution of 0.5 × 0.5 × 0.5 mm^3 . (c) and (f) demonstrate the elevation angle for the multi-scale cardiac fiber model with a spatial resolution of 1 × 1 × 1 mm^3.

FA and MD

Besides the cardiac fiber orientation, the diffusion indices including FA and MD are also the major parameters to reflect the diffusion properties of the tissue. We analyze the variation of the FA and MD values with the observation scales in the following paragraphs. Fig. 5.14 shows the simulated FA value and it amplitude distribution histogram at different scales. Comparing (a), (b) and (c) and their corresponding histograms (e), (d) and (f), it can be seen that, for the same cardiac fiber structure, the obtained FA values decreases slightly while the spatial resolution increases. The average FA values for (a), (b) and (c) are respectively 0.34, 0.33 and 0.32. Moreover, increasing the observation scale leads to a smaller range of FA values. FA reflects the diffusion preference of water molecules along different spatial directions, which is determined by the structure of the diffusion environment. When the diffusion environment has a privileged directional dependent structure, the measured FA is higher. In our case, when the observation scale increases, the fiber orientation in each voxel becomes more diversified which makes the water molecules have almost the same probability to diffuse in any directions and therefore reduces the diffusion anisotropy. At the same time, the orientation difference between neighboring voxels becomes less obvious, therefore narrowing the range of FA values.

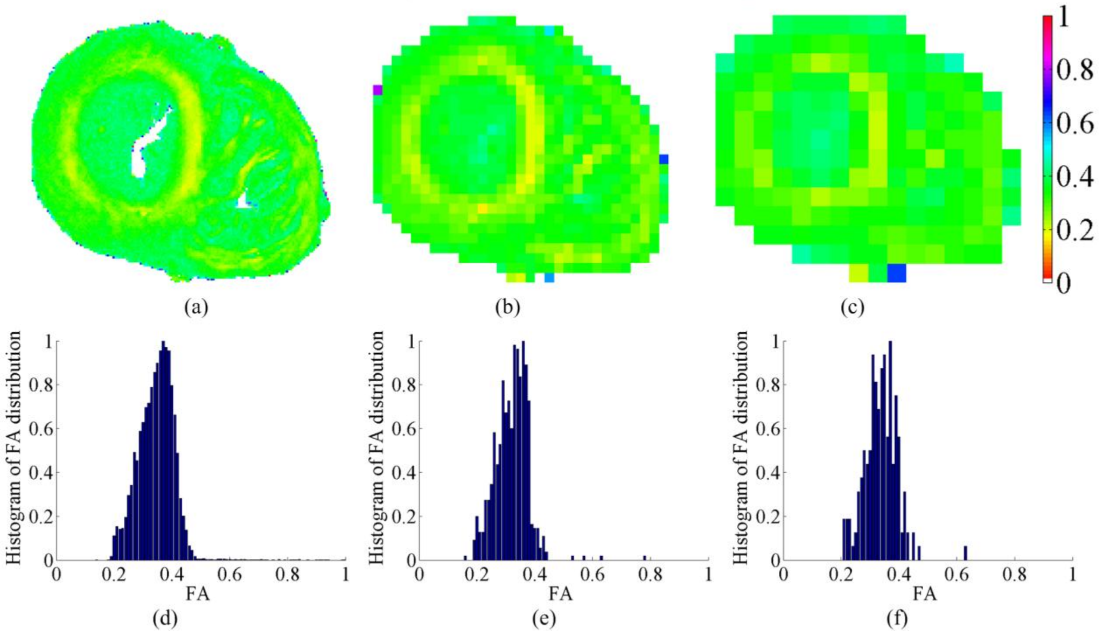

Fig. 5.14 FA values and their distribution histograms obtained at different scales. (a) shows the FA values and (d) the corresponding histogram for the multi-scales cardiac fiber model with a spatial resolution of 0.1 × 0.1 × 0.5 mm^3. (b) and (e) are the simulated FA for the multi-scale cardiac fiber model with a spatial resolution of 0.5 × 0.5 × 0.5 mm^3. (d) and (f) give the FA values and distribution for the multi-scale cardiac fiber structure obtained with a spatial resolution of 1 × 1 × 1 mm^3.

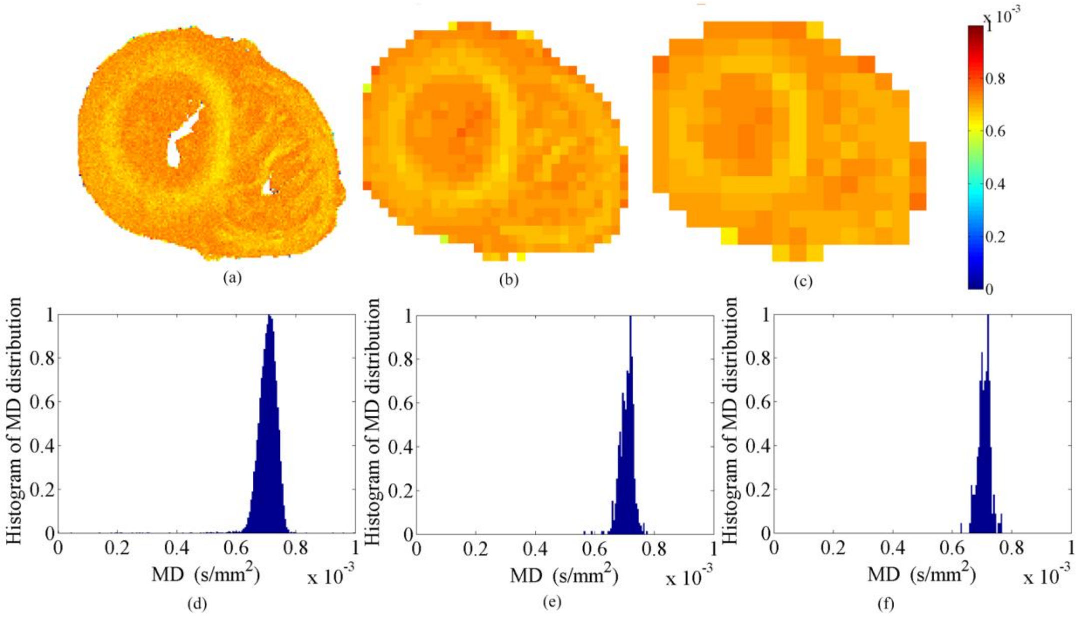

Fig. 5.15 MD values and their histograms obtained at different scales. (a) and (d) show the MD values and the corresponding histogram for multi-scales cardiac fiber model with a spatial resolution of 0.1 × 0.1 × 0.5 mm^3. (b) and (e) are the simulated MD values and the related histogram for multi-scale cardiac fiber model with a spatial resolution of 0.5 × 0.5 × 0.5 mm^3. (c) and (f) give the MD values and the histogram for multi-scale cardiac fiber structure obtained with a spatial resolution of 1 × 1 × 1 mm^3.

Fig. 5.15 shows the MD values and their corresponding histograms obtained at different observation scales. Comparing (a), (b) and (c) and their corresponding histograms (d), (e) and (f), we note that as the spatial resolution increases, the MD increases and its variation range becomes narrower. This can be explained by the variations of the diffusion signal intensity. A big size voxel contains more cardiac fibers, which enables the water molecules to have high probability to diffuse freely in many directions and therefore inducing more signal attenuation and leading to a high measured MD value. Moreover, when the observation scale increases, the diffusion preference, preferred direction of water molecules in each voxel, becomes less significant which leads to a narrow range of MD values.

5.6 Simulation for possible pathological heart

As we mentioned in the chapter 1, the cardiac muscle diseases are often correlated with a damage of the cardiac fibers, such as some arrangement disorder of the fiber orientations, changes in the cardiac myocytes size, extracellular space variations etc. For better understanding the relationships between the diffusion image properties and the cardiac fiber structures variations, we simulate in this section the effects of several cardiac fiber structure changes on the diffusion properties including FA and MD. In the following simulations of this chapter, the imaging parameters remain the same, with a diffusion time of 200 ms, a diffusion gradient with strength of 148.1 mT/m and duration of 2 ms, and the 42 diffusion gradient directions. The time interval for each random walk step of a water molecule is set to 2.1 ms to avoid the influence of diffusion during the gradient duration.

5.6.1 Changing the intercalated disk size

Intercalated disks are cross-bands that separate the opposing ends of two cardiac muscle cells. They help to hold adjacent cells together and transmit the force of contraction from cell to cell, thus a damage of intercalated disks will influence the myocyte function. In our multi-scale cardiac fiber model, the intercalated disk is considered as one part of the extracellular space. As the thickness of the intercalated disk increases, the extracellular space volume becomes larger and therefore the cardiac myocytes number in the voxel decreases. The variation of the intercalated disks thickness may influence the measured FA and MD values. For analyzing the influence of intercalated disk size, we simulate the DW images with various *diskRatio*. *Diskratio* is an input parameter of our multi-scale simulation model defined as the ratio of the intercalated disk thickness to the myocyte radius. For a normal dog heart, the intercalated disk thickness is about 1 µm [LAKS *et al.*, 1970] which results in a *diskRatio* of 0.1 for a myocyte radius of 10 µm. Thus, accordingly, in this simulation we use three different *diskRatios* of 0.1, 1 and 2 respectively. Its influences on the FA and MD values are analyzed at an observation scale corresponding to a spatial resolution of 0.1 × 0.1 × 0.5 mm^3.

Fig. 5.16 shows the FA images and their corresponding histogram simulated with different *diskRatio* values. The mean FA values are respectively 0.343, 0.342 and 0.344 for a *diskRatio* value of 0.1, 1 and 2. It implies that the variation of the intercalated disk thickness has almost no influence on the FA values.

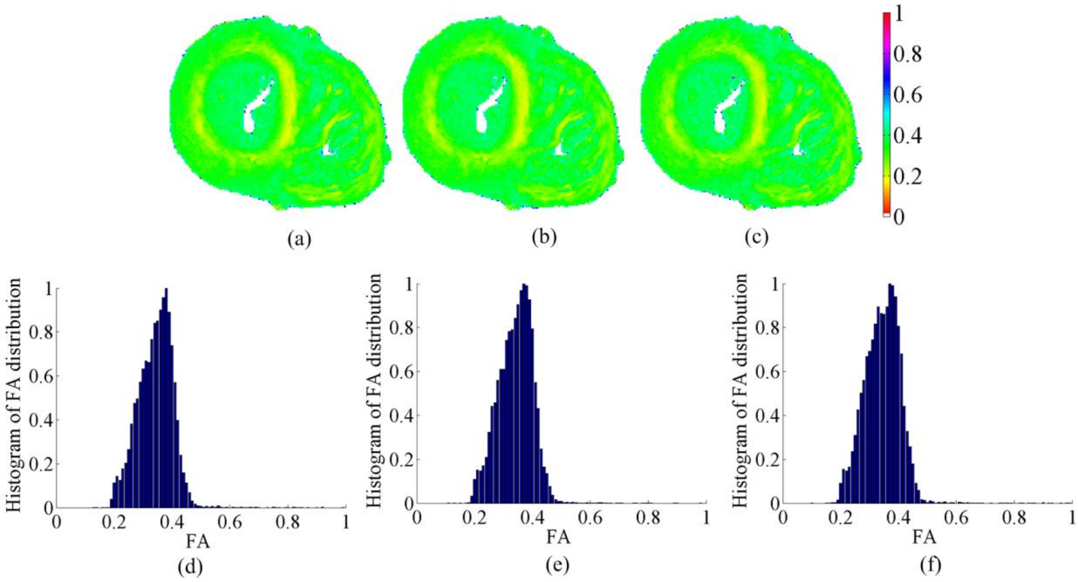

Fig. 5.16 FA variations with the *diskRatio* observed with a spatial resolution of 0.1 × 0.1 × 0.5 mm^3. (a) FA images its corresponding histogram (d) simulated with a *diskRatio* of 0.1. (b) and (e) are FA values and the related histogram obtained with a *diskRatio* of 1. (d) and (f) demonstrate the FA values and the histogram simulated with a diskRatio of 2.

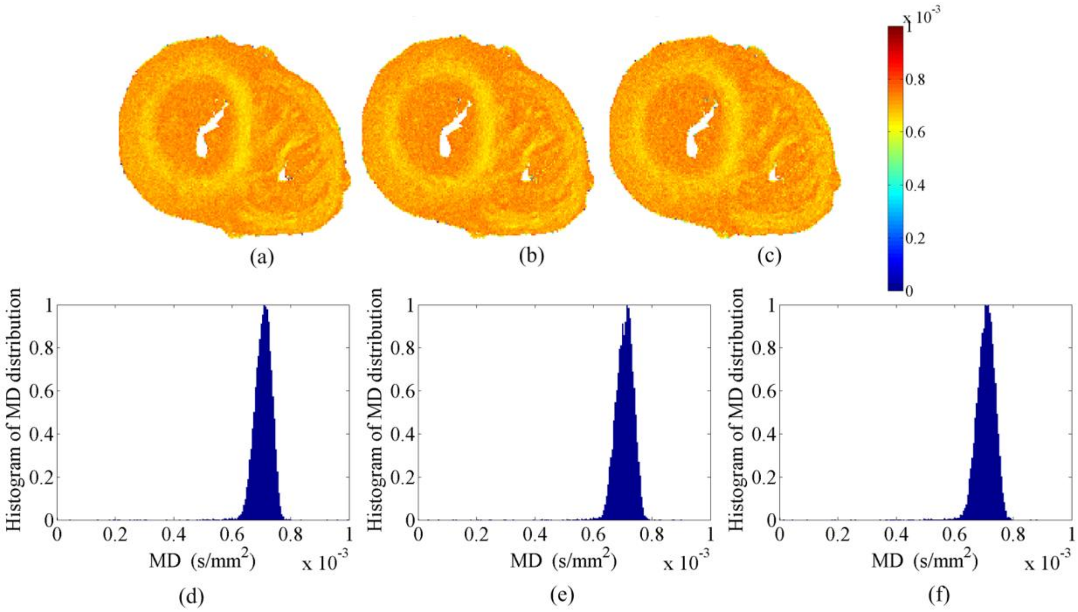

Fig. 5.17 MD variations with the diskRatio observed with a spatial resolution of 0.1 × 0.1 × 0.5 mm^3. (a) and (d) illustrate the MD images and the corresponding histogram simulated with a diskRatio of 0.1. (b) and (e) are MD values and the related histogram obtained with a diskRatio of 1. (c) and (f) show the MD values and the histogram simulated with a diskRatio of 2.

Fig. 5.17 illustrates the distribution of the MD values simulated with different *diskRatio*. The obtained average MD values for these three *diskRatio* are the same with a value of 7.05×10^{-4} mm^2/s. It implies that the variation of the *diskRatio* affects neither the FA, nor the

MD. This can be explained by the changes in the number of cardiac myocytes. When the *diskRatio* is 0.1, the total number of cardiac myocytes for this slice is 324898, when the *diskRatio* is 2, the number of myocyte is reduced to 230948. For the spatial resolution of 0.1 × 0.1 × 0.5 mm^3, the number of voxels for this slice is 14648. As the *diskRatio* changes from 0.1 to 2, the variation of the number of myocytes in each voxel is only about 7, thus its influence can be ignored.

5.6.2 Changing the radial distance between the cardiac myocytes

The cardiac myocytes are surrounded by the extracellular space, mainly composed by of several types of collagen. The collagen has many functions including transmitting forces, maintaining alignment of the myocytes and the muscle bundles, preventing over-distention of the myocardium, determining the shape and architecture of the heart, etc. Failure heart has shown an increase in the collagen content from 4% (normal) to 25%, which causes progressive functional impairment [Masood *et al.*, 2001]. The increased collagen content can impair both diastolic relaxation and systolic contraction. Therefore analyzing the effects of a change in the size of the extracellular space on the diffusion image properties appears to be necessary.

DW images

To be able to simulate extracellular structural modifications, we model the cardiac fiber structure with different *distanceRatio*. The *distanceRatio* parameter represents the ratio of the radial distance between cardiac myocytes to the radius of myocyte. In this simulation, five different *distanceRatio* values of 0.1, 0.9, 1.9, 3 and 4 are used respectively. The simulated DW images are shown in Fig. 5.18. We can observe that the image becomes a little noisy as the *distanceRatio* is increased.

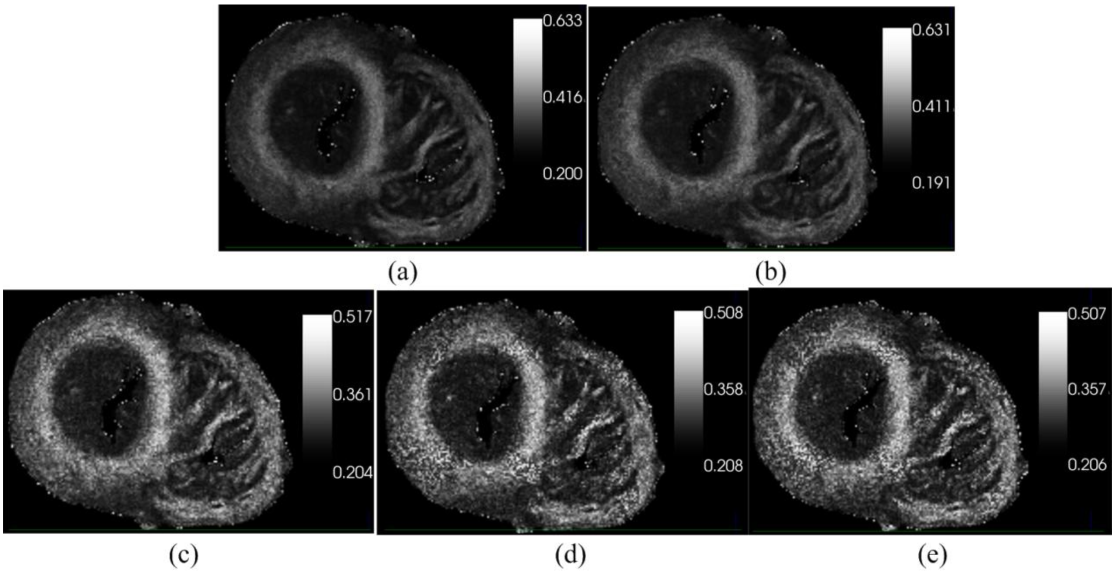

Fig. 5.18 DW images simulated with different distanceRatio. From (a) to (e) the value of the distanceRatio are 0.1, 0.9, 1.9, 3 and 4 respectively.

FA and MD

We calculate the diffusion properties including FA and MD from the DW images, as shown in Fig. 5.19 and Fig. 5.20. We see that with the increment of the *distanceRatio*, FA increases, MD decreases, and both ranges of the FA and MD values become larger. Increasing the *distanceRatio* leads to decrease the number of myocytes inside a given voxel. This highlights the water diffusion preference in a certain direction and therefore leads to a high FA value. Meanwhile, as the number of myocytes in one voxel is decreased, the difference of directional preference among the neighboring voxels becomes more obvious, which leads to increase the range of FA values.

Decreasing the number of myocytes in one voxel reduces the restricted diffusion effects, which leads to a bigger measured MD value a wide range of MD values

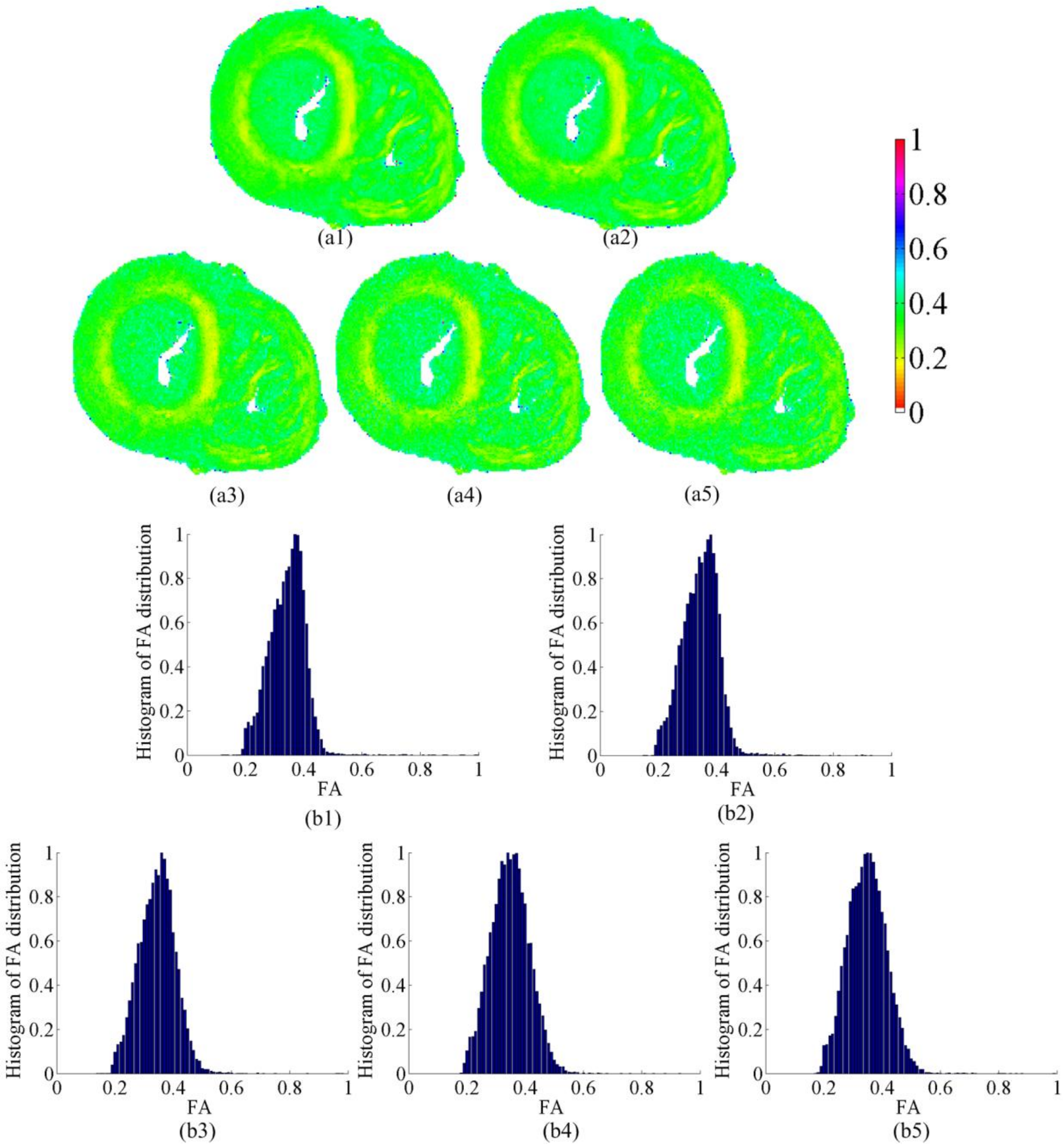

(a1) (a2)

(a3) (a4) (a5)

(b1) (b2)

(b3) (b4) (b5)

Fig. 5.19 FA varies as a function of the radial distance between the myocytes. From (a1) to (a5), the FA values with the *distanceRatio* of 0.1, 0.9, 1.9, 3 and 4 are shown. The corresponding histograms are illustrated in figures (b1) to (b5).

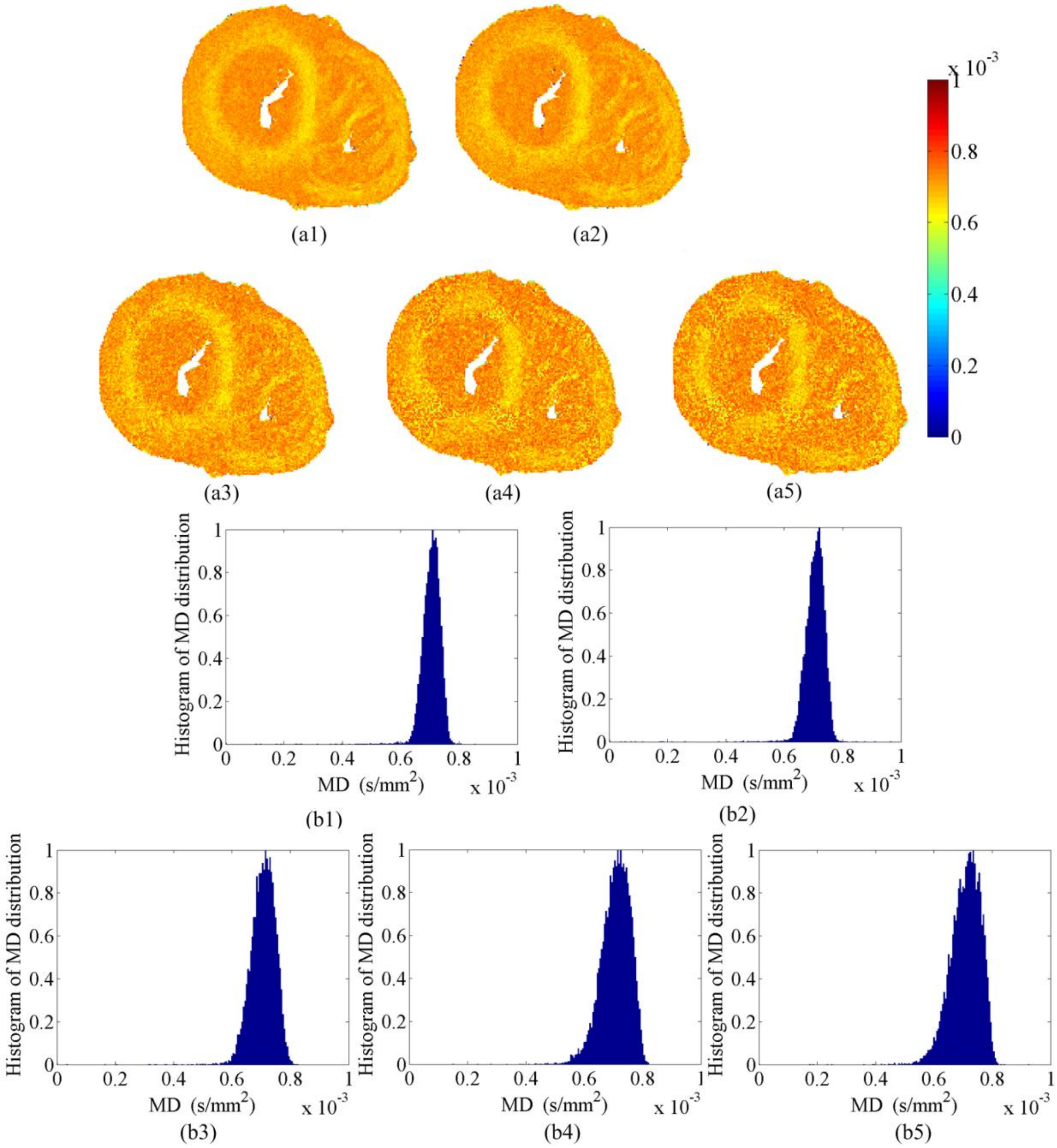

Fig. 5.20 MD value varies as a function of the radial distance between the myocytes. (a1) to (a5) correspond to the MD values with the *distanceRatio* of 0.1, 0.9, 1.9, 3 and 4. (b1) to (b5) give the related histogram.

5.6.3 Changing the elevation angle heterogeneity

It is well known that the structure of the cardiac muscle influences the electrical propagation and force development throughout the myocardium [Weiss *et al.*, 2007]. This is due to the anisotropy of the electrical and mechanical properties. The conductivity of ventricular tissue is determined by the direction of the fibers and is highest in the direction of their longitudinal axis. Thus observing the diffusion image properties variations caused by the changes in fiber orientation may provide a useful mean to detect the abnormality of cardiac mechanical functions. The heterogeneity of the fiber orientations can both provide from variations of the elevation α and azimuth β angles. The azimuth angle does not change when observed from the axial view, so we now analyze the influence of the heterogeneity of the elevation angle on the diffusion image properties.

DW images

PLI provides the main fiber orientation in each voxel, described by both the elevation and azimuth angles. In each voxel, the mean elevation angle is given by PLI, and its variance is defined by the heterogeneity, here we use five different heterogeneities with values of 10°, 30°, 50°, 70° respectively, the corresponding simulated DW images along one diffusion direction are shown in Fig. 5.21.

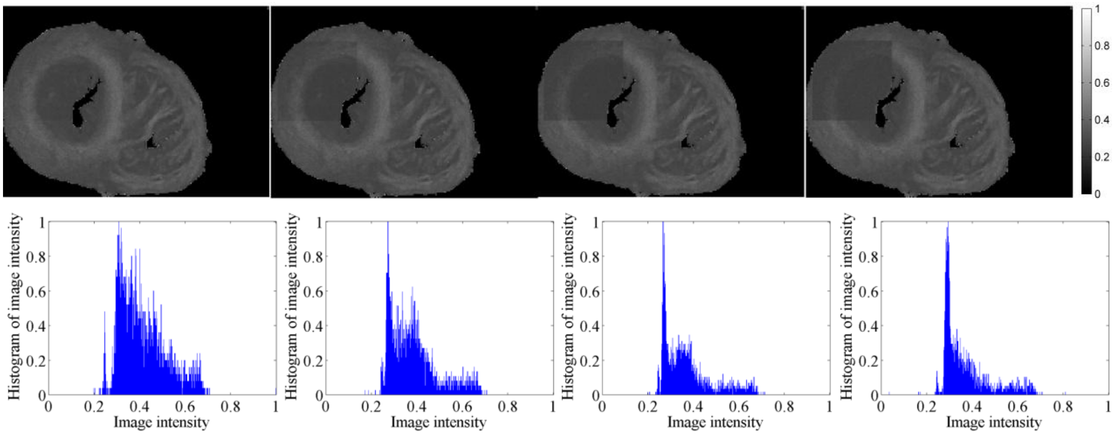

(b1) (b2) (b3) (b4)

Fig. 5.21 Simulated DW images and their corresponding intensity histogram along z direction for the different elevation angle heterogeneities. (a1) and (b1): 10º; (a2) and (b2): 30º; (a3) and (b3): 50º; (a4) and (b4): 70º.

It can be observed that an increase of the elevation angle heterogeneity decreases the image intensity and image contrast. This is because an increase of the elevation angle heterogeneity corresponds to decrease of the directionality of the structure, so the water molecules can diffuse quasi-freely along more directions, which therefore results in a more attenuated signal.

FA and MD

To better understand the effects of the elevation angle heterogeneity on the DW images properties, we calculate the FA and MD values. Fig. 5.22 shows the FA values and their corresponding histograms for different heterogeneity values. As the heterogeneity of the elevation angle increases, the FA value increases and its variation range becomes narrower and narrower. This variation trend appears to lead to contrary conclusions where we demonstrated that increasing the heterogeneity of the fiber orientations leads to a smaller FA. This point has also already been validated by our multi-scale simulations (when the observation scale increases, the presence of multiple orientations leads to a lower FA). The previous observation implies that the influence of the fiber orientation heterogeneity and the elevation angle heterogeneity on the FA value is not of same nature. Let us analyze the simulation. FA is calculated from the tensors of diffusion which usually are represented by ellipsoids. Inspired by the refractive ellipsoid illustrated in chapter 2, we explain this phenomenon by a kind of “diffusion ellipsoid” as shown in Fig. 5.23.

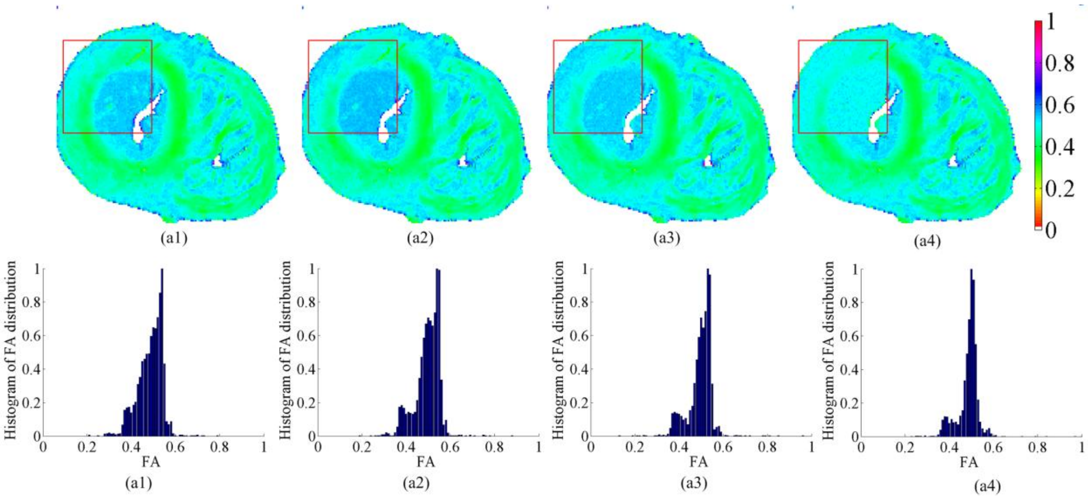

Fig. 5.22 FA variations with the orientation heterogeneity. (a1) to (a5) illustrate the FA spatial distribution for heterogeneity values equal to 10º, 30º, 50º, 70º and 90º respectively. (b1) to (b5) correspond to the related FA histograms.

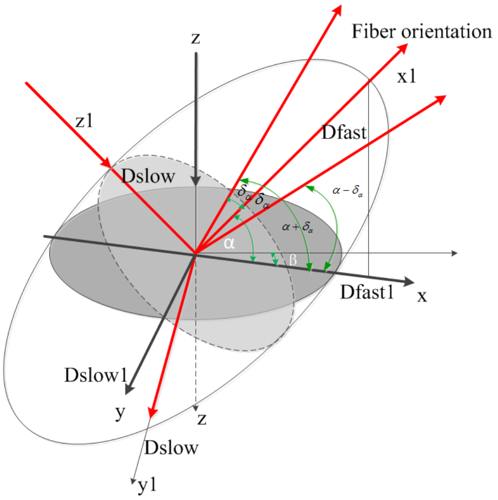

Fig. 5.23 Diffusion ellipsoid for explaining the FA variations as a function of the elevation angle heterogeneity.

Let us define the diffusion along the fiber orientation as *Dfast* and in the perpendicular direction as *Dslow*. The fiber orientaion is described by the elevation angle α and the azimuth angle β. Viewd from the z direction, the diffusion process can be described by Dfast1 and Dslow1. According to the ellipsoid sphere, the difference *Ddiff* between *Dfast1* and *Dslow1* can be expressed by:

$$\begin{aligned} Ddiff &= Dfast1 - Dslow1 \\ &= (Dfast - Dslow) \times \sin^2(\alpha) \end{aligned} \tag{5.1}$$

The *Ddiff* represents the difference between the measured fast diffusion and slow diffusion. If the elevation angle heterogeneity is defined as δ_α , the elevation angle range is then between $(\alpha-\delta_\alpha)$ and $(\alpha+\delta_\alpha)$. Let us consider the special case where we assume that the elevation angle of the myocytes in one voxel only has three choices, namely α, α-δ_α and α+δ_α. Thus the average difference between *Dfast1* and *Dslow1* for fibers in one voxel becomes:

$$\begin{aligned} Ddiff &= Dfast1 - Dslow1 \\ &= (Dfast - Dslow) \times (\sin^2(\alpha) + \sin^2(\alpha-\delta_\alpha) + \sin^2(\alpha+\delta_\alpha)) \\ &= (Dfast - Dslow) \times (1 + \sin^2(\alpha) - \cos(2\alpha)\cos(2\delta_\alpha)) \end{aligned} \tag{5.2}$$

The elevation angle α being kept as constant, we see that the increase of heterogeneity δ_α from 0º to 90º leads to the increase of *Ddiff*. As this difference increases, the measured diffusion anisotropy gets higher.

Fig. 5.24 shows the MD values and their corresponding histogram. Increasing the heterogeneity of the elevation angle leads to a larger MD and a smaller MD variation range. The multiple myocyte orientations enable the molecules to have almost the same probability to diffuse quasi-freely in all the directions, this therefore results in a high diffusivity. By comparing the diffusivity along the fast and slow diffusion directions calculated from the tensors of diffusion, we note that an increase of the elevation angle heterogeneity increases the diffusivity along both directions with more obvious high amplitude along the main diffusion direction. This point also explains why the measured FA value is higher. This result is in accordance with the conclusions of other research works in the brain diseases applications [Salat *et al.*, 2010; Douaud, 2011].

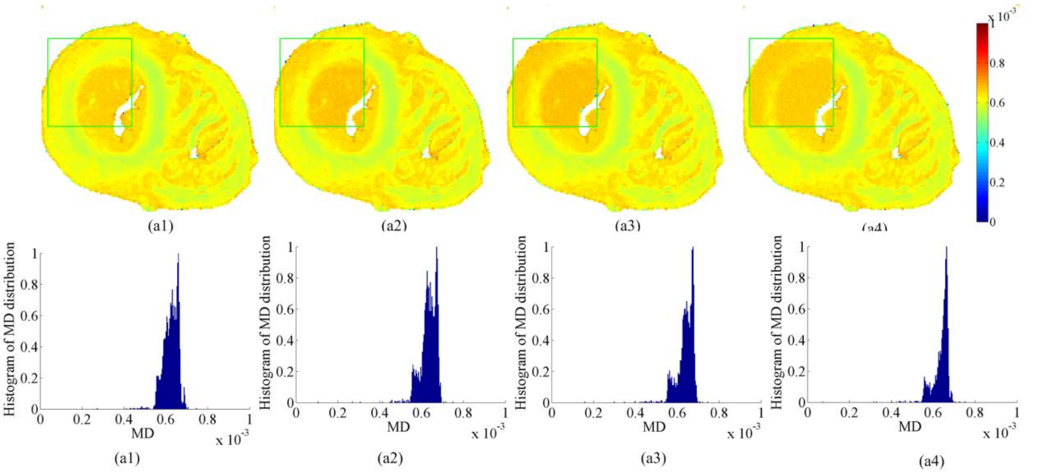

Fig. 5.24 Variation of MD values for different fiber orientation heterogeneity. In (a1) to (a5) MD values for heterogeneity of 10, 30, 50, 70 and 90 are given. (b1) to (b5) show the corresponding MD histograms.

5.6.4 Changing the myocytes size

As stated in chapter 1, heart failure due to ischemic or dilated cardiomyopathy is characterized by dilated, relatively thin-walled ventricles. The hypothesis has been proposed that the variation of cardiac myocyte morphology may be the reason for this kind of heart failure [Gerdes *et al.*, 1995]. For instance, the increases of myocyte length will increase the number of sarcomeres and result in an increasing chamber diameter. Evidences also indicate that these long and slender myocytes have a reduced ability to shorten or to develop adequate forces to compensate the extent of chamber dilation. Thus, myocyte size variations are postulated to be the primary event involved in the heart failure. In order to detect myocyte size changes using dMRI, we simulate the DW images for our multi-scale cardiac fiber model using different ratios of cardiac myocyte length to radius and calculate the corresponding diffusion properties.

DW images

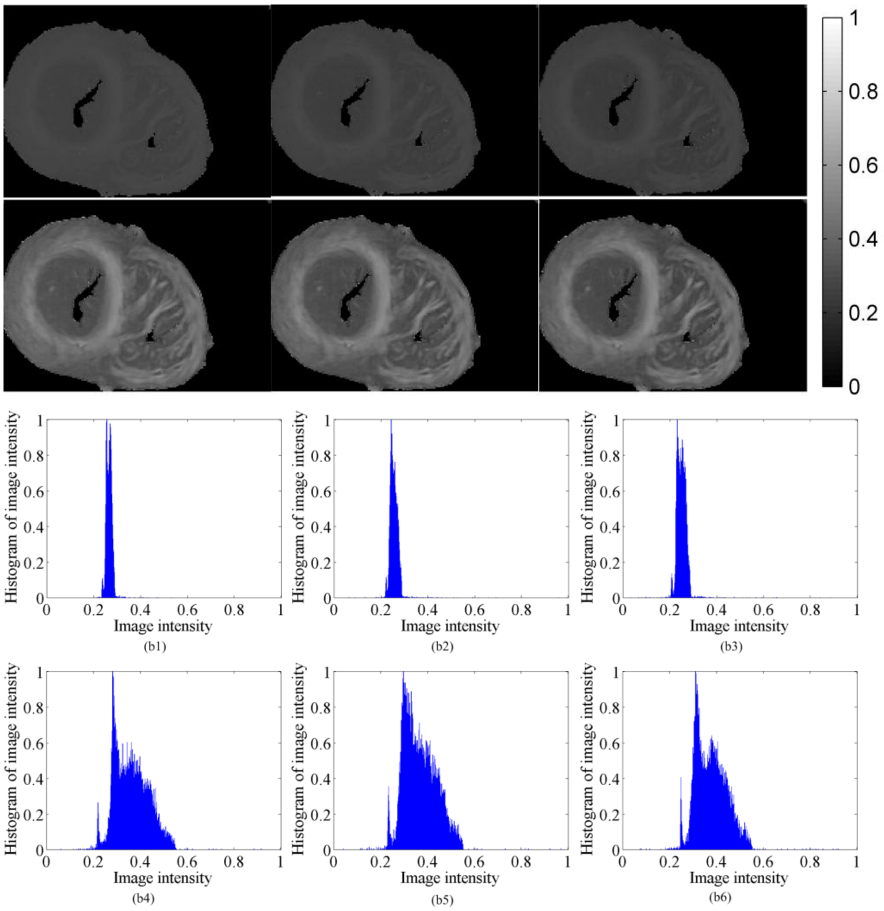

Fig. 5.25 DW images simulated with different myocyte sizes. From (a1) to (a3) the radius of myocyte is 20 μm, and the lengths are 60, 80 and 100 μm respectively. In subfigures (b1), (b2) and (b3) are the image intensity histograms of (a1), (a2) and (a3). From (a4) to (a6) the myocytes have a radius of 10 μm and a length of 100, 800 and 600 μm respectively. (b4), (b5) and (b6) correspond to the intensity histogram of (a4), (a5) and (a6).

Fig. 5.25 shows the simulated DW images along one diffusion gradient direction and the corresponding image intensity histograms. In subfigures (a1), (a2) and (a3), the radius of the myocytes is chosen as 20 μm, and the lengths as 60, 80 and 100 μm respectively, which correspond to the length to radius ratios of 3, 4 and 5. Note that with the increasing of length to radius ratio, the noisy intensity points in the pericardial layer make the image unperceivable and give us a wrong impression that the image quality is importantly impaired. However, comparing the corresponding intensity histograms (b1), (b2) and (b3), we observe that increasing the length to radius ratio leads to a better image contrast. As the length of myocyte is prolonged, which makes the water molecules diffuse more freely in this direction and causes bigger difference in signal intensity between the orientations parallel and perpendicular to the cardiac fiber, thus improving the image intensity contrast.

In the subfigures (a4), (a5) and (a6) are the DW images simulated for the myocytes with a radius of 10 µm and a length of 60, 80 and 100 µm respectively, which results in a length to radius ratio of 6, 8 and 10, respectively. Comparing them with the images simulated with a radius of 20 µm, the image contrast is significantly improved. As the radius of myocytes is reduced, the difference between the restricted diffusion and free diffusion become more obvious, which leads to a better image intensity contrast.

FA and MD

For further understanding the effects of myocyte size variations on diffusion image properties, the FA and MD are calculated, as shown in Fig. 5.26 and Fig. 5.27.

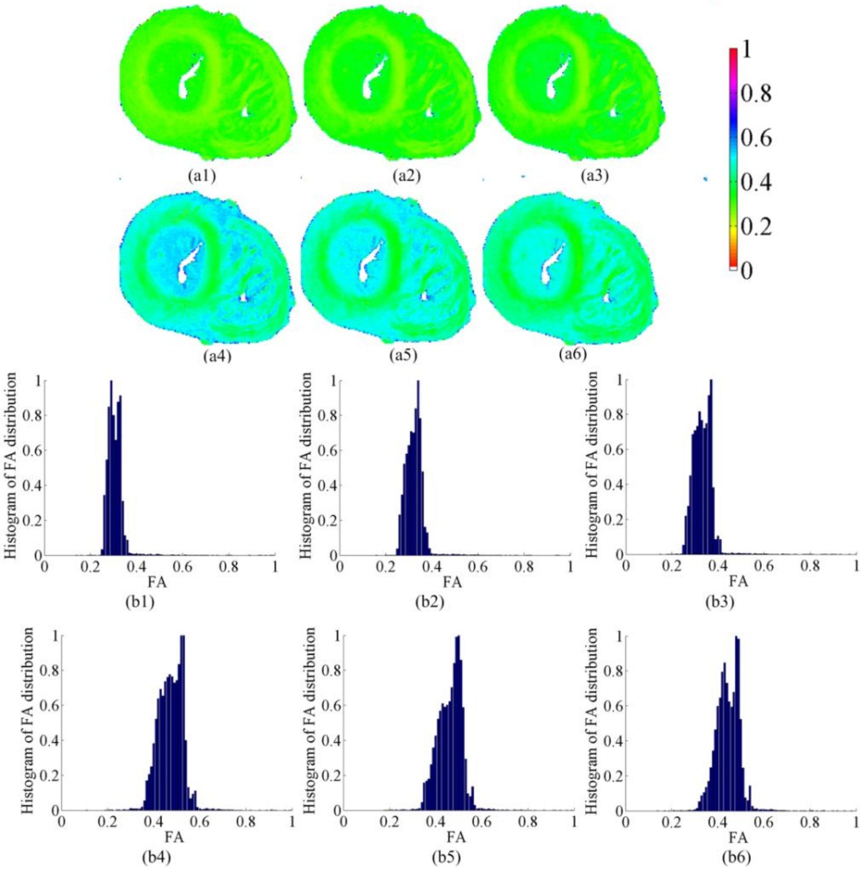

Fig. 5.26 Variation of FA with myocyte size. From (a1) to (a3), the radius of the myocyte is taken as 20 µm and the lengths are 60, 80 and 100 µm respectively. In figures from (a4) to (a6) are shown the FA values obtained when simulating with a radius of 10 µm and a length of respectively 60, 80 and 100 µm. The images from (b1) to (b6) correspond to the FA distribution histogram.

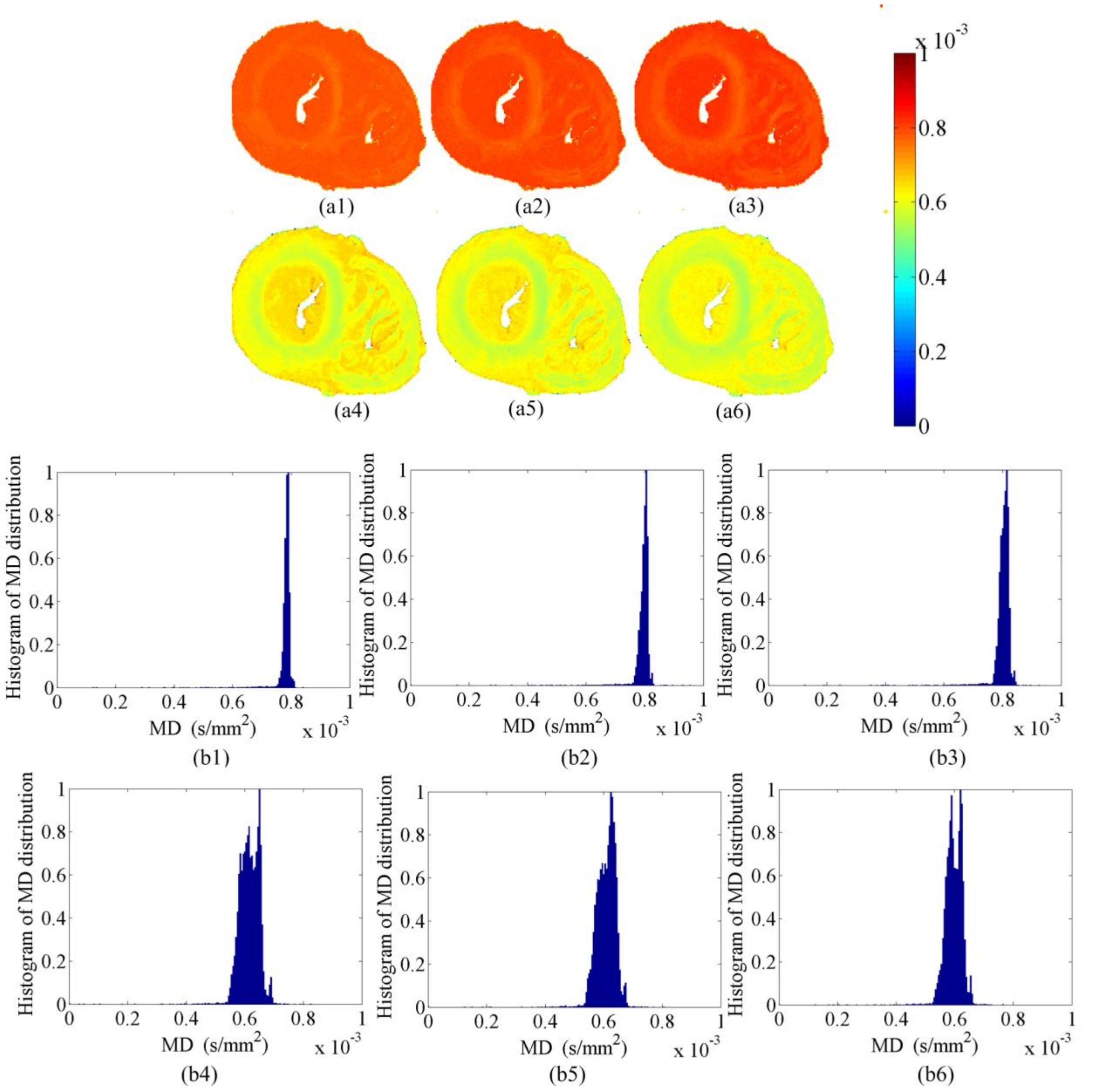

Fig. 5.27 Variation of MD with myocyte size. From (a1) to (a3), the radius of the myocyte is taken as the maximum value of 20 µm and the lengths are taken as 60, 80 and 100 µm, respectively. In figures from (a4) to (a6) are shown the MD values when simulating with the minimum radius of 10 µm and the length of respectively 60, 80 and 100 µm. The images from (b1) to (b6) correspond to the MD distribution histogram.

From Fig. 5.26 (a1) to (a3) are the FA images obtained with a length to radius ratio of 3, 4 and 5, and the corresponding distribution histograms are shown in (b1), (b2) and (b3) with mean FA values of 0.31, 0.32 and 0.33 respectively. It can be observed that when the length to radius ratio increases, the measured FA value becomes a little bigger. As to the MD values illustrated in Fig. 5.27 (a1), (a2) and (a3), the average value are 7.81×10^{-3}, 7.95×10^{-3} and 8.03×10^{-3} mm^2/s respectively. It indicates that the increment of myocyte length leads to a higher diffusion coefficient estimation. This variation trend of FA and MD with the length to radius ratio can be readily understood in light of free and restricted diffusion phenomena. As the myocyte length increases, the diffusion along the myocyte orientation becomes faster but remains unchanged along the direction perpendicular to the myocyte orientation. Consequently, the diffusion anisotropy and the diffusivity are increased. We also note that when the radius of the myocyte is 20 μm, the variation of myocytes size influences neither FA nor MD values significantly. This is because the diffusion is a time related process. In our simulation, the diffusion coefficient was selected as 10^{-3} mm^2/s. According to the Einstein diffusion equation, during the diffusion time of 200 ms, the maximum displacement of water molecules is about 35 μm. If diffusion takes place in a myocyte with radius of 20 μm, only a few molecules can sense the myocyte boundary, most of the molecules diffuse freely, thus increasing the length of myocyte does not alter the diffusion properties too much. But if the myocyte becomes slender, the restricted diffusion contributes mainly to the diffusion signal, the variation of diffusion properties with the length to radius ratio is more obvious, as shown in Fig. 5.26 (a4) (a5) and (a6). As the myocyte length changes from 60 to 100 μm, the mean FA value varies from 4.4 to 4.7 and the averaged MD value ranges from 5.9×10^{-3} to 6.2×10^{-3} mm^2/s.

By comparing the FA and MD variations with myocyte radius and length changes, we observe that both of them are related to diffusion time, which means that if the diffusion time allows sufficient molecules to contact the myocyte boundary, FA and MD are able to reflect the structure characteristics. On the contrary, if not enough molecules experience the myocyte boundary, the measured FA will be smaller and MD is higher than the real value. Therefore, for a given diffusion time, FA and MD values are greatly influenced by the small dimension (radius or width) of myocytes. The slenderer the myocyte, the bigger FA but the smaller MD is. If the myocyte radius is kept as a constant, increasing the length to radius ratio results in the increment of both FA and MD, but the effects is not obvious.

5.7 Conclusion

In this chapter, we have integrated for the first time the PLI data and dMRI principle to derive a model-based dMRI simulator allowing investigating the cardiac fiber architecture of the human heart and the diffusion image properties at multi-scales. We have first introduced the cardiac fiber modeling based on PLI data for both single scale and multi-scales. Then by comparing the simulated fiber orientation and ground-truth provided by PLI, we have validated the dMRI simulation approach on single scale cardiac fiber model. Finally, the DW images at three different observation scales have been simulated using a multi-scale cardiac fiber model and the variation of diffusion indices with observation scales has been analyzed. Meanwhile, by changing the modeling parameters, the DW images and diffusion indices for some possible pathological fiber architectures have been simulated, which enables us to establish the possible relationship between cardiac diseases and diffusion properties.

For clarity, the main results and conclusions that we obtained in those preliminary simulations are enumerated as follows.

1) The increasing of observation scales decreases the image contrast and leads to a smaller FA and a higher MD value. As to the cardiac fiber orientation described by elevation and azimuth angle, the elevation angle decreases but the azimuth angle does not change too much, as the observation scale increases.
2) The change in size of intercalated disks does not influence FA and MD values.
3) The increasing of the distance between the myocytes increases the range of variation of both FA and MD.

4) The increasing of elevation angle heterogeneity in one voxel increases both FA and MD values due to the increase of diffusivity along main diffusion direction.
5) The variation of myocyte sizes is the main reason for the change of diffusion indices. For a given diffusion time, FA increases but MD decreases with the increment of myocyte length to radius ratios. When the myocyte radius becomes smaller, this change trend becomes more obvious.

Because FA and MD are diffusion time related parameters, all the above conclusions are derived from a given diffusion time. When the diffusion imaging parameters change, such as the diffusion time and diffusion gradient duration, their influences on diffusion image properties should be accordingly considered. Hence, in the next chapter, for a given cardiac fiber structure, we will analyze the effect of imaging parameters on the diffusion indices in details.

Chapter 6

Influence of imaging parameters on diffusion properties of cardiac fibers

Contents

Résumé en français

L'architecture des fibres cardiaques est généralement reconstruite à partir de l'orientation des fibres estimée à chaque voxel de l'image de diffusion en utilisant des algorithmes de tractographie de fibres, et la maladie cardiaque est généralement étudiée en termes d'indices de diffusion, tels que le coefficient apparent de diffusion (ADC), l'anisotropie fractionnelle (FA), et la fonction de distribution d'orientations (ODF-Orientation Distribution Function en anglais). La fiabilité de reconstruction des structures de fibres et de calcul des indices de diffusion dépend de la précision de l'estimation des orientations de fibres à chaque voxel, qui à son tour dépend des méthodes d'estimation utilisées, des paramètres d'imagerie et de la qualité des images pondérées en diffusion.

Récemment, avec le développement des applications de l'imagerie de hautes valeurs de b, de nombreux travaux ont été consacrés à l'évaluation de l'influence des paramètres d'imagerie sur l'estimation de l'orientation des fibres. Comme les hautes valeurs de b sont souvent utilisées dans l'imagerie de l'espace q, qui nécessitent des impulsions étroites de gradient de diffusion afin de garantir la précision de l'estimation de l'orientation des fibres, la plupart des travaux se sont concentrés sur l'analyse de l'influence de la durée du gradient.

Pour des scanners d'IRM dont l'amplitude du gradient est trop faible pour générer une grande valeur de b, celle-ci est souvent réalisée en augmentant la durée du gradient, ce qui va détruire la condition du gradient court qui est nécessaire pour l'imagerie de diffusion. Dans ces conditions, l'augmentation du temps de diffusion devient un choix alternatif. Pour cette raison, l'influence du temps de diffusion sur les images de diffusion ont été beaucoup étudiées. D'autre part, pour extraire la taille du tissu dans lequel la diffusion se passe, la distance de diffusion doit être plus longue ou comparable à la dimension du tissu. Si le temps de diffusion est si court que les molécules d'eau ne peuvent pas toucher le bord du tissu, le déplacement des molécules d'eau ne pourra pas révéler la structure du tissu. De même, si le temps de diffusion est trop long, les effets de relaxation T_2 atténueront trop le signal et donc dégraderont la qualité d'image.

Donc, l'étude de l'influence des paramètres d'imagerie sur les propriétés de diffusion nous fournira une référence utile pour leur optimisation dans différentes situations. Cependant, la plupart des travaux reportés dans la littérature se portaient sur l'imagerie du cerveau, et quasiment rien sur les fibres cardiaques. Il est donc nécessaire d'aborder le sujet d'optimiser les paramètres d'imagerie en dMRI cardiaque. En outre, toutes les analyses actuelles sur ces influences étant basées sur des expérimentations réelles, leur fiabilité dépend fortement de la qualité des images acquises car, de nombreux facteurs incertains peuvent influencer la conclusion, tels que le mouvement du patient, le bruit, les artéfacts, et l'impulsion non parfaite du gradient de diffusion.

Afin d'obtenir une vision certaine et fiable de l'influence des paramètres d'imagerie sur les propriétés de diffusion des fibres cardiaques, nous proposons dans ce chapitre d'étudier ces influences au moyen de notre simulateur d'IRMd. En fonction des propriétés des séquences d'impulsion d'imagerie, trois types de simulations et d'analyses sont effectués. Nous utilisons tout d'abord le gradient de diffusion parfait pour simuler les images pondérées en diffusion et pour analyser l'influence du temps de diffusion, de l'amplitude et la durée du gradient de diffusion sur des indices de diffusion. Ensuite, en tenant compte des caractéristiques réelles de l’impulsion de gradient de diffusion, nous améliorons la théorie de la simulation et analysons l'influence de la durée du gradient de diffusion, le temps de diffusion, le temps de rampe du gradient de diffusion sur des indices de diffusion. Enfin, les effets sur les propriétés de diffusion des gradients d'imagerie comprenant le gradient de sélection de coupe, le gradient de codage de phase et le gradient de lecture sont simulés.

6.1 Objectives

Cardiac fiber architecture is generally reconstructed from the fiber orientations estimated at each dMRI voxel using some fiber tracking algorithms, and cardiac disease is usually assessed using diffusion related indices such as Apparent Diffusion Coefficient (ADC), Fractional Anisotropy (FA), and Orientation Distribution Function (ODF)[Sosnovik, 2009a; Sosnovik *et al.*, 2009b]. The reliability of fiber architecture reconstruction and diffusion indices calculation depends on the accuracy of the estimated fiber orientation at each voxel, which in turn is dependent on the estimation methods for fiber orientations, imaging parameters and quality of diffusion-weighted images.

Recently, with the surge of high b-value imaging applications, extensive efforts have been dedicated to evaluating the effects of imaging parameters on fiber orientation estimations in dMRI [Avram *et al.*, 2004; Nossin-Manor *et al.*, 2005; Nezamzadeh, 2012]. Since high b-values are often used in q-space imaging that requires narrow diffusion gradient pulses for guaranteeing the accuracy of fiber orientation estimation, most of works have focused on analyzing the influence of gradient duration. In practice, high b-values can only be achieved with long diffusion gradient pulses because of the relatively weak gradient strength for the current MRI setup. Thus the short gradient pulse is not satisfied in such experimental conditions and increasing the ratio of diffusion time to pulse duration becomes an alternative choice, which has led to several studies on the effects of such ratio on the diffusion images [Bar-Shir, 2008; Shemesh *et al.*, 2009; Yeh *et al.*, 2010]. In addition, to reflect the structure of tissues in which the diffusion takes place, the diffusion distance performed during a given diffusion time must be longer or comparable with the tissue dimension. If the diffusion time is so short that the water molecules are unable to reach the tissue boundaries, the displacement distribution of water molecules cannot reveal the tissue structure. If the diffusion time is too long, the effects of T2 relaxation will attenuate too much the signal and therefore influence the image quality [Nilsson *et al.*, 2009; Chou *et al.*, 2012; Nezamzadeh, 2012].

All above works about the effects of imaging parameters on diffusion properties provide us a useful reference for optimizing imaging parameters under different situations. However, most of these works focused on the brain, and almost nothing is about the cardiac fiber. In view of the difference between cardiac fiber and brain, finding a mean of optimizing cardiac fiber dMRI parameters becomes fundamental. In addition, all the current analyses about these effects have been based on the acquired images. The reliability of these analyses greatly depends on the quality of diffusion images, which can be influenced by many uncertain factors, such as patient motion, artifacts and noise. In order to obtain a reliable view of the influence of imaging parameters on the cardiac fiber dMRI properties, this chapter proposes to use our dMRI simulator for cardiac fiber to analyze this kind of effects. According to the properties of imaging sequence pulse, three kinds of simulation and analysis are performed. We use firstly the perfect diffusion pulse gradient to simulate DW images and analyze the influence of diffusion time, diffusion gradient strength and duration on the diffusion properties. After that, taking into account the real diffusion gradient pulse characteristics, we improve the dMRI simulation theory and use it to analyze the influence of diffusion gradient duration, diffusion gradient ramp time and diffusion time on the DW images and diffusion indices. Finally, the effects of k-space encoding gradients including slice selection, phase encoding and readout gradients on the diffusion properties are simulated.

6.2 Influence of perfect diffusion gradient parameters

The perfect diffusion gradient mentioned here means that: 1) the ramp time of diffusion gradient is very short, thus the diffusion during this time interval is overlooked; 2) the diffusion during the gradient pulse duration is not taking into account. Under these conditions, the q-value and b-value used in the simulation can be expressed as:

$$q = \gamma G \delta \tag{6.1}$$

$$b = q^2(\Delta - \delta/3) \tag{6.2}$$

with G the diffusion gradient strength, δ the diffusion gradient duration and Δ the diffusion time. Using the simulation theory stated in the chapter 4, the effects of diffusion gradient parameters are analyzed as follows.

6.2.1 Effects of diffusion time

For extracting the structure information from MR experiments, diffusion should be performed in a long enough diffusion time, namely, the diffusion time Δ should satisfy $\Delta >> l^2/2D$, where l is the dimension of the tissues in which the molecules diffuse and D is the diffusion coefficient. In this paper, the diffusion coefficient is selected as $10^{-3}\mathrm{mm}^2/\mathrm{s}$, the diameter of the myocyte is 20 μm and the length is 100 μm. Thus, in order to distinguish the smallest structure, the diffusion time should be longer than $200\,\mathrm{ms}$. However, in real dMRI experiments, long diffusion time will introduce many problems, such as the image ghost caused by patient motion and the undesirable signal attenuation due to the long echo time. Therefore, the diffusion time in practice is usually about $50\,\mathrm{ms}$. Here, in the absence of influence of real imaging conditions, simulating the effect of diffusion time on diffusion properties will allow us to choose an optimal value of this parameter. To do that, the diffusion gradient strength keeps as a constant of 45 mT/m, δ is chosen as $10\,\mathrm{ms}$, which results in a q-value of 19.16 mm^{-1}. The dMRI simulation is performed with a diffusion time of 20, 50, 100, 150, 200, and 300 ms respectively. The corresponding simulated DW images are shown in Fig. 6.1. It can be seen that with increasing of the diffusion time, the image contrast is improved.

From these DW images, diffusion tensor images are calculated. In order to quantitatively describe the influence of diffusion time on diffusion properties, the average fractional anisotropy (FA), the mean diffusivity (MD) and the fiber orientation deviation are extracted from diffusion tensors (Fig. 6.2). The results show that FA increases slowly but MD drops quickly when the diffusion time becomes longer. Meanwhile, the fiber orientation derived from simulation and that measured by PLI are getting closer and closer with increment of diffusion time. This can be explained by the restricted diffusion phenomenon. When the diffusion time is so short that the water molecules cannot reach the boundary of the cardiac myocyte, the diffusion process behaves like free diffusion with high diffusivity and low anisotropy. As no water molecules sense the cardiac fiber, the displacement of water molecules is therefore unable to reflect the cardiac fiber structure. That is why the angle deviation between the simulation and PLI results is so important when the diffusion time is short. Moreover, according to the angle deviation curve with diffusion time, it can be seen that the deviation angle is about 3° when the diffusion is 50 ms , which is acceptable. Considering actual dMRI acquisitions, long diffusion time will introduce undesirable signal attenuation and increase the acquisition time. For this reason, the diffusion time of 50 ms would be an appropriate choice.

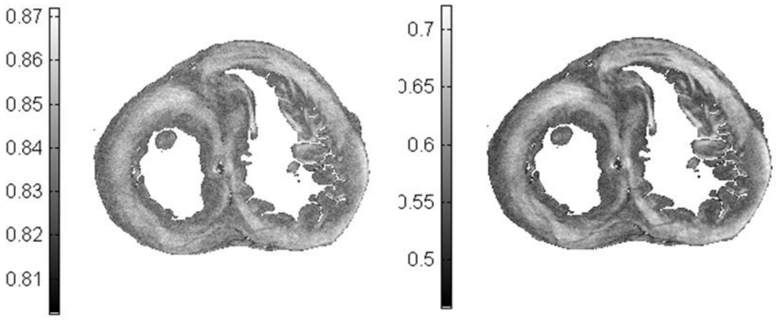

(a) Δ= 20 ms, b = 245 mm^2s^{-1} (b) Δ= 50 ms, b = 685mm^2s^{-1}

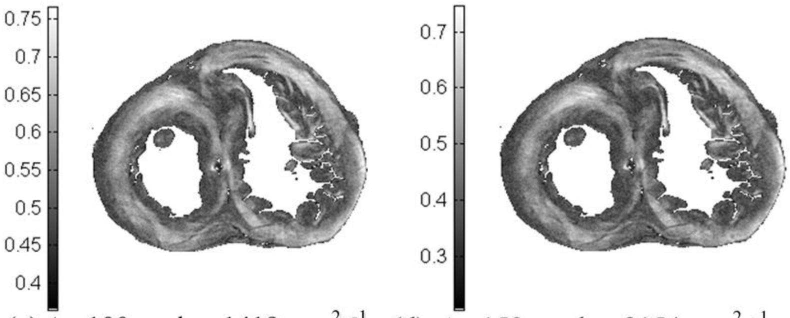

(c) Δ= 100ms, b = 1419 mm^2s^{-1} (d) Δ= 150 ms, b = 2154 mm^2s^{-1}

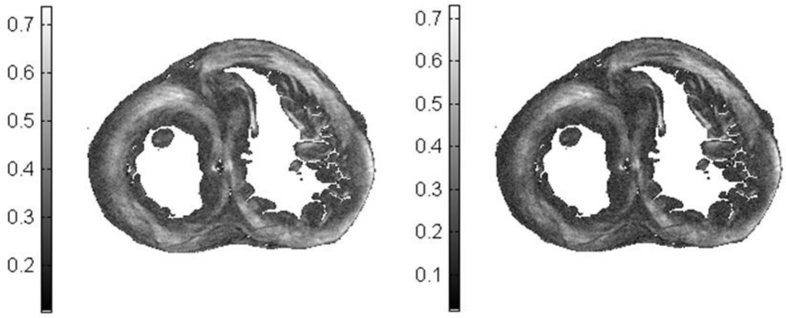

(e) Δ= 200 ms, b = 2887mm^2s^{-1} (f) Δ= 300ms, b = 4356 mm^2s^{-1}

Fig. 6.1 Simulated diffusion weighted (DW) images with different diffusion time. For simplicity of demonstration, for each diffusion time, we just compare DW image simulated along one direction (z direction). Note that with the increase of diffusion time, b-value increases and accordingly the DW image contrast is improved.

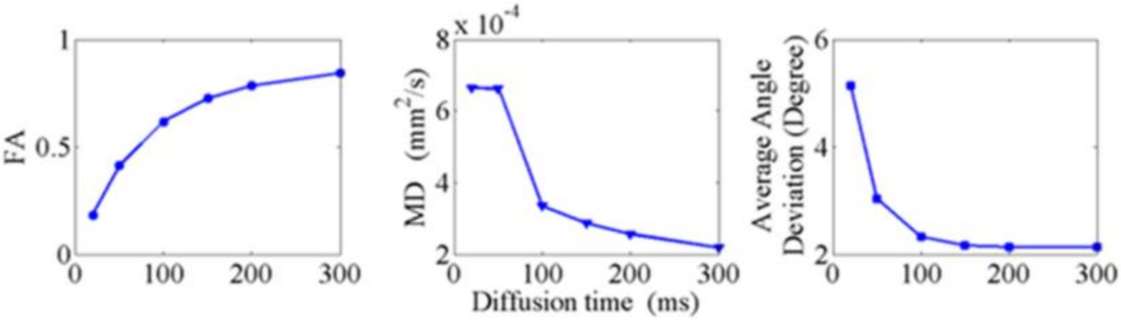

Fig. 6.2 Variation of FA, MD and angle deviation as a function of diffusion time. FA, MD and angle deviation represent the average of all the values in the image.

6.2.2 Effects of gradient strength

Strong gradient intensity is usually required in q-space imaging modalities. If the other imaging parameters do not change, increasing the gradient strength leads to a high q-value and b-value. According to the simulation theory stated in chapter 4, high q-value introduces more diffusion signal attenuation, which will decrease the signal-to-noise ratio (SNR) in actual experiments. Thus choosing an appropriate diffusion gradient strength according to the q-value will be important. The DW images simulated with different gradient strengths are illustrated in Fig. 6.3. The simulation parameters used here are: diffusion time $\Delta = 50\ \mathrm{ms}$, gradient duration $\delta = 2.5\ \mathrm{ms}$ and gradient strengths are 93.95, 187.9, 281.2 and 375.8 mT/m respectively, which correspond to the q-values of 10, 20, 30, and 40 mm^{-1}. By comparing the DW images in Fig. 6.3, it can be seen that increasing the diffusion gradient strength improves the image contrast but induces more signal attenuation. When G is 375.8 mT/m and q-value is 40 mm^{-1}, the DW image becomes a little noisy. In light of diffusion signal intensity, we note that in our simulation case, the appropriate q-value should be between 20 and 30 mm^{-1}. Therefore, the diffusion gradient strength should be selected according to this q-value range and the given gradient duration.

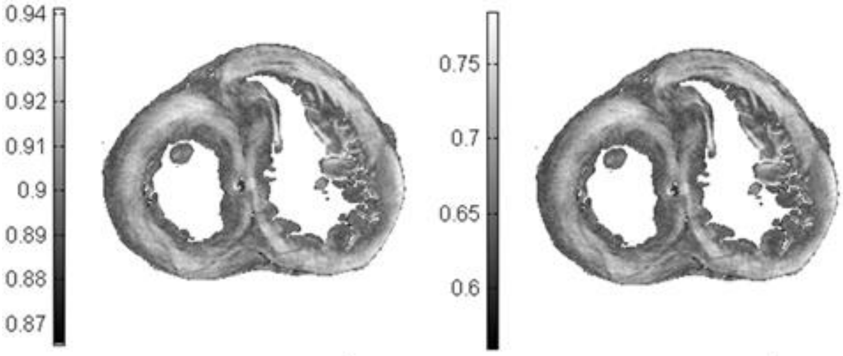

(a) q = 10 mm^{-1} (b) q = 20 mm^{-1}

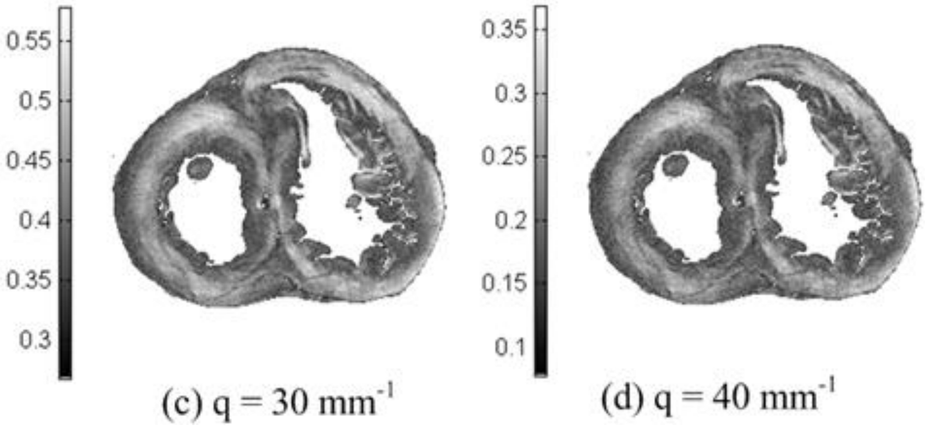

Fig. 6.3 DW images simulated with different gradient strengths. Here just the DW images along one direction are given. The simulation parameters used are: Diffusion time is 50 ms, diffusion gradient pulse duration is 2.5 ms, the diffusion gradient strength are respectively 93.95, 187.9, 281.2 and 375.8 mT/m, which leads to the q-values of 10, 20, 30, and 40 mm^{-1} and the corresponding b-values of 197, 787, 1740 and 3147 s/mm^2.

Besides the DW images, the FA, MD and orientation deviation between simulation and PLI experiments for different gradient strengths were also analyzed, as shown in Fig. 6.4. FA and MD do not have a significant change, but when gradient strength increases, the orientation estimated from simulation results deviates more from the ground-truth.

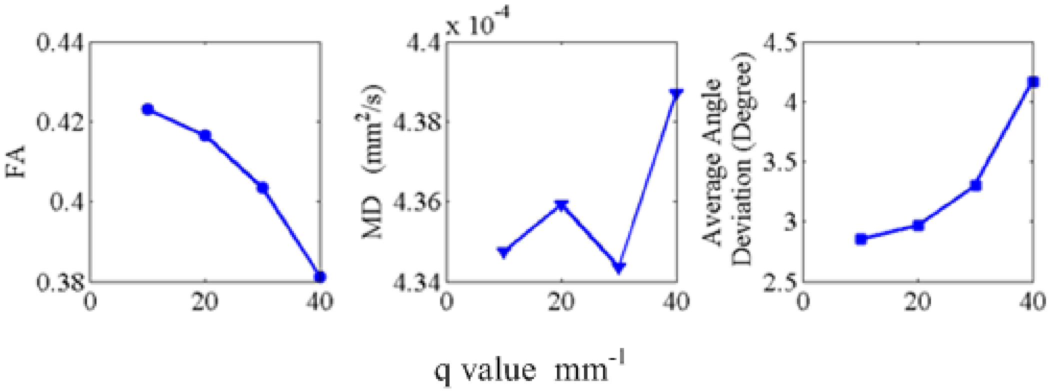

Fig. 6.4 Influence of q-values (gradient pulse strength) on FA, MD and angle deviation. FA varies from 0.42 to 0.38 when the q-value changes from 10 to 40 mm^{-1}, and MD almost makes no change. The orientation deviation angle between simulation and PLI experiments increases when q becomes bigger.

6.2.3 Effects of the gradient pulse duration

Q-space imaging (high b-value) requires strong gradient pulse that is generally not available on the current clinical MRI scanners. Therefore, high b-value is usually realized by increasing diffusion gradient duration. In dMRI analysis, it assumes that the diffusion gradient pulse duration is very short so that the displacement performed by the water molecules during this period can be ignored. This assumption is reasonable for DTI because it does not need to increase the pulse duration for compensating the relatively small gradient strength. However, for q-space imaging, the displacement of water molecules during the long pulse duration can no longer be ignored. Thus comparing the effects of gradient duration for both DTI (low b-value) and q-space imaging (high b-value) is necessary.

For better understanding the influence of pulse duration, before simulating the DW images for low b-values and high b-values, the diffusion signal along one of the radial direction of myocyte is simulated. The diffusion time Δ is set to 50 ms, the pulse durations δ are 2.5, 5, 10, 25 and 50 ms respectively, and the gradient strength is 45 mT/m. The results are shown in Fig. 6.5.

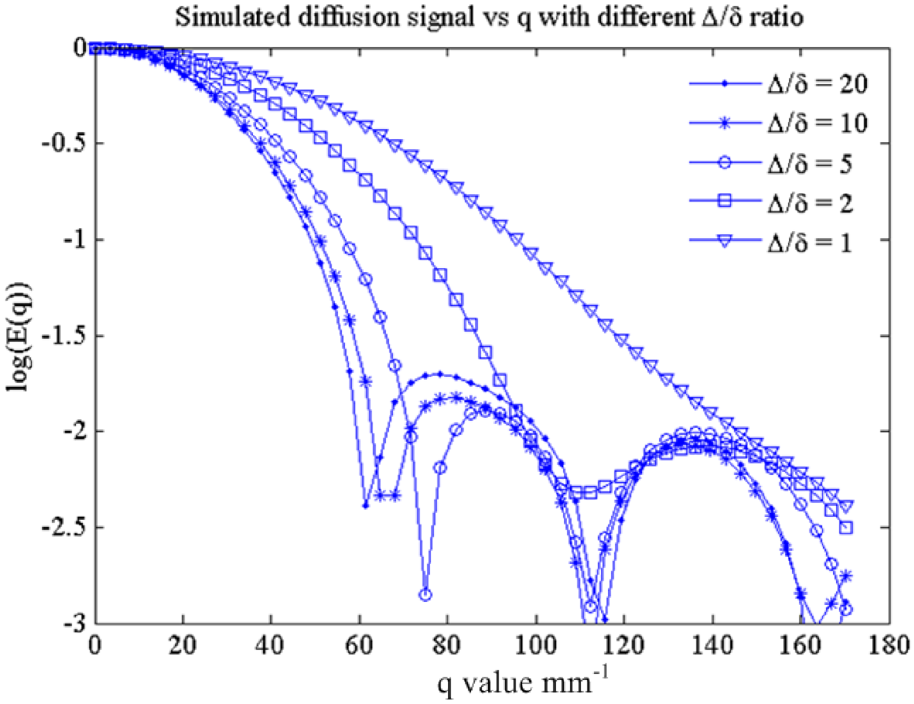

Fig. 6.5 Effects of Δ/δ on diffusion signal attenuation as a function of q-value. Diffusion time Δ is fixed as 50 ms. δ is set to 2.5, 5, 10, 25 and 50 ms respectively, which results in a Δ/δ value of 20, 10, 5, 2 and 1. The first signal diffraction minima are found at q = 61.3, 64.7, 74.9 109 mm^{-1} for δ of 2.5, 5, 10 and 25 ms respectively. When δ is equal to Δ, no signal diffraction happens.

According to the work of [Price, 1997], the first minimum of restricted diffusion magnetic resonance signal corresponds to the size of the restricted environment. If the diffusion environment is a cylinder, the relationship between the cylinder diameter l and the q-value where the signal minimum locates at is:

$$l = \frac{1.22}{q} \tag{6.3}$$

In the present study, the myocyte is modeled by the cylinder with a diameter of 20 μm. Thus, the q-value corresponding to the first signal diffraction minimum should be about 61 mm^{-1}. From Fig. 6.5, it can be seen that when $\Delta/\delta = 20$, the simulated signal diffraction minimum locates at the q value of 61.3 mm^{-1} that is very close to the theoretical result. Thus $\Delta/\delta = 20$ is the optimal ratio for dMRI simulation in this case. When Δ/δ decreases, diffraction minima appears at higher q-value and is shallower than the diffraction minimum observed with $\Delta/\delta = 20$. This implies that the diameter of myocyte inferred from the diffusion signal is smaller than the actual size when Δ/δ is smaller.

1) Effects of Δ/δ on low b-value imaging with $b = 1000\ \mathrm{s/mm^2}$

Fig. 6.6 shows the simulated DW images along one diffusion gradient direction with a low-b-value of $1000\,\mathrm{s/mm^2}$ for different δ values of 2.5, 5, 10, 25, and 50 ms. The diffusion time Δ is set to 50 ms and the gradient strengths are chosen as 213, 108, 55, 23 and 13 mT/m respectively, which result in a q-value of 22.7, 22.9, 23.3, 24.7 and 27.6 $\mathrm{mm^{-1}}$. It can be observed that when δ increases, the intensity of the images increases firstly and then decreases but the image contrast does not experience great variations. As explained for the diffusion diffraction signal curves, when Δ is fixed and δ increases, the resulting Δ/δ value decreases and correspondingly the diffusion weighted signal increases. That is why the image intensity in Fig. 6.6(b) and (c) is bigger than that in Fig. 6.6(a). However, the increment of δ also increases the q-value, and then leads to more diffusion signal attenuation. When the effect of q-values is stronger than that of Δ/δ, the image intensity decreases, as shown in Fig. 6.6(d) and (e).

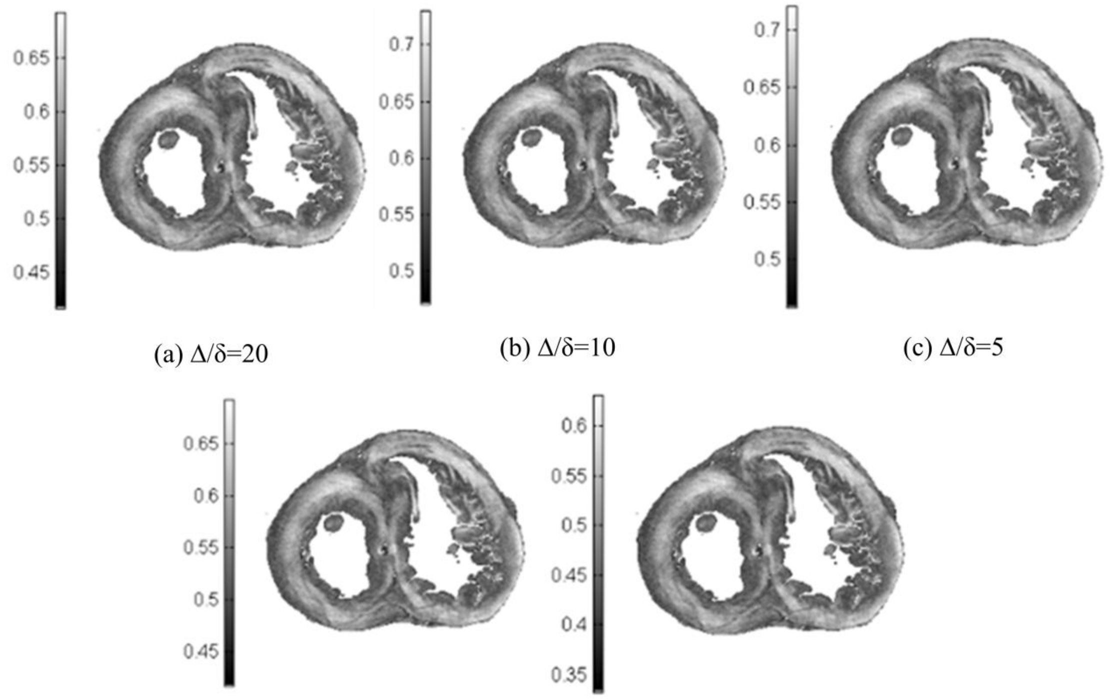

(a) Δ/δ=20 (b) Δ/δ=10 (c) Δ/δ=5

(d) Δ/δ=2 (e) Δ/δ=1

Fig. 6.6 Effects of ratio of diffusion time to gradient duration on DW images for low b-value imaging. Simulation parameters: Δ =50 ms, b = 1000 s/mm^2. For δ = 2.5, 5, 10, 25 and 50 ms, the gradient strengths are respectively 213, 108, 55, 23 and 13 mT/m, and the corresponding q-values are 22.7, 22.9, 23.3, 24.7 and 27.6 mm^{-1}.

Fig. 6.7 shows the effects of Δ/δ on FA, MD and orientation deviation angle for low b-value imaging with 1000 $\mathrm{s/mm^2}$. It can be seen that with increment of Δ/δ, FA increases and MD decreases but not significantly. As illustrated in Fig. 6.5, the diffusion signal along the radial direction of the myocyte is less attenuated when Δ/δ becomes smaller. However, the diffusion signal in other directions is not greatly influenced by the variation of Δ/δ. Therefore, the diffusion signal intensity difference between different directions becomes smaller when Δ/δ decreases, and accordingly, the measured diffusion anisotropy FA is reduced. For the same reason, the increasing of diffusion-weighted signals leads to the over-estimation about the diffusion coefficient MD. As to the orientation deviation angle between the simulation and PLI experiment, when Δ/δ ranges from 1 to 20, the deviation angle varies from 3.2º to 3º, which means that the variation of Δ/δ does not influence the fiber orientation estimation in low b-value imaging.

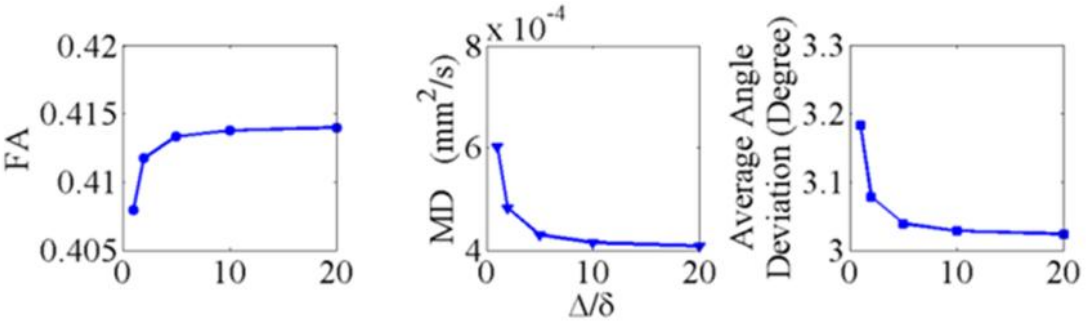

Fig. 6.7 Effects of Δ/δ on FA, MD and orientation deviation angle for low b-value imaging.

2) Effects of Δ/δ on high b-value imaging with $b = 4000$ s/mm^2

The simulated DW images along one direction with $b = 4000$ s/mm^2 for different Δ/δ values are shown in Fig. 6.8. The diffusion time Δ is set to 50 ms, the gradient pulse duration δ of 2.5, 5, 10, 25 and 50 ms are used, which results in the diffusion gradient strengths of 427, 215, 109, 46 and 26 mT/m respectively, and accordingly the q-values of 45.4, 45.8, 46.6, 49.3 and 55.1 mm^{-1}. From these images, we note that when Δ/δ is 20, 10 and 5, the diffusion image intensity does not experience changes, because the change of Δ/δ does not induce a big variation of q-values and consequently the image intensity. When Δ/δ is 2 and 1, the q-value becomes bigger and the diffusion signal decreases a little, as shown as in Fig. 6.8(d) and (e).

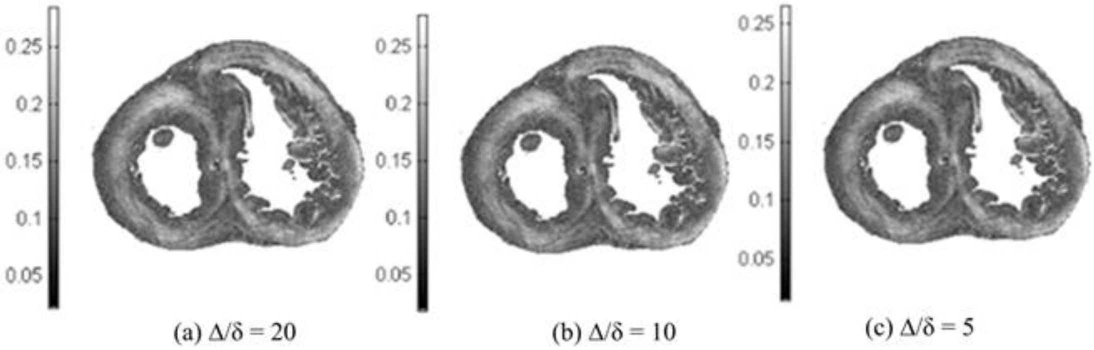

(a) Δ/δ = 20 (b) Δ/δ = 10 (c) Δ/δ = 5

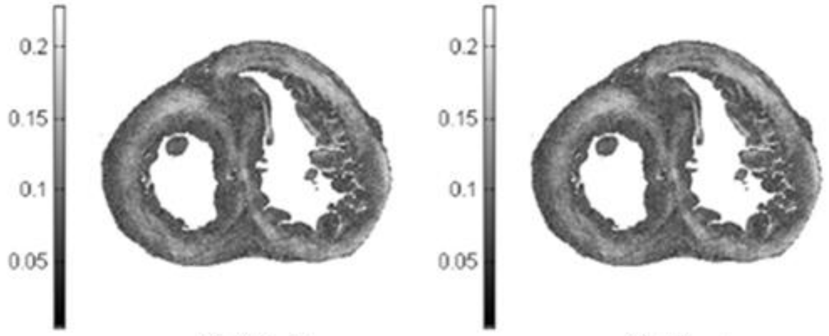

(d) Δ/δ = 2 (e) Δ/δ = 1

Fig. 6.8 Effects of ratio of diffusion time to gradient duration on DW images for high b-value imaging. Simulation parameters: Δ=50 ms, b = 4000 s/mm^2. For δ = 2.5, 5, 10, 25 and 50 ms, the used gradient strength are respectively 427,215,109,46 and 26 mT/m, the corresponding q-values are 45.5,45.8, 46.6,49.3 and 55.1 mm^{-1}.

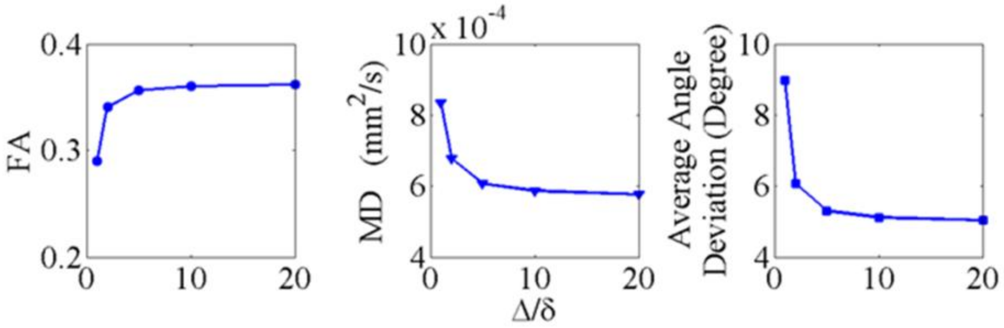

Fig. 6.9 Effects of Δ/δ on FA, MD and orientation deviation angle for high b-value imaging

Fig. 6.9 illustrates the effects of Δ/δ variation on FA, MD and orientation deviation angle for high b-value imaging. We can see that FA and MD have the same variation trends as that in low b-value imaging. But due to the influence of gradient strength, the FA value measured in high b-value imaging is smaller than that obtained in low b-value imaging, while for MD, it is in reverse. For the deviation angle, it changes from 5º to 9º when Δ/δ varies from 20 to 1. Thus, in high b-value imaging, the ratio of Δ/δ influences greatly the fiber orientation estimation accuracy.

6.2.4 Discussion

By comparing the simulated DW and diffusion tensor images with the ground-truth provided by PLI, the effects of imaging parameters on the diffusion image properties are evaluated. When the diffusion time increases, the image contrast is improved and the FA increases but MD decreases, which is consistent with the findings of [Nossin-Manor, 2005; Nilsson, 2009]. An appropriate choice of diffusion time should take into account the following factors: the apparent diffusion coefficient D of water molecules, the size of diffusion environment l and the additional attenuation caused by long echo time. The simulation results suggest that the diffusion time is not necessary to satisfy the condition of $\Delta >> l^2 / 2D$ which is mentioned in [Bar-Shir, 2008].

The diffusion gradient pulse strength and duration determine the q-value and b-value and as a result influence the DW image properties, especially for high b-value imaging used in the q-space formalism, in which the image data is usually acquired with a b-value of 3000 or 4000 s/mm^2. According to the relationship between b-value and q-value given by Eq.(6.2), a high b-value requires either a high q-value or a long diffusion time. As we elaborated, in actual dMRI acquisitions, increasing the diffusion time leads to the increment of echo time and subsequently induces more signal attenuation caused by T_2 relaxation. Meanwhile, the diffusion signal intensity drops quickly with increment of q-value. This implies that the diffusion image intensity will definitely drop no matter which parameter we choose to increase. Therefore, making a reasonable compromise between q-values and diffusion time in high b-value imaging is necessary. In comparison with the DW images obtained with different q-values in Fig. 6.3, it can be seen that the image quality is better when the q-value ranges from 20 to 30 mm^{-1}. To get a b-value of more than 3000, for a q-value of 20 mm^{-1}, the diffusion time should be greater than 200 ms, and for a q-value of 30 mm^{-1}, the diffusion time is about 100 ms. Taking into account the influence of diffusion time, a q-value of 30 mm^{-1} and a diffusion time Δ of 100 ms should be the best choice for achieving a b-value of 3000 s/mm^2 in our case.

The requirement for a strong gradient strength in high q-value imaging introduces another problem. The gradient strength of current clinical MRI systems used for myocardium imaging ranges from 45 to 87 mT/m. Therefore, achieving a high q-value needs to increase the gradient pulse duration, which violates the assumption of short pulse duration made in dMRI analysis. As illustrated in Fig. 6.9, for $b = 4000\ \mathrm{s/mm^2}$, $\Delta = 50$ ms, and Δ/δ =1, which corresponds to a long pulse duration, the deviation angle between simulated cardiac fiber orientation and PLI measurement is about 9º instead of 3° obtained in case $b = 4000\ \mathrm{s/mm^2}$, $\Delta = 50$ ms, and Δ/δ =20. Note that this result was obtained in the absence of noise and artifacts. In practical acquisitions, more errors could be introduced, which may increase the deviation angle beyond 9°. To reduce the deviation angle while obtaining high b-values, increasing diffusion time will then be another choice. For instance, if diffusion time is increased to 100 ms, a b-value of more than 3000 can then be achieved by using a δ of 10 ms and a gradient strength of about 80 mT/m. This results in a Δ/δ ratio of 10, which does not influence greatly the accuracy of fiber orientation estimation.

The above optimized imaging parameters are predicted for a given cardiac fiber architecture. However, when the cardiac fiber structure changes due to diseases, the imaging parameters should change accordingly. Since there is a relationship between the q-value and the myocyte dimension, the q-space dMRI could be extremely sensitive to the pathological state of the myocardium.

Our dMRI simulation model provides a valuable tool for evaluating the effects of imaging parameters on diffusion properties based on the ground-truth given by PLI. For a given structure, this simulation model enables us to optimize the imaging parameters. However, up to now, this model does not consider the influence of the gradient ramp time and the k-space encoding gradients including the slice selection, phase encoding and frequency encoding. In the following paragraphs, the simulation theory will be improved based on the real dMRI acquisition sequences and the effects of pulse sequence parameters will subsequently be analyzed.

6.3 Influence of practical diffusion gradient pulse parameters

In our previous simulation, we assumed that the diffusion signal is only induced by the displacement performed by water molecules during the diffusion time. However, during the entire imaging period, from the beginning of RF pulse excitation to the acquisition moment, the diffusion of water molecules is always present and therefore all the gradients contribute to the diffusion-weighted signal. Thus in this section, we analyze the influence of the parameters of each gradient involved in practical diffusion imaging pulse sequence on the properties of diffusion images. Here, we choose the most commonly used sequence: spin echo (SE), as shown in Fig. 6.10, **to provide a first study of the influences of practical imaging sequence parameters on the resulting diffusion image properties**.

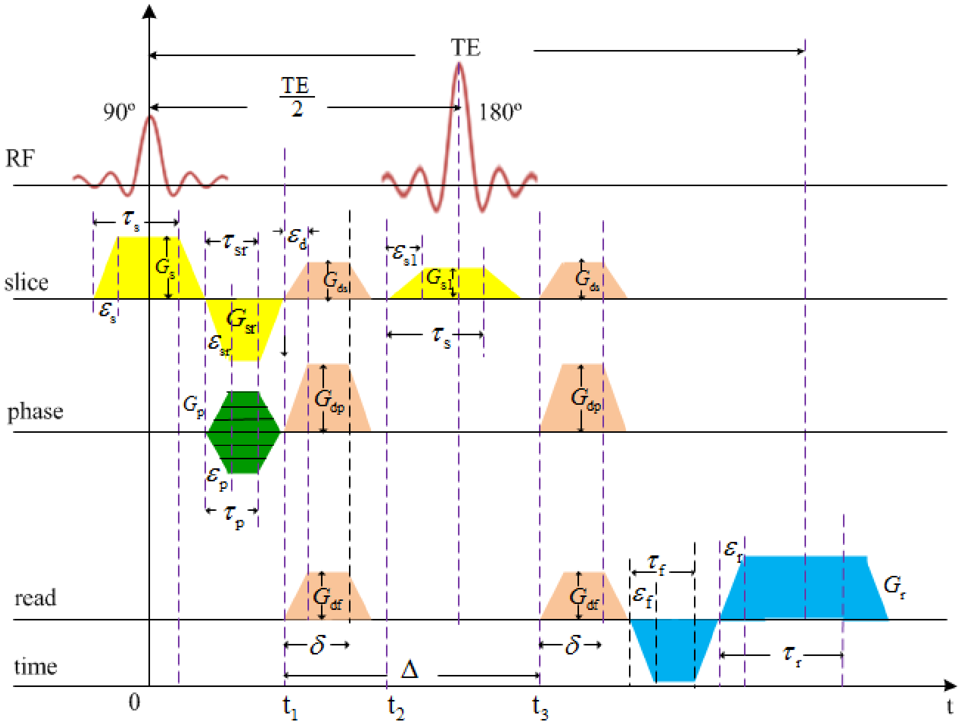

Fig. 6.10 Spin Echo (SE) sequence for diffusion imaging. It consists of: a slice selection gradient with a strength of G_s, a duration of τ_s and a ramp time of ε_s; a slice refocusing gradient with strength G_{sr}, duration τ_{sr} and ramp time ε_{sr}; a phase encoding gradient whose strength is G_p, duration is τ_p and ramp time is ε_p; the diffusion gradients along three imaging encoding directions with strength of G_{ds}, G_{dp} and G_{dr} respectively, duration of δ and ramp time of ε_d; a 180° RF reverse pulse with a duration of τ_s and a ramp time of ε_{sl}; a readout (frequency encoding) gradient G_r, which has a duration of τ_r and a ramp time of ε_r; a readout refocusing gradient G_f with duration τ_f and ramp time ε_f.

6.3.1 The improved simulation theory

Calculation of dMRI signal with the classical Stejskal-Tanner equation [Stejskal, 1965] has been well known and widely used in diffusion image analysis. However, it overlooked the effects of k-space encoding gradients on diffusion properties because compared to the diffusion gradient, the amplitude of k-space encoding gradients (slice selection, phase encoding and readout gradients) are so small. However, with the development of MRI devices and the requirement for high image spatial resolutions, the amplitude of the k-space encoding gradients could be the same and even higher than that of diffusion gradient. Thus, in this situation, the influence of the k-space encoding gradients must be taken into account. Considering the current two significant imaging modalities DTI and q-space imaging, the diffusion signal accounting for all the gradients is analyzed in the following paragraphs in two manners: b-value and q-value interpretations.

1) b-value interpretation

According to the Stejskal-Tanner equation, the diffusion signal detected at time t is

$$s(t) = s_0 \exp(-b\underline{\underline{D}}) \tag{6.4}$$

where s_0 is the signal detected in the absence of the diffusion gradient, D is the diffusion coefficient of the water molecules in the tissue under investigation, and b is the parameter related to the all the gradients used in the pulse sequence and is defined as [Price, 1997, 1998]

$$b = \gamma^2 \int_0^{TE} \left(\int_0^t \vec{G}(t)dt'\right)^2 dt \tag{6.5}$$

with TE echo time, $\vec{G}(t)$ all the gradients used in the experiments, and γ the gyromagnetic ratio. In this work, the coordinate reference being chosen along the slice selection gradient, phase encoding gradient and read out gradient directions, the gradient $\vec{G}(t)$ can be written as

$$\vec{G}(t) = G_{sl}(t)\vec{s} + G_{pe}(t)\vec{p} + G_{ro}(t)\vec{r} \tag{6.6}$$

It implies that, actually the b parameter given in Eq. (6.5) is not a scalar value but a matrix because the gradient is a vector. Generally, the b-value usually mentioned in the literatures is in fact the trace of such b matrix, namely

$$b = b_{pe} + b_{ro} + b_{sl} \tag{6.7}$$

where b_{pe} is the parameter related to the gradient along the phase encoding direction, b_{sl} along the slice selection direction, and b_{ro} along the read out direction.

Indeed, if we define $\vec{F}(t)$ as

$$\vec{F}(t) = \int_0^t \vec{G}(t)dt' \tag{6.8}$$

Then the b-matrix corresponding to Eq. (6.5) could be written as

$$b = \gamma^2 \int_0^{TE} \vec{F}(t)\vec{F}^T(t)dt \tag{6.9}$$

Accordingly, b_{sl}, b_{pe} and b_{ro} are calculated by

$$b_{sl} = \gamma^2 \int_0^{TE} (F_{sl}(t))^2 dt \tag{6.10}$$

$$b_{pe} = \gamma^2 \int_0^{TE} (F_{pe}(t))^2 dt \tag{6.11}$$

$$b_{ro} = \gamma^2 \int_0^{TE} (F_{ro}(t))^2 dt \tag{6.12}$$

In the spin-echo sequence shown in Fig. 6.10, the introduce of the 180° RF pulse will change the integration of $\vec{G}(t)$ and accordingly change the definition of $\vec{F}(t)$

$$\vec{F}(t) = \begin{cases} \int_0^t \vec{G}(t')dt' & 0 < t \le \frac{\mathrm{TE}}{2} \\ \int_0^t \vec{G}(t')dt' - \vec{F}(\frac{\mathrm{TE}}{2}) & \frac{\mathrm{TE}}{2} < t \le \mathrm{TE} \end{cases} \tag{6.13}$$

The detailed process to calculate $\vec{F}(t)$ is explained in the appendix. Generally, for spin-echo sequence, the amplitude of the slice refocusing gradient G_{sr} is equal to that of the slice selection gradient G_s, but the duration is half of latter. For exciting the same slice, as switching on the 180° RF pulse, one another slice selection gradient G_{s1} with half amplitude and twice duration of the first one is switched on. The readout gradient G_r and the frequency encoding gradient G_f are usually the same. Therefore, taking into account all of these factors and assuming that the slew rate for all the gradients in one system is the same, we will have the following relationship: $G_{\mathrm{sr}} = G_{\mathrm{s}}$, $G_{\mathrm{s1}} = G_{\mathrm{s}}/2$, $\epsilon_{\mathrm{s1}} = \epsilon_{\mathrm{s}}/2$, $\epsilon_{\mathrm{sr}} = \epsilon_{\mathrm{s}}$, $\tau_{\mathrm{sr}} = \tau_{\mathrm{s}}/2$, $\tau_{\mathrm{s1}} = \tau_{\mathrm{s}}$, $G_f = G_r$, $\epsilon_f = \epsilon_r$ and $\tau_f = \tau_r/2$, and accordingly the b-value can be calculated. The detailed calculation process is given in appendix.

$$\begin{aligned} b_{sl} = {} & \lambda^2 G_{\mathrm{ds}}^2 \left(\delta^2(\Delta - \frac{\delta}{3}) - \frac{1}{6}\delta\epsilon^2 + \frac{1}{30}\epsilon^3 \right) + \frac{1}{48}\lambda^2 \delta G_{\mathrm{ds}} G_s \left(\epsilon^2 + 12\tau_s^2 \right) \\ & + \frac{1}{1920} G_s^2 \lambda^2 \left(49\epsilon^3 - 160\epsilon^2\tau_s + 480\epsilon\tau_s^2 + 200\tau_s^3 \right) \end{aligned} \tag{6.14}$$

$$\begin{aligned} b_{pe} = {} & \lambda^2 G_{\mathrm{dp}}^2 \left(\delta^2(\Delta - \frac{\delta}{3}) - \frac{1}{6}\delta\epsilon^2 + \frac{1}{30}\epsilon^3 \right) + 2\lambda^2 \delta\Delta G_{\mathrm{dp}} G_p \tau_p \\ & + \frac{1}{60}\lambda^2 G_p^2 \left(\epsilon^3 - 5\epsilon^2\tau_p + 30\tau_p^2 \left(\delta + \Delta + 2\epsilon + TE \right) + 20\tau_p^3 \right) \end{aligned} \tag{6.15}$$

$$\begin{aligned} b_{ro} = {} & \gamma^2 [G_{\mathrm{df}}^2 \left(\delta^2(\Delta - \frac{\delta}{3}) - \frac{1}{6}\delta\epsilon^2 + \frac{1}{30}\epsilon^3 \right) \\ & + \frac{1}{120} G_r^2 \left(123\epsilon^3 - 70\epsilon^2\tau_r + 10\tau_r^3 \right)] \end{aligned} \tag{6.16}$$

$$b_{sr} = -\frac{1}{30}\gamma^2 G_{\mathrm{df}} G_{\mathrm{ds}} (10\delta^3 - 30\delta^2\Delta + 5\delta\epsilon^2 - \epsilon^3) + \frac{1}{96}\gamma^2 G_{\mathrm{df}} G_s \delta\left(\epsilon^2 + 12\tau_s^2\right) \tag{6.17}$$

$$\begin{aligned} b_{rp} = &-\frac{1}{30}\gamma^2 G_{\mathrm{df}} G_{\mathrm{dp}} (10\delta^3 - 30\delta^2\Delta + 5\delta\epsilon^2 - \epsilon^3) \\ &+\gamma^2 G_{\mathrm{df}} G_p \delta\Delta\tau_p - \frac{1}{24}\gamma^2 G_p G_r \tau_p \left(25\epsilon^2 - 6\tau_r^2\right) \end{aligned} \tag{6.18}$$

$$\begin{aligned} b_{sp} = &\frac{1}{30}\gamma^2 G_{\mathrm{dp}} G_{\mathrm{ds}} \left(-10\delta^2(\delta - 3\Delta) - 5\delta\epsilon^2 + \epsilon^3\right) \\ &+\frac{1}{96}\gamma^2 G_{\mathrm{dp}} G_s \delta\left(\epsilon^2 + 12\tau_s^2\right) + G_p G_{\mathrm{ds}} \delta\Delta\tau_p \\ &+\frac{G_p G_s}{480}(-8\epsilon^3 + 25\epsilon^2\tau_p - 40\epsilon\tau_p^2 + 10\epsilon^2\tau_s + 40\epsilon\tau_p\tau_s - 10\epsilon\tau_s^2 + 60\tau_p\tau_s^2 + 10\tau_s^3) \end{aligned} \tag{6.19}$$

$$\begin{aligned} b &= b_{sl} + b_{pe} + b_{ro} \\ &= \gamma^2 \left\{ G_{\mathrm{d}}^2 \left(\delta^2(\Delta - \frac{\delta}{3}) - \frac{1}{6}\delta\epsilon^2 + \frac{1}{30}\epsilon^3 \right) \right. \\ &\quad +2\delta\Delta G_{\mathrm{dp}} G_p \tau_p + \frac{1}{48}\delta G_{\mathrm{ds}} G_s \left(\epsilon^2 + 12\tau_s^2\right) \\ &\quad +\frac{1}{60} G_p^2 \left(\epsilon^3 - 5\epsilon^2\tau_p + 30\tau_p^2\left(\delta + \Delta + 2\epsilon + TE\right) + 20\tau_p^3\right) \\ &\quad +\frac{1}{120} G_r^2 \left(123\epsilon^3 - 70\epsilon^2\tau_r + 10\tau_r^3\right) \\ &\quad \left. +\frac{1}{1920} G_s^2 \left(49\epsilon^3 - 160\epsilon^2\tau_s + 480\epsilon\tau_s^2 + 200\tau_s^3\right) \right\} \end{aligned} \tag{6.20}$$

where G_d is the amplitude of the diffusion gradient, G_{df}, G_{ds} and G_{dp} are the projections of the diffusion gradient on respectively the frequency encoding, slice selection and phase encoding directions. G_s, G_p and G_r are respectively the amplitudes of slice selection gradient, phase encoding gradient and read out gradient. τ_s, τ_p and τ_r correspond to their durations. Δ is the diffusion time and δ is the duration of the diffusion gradient. ϵ is the ramp time of all the gradients.

From the formula of the b value, it can be seen that not only the diffusion gradient weights the diffusion but also the imaging gradients including G_s, G_p and G_r. Thus the expression of b-value can be divided into three parts. The first is related to the diffusion gradient and called b_{diff}, the second one to the imaging gradients (G_s, G_p and G_r) and is named $b_{imaging}$, and the last one to the common contribution of the above two kinds of gradients we called b_{cross}. For the spin-echo sequence used here, their expressions are given as follows

$$b_{diffu} = \gamma^2 G_{\mathrm{d}}^2 \left(\delta^2 (\Delta - \frac{\delta}{3}) - \frac{1}{6}\delta\epsilon^2 + \frac{1}{30}\epsilon^3 \right) \tag{6.21}$$

$$\begin{aligned} b_{imaging} = \gamma^2 \Big\{ & \frac{1}{60} G_p^2 \left(\epsilon^3 - 5\epsilon^2 \tau_p + 20\tau_p^3 + 30\tau_p^2 \left(\delta + \Delta + TE + 2\epsilon \right) \right) \\ & + \frac{1}{120} G_r^2 \left(123\epsilon^3 - 70\epsilon^2 \tau_r + 10\tau_r^3 \right) \\ & + \frac{1}{1920} G_s^2 \left(49\epsilon^3 - 160\epsilon^2 \tau_s + 480\epsilon\tau_s^2 + 200\tau_s^3 \right) \Big\} \end{aligned} \tag{6.22}$$

$$b_{cross} = \gamma^2 (2\delta\Delta G_{\mathrm{dp}} G_p \tau_p + \frac{1}{48}\delta G_{\mathrm{ds}} G_s \left(\epsilon^2 + 12\tau_s^2 \right)) \tag{6.23}$$

According to Eq.(6.4), before applying the diffusion gradient, the signal acquired is

$$s_1(t) = s_0 \exp(-b_{imaging})\underline{\underline{D}} \tag{6.24}$$

With the presence of the diffusion gradient, the signal detected becomes

$$s_2(t) = s_0 \exp(-b_{imaging} - b_{cross} - b_{diffu})\underline{\underline{D}} \tag{6.25}$$

Thus, the signal that we are actually dealing with for analyzing diffusion anisotropy can be expressed as

$$E(t) = \frac{s_2(t)}{s_1(t)} = \exp(-b_{diffu} - b_{cross})\underline{\underline{D}} \tag{6.26}$$

However, the signal $E_0(t)$ we usually find in the literatures is given by

$$E_0(t) = \exp(-b_0)\underline{\underline{D}} \tag{6.27}$$

with

$$b_0 = \gamma^2 G_d^2 \delta^2 (\Delta - \frac{\delta}{3}) \tag{6.28}$$

Then, the difference between the actually measured signal and the usually employed signal can be described by the ratio

$$E = \frac{E(t)}{E_0(t)} = \exp[(-b_{diffu} - b_{cross} + b_0)\underline{\underline{D}}] \tag{6.29}$$

From Eq.(6.29), it can be seen that the signal difference depends on the b_{cross} value, which reflects the interaction of imaging gradients and diffusion gradient. It also depends on the ramp time of the gradients. For this reason, in our simulation, the influence of b_{cross} and the ramp time is analyzed.

2) q-value interpretation

All of MRI theory can be understood as the effects of gradients on the precession frequency of spins. If at time t', applying an additional spatially dependent magnetic field gradient $\vec{G}(t')$, the precession frequency of a spin located at the position $\vec{r}(t')$ becomes

$$\omega(t') = \omega_0 + \gamma(\vec{G}(t') \cdot \vec{r}(t')) \tag{6.30}$$

where ω_0 is the precession frequency of spins before adding the gradients. During the time interval t, the cumulative phase shift induced by a single spin is

$$\phi(t) = \int_0^t \omega(t') = \phi_0 + \int_0^t \gamma(\vec{G}(t') \cdot \vec{r}(t'))dt' \tag{6.31}$$

with $\phi_0 = \int_0^t \omega_0 dt$. In real experiments, it is impossible to detect the phase shift caused by only one single spin because it is too small compared to our imaging voxel size. Therefore, the phase shift measured by a MRI scanner is the ensemble-averaged one of all spins within that voxel. For SE sequence illustrated in Fig. 6.10, at time t_1, if the average position of the spins is $\vec{r}_1(t_1)$, the phase $\phi_1(t)$ accumulated is then given by

$$\phi_1(t_1) = \phi_0 + \vec{r}_1(t_1) \cdot \gamma \int_0^{t_1} \vec{G}(t')dt' \tag{6.32}$$

Similarly, at time t_2, the spins diffuse to the position of $\vec{r}_2(t_2)$ and the phase $\phi_2(t)$ accordingly becomes

$$\phi_2(t_2) = \phi_0 + \vec{r}_2(t_2) \cdot \gamma \int_0^{t_2} \vec{G}(t')dt' \tag{6.33}$$

Then, from time t_1 to t_2, the phase shift $\Delta\phi$ is

$$\Delta\phi(t_2 - t_1) = \vec{r}_2(t_2) \cdot \gamma \int_0^{t_2} \vec{G}(t')dt' - \vec{r}_1(t_1) \cdot \gamma \int_0^{t_1} \vec{G}(t')dt' \tag{6.34}$$

Defining

$$\vec{q}(t) = \begin{cases} \gamma \int_0^t \vec{G}(t')dt' & 0 < t \le \dfrac{\mathrm{TE}}{2} \\ \gamma \int_0^t \vec{G}(t')dt' - \vec{q}(\frac{\mathrm{TE}}{2}) & \dfrac{\mathrm{TE}}{2} < t \le \mathrm{TE} \end{cases} \tag{6.35}$$

Then Eq.(6.34) becomes

$$\Delta\phi(t_2 - t_1) = \vec{q}(\mathrm{t}_2) \cdot \vec{r}_2(t_2) - \vec{q}(\mathrm{t}_1) \cdot \vec{r}_1(t_1) \tag{6.36}$$

For the SE sequence used in Fig. 6.10, $t_2 - t_1$ ranges from 0 to TE, thus the total phase shift is

$$\Delta\phi = \int_0^{TE} [\vec{q}(\mathrm{t+t}_1) \cdot \vec{r}_2(t + t_1) - \vec{q}(\mathrm{t}_1) \cdot \vec{r}_1(t_1)]dt \tag{6.37}$$

At the end of the echo time, the signal attenuated by the phase shift is

$$s_2(t) = s_0 \exp(-\Delta\phi) \tag{6.38}$$

where s_0 is the MRI signal intensity without considering the diffusion. It is obvious that the phase shift is related to the q-value that depends on gradients switched on during the acquisition. Before applying the diffusion gradient, the phase shift caused by the imaging gradients is given by $\Delta\phi_{imaging}$.

$$\Delta\phi_{imaging} = \int_0^{TE} [\vec{q}_{imaging}(\mathrm{t+t_1}) \cdot \vec{r}2(t+t_1) - \vec{q}_{imaging}(\mathrm{t_1}) \cdot \vec{r}1(t_1)]dt \tag{6.39}$$

At this moment, the signal detected is

$$s_1(t) = s_0 \exp(-\Delta\phi_{imaging}) \tag{6.40}$$

Therefore, the signal finally used for analyzing diffusion anisotropy is

$$E = \frac{s_2(t)}{s_1(t)} = \exp[(-\Delta\phi + \Delta\phi_{imaging})] \tag{6.41}$$

From Fig. 6.10, it can be seen that the q-value will change with time since the applied gradients vary during the echo time. For the SE sequence shown in Fig. 6.10, the q-values during the different time intervals along the three directions are given by Eq. (6.42), (6.43)and (6.44). The details about the derivations are provided in the appendix.

$$q_{pe}(t) = \begin{cases} 0 & 0 < t \le (\tau_s + \epsilon)/2 \\ \dfrac{\gamma G_p (2t + \epsilon - \tau_s)^2}{8\epsilon} & (\tau_s + \epsilon)/2 < t \le (\tau_s + 3\epsilon)/2 \\ \dfrac{1}{2}\gamma G_p (2t - \tau_s) & (\tau_s + 3\epsilon)/2 < t \le (\tau_s + \epsilon)/2 + \tau_p \\ -\dfrac{\gamma G_p \left(4\tau_p^2 + 4\tau_p(-2t + \epsilon + \tau_s) + (-2t + 3\epsilon + \tau_s)^2\right)}{8\epsilon} & (\tau_s + \epsilon)/2 + \tau_p < t \le (\tau_s + \epsilon)/2 + \tau_p + \epsilon \\ \dfrac{\gamma\left((2t + \delta + \Delta + \epsilon - 2\tau)^2 G_{\mathrm{dp}} + 8\epsilon G_p \tau_p\right)}{8\epsilon} & \tau - \Delta/2 - \epsilon/2 - \delta/2 < t \le \tau - \Delta/2 + \epsilon/2 - \delta/2 \\ \dfrac{1}{2}\gamma\left((2t + \delta + \Delta - 2\tau)G_{\mathrm{dp}} + 2G_p\tau_p\right) & \tau - \Delta/2 + \epsilon/2 - \delta/2 < t \le \tau - \Delta/2 - \epsilon/2 + \delta/2 \\ \dfrac{-\gamma\left(\left(4t^2 + \delta^2 - 2\delta(\Delta + 3\epsilon - 2\tau) + (-\Delta + \epsilon + 2\tau)^2 - 4t(\delta - \Delta + \epsilon + 2\tau)\right)G_{\mathrm{dp}} - 8\epsilon G_p \tau_p\right)}{8\epsilon} & \tau - \Delta/2 - \epsilon/2 + \delta/2 < t \le \tau - \Delta/2 + \epsilon/2 + \delta/2 \\ \gamma\left(\delta G_{\mathrm{dp}} + G_p\tau_p\right) & \tau - \Delta/2 + \epsilon/2 + \delta/2 < t \le \frac{TE}{2} \\ -\gamma\left(\delta G_{\mathrm{dp}} + G_p\tau_p\right) & \frac{TE}{2} < t \le \tau + \Delta/2 - \epsilon/2 - \delta/2 \\ \dfrac{\gamma\left(\left(4t^2 + \delta^2 + 4t(\delta - \Delta + \epsilon - 2\tau) + (\Delta - \epsilon + 2\tau)^2 - 2\delta(\Delta + 3\epsilon + 2\tau)\right)G_{\mathrm{dp}} - 8\epsilon G_p \tau_p\right)}{8\epsilon} & \tau + \Delta/2 - \epsilon/2 - \delta/2 < t \le \tau + \Delta/2 + \epsilon/2 - \delta/2 \\ \dfrac{1}{2}\gamma\left((2t - \delta - \Delta - 2\tau)G_{\mathrm{dp}} - 2G_p\tau_p\right) & \tau + \Delta/2 + \epsilon/2 - \delta/2 < t \le \tau + \Delta/2 - \epsilon/2 + \delta/2 \\ -\dfrac{\gamma\left((-2t + \delta + \Delta + \epsilon + 2\tau)^2 G_{\mathrm{dp}} + 8\epsilon G_p\tau_p\right)}{8\epsilon} & \tau + \Delta/2 - \epsilon/2 + \delta/2 < t \le \tau + \Delta/2 + \epsilon/2 + \delta/2 \\ -\gamma G_p \tau_p & \tau + \Delta/2 + \epsilon/2 + \delta/2 < t \le \mathrm{TE} \end{cases} \tag{6.42}$$

$$q_{sl}(t)=\begin{cases} t\gamma G_s & 0<t\le(\tau_s-\epsilon_s)/2 \\ -\dfrac{\gamma G_s\left((-2t+\epsilon)^2-2(2t+\epsilon)\tau_s+\tau_s^2\right)}{8\epsilon} & (\tau_s-\epsilon_s)/2<t\le(\tau_s+\epsilon_s)/2 \\ -\dfrac{\gamma G_s\left((-2t+\epsilon)^2-2(2t+\epsilon)\tau_s+\tau_s^2\right)}{8\epsilon} & (\tau_s+\epsilon_s)/2<t\le(\tau_s+\epsilon_s)/2+\epsilon_s \\ \gamma G_s(-t+\epsilon+\tau_s) & (\tau_s+\epsilon_s)/2+\epsilon_s<t\le(\tau_s+\epsilon_s)/2+\tau_s/2+\epsilon_s \\ \dfrac{\gamma G_s(-2t+3\epsilon+2\tau_s)^2}{8\epsilon} & (\tau_s+\epsilon_s)/2+\tau_s/2+\epsilon_s<t\le(\tau_s+\epsilon_s)/2+\tau_s/2+2\epsilon_s \\ 0 & (\tau_s+\epsilon_s)/2+\tau_s/2+2\epsilon_s<t\le \mathrm{t}_1 \\ \dfrac{\gamma G_{ds}(2t+\delta+\Delta-\mathrm{TE}+\epsilon)^2}{8\epsilon} & \mathrm{t}_1<t\le t_1+\epsilon_d \\ \dfrac{1}{2}(2t+\delta+\Delta-\mathrm{TE})G_{ds} & \mathrm{t}_1+\epsilon_d<t\le \mathrm{t}_1+\delta \\ -\dfrac{\gamma\left(4t^2+\delta^2-2\delta(\Delta+3\epsilon-\mathrm{TE})+(-\Delta+\epsilon+\mathrm{TE})^2-4t(\delta-\Delta+\epsilon+\mathrm{TE})\right)G_{ds}}{8\epsilon} & \mathrm{t}_1+\delta<t\le \mathrm{t}_1+\delta+\epsilon_d \\ \gamma\delta G_{ds} & \mathrm{t}_1+\delta+\epsilon_d<t\le \mathrm{t}_2 \\ \dfrac{\gamma\left(32\delta\epsilon G_{ds}+G_s(4t+\epsilon-2\mathrm{TE}+2\tau_s)^2\right)}{32\epsilon} & \mathrm{t}_2<t\le \mathrm{t}_2+\epsilon_s \\ \dfrac{1}{4}\gamma\left(4\delta G_{ds}+G_s(2t-\mathrm{TE}+\tau_s)\right) & \mathrm{t}_2+\epsilon_s<t<\dfrac{\mathrm{TE}}{2} \\ -\dfrac{1}{4}\gamma\left(4\delta G_{ds}+G_s(-2t+\mathrm{TE}+\tau_s)\right) & \dfrac{\mathrm{TE}}{2}<t\le \mathrm{t}_2+\tau_s \\ -\dfrac{\gamma\left(32\delta\epsilon G_{ds}+G_s(-4t+\epsilon+2\mathrm{TE}+2\tau_s)^2\right)}{32\epsilon} & \mathrm{t}_2+\tau_s<t\le \mathrm{t}_2+\tau_s+\epsilon_s \\ -\gamma\delta G_{ds} & \mathrm{t}_2+\tau_s+\epsilon_s<t\le \mathrm{t}_3 \\ \dfrac{\gamma\left(4t^2+\delta^2+4t(\delta-\Delta+\epsilon-\mathrm{TE})+(\Delta-\epsilon+\mathrm{TE})^2-2\delta(\Delta+3\epsilon+\mathrm{TE})\right)G_{ds}}{8\epsilon} & \mathrm{t}_3<t\le \mathrm{t}_3+\epsilon_d \\ \dfrac{1}{2}\gamma(2t-\delta-\Delta-\mathrm{TE})G_{ds} & \mathrm{t}_3+\epsilon_d<t\le \mathrm{t}_3+\delta \\ -\dfrac{\gamma(-2t+\delta+\Delta+\epsilon+\mathrm{TE})^2G_{ds}}{8\epsilon} & \mathrm{t}_3+\delta<t\le \mathrm{t}_3+\delta+\epsilon_d \\ 0 & \mathrm{t}_3+\delta+\epsilon_d<t\le\mathrm{TE} \end{cases} \tag{6.43}$$

$$q_{ro}(t)=\begin{cases} 0 & 0<t\le(TE-\Delta-\delta-\epsilon)/2 \\ \dfrac{\gamma(2t+\delta+\Delta+\epsilon-\mathrm{TE})^2G_{\mathrm{df}}}{8\epsilon} & (TE-\Delta-\delta-\epsilon)/2<t\le(TE-\Delta-\delta+\epsilon)/2 \\ \dfrac{1}{2}\gamma\left((2t+\delta+\Delta-\mathrm{TE})G_{\mathrm{df}}+G_r\tau_r\right) & (TE-\Delta-\delta+\epsilon)/2<t\le(TE-\Delta+\delta-\epsilon)/2 \\ -\dfrac{\gamma\left(4t^2+\delta^2-2\delta(\Delta+3\epsilon-TE)+(-\Delta+\epsilon+TE)^2-4t(\delta-\Delta+\epsilon+TE)\right)G_{\mathrm{df}}}{8\epsilon} & (TE-\Delta+\delta-\epsilon)/2<t\le(TE-\Delta+\delta+\epsilon)/2 \\ \gamma\delta G_{\mathrm{df}} & (TE-\Delta+\delta+\epsilon)/2<t\le\frac{\mathrm{TE}}{2} \\ -\gamma\delta G_{\mathrm{df}} & \frac{\mathrm{TE}}{2}<t\le(TE+\Delta-\delta-\epsilon)/2 \\ \dfrac{\gamma\left(4t^2+\delta^2+4t(\delta-\Delta+\epsilon-TE)+(\Delta-\epsilon+TE)^2-2\delta(\Delta+3\epsilon+TE)\right)G_{\mathrm{df}}}{8\epsilon} & (TE+\Delta-\delta-\epsilon)/2_3<t\le(TE+\Delta-\delta+\epsilon)/2 \\ \dfrac{1}{2}\gamma(2t-\delta-\Delta-TE)G_{\mathrm{df}} & (TE+\Delta-\delta+\epsilon)/2<t\le(TE+\Delta+\delta-\epsilon)/2 \\ -\dfrac{\gamma(-2t+\delta+\Delta+\epsilon+TE)^2G_{\mathrm{df}}}{8\epsilon} & (TE+\Delta+\delta-\epsilon)/2<t\le(TE+\Delta+\delta+\epsilon)/2 \\ 0 & (TE+\Delta+\delta+\epsilon)/2<t\le(TE-3\epsilon/2-\tau_r) \\ -\dfrac{\gamma G_r(2t+3\epsilon-2TE+2\tau_r)^2}{8\epsilon} & (TE-3\epsilon/2-\tau_r)<t\le(TE-\epsilon/2-\tau_r) \\ -\gamma G_r(t+\epsilon-TE+\tau_r) & (TE-\epsilon/2-\tau_r)<t\le(TE-3\epsilon/2-\tau_r/2) \\ \dfrac{\gamma G_r\left(4t^2+13\epsilon^2+4t(3\epsilon-2TE)-24\epsilon\tau+4TE^2+2(2t+\epsilon-2TE)\tau_r+\tau_r^2\right)}{8\epsilon} & (TE-3\epsilon/2-\tau_r/2)<t\le(TE-\epsilon/2-\tau_r/2) \\ \dfrac{\gamma G_r\left(4t^2+9\epsilon^2+4t(\epsilon-2TE)-8\epsilon\tau+4TE^2+(4t-2(\epsilon+2TE))\tau_r+\tau_r^2\right)}{8\epsilon} & (TE-\epsilon/2-\tau_r/2)<t\le(TE+\epsilon/2-\tau_r/2) \\ \gamma(t+\epsilon-TE)G_r & (TE+\epsilon/2-\tau_r/2)<t\le TE \end{cases} \tag{6.44}$$

However, in traditional q-space imaging, q-value was defined only by the parameters of the diffusion gradient

$$\vec{q}_0 = \gamma \vec{G}_d \delta \tag{6.45}$$

The phase shift during the diffusion time Δ is

$$\Delta\phi_0 = \int_0^{\Delta} \vec{q}_0 \cdot \vec{r}(t) dt \tag{6.46}$$

Accordingly, the signal is expressed by

$$E_0 = \exp[-\Delta\phi_0] \tag{6.47}$$

Comparing Eqs. (6.41) and (6.47) leads us to analyze the influence of imaging gradients on the diffusion image properties by means of the new simulation theory described in the following section. We use the time-varying q-values to weight the displacements of water molecules, from which the phase shift caused by the diffusion and the corresponding diffusion signal can be calculated.

6.3.2 Monte-Carlo simulation with experimental gradient pulses

A three-dimensional Monte-Carlo simulation in the cardiac fiber model is performed using a random walking method to mimic the diffusion behavior of water molecules. Collisions of water molecules with the surface of fibers is described by reflection and permeability model, which means that if the penetration is allowed, the water molecule will pass through the membrane and diffuse with another velocity which depends on the diffusion coefficient therein. Otherwise, after the collision, the molecule will change the direction and go on walking. According to the principle of dMRI, the cardiac fiber structure information is derived from the displacement of water molecules, and the displacement can be translated to MR signals by using several kinds of gradient pulses. In our previous study, we assumed that the strength of k-space encoding gradients is so small compared to the diffusion gradient that it can be overlooked in the simulation, and we also thought that the diffusion gradient pulse duration is so short ($\delta \ll \Delta$) that the movement of water molecules during this time interval can be ignored. However, in real dMRI acquisitions, especially in high b-value imaging, the absence of diffusion gradient pulse with strong intensity is usually compensated by long pulse duration δ, which violates completely our assumption so that the influence of these parameters can no longer be overlooked.

According to Eq.(6.34), the phase shift of spin i caused by one random walking step j can be described by

$$\phi_i^j(t) = \vec{q}_j(t) \cdot \vec{r}_i^{\,j}(t) - \vec{q}_{j-1}(t) \cdot \vec{r}_i^{\,j-1}(t) \tag{6.48}$$

which depends not only on the position of the spin before and after the random walk ($\vec{r}_i^{\,j-1}(t)$ and $\vec{r}_i^{\,j}(t)$), but also on the local q-values $\vec{q}_{j-1}(t)$ and $\vec{q}_j(t)$. For convenience, we project the vector $\vec{q}$ and the position vector $\vec{r}$ onto the slice-selection, phase encoding and frequency encoding directions. Eq. (6.48) can then be rewritten as

$$\phi_i^j(t) = \phi_{sl,i}^j(t) + \phi_{pe,i}^j(t) + \phi_{ro,i}^j(t) \tag{6.49}$$

where

$$\phi_{sl,i}^j(t) = \vec{q}_{sl,j}(t) \cdot \vec{r}_{sl,i}^{\,j}(t) - \vec{q}_{sl,(j-1)}(t) \cdot \vec{r}_{sl,i}^{\,j-1}(t) \tag{6.50}$$

$$\phi_{pe,i}^j(t) = \vec{q}_{pe,j}(t) \cdot \vec{r}_{pe,i}^{\,j}(t) - \vec{q}_{pe,(j-1)}(t) \cdot \vec{r}_{pe,i}^{\,j-1}(t) \tag{6.51}$$

$$\phi_{ro,i}^j(t) = \vec{q}_{ro,j}(t) \cdot \vec{r}_{ro,i}^{\,j}(t) - \vec{q}_{ro,(j-1)}(t) \cdot \vec{r}_{ro,i}^{\,j-1}(t) \tag{6.52}$$

If during the acquisition time, the total number of random walks is ns, the phase shift accumulated by the spin i is

$$\Phi_i = \sum_{j=1}^{ns} \phi_i^j(t) = \sum_{j=1}^{ns} (\phi_{sl,i}^j(t) + \phi_{pe,i}^j(t) + \phi_{ro,i}^j(t)) \tag{6.53}$$

If there are np spins involved in the simulation, the average phase shift is

$$\Phi = \sum_{i=1}^{np} \Phi_i = \frac{1}{np} \sum_{i=1}^{np} \sum_{j=1}^{ns} \phi_i^j(t) = \frac{1}{np} \sum_{i=1}^{np} \sum_{j=1}^{ns} (\phi_{sl,i}^j(t) + \phi_{pe,i}^j(t) + \phi_{ro,i}^j(t)) \tag{6.54}$$

For a given pulse sequence, q value was fixed by Eq.(6.42), (6.43) and (6.44). Thus, what we require is to track the trajectory of the spins. At $t = 0$, the spins are distributed evenly in the cardiac fiber structure model. The initial position of spin i is recorded as $\vec{r}_{i0}$. Assuming that the time interval for each random walk j is τ, based on the Einstein equation, the walking displacement of molecule i during the time interval τ is given by:

$$\vec{s}_i^{\,j} = \sqrt{6D\tau} \tag{6.55}$$

where D is the diffusion coefficient of the tissues under investigation.
Thus after the j^{th} walking steps, the position of the spins is

$$\vec{r}_i^{\,j} = \vec{r}_i^{\,j-1} + \vec{s}_i^{\,j} \tag{6.56}$$

If expressed in the coordinate reference, the location $\vec{r}_i^{\,j}$ becomes

$$r_{sl,i}^j = r_{sl,i}^{j-1} + s_{sl,i}^j \tag{6.57}$$

$$r_{pe,i}^j = r_{pe,i}^{j-1} + s_{pe,i}^j \tag{6.58}$$

$$r_{ro,i}^j = r_{ro,i}^{j-1} + s_{ro,i}^j \tag{6.59}$$

After each walking step, we use Eq.(6.48) and (6.49) to calculate the phase shift. At the end of the echo time, the diffusion signal in the different directions can be derived from Eq. (6.41).

In order to assess the influence of the imaging and diffusion gradient parameters on diffusion properties in high-b-value imaging, we simulate and analyze, in the following sections, the DW images, diffusion tensor images, FA and MD.

6.3.3 Effects of diffusion time on diffusion properties

As we mentioned, for reflecting the structure of tissues in which diffusion happens, the diffusion distance performed by the spins must be longer or comparable to the size of the tissues, which means the diffusion time Δ should satisfy the following relationship

$$\Delta \geq l^2 / 2D \tag{6.60}$$

where l is the size of the myocyte and D is the diffusion coefficient of water molecules therein. In this work, the minimum size of the myocyte is 10 µm and the diffusion coefficient of water molecules therein is 0.001 mm^2/s. Thus the appropriate diffusion time should be larger than 200 ms. In order to avoid the influence of other parameters such as the gradient pulse duration and ramp time, the duration of one random walk step is chosen as 2.1 ms, gradient pulse duration as 2 ms and the diffusion gradient ramp time as 0.25 ms. In other words, we volonteerly ignore the motion of water molecules during the gradient pluse duration and the gradient ramp time. The diffusion time involved in this simulation ranges from 64 to 208 ms which correspond to the diffusion gradient amplitude of 407 (maximum) and 225 mT/m (minimum) for a b-value of 3000 s/mm^2. The diffusion gradient amplitude is adjusted by applying three gradients with the same amplitude along slice selection, phase encoding and readout directions. For instance, to get a gradient amplitude of 407 mT/m, the gradients with amplitude of 235 mT/m are switched on simultaneously along the above three different directions. The simulation results using different diffusion time are given in Fig. 6.11.

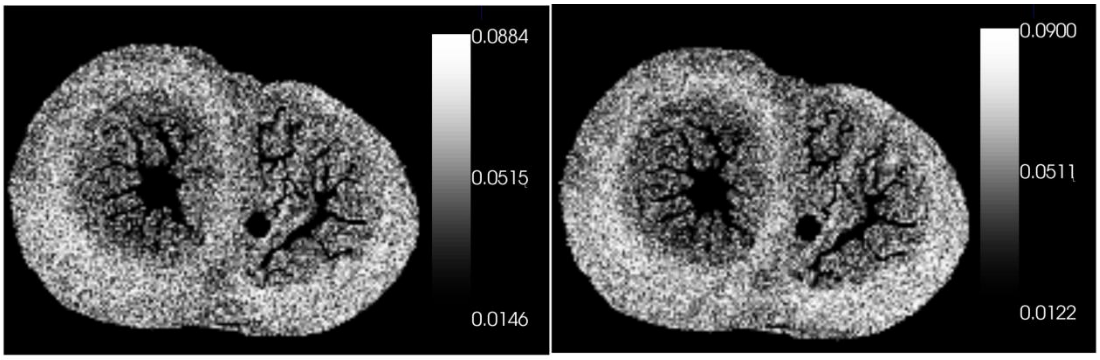

$\Delta = 64$ms, δ=2ms $\Delta = 80$ms, δ=2ms

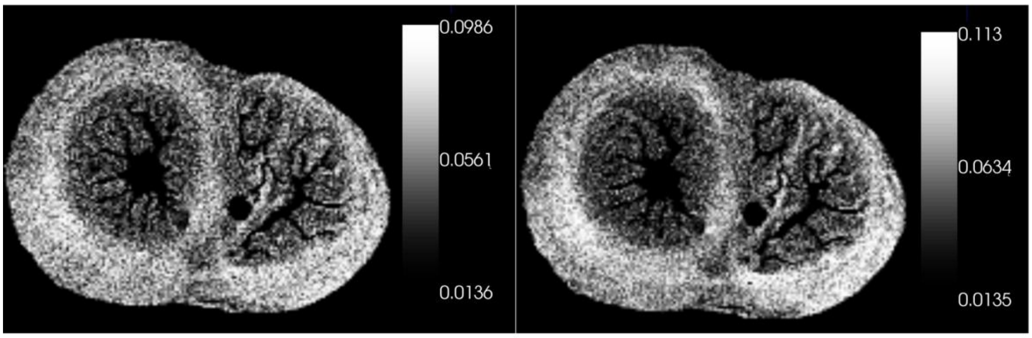

Δ = 96ms, δ=2ms Δ = 112ms, δ=2ms

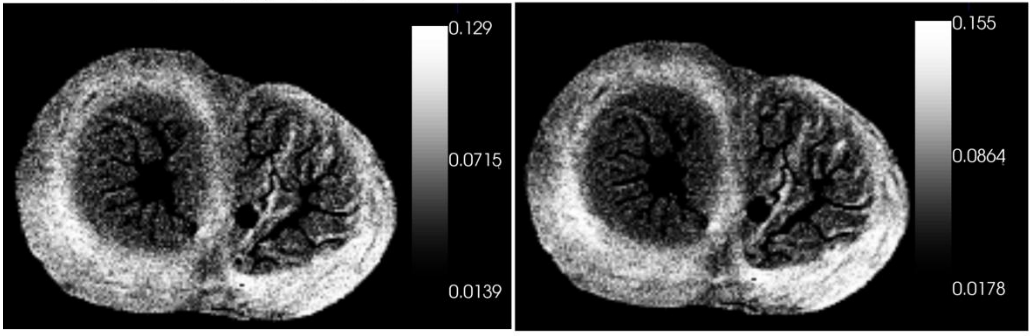

Δ = 128ms, δ=2ms Δ = 144ms, δ=2ms

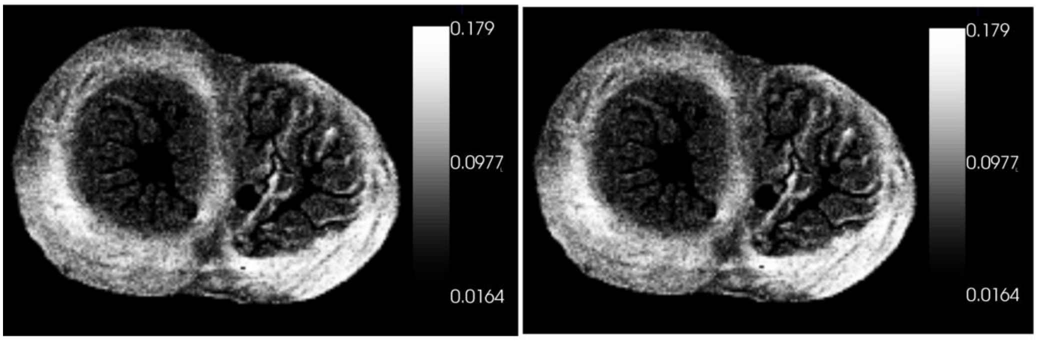

Δ = 160ms, δ=2ms Δ = 178ms, δ=2ms

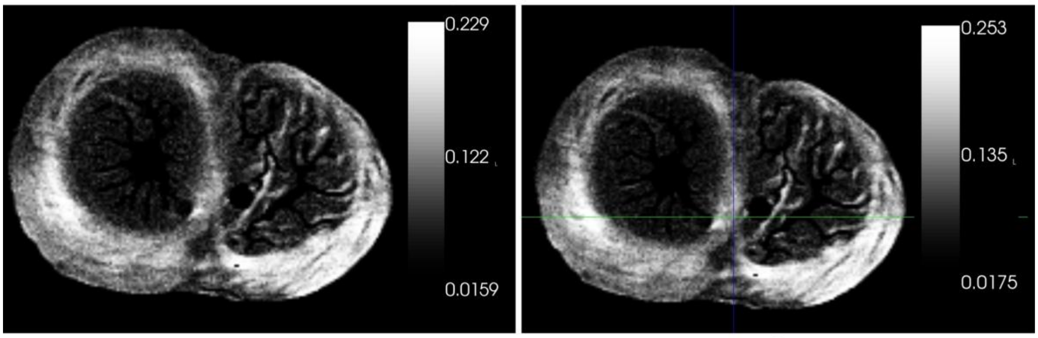

Δ = 192ms, δ=2ms Δ = 208ms, δ=2ms

Fig. 6.11 DW images along one diffusion gradient direction for different diffusion times obtained with practical diffusion gradient pulses. Diffusion times are respectively 64, 80, 96, 112, 128, 144, 160, 176, 192 and 208 ms. Diffusion gradient pulse duration is 2 ms and b-values is 3000 s/mm^2 . The corresponding gradient strengths are 407, 364, 332, 307, 287, 270, 257, 245, 233 and 225 mT/m and the q-values are about 35, 31, 28, 26, 24, 23, 22, 21, 20 and 19 mm^{-1}.

In Fig. 6.11, the simulated DW images in one direction with different diffusion times are given. We note that if b-value is constant, the image intensity increases and the image contrast is improved with the increment of diffusion time. This result is the same as that obtained in the previous simulation with perfect diffusion gradient pulses. The long diffusion time allows more molecules to sense the tissue structure's boundaries and therefore the resulting diffusion images have a better contrast.

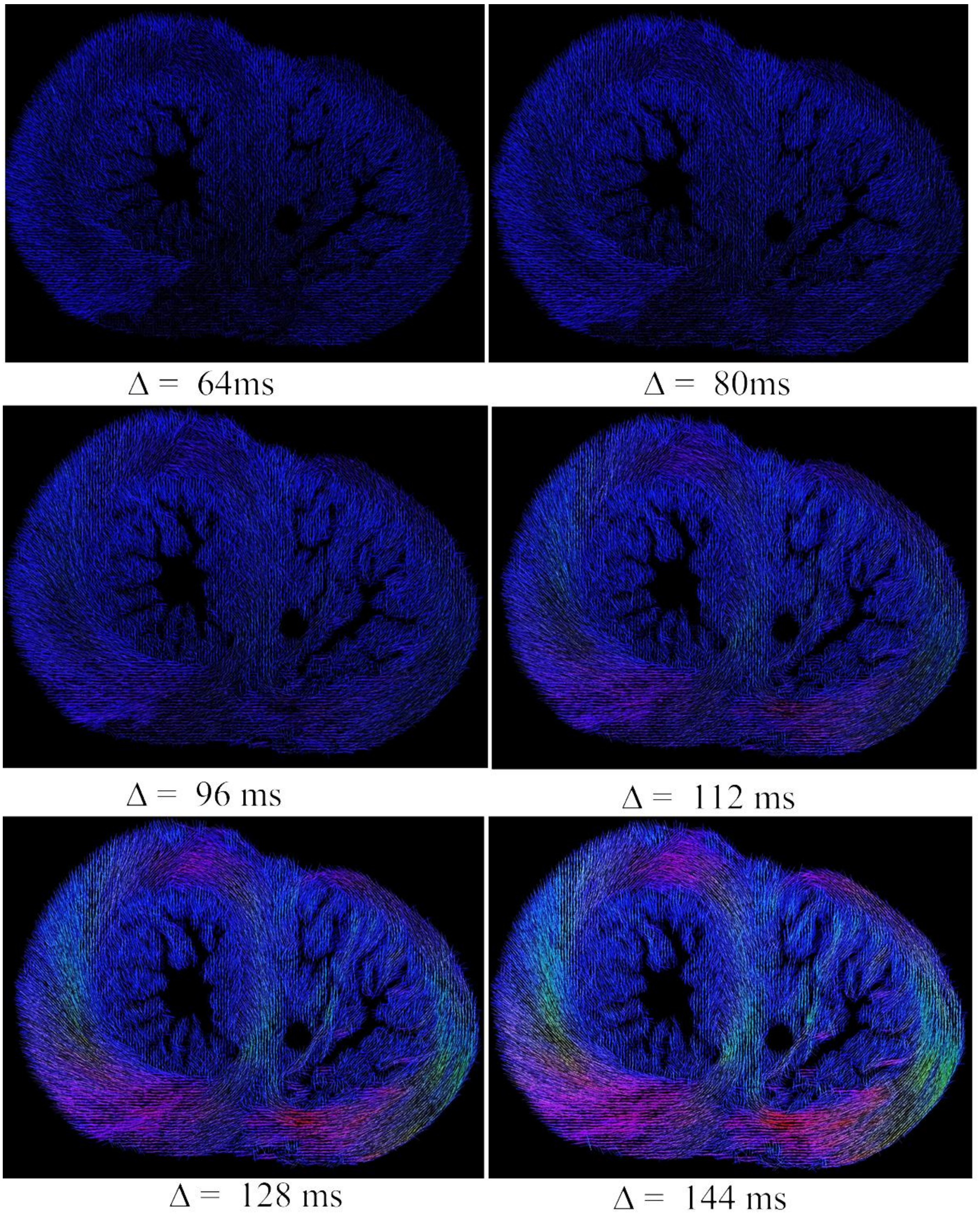

$\Delta = 64$ms $\Delta = 80$ms

$\Delta = 96$ ms $\Delta = 112$ ms

$\Delta = 128$ ms $\Delta = 144$ ms

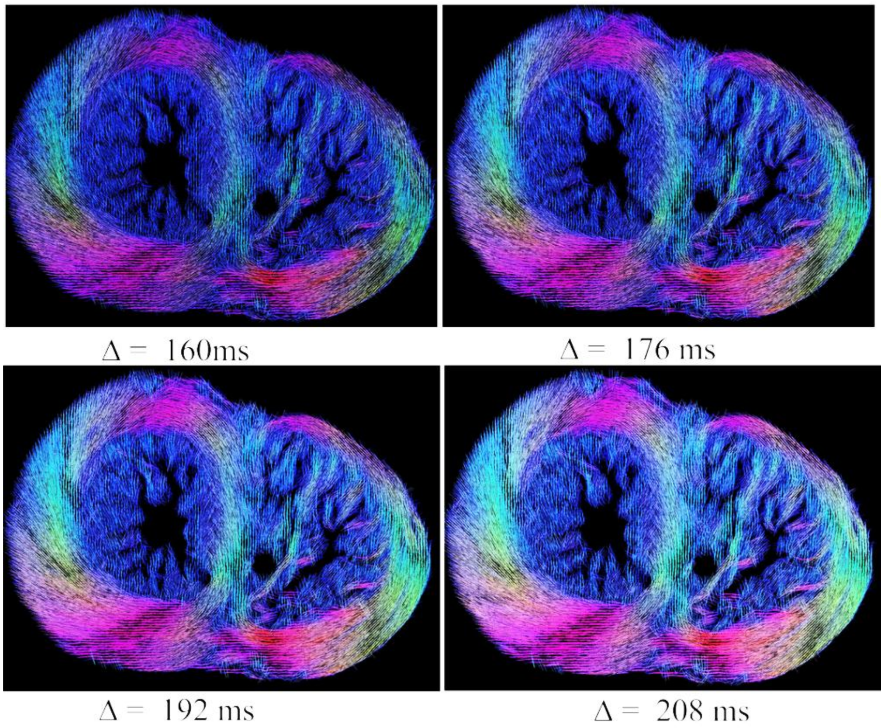

Fig. 6.12 Simulated fiber orientations obtained with different diffusion times and a high b-value of 3000 s/mm^2.

From the DW images and the corresponding gradient directions, the diffusion tensor images are calculated as shown in Fig. 6.12. We can observe that when the diffusion time is less than 80 ms, it is difficult to distinguish fiber orientation differences. With the increment of the diffusion time, the fiber orientation derived from the DW images becomes more obvious. Fig. 6.13 illustrates the histogram of the deviation angle between the simulated fiber orientations and the ground-truth obtained with different diffusion time. Evidently, increasing the diffusion time will increase the detection accuracy for the fiber orientation. In this simulation, when the diffusion time is longer than 160 ms, the detection accuracy becomes stable.

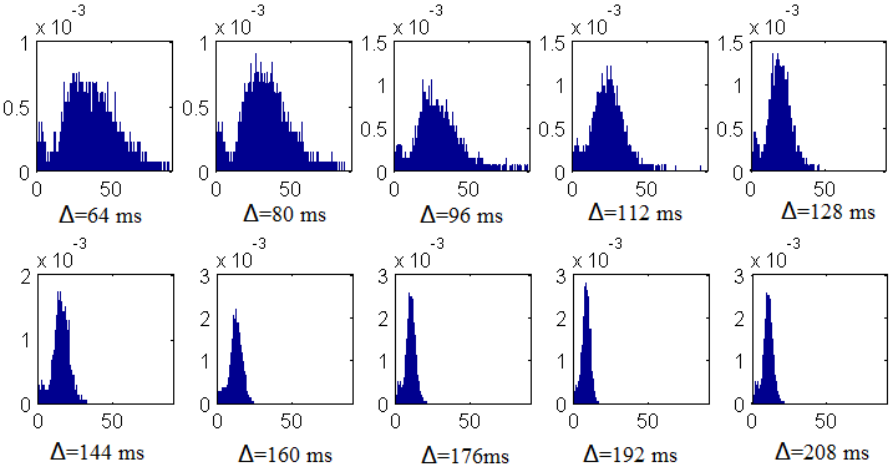

Fig. 6.13 Distribution of deviation angles between the simulated cardiac fiber orientations and the ground-truth provided by PLI, for different diffusion times.

Besides the fiber orientation, FA and MD values are also the most important diffusion indices for inferring tissue structures. For this reason, the effects of diffusion time on FA and MD are also simulated using our improved Mont-Carlo algorithm. The obtained results are shown in Fig. 6.14 and Fig. 6.15. It shows that FA increases when the diffusion time becomes longer but MD decreases. This is consistent with the previous analysis in the simulation using perfect diffusion gradients.

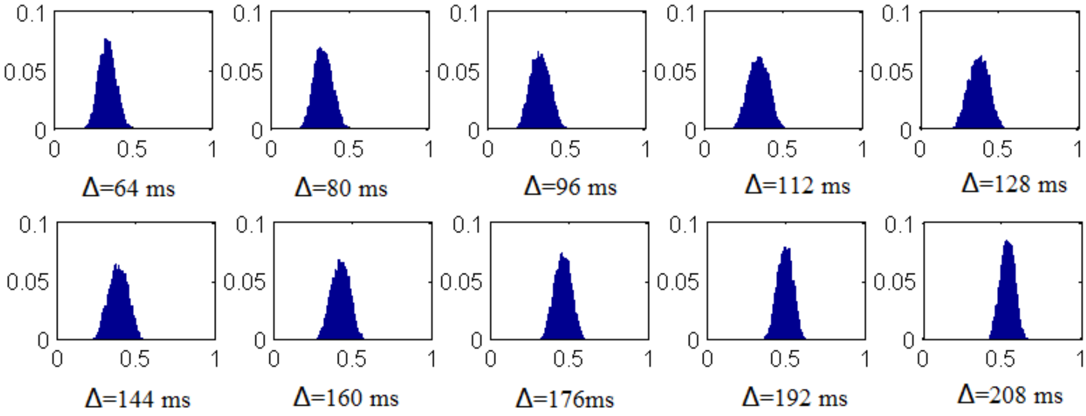

Fig. 6.14 Variation of FA values as a function of diffusion time. The FA ranges from 0.2 to 0.7 when the diffusion time changes from 64 ms to 208 ms.

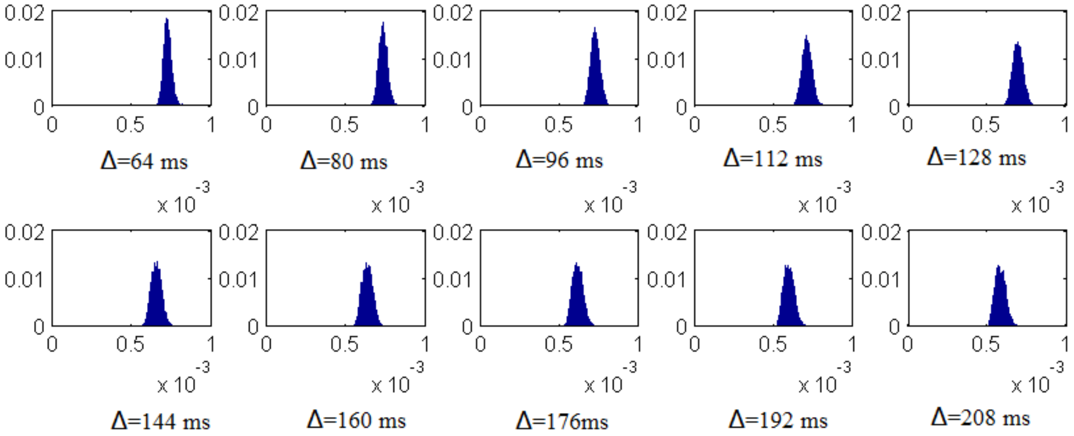

Fig. 6.15 Variation of MD values as a function of diffusion time.

In the previous simulation with the perfect diffusion gradients, the effect of diffusion time was investigated by fixing the diffusion gradient strength and changing therefore the b-values. However in the simulation with the practical gradient pulses, the b-value is taken as a constant, but the diffusion gradient strength varies with diffusion time. The simulation results illustrate that no matter what changes, the diffusion time has the same influence on the diffusion properties.

6.3.4 Diffusion gradient pulse duration

Diffusion gradient pulse duration is an essential parameter for determining the DW image quality and the diffusion properties estimation accuracy. In diffusion MRI analysis, short gradient pulse approximation was assumed to interpret the acquired data, in which the diffusion that takes place during the pulse duration is not considered. However, with the advent of the q-space imaging modalities, the high diffusion gradient strength is gradually required that is not yet available in clinical MRI scanners and usually the high gradient strength is compensated by the long diffusion gradient pulse. In such case, the displacement of water molecules accumulated during the pulse duration is no longer negligible, and it is necessary to analyze the effects of pulse duration for high b-value imaging.

In our previous simulation using the perfect gradient pulses, the influence of the gradient duration was analyzed based on the relationship between the b-value and the duration δ rather than by considering the diffusion displacement during the pulse duration. That corresponds to the commonly used method in the literatures because from the practically acquired data, it is impossible to know the displacements during a certain period. However, using our improved Monte-Carlo algorithm, the signal attenuation caused by diffusion during pulse gradient duration could be derived.

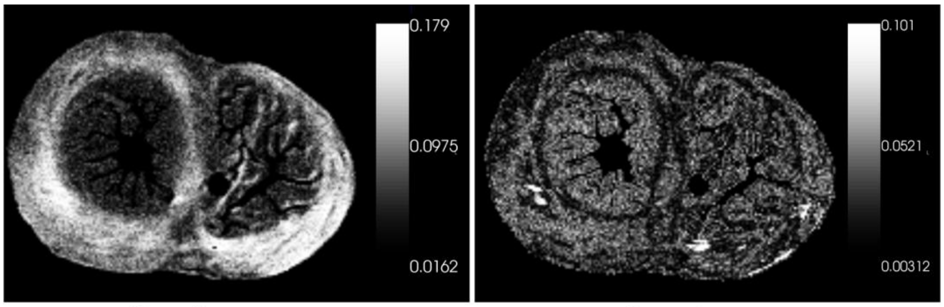

$\delta =$ 2ms $\delta =$ 4 ms

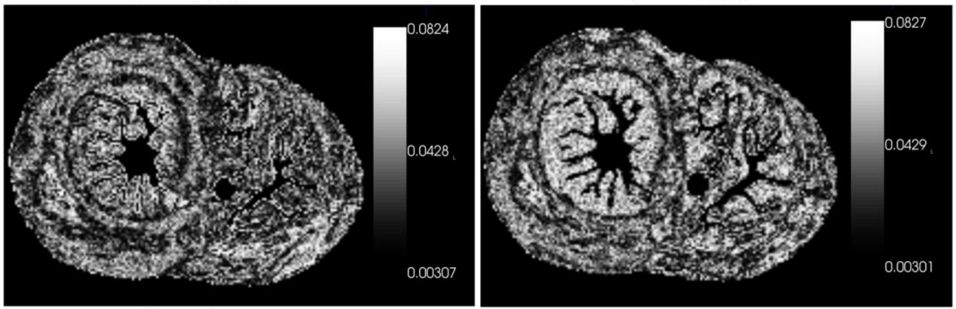

$\delta =$ 8 ms $\delta =$ 12ms

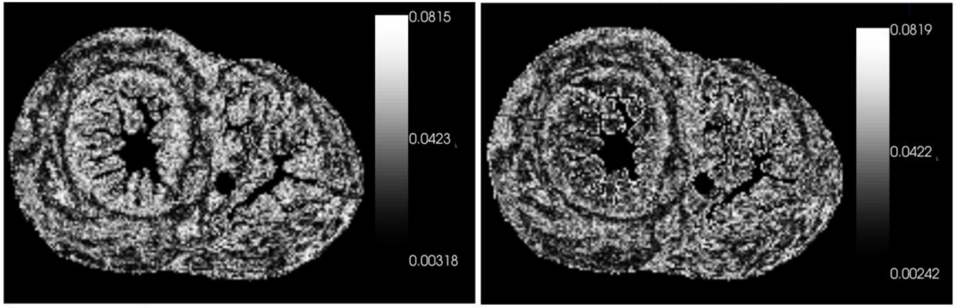

$\delta =$ 16ms $\delta =$ 24ms

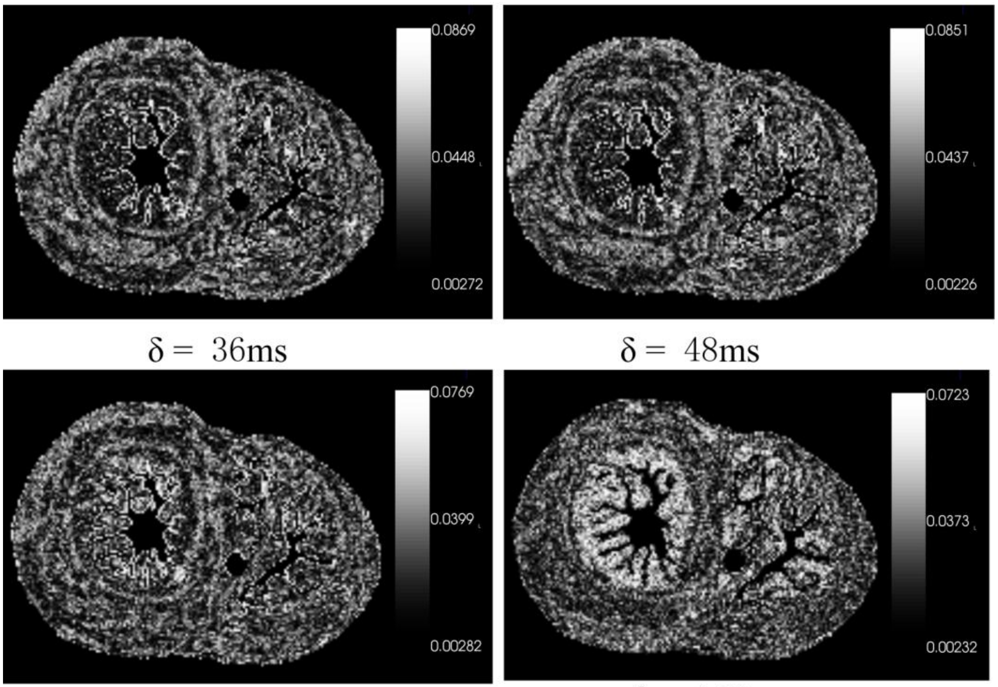

δ = 36ms

δ = 48ms

δ = 80ms

δ = 120ms

Fig. 6.16 DW images simulated with different pulse durations using practical diffusion gradients and a high b-value of 3000 s/mm^2. Diffusion time is 160 ms and gradient ramp time is 0.25 ms. The pulse durations are respectively 2, 4, 8, 12, 16, 24, 26, 48, 80 and 120 ms. For keeping the q-value (about 23 mm^{-1}) and b-value (3000 s/mm^2) as constant, the gradient strengths are correspondingly 256.5, 128.5, 64.5, 43.2, 32.55, 21.9, 14.8, 11.2, 7 and 5 mT/m.

Fig. 6.16 shows the DW images simulated with different pulse durations for a high b-value of 3000 s/mm^2. During the simulation, the time interval for each random walking step is chosen as 2.1 ms. Thus, the simulation image obtained with the gradient pulse duration δ of 2 ms can be considered as the comparison reference because no random walks were performed during this duration. By comparing the images simulated with and without influences of the pulse duration, it can be seen that in consideration of the pulse duration, the image intensity decreases dramatically. For better understanding this result, the corresponding diffusion tensor images (Fig. 6.17) are calculated.

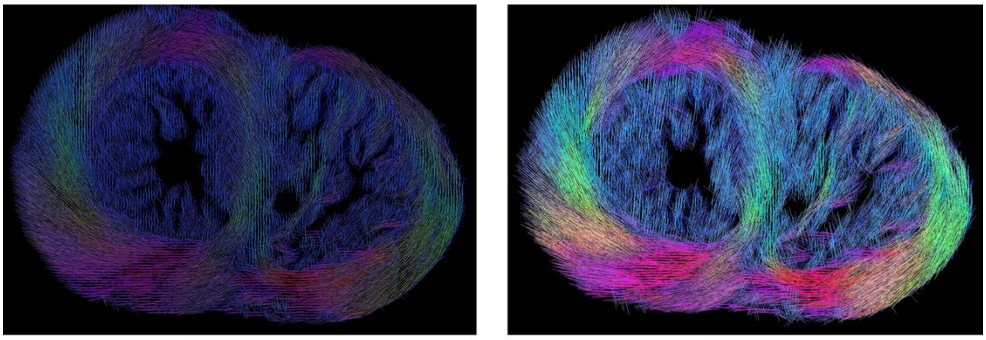

δ = 2ms

δ = 4 ms

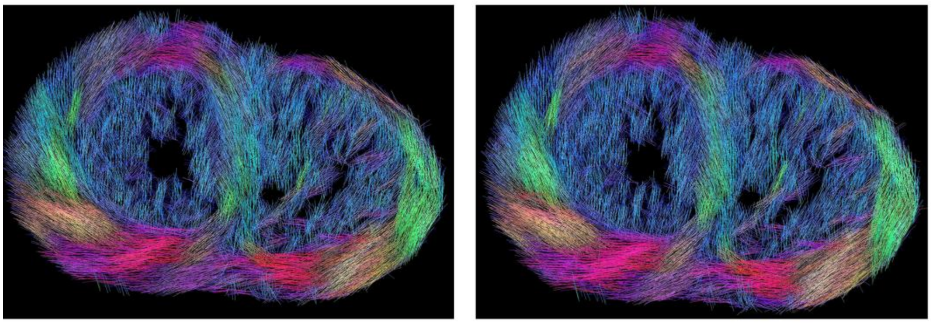

$\delta = 8$ ms

$\delta = 12$ ms

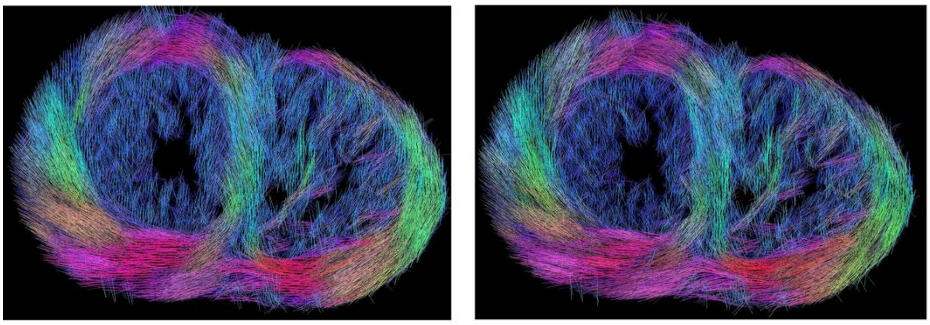

$\delta = 16$ ms

$\delta = 24$ms

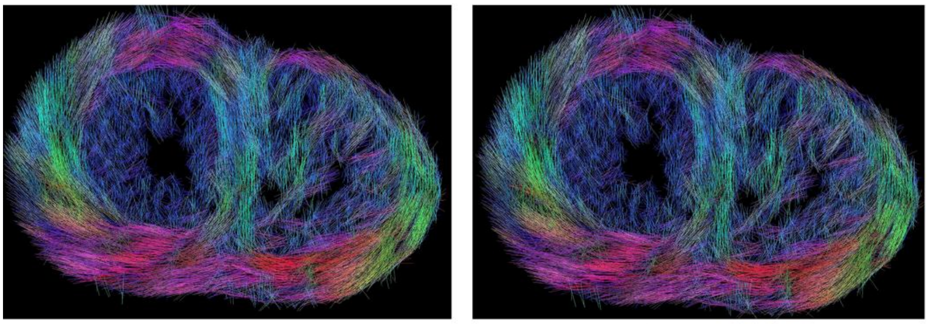

$\delta = 36$ ms

$\delta = 48$ ms

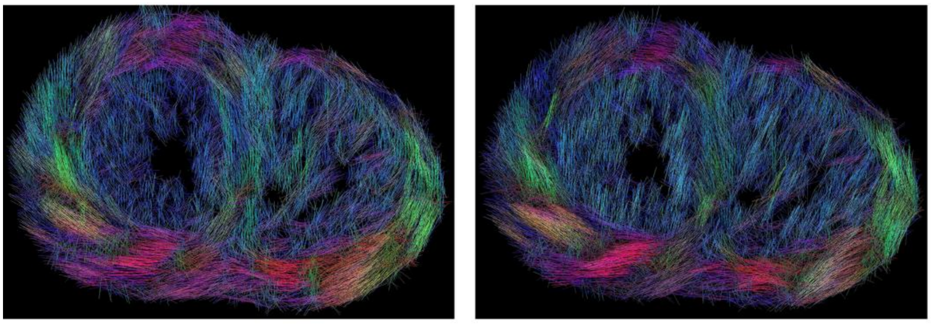

$\delta = 80$ ms

$\delta = 120$ ms

Fig. 6.17 Fiber orientations obtained with different gradient pulse durations using practical diffusion gradients and a high b-value of 3000 s/mm^2.

From the diffusion tensor images, we cannot observe big difference between the fiber orientation distributions. For quantitatively analyzing the effects of pulse duration, the measurement accuracy of fiber orientation, FA and MD values are calculated from the diffusion tensor images.

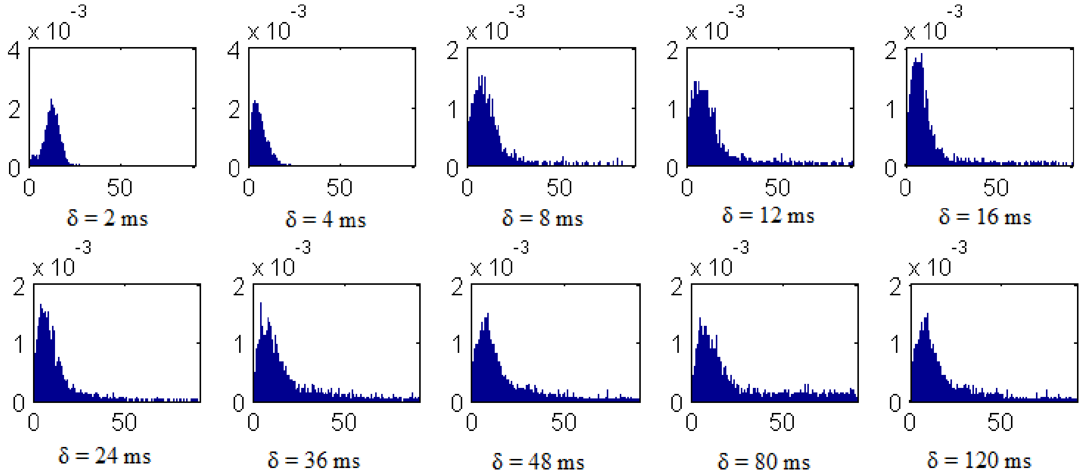

δ = 2 ms δ = 4 ms δ = 8 ms δ = 12 ms δ = 16 ms

δ = 24 ms δ = 36 ms δ = 48 ms δ = 80 ms δ = 120 ms

Fig. 6.18 Distribution of deviation angles between the simulated fiber orientation and the ground-truth provided by PLI, for different pulse durations.

Fig. 6.18 illustrates the distribution of deviation angle between the simulated cardiac fiber orientations and the ground-truth. With no consideration of the effects of gradient pulse duration, the angle has an approximated Gaussian distribution (δ = 2 ms). But as the diffusion process during the pulse gradient is taken into account, with the increment of the pulse duration, the deviation angle becomes more and more significant. This is caused by the phase shift introduced by the variation of the magnetic field strength. Even the molecules are immobile, the inhomogeneity of the magnetic field will also make the molecules dephase and then introduce the measurement error.

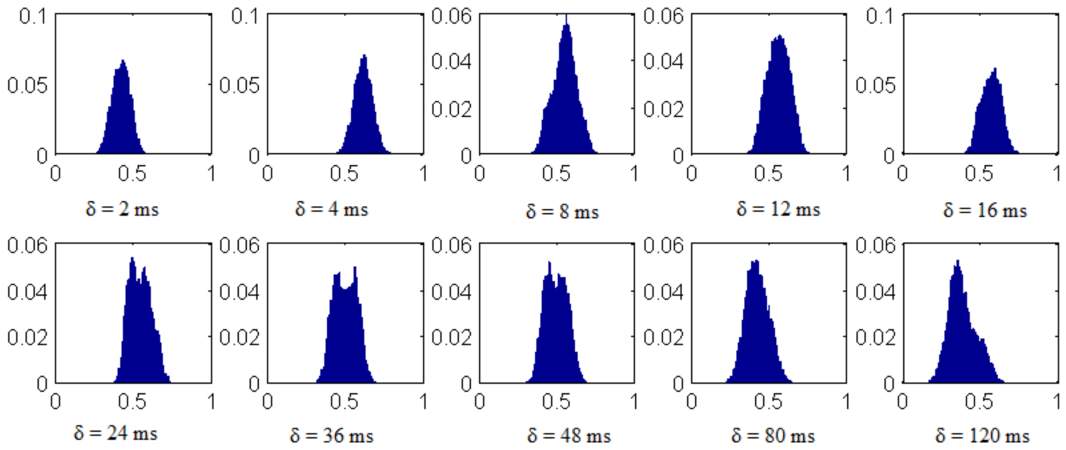

δ = 2 ms δ = 4 ms δ = 8 ms δ = 12 ms δ = 16 ms

δ = 24 ms δ = 36 ms δ = 48 ms δ = 80 ms δ = 120 ms

Fig. 6.19 Distribution of FA values for different gradient pulse durations.

By comparing the FA distributions (Fig. 6.19), it can be noted that the effect of diffusion pulse duration on FA is very evident. Without considering the influences of gradient pulse duration, the mean FA value is about 0.5 ($\delta = 2\ \mathrm{ms}$). However, when the displacement of water molecules that diffuse during the pulse duration is taken into account, the FA increases quickly, leading to an average FA value of about 0.8 ($\delta = 4$ ms). In the company of the subsequent increasing of δ, the range of FA becomes wider.

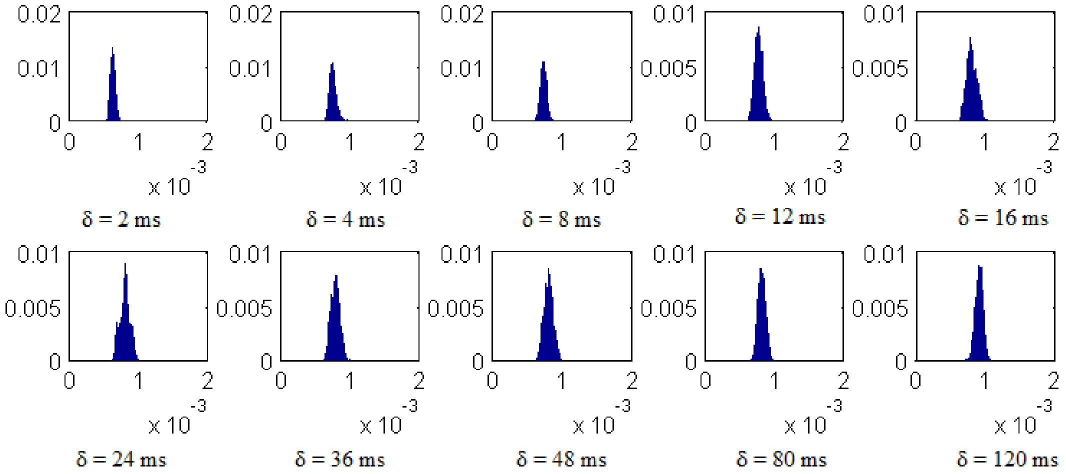

δ = 2 ms δ = 4 ms δ = 8 ms δ = 12 ms δ = 16 ms

δ = 24 ms δ = 36 ms δ = 48 ms δ = 80 ms δ = 120 ms

Fig. 6.20 Distribution of MD values for different gradient pulse durations.

In Fig. 6.20 are shown the MD distributions. In the presence of the pulse duration, the MD increases dramatically, and the mean value varies from 0.5 to 0.9×10^{-3} mm^2/s.

The effects of pulse duration on fiber orientation estimation, FA and MD can be explained by the varying q-value. In the perfect diffusion gradient pulses, during the diffusion time, q-value is a constant and defined as $\vec{q} = \gamma\vec{G}\delta$. Thus the phase shift ϕ accumulated during each random walking step in which molecule diffuses from position of $\vec{r}_1$ to $\vec{r}_2$ is:

$$\phi = \vec{q}(\vec{r}_2 - \vec{r}_1) \tag{6.61}$$

If the molecules do not move, the phase shift is zero. However, in the presence the gradient pulse, q-value changes with time and consequently with walking steps, leading to the phase shift that can be rewritten as:

$$\phi = \vec{q}_2 \cdot \vec{r}_2 - \vec{q}_1 \cdot \vec{r}_1 = \vec{q}_2 \cdot (\vec{r}_1 + \vec{r}) - \vec{q}_1 \cdot \vec{r}_1 = (\vec{q}_2 - \vec{q}_1) \cdot \vec{r}_1 + \vec{q}_2 \cdot \vec{r} \tag{6.62}$$

In this case, the variation of q-value also produces the phase shift even the molecules keep immobile during one walk step and therefore introduces measurement errors. According to Eq. (6.42), (6.43), and (6.44), the variation of q-value for each walking step is calculated and shown in Fig. 6.21.

It can be observed that the lasting time of q-value variations is proportional to the pulse duration but the variation amplitude of q-value is determined by the gradient strength. Pulse duration influences mainly the measurement accuracy of fiber orientation, but the gradient pulse strength has a greater effect on FA and MD values. As the pulse is very short, there is almost no diffusion happens, but the dramatic changes in the gradient strength and q-value can introduce a phase shift that keeps as constant during the diffusion evolution. After 180° RF pulse, the q-value experiences an opposite variations. Thus phase shift accumulated during the second imaging gradient pulse offsets somewhat the previous phase shift, and the diffusion signal is not attenuated so much. The dramatic q-value changes highlight the displacement differences and therefore result in an overestimation of FA value. Due to the short pulse duration, the inconsistent weighting for displacement is not so much. The displacement can then be well interpreted by the phase shift, and subsequently the fiber orientation derived from the diffusion signal is reliable (the case of $\delta = 4\ \mathrm{ms}$). However, with the increasing of the pulse duration, the gradient pulse strength used in the simulation decreases, which makes the phase shift caused by diffusion displacements become more significant than that introduced by the q-value variations. Since during a long time interval, the diffusion displacement is always weighted by varying q-values, the resulting phase shift has no longer linear relationship with the displacement, and consequently the fiber orientation derived from the diffusion images deviates significantly from the ground-truth, as shown in Fig. 6.18. Meanwhile, in company of the decreasing of gradient strength, the amplitude of q-value varies slowly and smoothes the diffusion weights. As a result, the range of FA becomes much wider compared to that for δ of 4 ms.

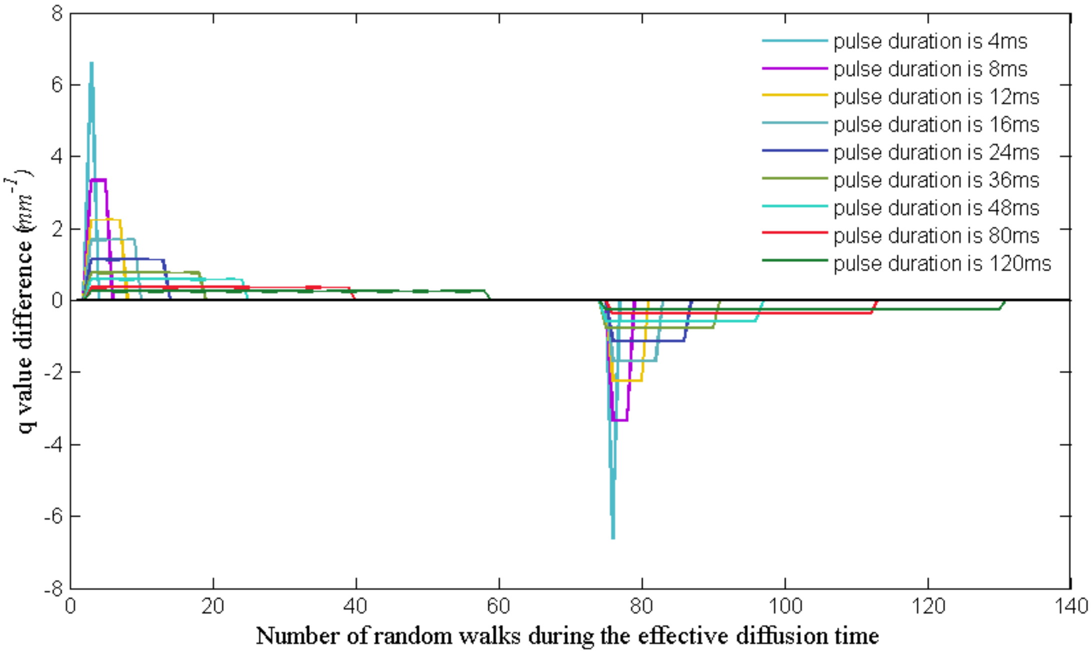

Fig. 6.21 Difference of the q-values between each walking step.

6.3.5 Diffusion gradient ramp time

Diffusion gradient ramp time ε is determined by both the maximum strength $G_{\max}$ of the diffusion gradient and the slew rate g_{slew}. Their relationship can be expressed by:

$$\varepsilon = G_{\max} / g_{slew} \tag{6.63}$$

In MRI systems, the shorter the ramp time, the faster the gradients and therefore echo spacing. Gradients with shorter echo spacing will have a better resolution. For a 3T scanner, its gradient strength is about 40~45 mT/m and the corresponding slew rate is 200 mT/m/ms. For

1.5T scanners that are commonly used in the clinical applications, the gradient strength of which is 30 mT/m and the slew rate is 150mT/m/ms. In order to obtain the stronger gradient strength, the slew rate is usually slowed and this will increase the ramp time. For this reason, in the following, the effect of ramp time on diffusion properties is analyzed. In such simulation, the b-value is fixed as 3000 s/mm^2, the duration for each random walk step is 0.25 ms, diffusion time is 160 ms, the gradient strength is about 257 mT/m and the pulse duration is 2 ms, which results in a q-value of 22 mm^{-1}. Because the pulse duration used here is 2 ms and the time interval for each random walk is 0.25 ms, the effect of pulse duration is therefore also accounted for in the simulation. The existence of gradient pulse duration produces an inhomogeneous magnetic field strength, but during this interval since the diffusion gradient has constant amplitude, the variation of magnetic field strength is the same. However, the introduction of ramp time changes not only the magnetic field strength but also its variation. The coexistence of both pulse duration and ramp time will affect greatly the simulation results.

Fig. 6.22 shows the DW images for different diffusion gradient ramp times of 0.25, 0.5, 0.75, 1, 1.25, 1.5, 1.75 and 2 ms respectively, from which it can be seen that the diffusion signal is attenuated when ramp time is very small and then the signal is highly enhanced with increasing of ramp times. But as the ramp time reaches a certain value, the signal intensity falls again.

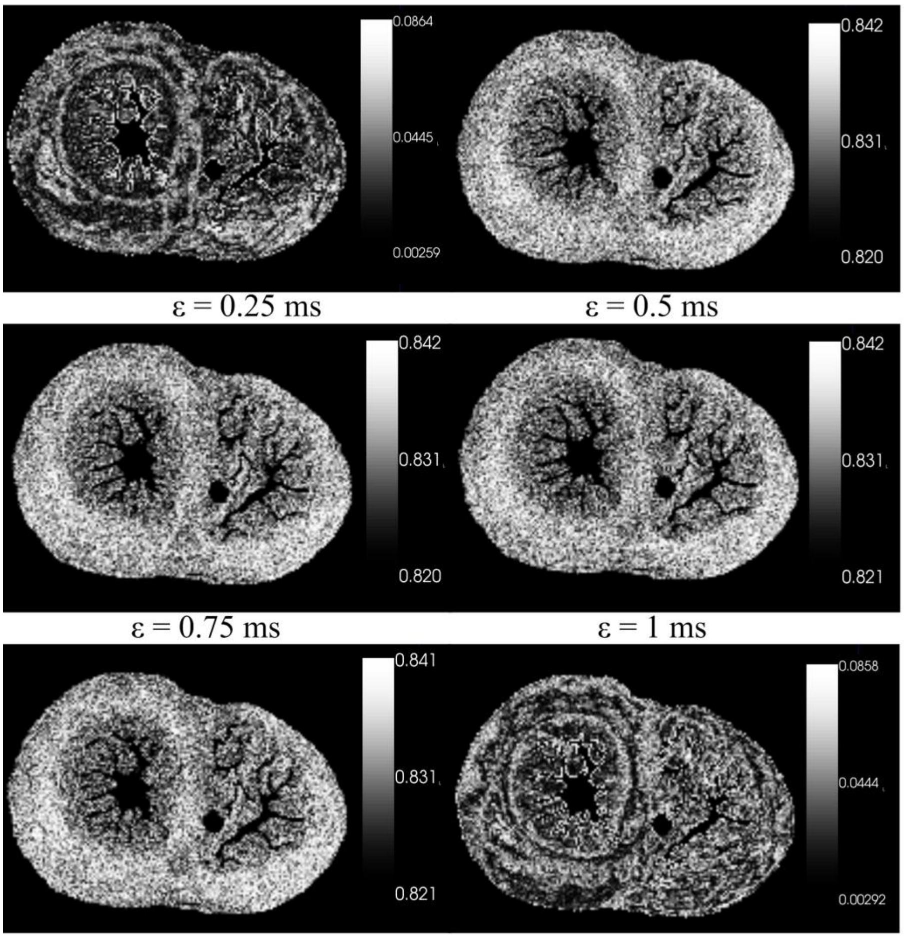

ε = 0.25 ms ε = 0.5 ms

ε = 0.75 ms ε = 1 ms

ε = 1.25 ms ε = 1.5 ms

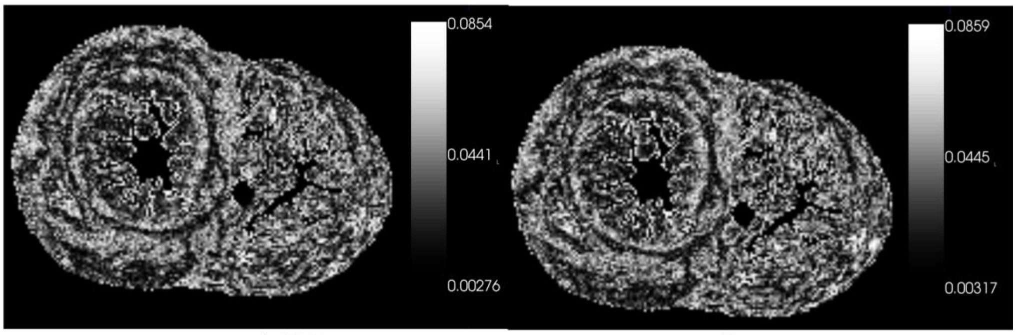

$\varepsilon = 1.75$ ms

$\varepsilon = 2$ ms

Fig. 6.22 DW images along one direction for different gradient ramp times. The b-value is 3000 mm^2/s. The diffusion time is 160 ms, the gradient pulse durations is 2 ms, and the gradient strength is 257 mT/m, walking step duration is 0.25 ms, which results in a q-value of 22 mm^{-1} .

This phenomenon can be explained by the Fig. 6.23 in which the q-value variation for each walk step is illustrated.

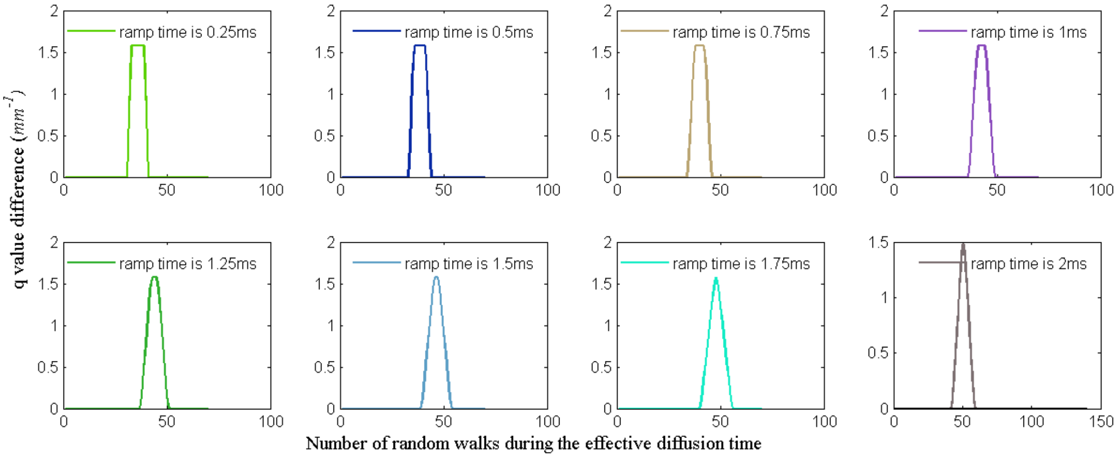

Fig. 6.23 Difference of q-values between each walking step for different gradient ramp times. For visualization convenience, we just illustrated the q-value variation before 180 RF pulse, for that after 180 RF pulse, the q-value experiences a negative change.

Because the ramp time and the pulse duration used in this simulation are very short, the phase shift caused by water displacement is negligible. In contrast, the variation of magnetic field strength accounts for the main phase shift. When ramp time is 0.25 ms, there is only one random walk step that is performed. If the molecules do not move, the phase shift can be written as $(q_2 - q_1)r_1$, where q_1 is the q-value at the beginning of the random walk, q_2 is the value at the end, and r_1 is the mean position of one water molecule during the random walk interval. As shown in Fig. 6.10, the diffusion gradient is a trapezoidal pulse presenting both raising and falling ramp time. Accordingly, if the molecule locates at the position of r_2 during the falling ramp time, the accumulated phase shift is $-(q_2 - q_1)r_2$, and the total phase shift induced by the ramp time is $(q_2 - q_1)(r_1 - r_2)$. For the ramp time of 0.25 ms, according to Eq. (6.43), (6.42) and (6.44), the change in q-value during this walk step is 0.78 mm^{-1}, which is so small that the phase shift caused by the ramp time can be overlooked. In such case, the phase shift is mainly induced by the pulse duration. That is why the DW images obtained with ε of 0.25 ms are similar to those obtained with δ of 4 ms.

With increasing of ramp time, the number of random walks during this period increases. If the number of random walk is n, the accumulated phase shift is therefore $(q_n - q_1)(r_n - r_1)$. From Fig. 6.23, we can observe that the q-value increases with the ramp time. Subsequently, if the displacement $(r_n - r_1)$ does not change too much, the accumulated phase shift also increases with the ramp time, which will seriously interfere with the phase shift caused by the real displacement. As a result, the DW images are no longer able to reflect the fiber structure, such as the images obtained with ε of 0.5, 0.75, 1 and 1.25 ms in Fig. 6.22. The corresponding cardiac fiber orientations derived from these DW images are shown in Fig. 6.24 (coded in blue color). However, when ε reaches a certain value (1.5 ms in this case), the trapezoidal diffusion gradient pulse gradually turns into a triangular pulse, and consequently the variation of q-value experiences the same transformation, as shown in Fig. 6.23. When $\varepsilon = \delta$, the inhomogeneity of the magnetic field strength is induced only by the ramp time, the rise and fall ramp times compensate completely this inhomogeneity. As a result, the resulting phase shift decreases and cardiac fiber orientation derived from the DW images makes sense again, as shown in Fig. 6.24 and Fig. 6.25.

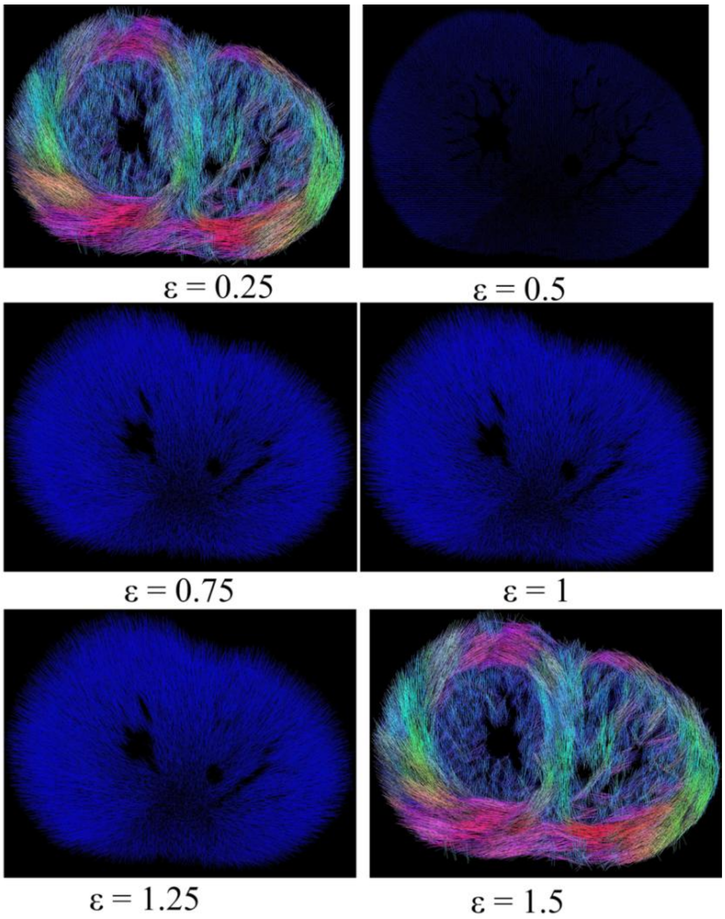

$\varepsilon = 0.25$ $\varepsilon = 0.5$

$\varepsilon = 0.75$ $\varepsilon = 1$

$\varepsilon = 1.25$ $\varepsilon = 1.5$

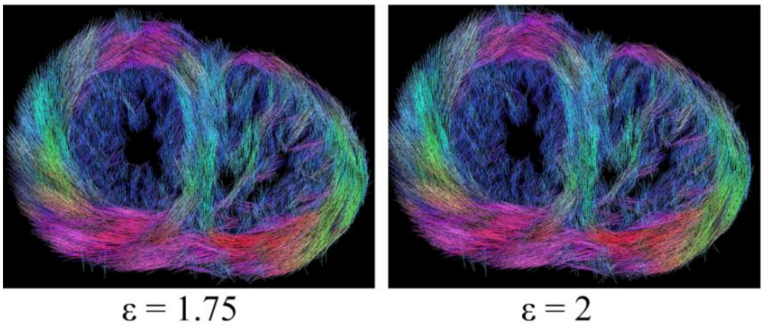

ε = 1.75   ε = 2

Fig. 6.24 Fiber orientations obtained with different gradient ramp times and a b-value of 3000 s/mm^2.

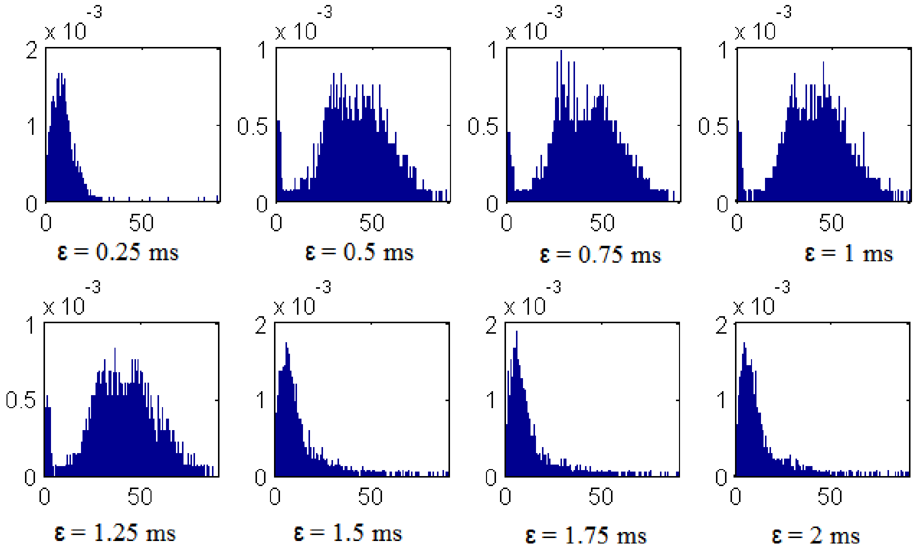

ε = 0.25 ms   ε = 0.5 ms   ε = 0.75 ms   ε = 1 ms

ε = 1.25 ms   ε = 1.5 ms   ε = 1.75 ms   ε = 2 ms

Fig. 6.25 Distribution of deviation angles between the simulated fiber orientation and the ground-truth for different gradient ramp time.

Besides the DW images, fiber orientations, simulation deviations, FA and MD values obtained with different ramp times are also calculated. The effects of the ramp time on FA and MD are shown in Fig. 6.26 and Fig. 6.27.

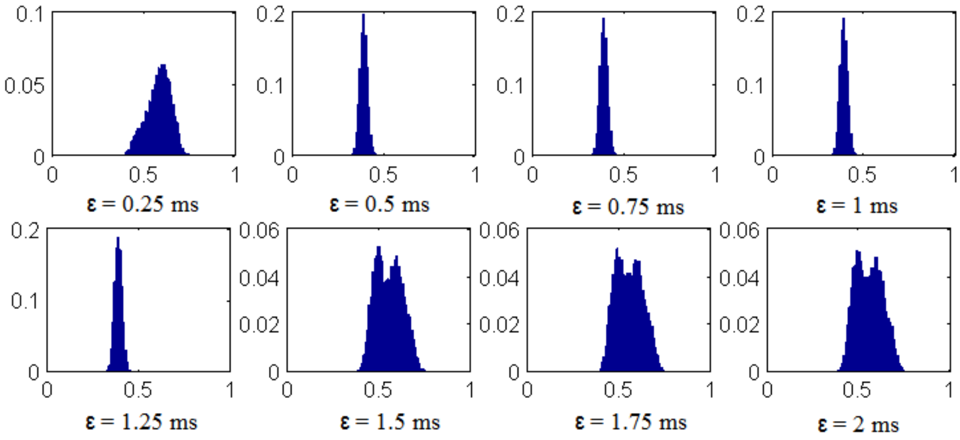

ε = 0.25 ms   ε = 0.5 ms   ε = 0.75 ms   ε = 1 ms

ε = 1.25 ms   ε = 1.5 ms   ε = 1.75 ms   ε = 2 ms

Fig. 6.26 Distribution of FA values for different gradient ramp time.

Note that the mean FA value is always about 0.5 for all the ramp times, but the ramp time influences greatly the variance of FA values. As the ramp time increases, due to the interference of the inhomogeneous magnetic field strength, the phase shift caused by the displacement of water molecules is drowned in that induced by the magnetic field inhomogeneity. As a result, the diffusion signal attenuation is caused mainly by the variation of magnetic field strength and is almost the same in all the diffusion directions. That is why the FA value does not change so much. When the effects of magnetic field inhomogeneity are reduced, such as the cases with ramp time of 1.5, 1.75 and 2 ms, the FA values come to the normal distribution again.

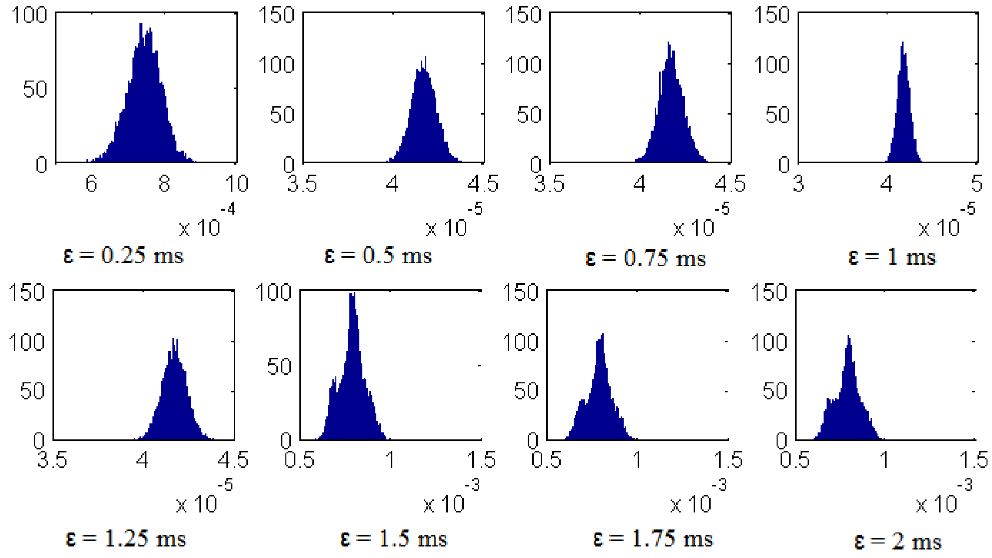

$\varepsilon = 0.25$ ms, $\varepsilon = 0.5$ ms, $\varepsilon = 0.75$ ms, $\varepsilon = 1$ ms

$\varepsilon = 1.25$ ms, $\varepsilon = 1.5$ ms, $\varepsilon = 1.75$ ms, $\varepsilon = 2$ ms

Fig. 6.27 Distribution of MD values for different gradient ramp time.

As ramp time increases, MD values decrease firstly and then increase (Fig. 6.27). From the previous analysis, we know that the simulation with ramp times of 0.5, 0.75, 1, and 1.25 ms cannot reveal the actual displacement of water molecules, and that the diffusion coefficients measured with these parameters are totally determined by the inhomogeneity of the magnetic field. Therefore, it will make no sense to compare these diffusion coefficients with those capable to reveal the diffusion process. Thus comparing the diffusion coefficients obtained with ramp times of 0.25, 1.5, 1.75 and 2 ms, we observe that the average MD value is always about 7×10^{-4} mm^2/s. With increasing of ramp time, the MD variation range becomes a little wider. This is because the phase shift accumulated during the rising and falling ramp times is not completely offset due to the tiny displacement of water molecules.

6.3.6 Discussion

We have investigated the influence of all the imaging parameters used in spin-echo sequence on the diffusion image properties from the perspectives of both b-value and q-value. Accordingly, the Monte-Carlo simulation algorithm has been improved, which has allowed the DW and diffusion tensor images with practical diffusion gradients to be simulated. The effects of diffusion time, gradient duration and ramp time have been analyzed. Comparing the simulation results obtained using respectively the perfect and practical diffusion gradients, we have observed that the influence of diffusion time is always the same, which means that long diffusion time highlights diffusion anisotropy and decreases the measured mean diffusion coefficient. The only difference between these two kinds of simulation is that the simulation accuracy for the fiber orientation using the perfect diffusion gradient pulse is better than that obtained with practical gradients. The average deviation angle is about 3º in the former but 10º in the latter. This is caused by the difference in water molecule number involved in the Monte-Carlo simulation. In the simulation using perfect diffusion gradient, the water molecule number in each myocyte is about 20000, but there are only 5000 molecules in each myocyte during the simulation using practical diffusion gradients. The more the molecules, the more accurate the simulation is but at the expense of calculation time.

As to the effects of diffusion gradient pulse duration, there is an appreciable distinction between the simulations with perfect and practical diffusion gradients. If analyzing the influence of pulse duration only from the relationship between the b-value and duration δ, the duration does not have a significant effect on fiber orientation estimation and diffusion indices including FA and MD, as shown in Fig. 6.7. This is commonly used in the current literature for analyzing the influence of δ. However, this relationship will be broken when taking into account the diffusion displacement during the pulse duration. Consequently, using the relationship between b-value and diffusion pulse duration to analyze the influence of δ is no longer correct. Our improved Monte-Carlo simulation approach overcomes this problem by considering the contribution of displacement during the gradient pulse duration to diffusion signal. The increment of δ deviates the estimated fiber orientation much more from the ground-truth and increases the measured MD and FA values. When Δ is 160 ms and $\delta > 80\,\text{ms}$, the MD value is bigger than the free diffusion coefficient, which means that under this condition, the diffusion tensor is not able to reveal the actual diffusion process any more.

In the light of the simulation results with different diffusion gradient ramp times, we can conclude that the gradient slew rate has a significant effect on the diffusion image quality and the resulting fiber orientation estimation. We should choose an appropriate ratio of gradient duration and ramp time to avoid simulation errors. The ramp time should be either much smaller than gradient duration or almost equal to the duration so that the influence of the variation of magnetic field inhomogeneity could be offset.

We have already analyzed the effects of practical diffusion gradient parameters on the diffusion properties. As stated, besides the diffusion gradients, the k-space encoding gradients, including the slice selection, phase encoding and frequency encoding gradients weight the molecular diffusion as well. We simulate their influences in the next section.

6.4 Influence of k-space encoding gradient parameters

The diffusion of water molecules is always present during dMRI signal acquisition, even during the time interval of slice selection, phase encoding and readout gradients. Therefore, k-space encoding gradients also contribute to diffusion-weighted signal. Currently, the spatial resolution of clinical acquisition data is about 2mm × 2mm × 2mm. Such resolution does not require strong encoding gradients, and the influence of the k-space encoding gradients is negligible. However, with the increasing requirement for dMRI with a high spatial resolution, the imaging gradients become stronger and stronger and their contribution to diffusion signal can be no longer ignored. In order to analyze the effects of the k-space encoding gradients on high-spatial diffusion image properties, the DW images with the presence of slice selection gradient, phase encoding gradient, read out gradient and all of them are simulated by means of our improved Monte-Carlo simulation. Meanwhile, according to the simulation theory elaborated in section 6.3.1, the k-space encoding gradients also contribute to both b-value and q-value, which means that even in the absence of the diffusion gradients along different directions, if we detect the MR signal along different directions, the resulting image should not be the same. It implies that a high spatial resolution MRI could be used as dMRI. In order to test this conjecture, DW images with a tiny diffusion gradient are simulated.

6.4.1 Simulation results

In order to compare the differences of DW images and diffusion properties with and without imaging gradients, we firstly simulated the DW images **in the absence of k-space encoding gradients**. The simulation parameters and the simulation results are shown in Fig. 6.28.

In the absence of imaging gradients

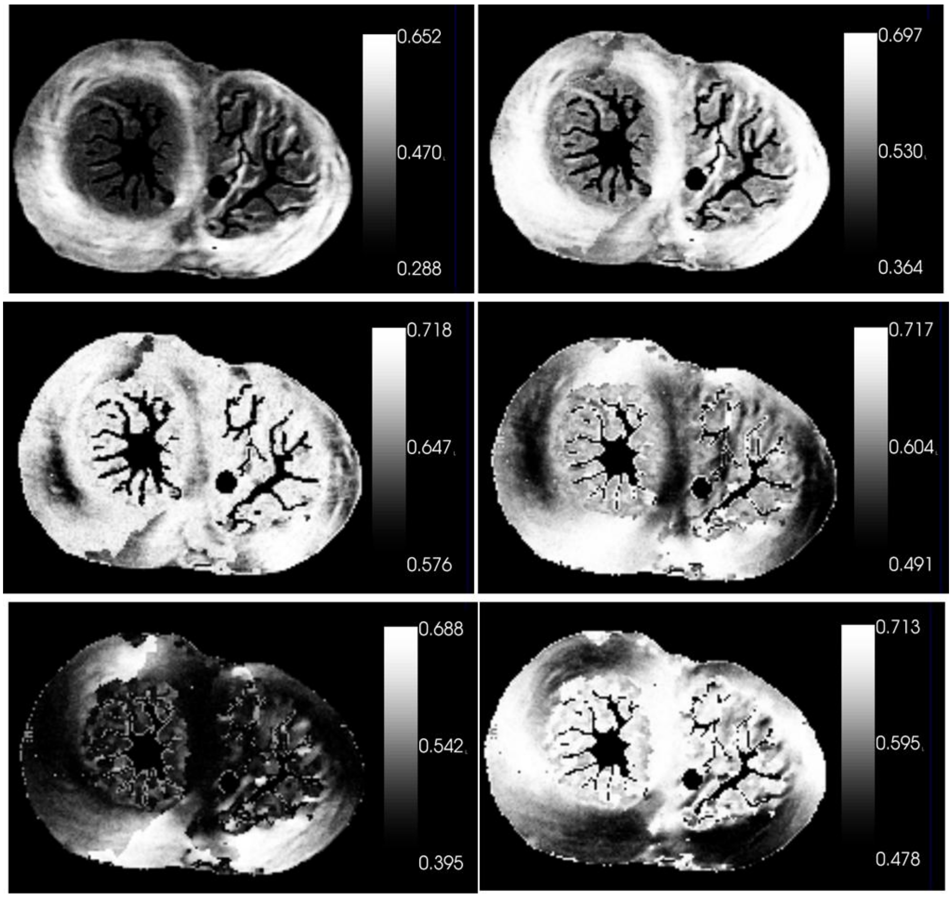

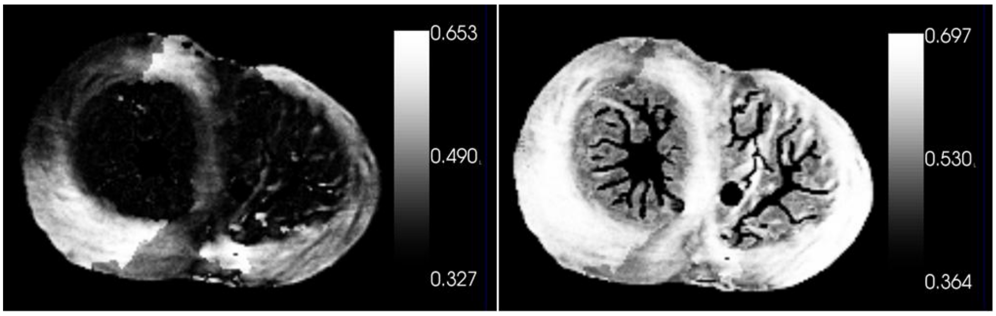

Fig. 6.28 DW images along 8 directions simulated in the absence of k-space encoding gradients. The simulation parameters used: diffusion time is 208 ms, gradient pulse duration is 2 ms, ramp time is 0.25 ms, random walk step time interval is selected as 2.1 ms to avoid the influences of the pulse duration and ramp time, and diffusion gradient strength is 129 mT/m, which results in a b-value of 1000 s/mm^2. The number of diffusion directions is 42. (All the following simulation in this chapeter use the same simulation parameters)

From these DW images, the diffusion properties without influence of k-space encoding gradients, including the fiber orientation, the distribution of deviation angle between the simulated fiber orientations and ground-truth, the FA and MD are calculated (Fig. 6.29). In the absence of imaging gradients, the mean deviation angle between the simulated fiber orientation and PLI ground-truth is about 5 degrees. The FA values range from 0.4 to 0.7, and MD values vary from 0.4 to 0.7×10^{-3} mm^2/s.

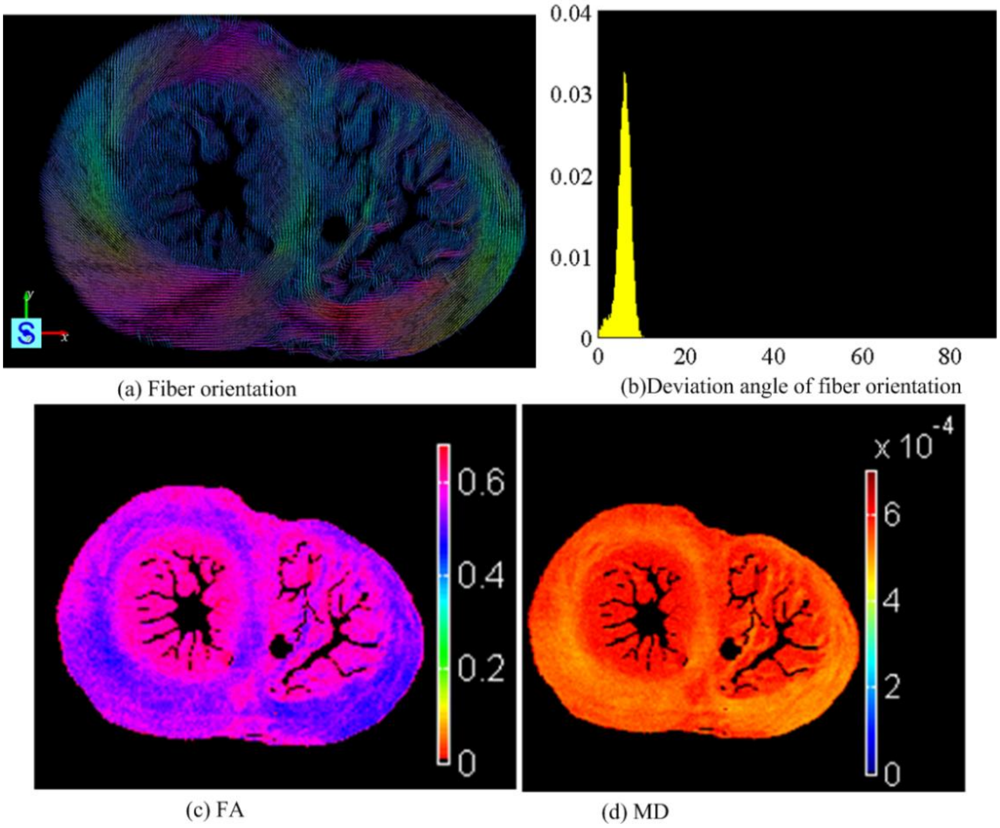

(a) Fiber orientation (b)Deviation angle of fiber orientation

(c) FA (d) MD

Fig. 6.29 Diffusion properties measured from the simulated DW images without influence of k-space encoding gradients: fiber orientation, distribution of deviation angles between the simulated fiber orientations and the ground-truth, FA and MD.

As mentioned above, the spatial resolution of PLI is 0.1 × 0.1 × 0.5 mm^3. In this simulation, the DW images have the same spatial resolution as PLI. In section 2.3.1.2, we have elaborated the relationship between the MRI spatial resolution and the imaging gradients strength. As a reminder, the corresponding spatial resolution calculations are given again as follows:

$$th = \frac{\Delta\omega}{\gamma G_{sl}} \tag{6.64}$$

$$res_{pe} = \frac{FOV_{pe}}{n_{pe}} = \frac{1}{\gamma \Delta G_{pe} \delta_{Gpe} n_{pe}} \tag{6.65}$$

$$res_{ro} = \frac{FOV_{ro}}{n_{ro}} = \frac{pbw}{\gamma G_{ro}} \tag{6.66}$$

where th represents slice thickness, γ is the gyromagnetic ratio of ^{1}H which is 42.5657 MHz/T, G_{sl} is the slice selection gradient strength, res_{pe} is the spatial resolution along the phase encoding direction which is determined by the phase encoding gradient strength variation ΔG_{pe}, duration δ_{Gpe} and the number of phase encoding n_{pe}. res_{ro} designates the spatial resolution along the readout direction (frequency encoding), which is related to the pixel bandwidth pbw and the readout gradient strength G_{ro}.

The dMRI pulse sequence used in this simulation is illustrated in Fig. 6.10. The excitation RF pulse bandwidth $\Delta\omega$ is 2 kHz and readout pixel bandwidth is 130 Hz, which results in a readout gradient pulse duration of 7.7 ms. The slice selection gradient duration is 7.7 ms and the duration of phase encoding gradient duration is 3.35 ms. The ramp times for all the gradients used here are taken as 0.25 ms, except the slice selection gradient switched on during the 180° RF pulse, which has a ramp time of 0.125 ms. The field of view (FOV) is determined by our cardiac fiber model. According to Eq.(6.64), to obtain a slice thickness of 0.5 mm, the corresponding slice selection gradient strength should be 93.97 mT/m. Calculated from Eqs. (6.65) and (6.66), the phase and frequency gradient strengths are 0.34 and 30.5 mT/m respectively for getting a spatial resolution of 0.1mm × 0.1mm. Using these parameters, a series of DW images and the diffusion properties are simulated in the presence of k-space encoding gradients.

In the presence of slice selection gradient

Fig. 6.30 illustrates the simulated DW images along 8 directions in the presence of only slice selection and diffusion gradients. By comparing Fig. 6.30 to Fig. 6.28, it can be seen that the introduction of slice selection gradient makes the diffusion signal to be attenuated more in certain directions, especially in slice selection direction. This is because the switch on of slice gradients increases the gradient strength along this direction and gives more diffusion weights.

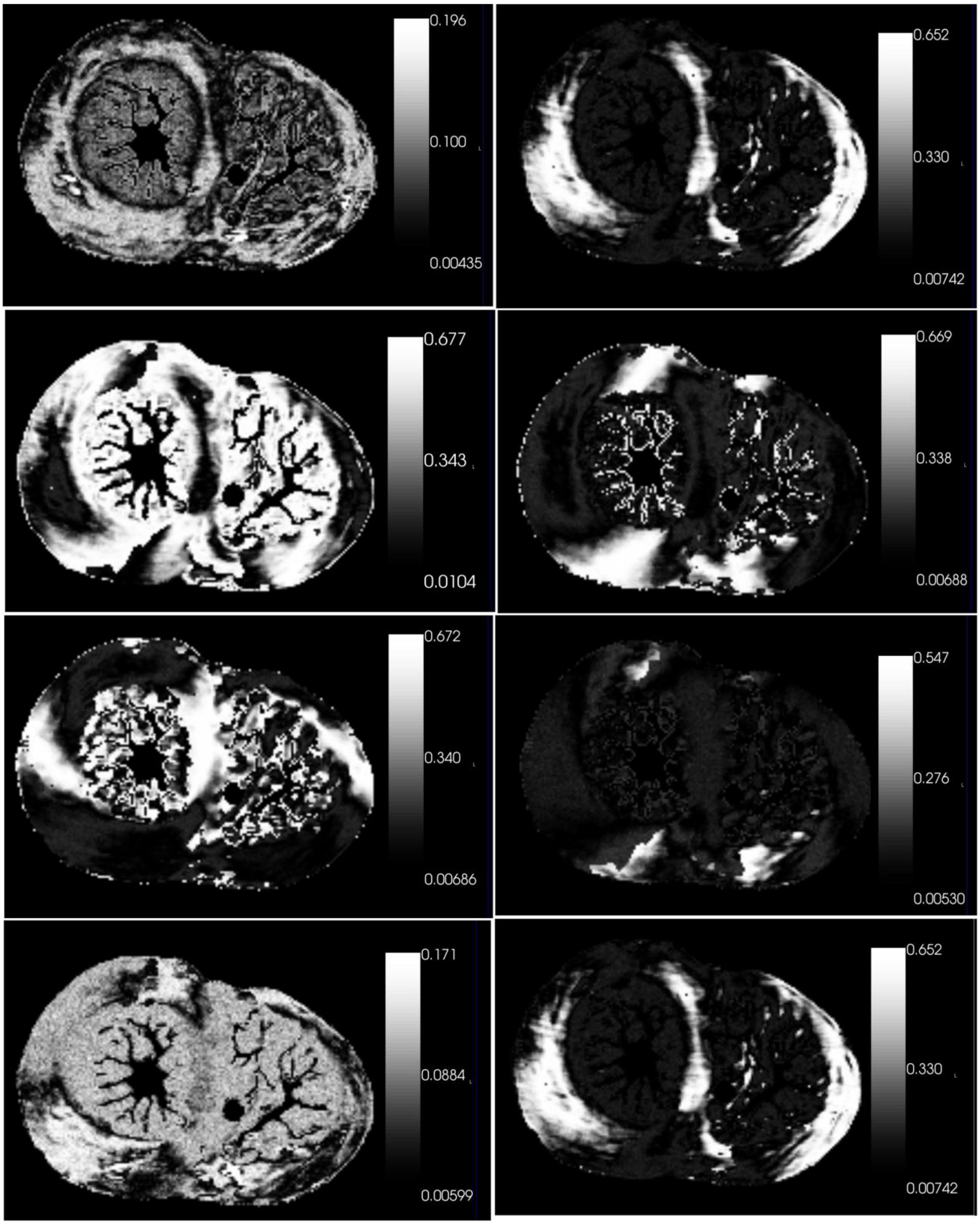

Fig. 6.30 DW images simulated with influence of the slice selection gradient. Slice thickness is 0.5 mm, the excitation RF bandwidth is 2kHz, the resulting slice selection gradient is 93.97 mT/m, and the duration of slice gradient is 7.7 ms.

Since the influence of k-space encoding gradients, the diffusion tensor can no longer be calculated simply using the original b-value. In section 6.3.1, the detailed computing process for b-value and B-matrix are given. We calculate the diffusion tensors with both H-matrix and

B-matix methods. In the H-matrix, the b-value is composed of b_{diffu} , $b_{imaging}$ and b_{cross} which are expressed in Eq.(6.21), (6.22) and (6.23). For the B-matrix method, its components b_{sl} , b_{pe} , b_{ro} , b_{sp} , b_{sr} and b_{rp} are formulated by Eq. (6.14) to (6.19). These two calculation means give the same diffusion results, including the fiber orientation, FA, and MD, which verifies that our B-Matrix and b-value calculated here are correct. Fig. 6.31 shows the diffusion properties obtained with influence of slice selection gradient.

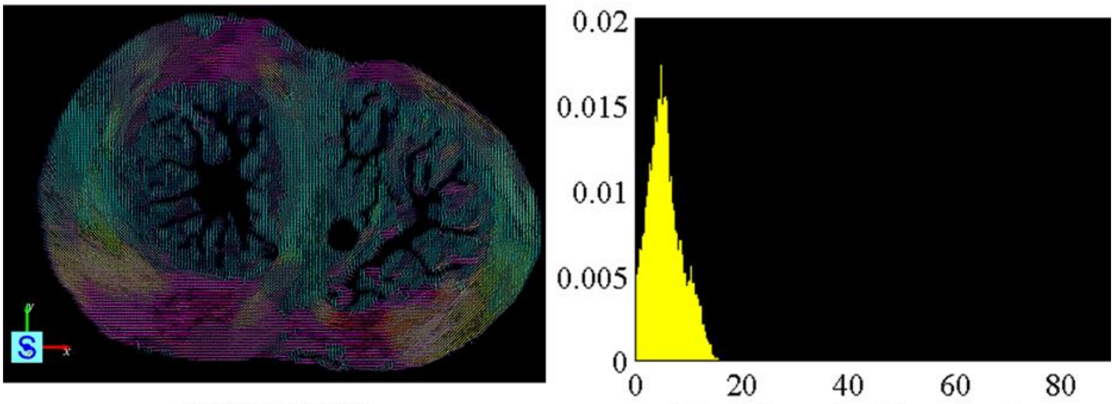

(a) Fiber orientation (b) Deviation angle of Fiber orientation

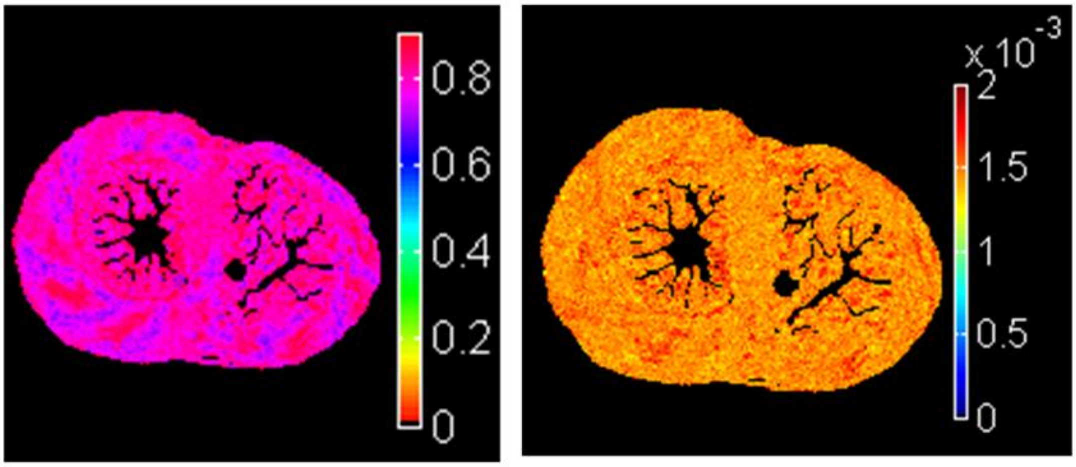

(c) FA (d) MD

Fig. 6.31 Diffusion properties calculated from the DW images in the presence of slice selection gradient using new b-value and B-matrix. (a) shows the fiber orientation represented by the main eigenvector of diffusion tensor, (b) illustrates the distribution of deviation angles (degree) between the simulated cardiac fiber orientation and PLI ground-truth. (c) and (d) represent respectively FA and MD values.

Comparing Fig. 6.31 to Fig. 6.29, we observe that the presence of slice selection gradient induces more measurement errors for fiber orientation estimation and increases FA and MD values. In the absence of slice selection gradient, the b-value generated by diffusion gradient is 999.8 s/mm^2. However, as the effect of slice selection gradient is taken into account, the b-value is 1049 s/mm2, where b_{diffu} is 999.8 s/mm^2, $b_{imaging}$ is 34.5 s/mm^2, and b_{cross} is 14.90 s/mm^2. Note that the slice selection gradient provides about 5% contribution to the b-value during the imaging period. Thus according to Stejskal-Tenner equation in which diffusion signal is expressed by $s = s_0 \exp(-bD)$, the influence of slice selection gradient should be negligible. But from our simulation results we see that the diffusion signal experiences a considerable variation, it implies that using b-value to explain the influence of slice selection gradient is not appropriate anymore, which leads us to interpret it using q-value. Fig. 6.32 shows the evolution of q-value during the imaging period. As the slice selection gradient is switched on, it changes dramatically q-value, varying q from 0 to 16 mm^{-1}. Once the slice selection gradient is switched off, the subsequent slice-refocusing gradient begins to decrease q-value until the diffusion gradient is turned on, and from then the q-value keeps constant. As the slice selection gradient is turned on again during the 180° RF pulse, the q-value is increased firstly and then drops off. With increasing of q-value, the resulted phase shift is increased. Along the restricted diffusion direction, because of the tiny displacement, the change of q-value will not influence greatly the phase shift. However, along the main diffusion direction, the increasing of q-value increases significantly the corresponding phase shift and therefore brings more signal attenuation. As a result, the diffusion coefficient along the main diffusion direction is overestimated, and consequently the measured FA and MD values are bigger, as shown in Fig. 6.31 (c) and (d). Due to the inconsistent weights of the slice selection gradients on diffusion displacement, the fiber orientation derived from the diffusion signal presents more errors.

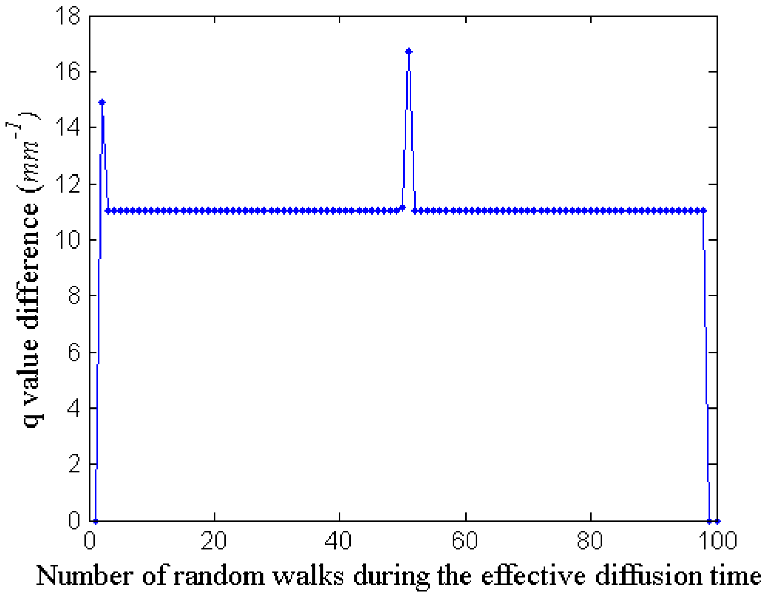

Fig. 6.32 Influence of slice selection gradient on the variation of q-values.

In the presence of phase encoding gradient

In Fig. 6.33, the DW images with the influence of phase encoding gradient are shown. Through the comparison between the image intensity in Fig. 6.33 and that in Fig. 6.28, we observe that the phase encoding gradient enhances greatly the diffusion image contrast, which implies that as the slice selection gradient, the phase encoding gradient also overweighs the water diffusion displacement in some directions.

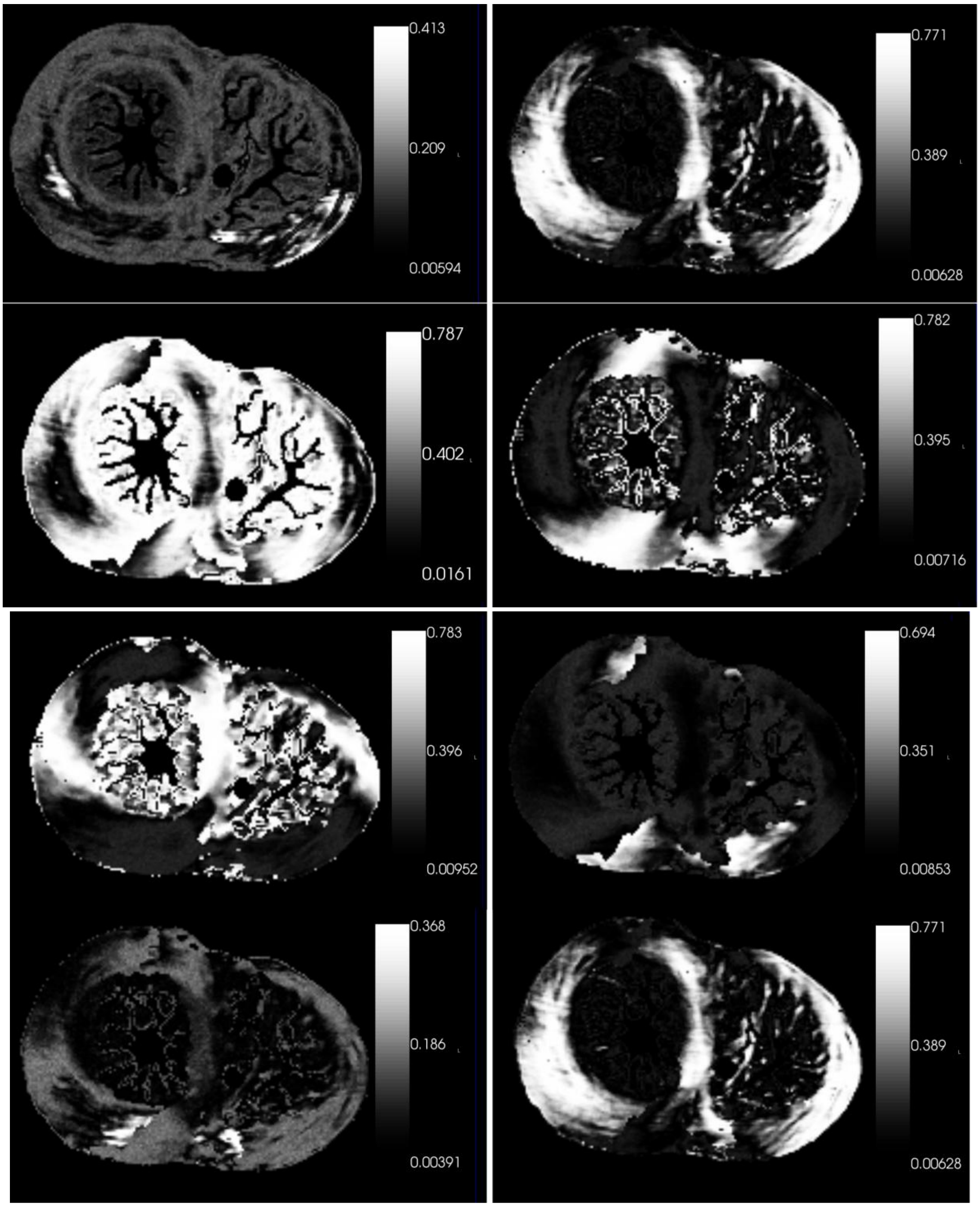

Fig. 6.33 DW images simulated with influence of phase encoding gradient. Spatial resolution along the phase encoding direction is 0.1 mm, the phase encoding gradient strength for each encoding step is 0.34 mT/m and lasting time is 7.7 ms.

The b-value generated by both diffusion and phase encoding gradient is 1004 s/mm^2, in which b_{diffu} is 999.8 s/mm^2, b_{cross} is 4.1 s/mm^2, and $b_{imaging}$ is 0.013 s/mm^2. Fig. 6.34 illustrates the corresponding diffusion properties calculated using this b-value. The angle deviation between the simulated fiber orientation and the ground-truth is about 10º. Compared to Fig.

6.29, the influence of phase encoding gradient on fiber orientation estimation is not so significant. However, for FA and MD values, they are increased greatly. According to Eq. (6.42), the presence of the phase encoding gradient increases the q-value during the whole imaging period. Since the variation of signal intensity with q-value for free and restricted diffusion is so different, thus in the direction of pseudo free diffusion, the signal is attenuated quickly, however, the signal decays slowly along the restricted diffusion direction. Such diffusion signal variation overweighs the diffusion anisotropy and increases FA and MD values.

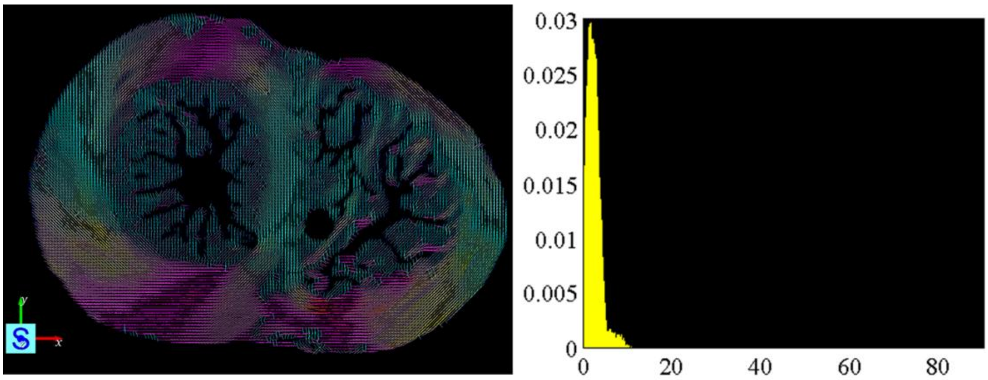

(a) Fiber orientation

(b) Deviation angle of fiber orientation

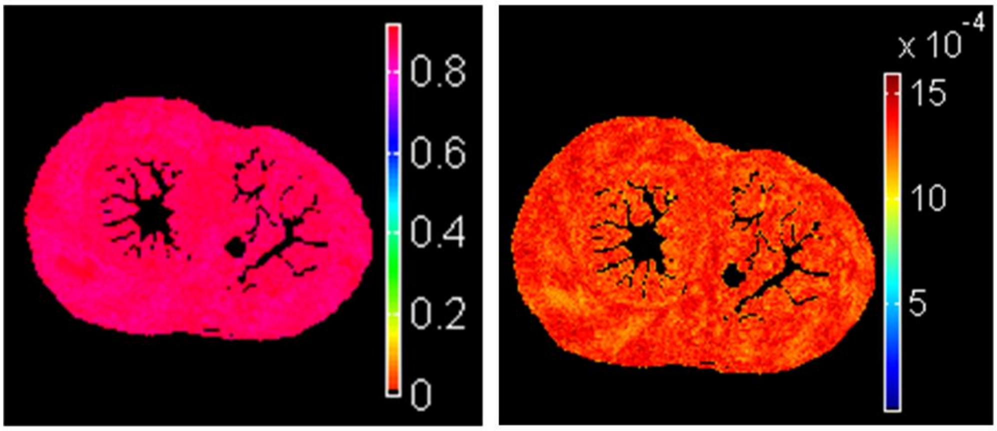

(c) FA

(d) MD

Fig. 6.34 Diffusion properties calculated from the DW images in the presence of phase encoding and diffusion gradients. (a) shows the fiber orientation represented by the main eigenvector of diffusion tensor, (b) illustrates the distribution of deviation angles (degree) between the simulated cardiac fiber orientation and PLI ground-truth. (c) and (d) are respectively FA and MD values.

In the presence of readout gradient

In clinical MRI scanner, the readout pixel bandwidth is about 130 Hz. Therefore, for obtaining a spatial resolution of 0.1 mm, the readout gradient strength should be 30.5 mT/m. With the above diffusion gradient parameters, the resulting b-value is 1002 s/mm^2, in which b_{diffu} is always 999.8 s/mm^2, b_{cross} is 0 and $b_{imaging}$ is 2.5 s/mm^2. The DW images along 8 directions with the influence of frequency encoding (readout) gradient are given in Fig. 6.35. By comparing the image intensity in Fig. 6.35 and that in Fig. 6.28, we can see that the diffusion signal is further attenuated in the presence of readout gradient.

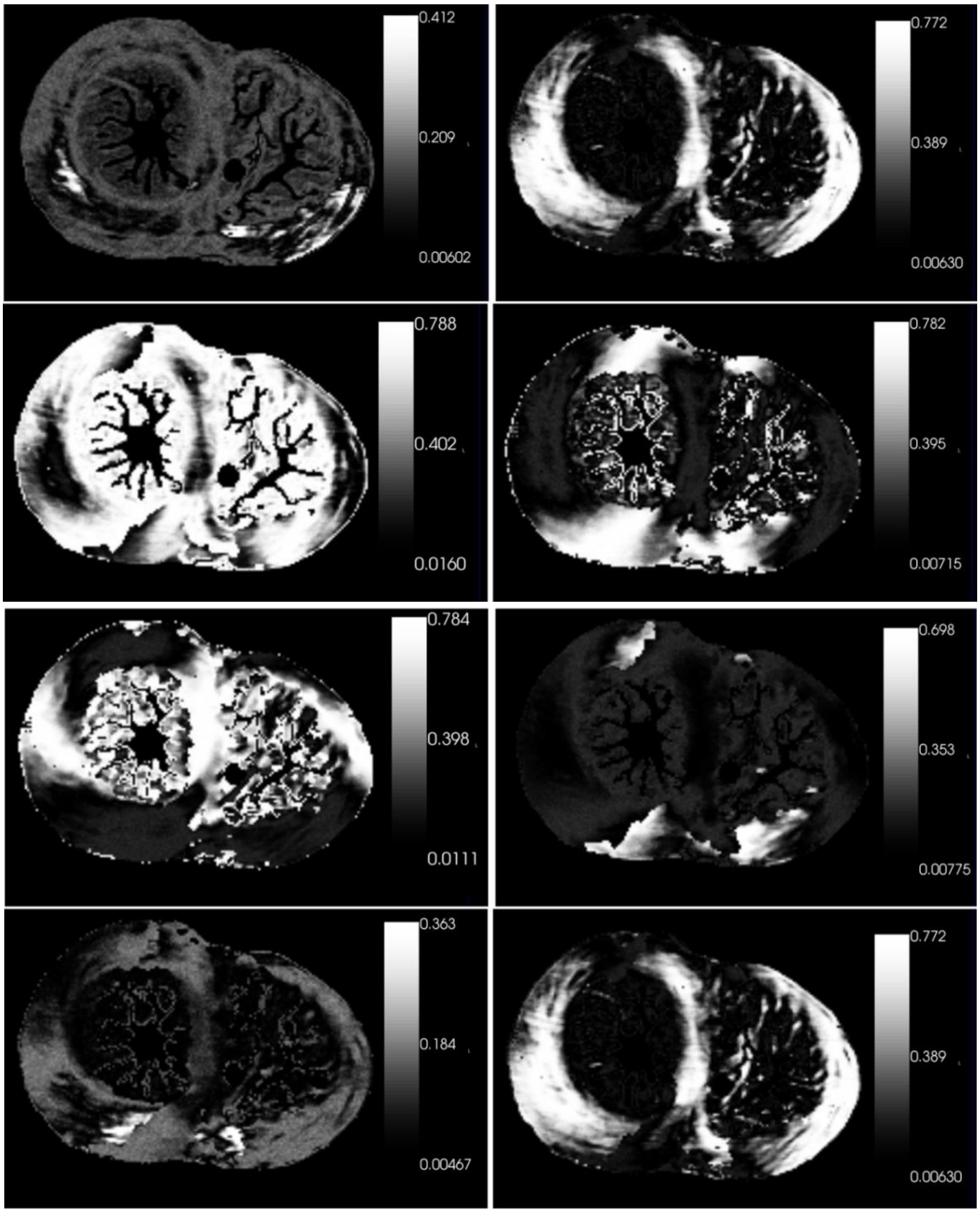

Fig. 6.35 DW images simulated with influence of readout gradient (frequency encoding). Spatial resolution along readout direction is 0.1 mm, the pixel bandwidth is 130 Hz (which results in a gradient pulse duration of 7.7 mm), and a gradient strength of 30.5 mT/m.

The corresponding diffusion properties are given in Fig. 6.36. The presence of readout gradient does not induce much error to the cardiac fiber orientation estimation. However, the FA and MD values increase slightly. This can be explained by the q-value variation during the diffusion time as illustrated in Fig. 6.37. Before acquiring the diffusion signal data, the q-value is always the same, which is determined only by the diffusion gradient duration and strength. However, at the end of diffusion gradient, the introduction of readout refocusing gradient firstly decreases the q-value. As the readout gradient is switched on, the q-value grows back again. This q variation during the time interval of readout gradient induces another phase shift and therefore attenuates the diffusion signal. Along the fast diffusion direction, the q-value variation attenuates more signal than along the slow diffusion direction. As a result, FA and MD values become bigger.

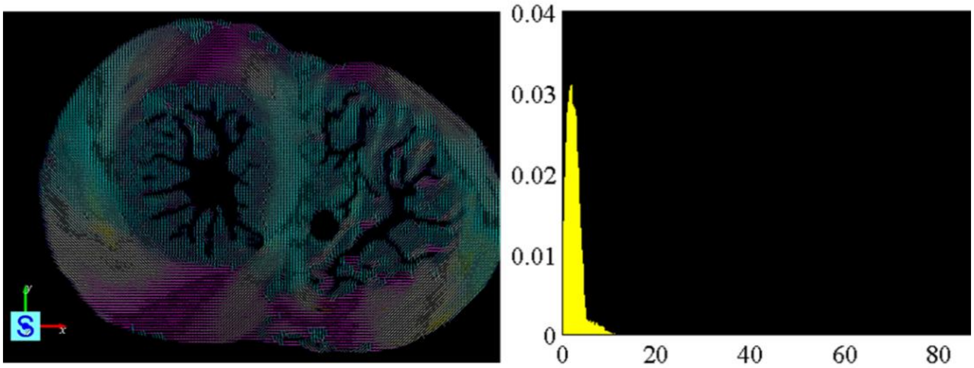

(a) Fiber orientation (b) Deviation Angle of fiber orientation

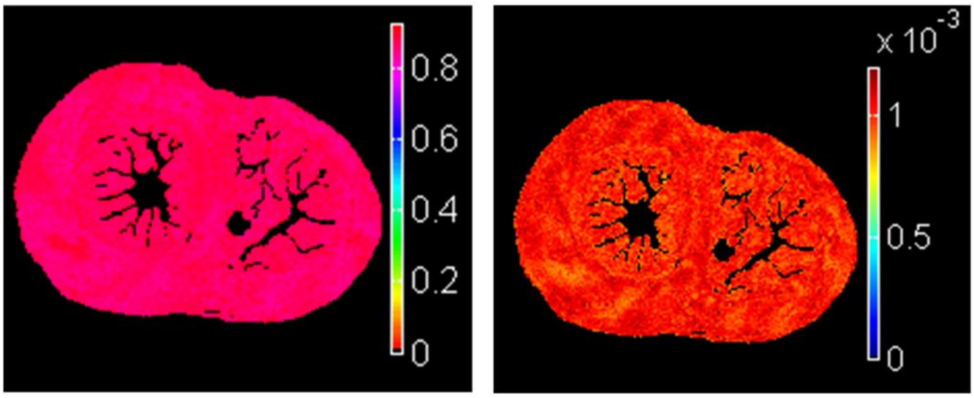

(c) FA (d) MD

Fig. 6.36 Diffusion properties derived from DW images with effects of read out (frequency encoding) gradient.

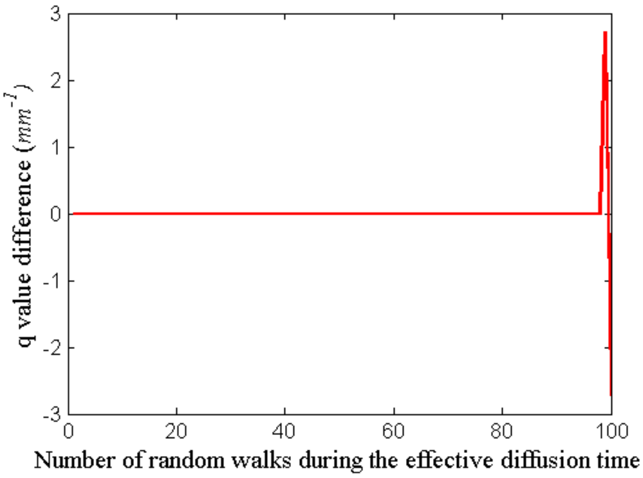

Fig. 6.37 Influence of read out gradient on the variation of q-values.

In the presence of all imaging gradients

We have already analyzed individually the influence of slice selection gradient, phase encoding gradient and the readout gradient on diffusion image intensity and diffusion properties. We now see what kind of variations that DW images and diffusion properties will experience in practical image acquisitions with the presence of all the imaging gradients. In Fig. 6.38 are shown the DW images along different diffusion directions in the presence of all the imaging gradients.

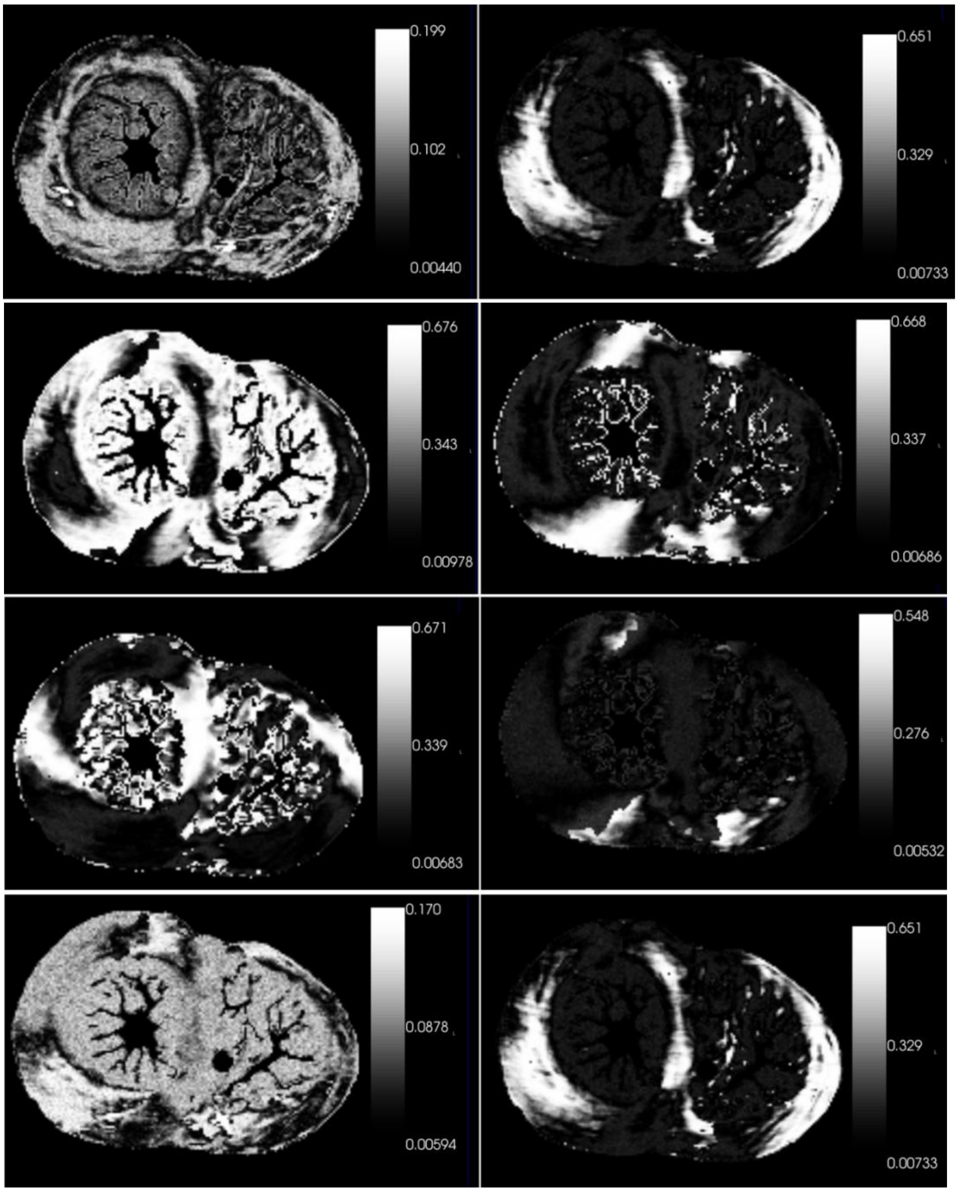

Fig. 6.38. DW images simulated with influence of all the imaging gradients, including the slice selection, phase encoding, readout and diffusion gradients. Slice selection gradient strength and duration are 93.97 mT/m and 7.7 ms respectively. Phase encoding gradient has strength of 0.34 mT/m and lasts 3.35 ms. The strength of readout gradient is 30.5 mT/m and the duration is 7.7 ms.

Notice that the intensity of DW images obtained in the presence of all the imaging gradients have the same variation trends as that of the DW images acquired with only slice selection gradients. This illustrates that the slice selection gradient has the most important effects on diffusion imaging quality and diffusion properties. Regarding the diffusion properties, as shown in Fig. 6.39, the deviation angle, FA and MD values have the same distribution as that obtained with the influence of slice selection gradient, but FA is a little bit bigger than that obtained with slice selection gradient, and MD is smaller.

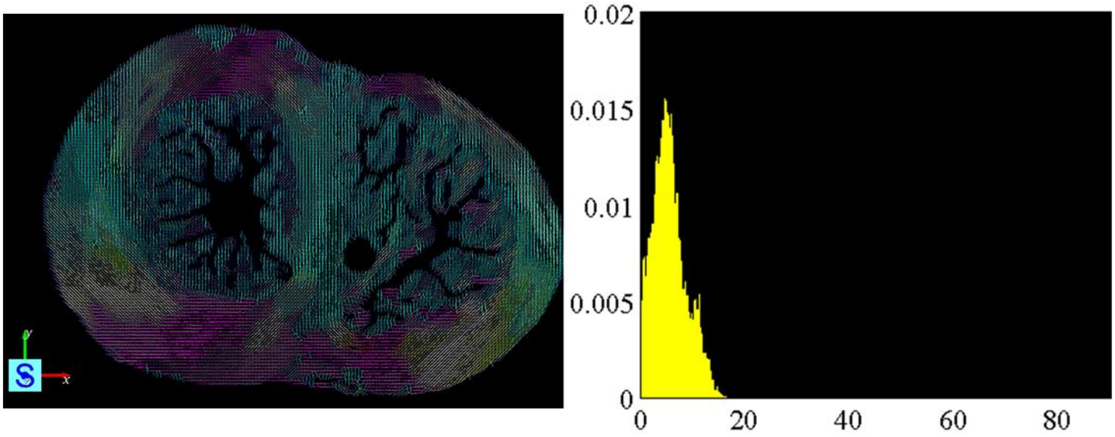

(a) Fiber orientation (b) Deviation angle of fiber orientation

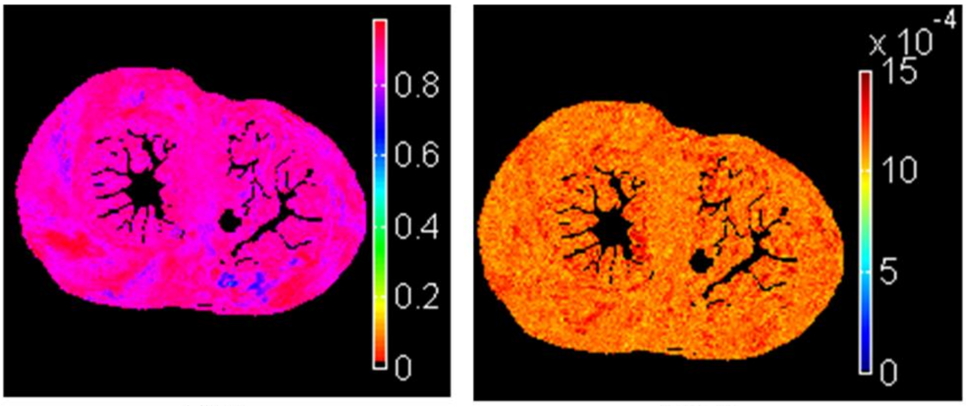

(c) FA (d) MD

Fig. 6.39 Diffusion properties derived from DW images with influence of all imaging gradients.

In the absence of diffusion gradient

In the process of using q-value to analyze diffusion signal, we can see that during the imaging period, the imaging gradients also weight the molecule diffusion. This leads us to assume that even in the absence of diffusion gradient, with high MRI imaging gradients, the DW images and fiber orientation can still be obtained. For testing our hypothesis, the DW images without diffusion gradient are simulated in Fig. 6.40. In order to have the diffusion gradient directions, the diffusion gradient amplitude is chosen as 0.02 mT/m, which results in a b_{diffu} of 7.1×10^{-5} s/mm^2 which is so small that it can be neglected. The imaging gradients generates a $b_{imaging}$ of 36.9653 s/mm^2 and b_{cross} of 0.0051 s/mm^2.

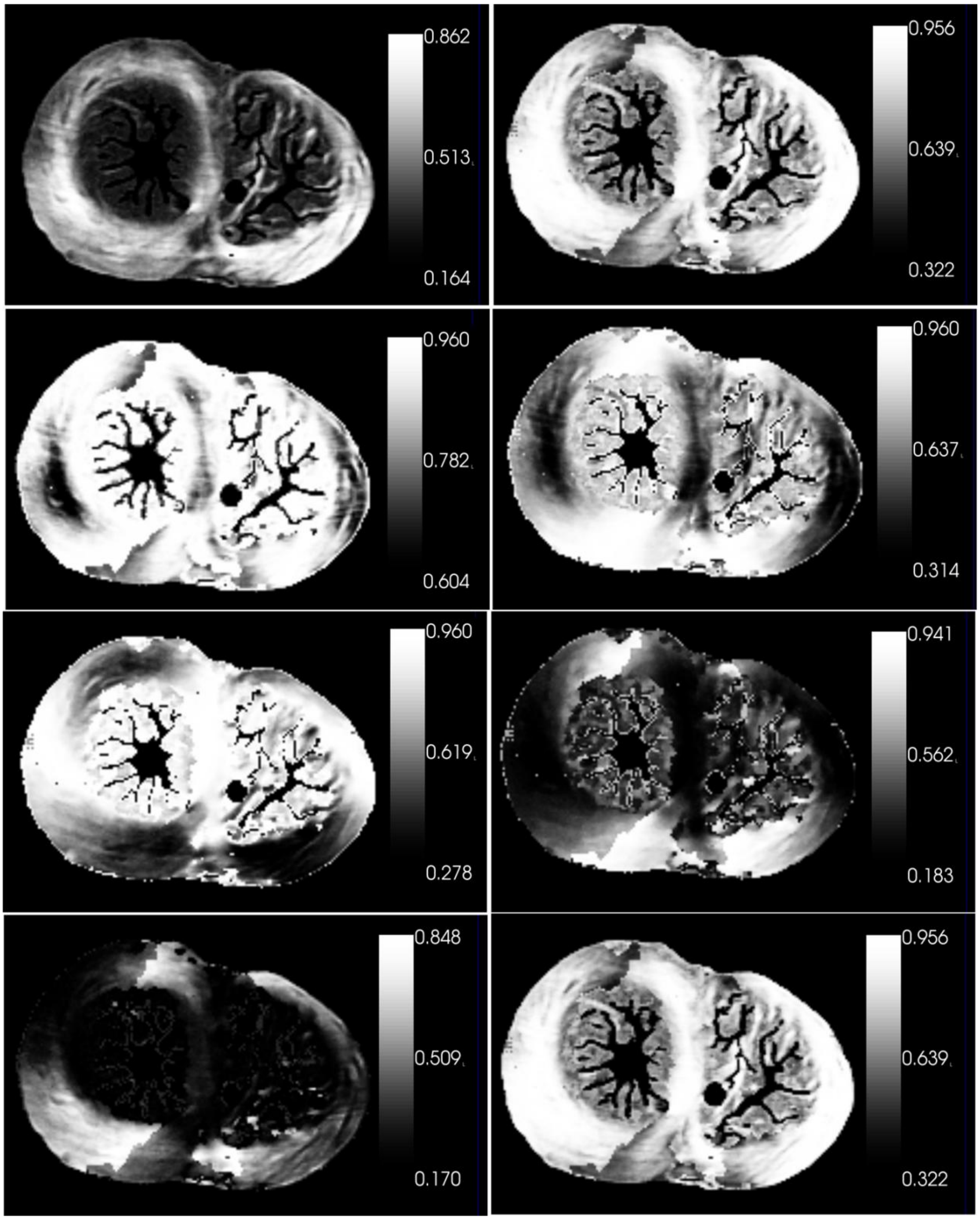

Fig. 6.40 DW images simulated with a tiny diffusion gradient. Slice selection gradient strength and duration are 93.97 mT/m and 7.7 ms respectively. Phase encoding gradient has strength of 0.34 mT/m and lasts 3.35 ms. The strength of readout gradient is 30.5 mT/m and duration is 7.7 ms. Diffusion gradient strength is 0.02 mT/m, duration is 2 ms, and diffusion time is 208 ms.

We can observe that even without diffusion gradient, along the different diffusion directions, the image intensity variation is also present in the images, which verifies our assumption that the k-space encoding gradients for high spatial resolution imaging (high imaging gradient amplitudes) are able to generate the DW images. From which, the diffusion tensor images and the corresponding diffusion properties are calculated (Fig. 6.41), where the deviation angle between the simulated fiber orientation and ground-truth is particular small, about 2°. FA reaches almost the maximum value everywhere about 1, and the simulated MD value is bigger than the free diffusion coefficient. It is difficult to explain this phenomenon using diffusion tensors. Fig. 6.42 shows the variation of q-value during each random walk step in the imaging period. The presence of the imaging gradients makes the q-value experience a dramatic change during the imaging gradients time interval. As we stated, the diffusion signal along the free diffusion direction is very sensitive to the slight changes of q-value. A tiny increment of q-value will induce a big signal intensity change. However, for restricted diffusion, the diffusion signal varies slowly with q-value changes, thus the different weights of q-value variation for the diffusion signal increases FA and MD.

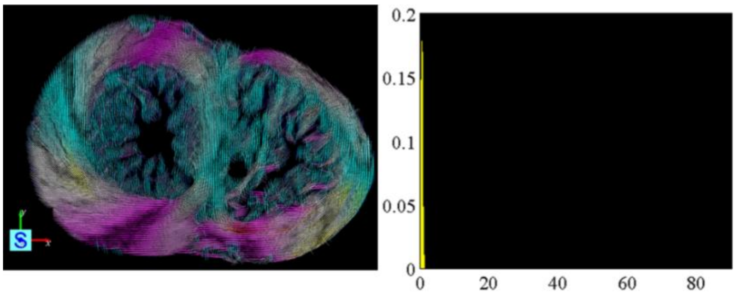

(a) Fiber orientation (b) Angle deviation of fiber orientation

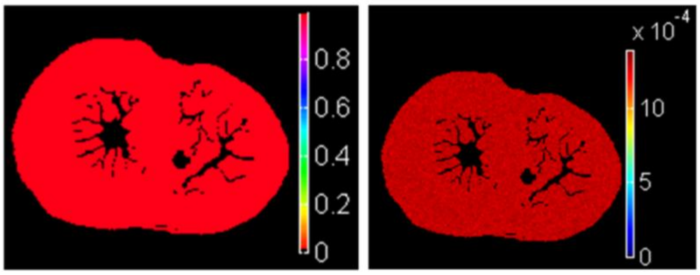

(c) FA (d) MD

Fig. 6.41 Diffusion properties simulated with a tiny diffusion gradient strength.

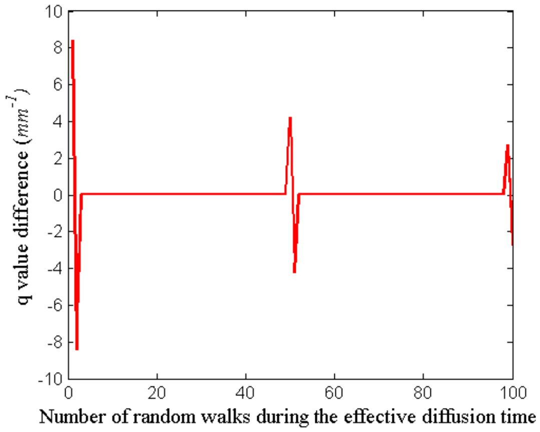

Fig. 6.42 Influence of all the imaging gradients on the variation of q-values.

6.4.2 Discussion

There are few studies in the literature about the effects of k-space encoding gradients on diffusion properties. In the work of [Basser *et al.*, 1994a; Mattiello *et al.*, 1997], the effects of all k-space encoding gradients and diffusion gradient pulses on the b-matrix and b-value calculation for echo-planar imaging (EPI) sequence were investigated, and through the experiments, the authors verified the b-matrix calculation by free diffusion signal analysis. Later, [Gullmar *et al.*, 2005] calculated the b-value for pulsed-gradient spin-echo (PGSE) sequence and validated the calculation with isotropic diffusion phantom. All the above analyses were used for explaining the isotropic diffusion and attempted to use b-matrix for exactly mapping the diffusion tensor. However, if the diffusion tensor can no longer explain the diffusion phenomenon, no matter how exact the b-matrix calculation is, the diffusion properties derived from diffusion tensors will not be correct. In this subsection, we used the q-space theory to simulate the effects of imaging gradients on the diffusion signal and applied the b-matrix to interpret the diffusion properties. The simulation results show that the diffusion properties derived from the diffusion tensors including FA and MD value are not correct, which implies that the diffusion tensor cannot completely explain the diffusion signal weighted by the imaging gradients. From diffusion tensors, fiber orientation can be estimated roughly, but due to the magnetic field inhomogeneity caused by the gradients, the diffusion indices calculated from the diffusion tensors are not accurate.

Moreover, by analyzing the respective influence of slice selection, phase encoding and readout gradients, we can see that the estimation error induced by diffusion tensors is determined by the interaction between the k-space encoding and diffusion gradients. For instance, the cross item between slice selection and diffusion gradients for b-value is about 14.9 s/mm^2, and that for phase encoding and readout encoding is only about 4.1 and 0 s/mm^2; thus the influence of slice selection is more significant.

Finally, through the simulation, we verified that without diffusion gradient, the DW images could also be obtained by strong imaging gradients, but that the diffusion indices such as FA and MD cannot be derived from the subsequently calculated diffusion tensors. Further experiments to verify our conjecture and further experiments to verify our conjecture and further interpretation of this kind of DW images are necessary in our future work.

6.5 Conclusion

Based on the simulation theory in the previous chapters, we firstly simulated the effects of diffusion gradient parameters including diffusion time, gradient strength and duration on the diffusion image properties with the aid of the perfect diffusion gradient. Our findings are consistent with those reported in the literature, which suggests that the proposed dMRI simulator could be used for optimizing diffusion gradient parameters following tissue properties. Then, according to the actual diffusion gradient characteristics in practice, the improvement in diffusion signal calculation theory and Monte-Carlo simulation algorithms was achieved, based on which the effects of diffusion time, gradient duration and ramp time on actually acquired image properties were analyzed. Through simulation and taking into account the relationship between gradient strength, duration and ramp time, we have been able to find a reasonable comprise between these parameters for high b-value imaging. Finally, the influence of k-space encoding gradients, including the slice selection, phase encoding and readout gradients, was considered. The improved dMRI simulator in this chapter allows us to analyze the influence of any imaging parameters on the cardiac fiber architecture properties. By means of the established relationship between the imaging parameters and in light of their influences on imaging properties, the proposed simulation model allows us to find optimal imaging parameters that satisfy a specific requirement.

Chapter 7

dMRI simulation of *in vivo* cardiac fibers

Contents

Résumé en français

L'architecture des fibres cardiaques joue un rôle très important pour maintenir la fonction cardiaque normale, elle relie les propriétés électrophysiologiques et mécaniques du muscle du cœur. Cependant, la relation entre l'architecture des fibres cardiaques et des pathologies cardiaques est inconnue. Dans ce contexte, l'étude de la structure des fibres cardiaques *in vivo* apparaît fondamentale et primordiale, et l'IRMd offre un moyen d'investigation non invasive très prometteuse pour y arriver. Malheureusement, l'IRMd *in vivo* pour les fibres cardiaques en 3D reste actuellement toujours un défi à cause de sa sensibilité aux variations de phase de spin, causées par le mouvement du cœur.

De nombreuses approches sur l'acquisition ont été proposées pour obtenir des images de diffusion *in vivo*. Mais, en raison du mouvement rapide du cœur, ces techniques se limitent actuellement à une seule coupe en 2D, et il fallait utiliser un modèle d'extrapolation pour obtenir des volumes 3D *in vivo*. Afin d'éliminer l'influence du mouvement cardiaque sur la qualité d'images pondérées en diffusion, la relation entre le mouvement cardiaque et le signal de diffusion a été étudiée. Les approches proposées estiment le mouvement minimum en fonction de la variation en intensité du signal, en se basant sur l'hypothèse que l'atténuation du signal de diffusion est essentiellement induite par le mouvement du cœur. Toutefois, dans la réalité, pendant un cycle cardiaque, le plus grand mouvement cardiaque peut atteindre jusqu'à environ 20 mm le long de la direction longitudinale, ce qui signifie que l'intensité du signal à ce voxel peut être produite par une zone assez grande du myocarde, où l'arrangement des fibres cardiaques peut ne pas être homogène, Dans ce cas, il serait difficile de savoir si la variation du signal est causée par le mouvement ou par la modification de la structure.

Afin de résoudre ce problème et de mieux comprendre la relation entre le mouvement cardiaque et les propriétés des images pondérées en diffusion, nous proposons de simuler les images de diffusion des fibres cardiaques *in vivo* à l'aide de notre simulateur d'IRMd. L'idée consiste à modéliser d'abord l'architecture des fibres cardiaques *in vivo* en utilisant une structure de fibres cardiaques référente et un champ de mouvement cardiaque connu disponible, et ensuite à simuler les images de diffusion à des instants différents, une première analyse des resultats est proposé.

7.1 Context and objectives

Cardiac fiber architecture has an important role in maintaining normal cardiac function, because it is able to reveal the electrophysiological and mechanical properties of the cardiac muscle [Kanai *et al.*, 1995]. If the relationship between the cardiac fiber architecture and the heart strain is elucidated, it will have an important impact on the clinical predictions of cardiac pathologies. For such reasons, investigating the *in vivo* cardiac fiber structure is highly necessary. dMRI then provides a great potential to achieve this owing to its noninvasive property. However, *in vivo* dMRI of 3D cardiac fibers is currently still a great challenge due to its sensibility to spin phase variations, which are usually affected by the heart physical motion [M-T Wu, 2006; Gamper, 2007]. Various acquisition approaches have been proposed for obtaining *in vivo* diffusion weighted images [Dou *et al.*, 2003; Gamper, 2007]. However, due to the fast heart motion, these techniques are currently limited to a single 2D slice, and they still require extrapolation models to obtain fully 3D *in vivo* images [Toussaint, 2010; Nielles-Vallespin, 2012]. In order to remove or reduce the influence of heart motion on the quality of diffusion weighted images, the relationship between cardiac motion and diffusion signal has been investigated [Rapacchi *et al.*, 2011]. It is considered that at a given voxel, the minimum motion point can be found according to the signal intensity variation. This method is based on the hypothesis that the main signal loss is just induced by the bulk heart motion. However, actually, during one cardiac cycle, the biggest cardiac motion can reach about 20 mm along the longitudinal direction, which implies that the signal intensity at this voxel is produced by a rather big myocardial region, where the arrangement of cardiac fibers may not be homogeneous. In this case, it would be difficult to distinguish the signal variation caused by motion from that caused by change in fiber structure.

Cardiac motion is a complex process and its accurate 3D estimation remains a persistent problem. As a first approach, we will use an existing basic 3D motion field to deform ex vivo cardiac fibers to get some insights into the relationship between cardiac motion and diffusion weighted image properties. To do that, we attempt to use our dMRI simulation method described in the above chapters. The idea consists in modeling the *in vivo* cardiac fiber architecture using a referential cardiac fiber structure and a heart motion field a priori known, and accordingly simulating its diffusion images. The obtained preliminary results are discussed.

7.2 Estimation of heart motion

The non-invasive and quantitative estimation of cardiac motion is fundamental for analyzing heart contractile abnormalities, and it provides a useful mean for characterizing cardiac pathologies. However, to date, estimating accurately the real heart motion is still a challenge due to the complexity of cardiac and vascular structures and their variability. Many methods have been proposed for the estimation of cardiac motion based on various imaging modalities. The most common modality for the evaluation of cardiac motion is MRI tissue tagging, which was introduced by [Zerhouni *et al.*, 1988]. It uses a special pulse sequence to spatially modulate the longitudinal magnetization of the tissues to create temporary features, called tags. The motion of these tags can be measured using MRI CINE sequence that enables us to track the material points in many 3D images acquired from different orientations and at different times. Tagged MRI has been intensively investigated in recent years [Petitjean *et al.*, 2005; Pai *et al.*, 2006]. For instance, it has been used to develop the models of normal and pathological myocardium structures [V Wang *et al.*, 2009], to analyze the activation patterns and to predict myocardial ischemia [Shehata *et al.*, 2009]. Despite these successful uses, tagged MRI lacks high spatial resolution since it requires clear tag-grid definition and the tagging post-processing costs much time.

Magnetic resonance phase contrast (PC) velocity encoding of the myocardial wall can provide functional information at high spatial resolution [Markl *et al.*, 2002; H Wang *et al.*, 2012]. Data processing with such method is easily performed since velocity information is directly extracted from the complex digitized signal. Bulk motion and rotation correction by post-processing can allow for data visualization with minimal user effort. However, PC velocity encoding techniques sample the first derivative of displacement with respect to time and therefore signal-to-noise ratio can be a limiting factor when considering the rate of motion variation.

Displacement encoding with simulated echoes (DENSE), a relatively novel method in cardiac MRI based on the work of Reese [Reese *et al.*, 1996] was previously demonstrated in canines *in vivo* [Aletras *et al.*, 1999]. DENSE encodes displacement onto the phase of the spin during the mixing time TM of a STEAM (stimulated echo acquisition mode) experiment. As such, extracting displacement information from the phase images is similar to PC velocity-encoding method. The measured displacement has sufficient precision for accurate strain calculations. Data processing involves little operator interaction.

In this thesis, we use an available rather "simple" motion model of the global heart [Haddad, 2007] to animate the 3D cardiac model including the fiber architecture for demonstrating the feasibility of our dynamic simulation approach. For better understanding the following modeling and simulation methods, we introduce here briefly the motion acquisition process, as illustrated in Fig. 7.1.

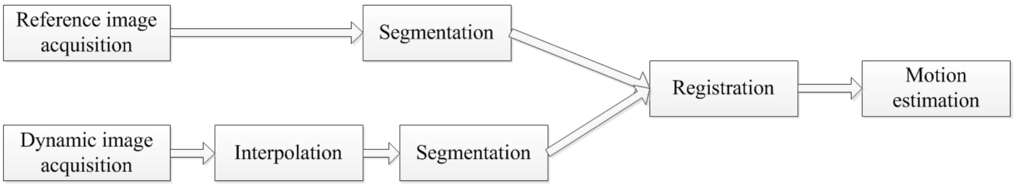

Fig. 7.1 Motion estimation process

[Haddad, 2007]:

Reference image acquisition: A 3D acquisition along transverse orientation was performed using 3D-Sense sequence at iso-volumic phase of the cardiac cycle, where the heart volume keeps almost constant. The image parameters are: spatial resolution is 0.53 × 0.53 mm^2, image matrix is 512 × 512, slice thickness is 2 mm and inter slice space is 1 mm, slice number is 165.

Dynamic image acquisition: A series of images for the same heart was acquired using the CINE balanced turbo field echo (TFE) sequence during one cardiac cycle (14 phases totally). Temporal resolution is 64 ms and spatial resolution in the transverse plane is 1.25 × 1.25 mm^2. Image matrix is 256 × 256. There are 19 slices with thickness of 7 mm and spacing of 7 mm.

Interpolation: In order to estimate the 3D cardiac motion, 3D volumes should be reconstructed from a series of acquired 2D slices.

Segmentation: After the interpolation, according to the cardiac structure properties, the whole heart was segmented into several parts: left ventricle (LV), right ventricle (RV), left atrial (LA), right atrial (RA), aorta and veins.

Registration: For the images acquired with same imaging modality, the motion estimation can be realized using image registration. Taking one image acquired at time t as the reference, through the rigid and free form deformation (FFD) transform [Rueckert *et al.*, 1999] we can match the reference image and the image acquired at time of $t+1$.

Motion estimation: According to the transformation derived from the registration above, the cardiac motion field for any positions can be calculated.

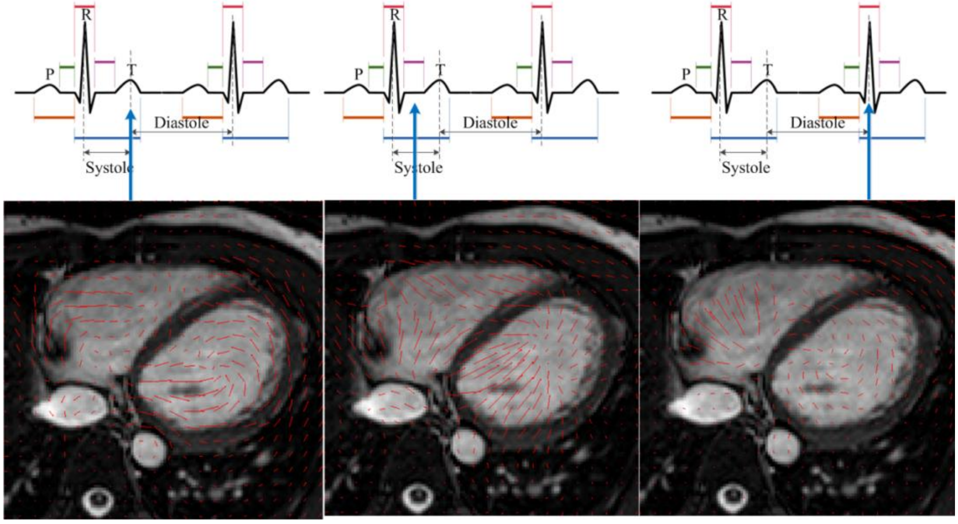

(a) (b) (c)

Fig. 7.2 Motion field for three cardiac circle phases. (a) At the beginning of diastole, (b) At the middle of systole, (c) At the end of diastole.

Fig. 7.2 illustrates the estimated motion field using the above process. It can be seen that the cardiac motion generally towards to the inner cavity in the middle of the LV systole and reverse this trend at the beginning of diastole.

7.3 *In vivo* cardiac fiber modeling

The above images allow us only to obtain “rough” 3D cardiac motion information of an adult heart, but are unable to provide us the related cardiac fiber structure. In order to simulate the diffusion images of *in vivo* hearts using our dMRI simulator, both fiber structure and motion information for the same heart are required. To this end, we propose to register the motion information of the heart proposed by [Haddad, 2007] to the heart with fiber structure a priori know provided by the Jonhs Hopkins university. The cardiac fiber architecture is derived from a cardiac diffusion tensor magnetic resonance imaging (DT-MRI) dataset of the human adult heart. This dataset was acquired using very long time repeated accumulation (more than 48 hours) to increase the signal-to-noise ratio. It is under the form of vector fields downloaded from the website http://www.ccbm.jhu.edu/research/DTMRIDS.php. The corresponding acquisition parameters are the following: gradient directions are 19, spatial resolution is 0.43 × 0.43 × 1 mm^3, and image size is 256 × 256 × 134. From this dataset is generated the cardiac fiber structure of an adult heart with the aid of our modeling approaches elaborated in chapter 5.

7.3.1 Registration

Combining the cardiac fiber architecture of one heart and the motion of another heart can be achieved by two kinds of registration. If we call the heart used for measuring the motion as the ADAM (A Dynamic Anthropomorphic Model) [Haddad, 2007], and the heart with the fiber structure as CCBM (since the human cardiac DI-MRI dataset comes from the Center for Cardiovascular Bioinformatics and Modeling, Johns Hopkins university), the registration can be performed from ADAM to CCBM or inversely. The former requires changing the motion information to adapt it to the CCBM heart, and the latter needs to change the cardiac fiber structure of the CCBM to make it conform to structure of the ADAM heart. In view of the fact that the cardiac fiber architecture is the most important information, the used registration should not alter the original cardiac fiber arrangement. Meanwhile, the correct motion estimation for the CCBM heart is also important for obtaining a meaningful simulated *in vivo* cardiac fiber structures. For these reasons, we make a mutual registration between the ADAM and CCBM hearts, namely we first perform a 3D rigid registration by aligning the CCBM heart to the ADAM heart. This rigid registration does not change the fiber arrangement and provides us an intermediate heart. Then, we register the ADAM heart to this intermediate heart using a 3D affine and deformable registration to match each other. Since the intermediate heart aligns with the ADAM heart, and the size and the shape of the two hearts are not identical, the motion information in the intermediate heart resulting from this registration will not be very accurate. The detailed registration steps are described hereafter.

Segmentation of the ADAM and CCBM hearts

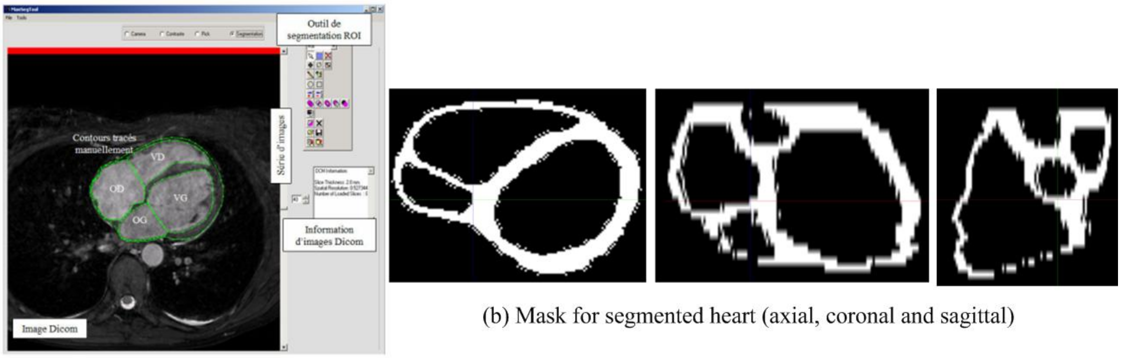

(a) Interface for segmentation

(b) Mask for segmented heart (axial, coronal and sagittal)

Fig. 7.3 Illustration of the segmentation interface and the segmented heart mask.

The ADAM is a module for describing the breathing thorax and beating heart. It can be used to generate the numerical model for *in vivo* cardiac and vascular anatomical structures. The acquired MR images of the heart include different structures such as LV, RV, RA, LA and the vascular. In order to perform the registration, the LV, RV, RA and LA should be firstly extracted from these images. This was realized by the interactive software developed by our lab, which is based on the VTK library and DaVaW library of the laboratory Creatis. The extracted contours are verified and modified by the medical doctors. Fig. 7.3 illustrates the segmentation interface and the corresponding segmented heart structure mask.

The CCBM dataset provides both vector field of cardiac fiber orientations and B0 image. Compared to the ADAM images, the heart structure in the B0 image of CCBM is easy to distinguish. Therefore, the segmentation is performed using the threshold segmentation algorithm and then using the additional manual segmentation to remove the tiny structures and finally convert it to the mask. The corresponding results are shown in Fig. 7.4.

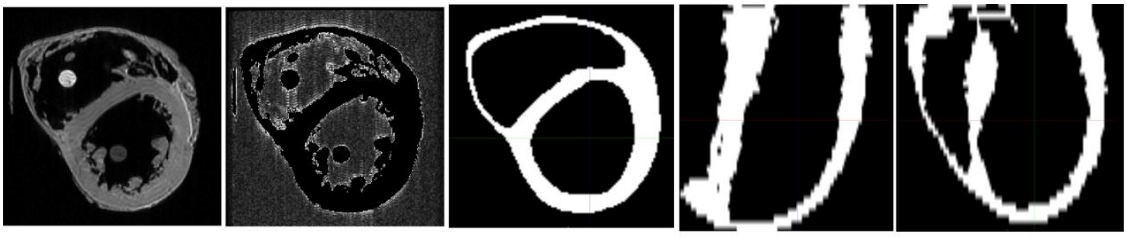
(a) One slice of b0 image for CCBM heart
(b) Result after threshold segmentation
(c) Axial mask for CCBM heart
(d) Coronal mask for CCBM heart
(e) Sagittal mask for CCBM heart

Fig. 7.4 Illustration of the segmentation results for the CCBM heart.

After the segmentation, in registering two types of images, the image voxel size and image dimensions should be adjusted. The ADAM heart mask has a spatial resolution of 1.25 × 1.25 × 4 mm^3 and the image dimension is 128 × 128 × 45. The spatial resolution of the original CCBM heart mask is 0.43 × 0.43 × 1 mm^3 and the image dimension is 256 × 256 × 134. Using sampling and interpolation methods, the CCBM mask is adjusted into the dimension of 128 × 128 × 38 with a resolution of 1.25 × 1.25 × 4 mm^3.

Rigid registration

Deforming the point (x, y, z) of one structure to another can be described by global (rigid or affine) and local transformation (deformable).

$$T(x,y,z) = T_{global}(x,y,z) + T_{local}(x,y,z) \tag{7.1}$$

$$T_{global} = \begin{bmatrix} x' \\ y' \\ z' \\ 1 \end{bmatrix} = \begin{bmatrix} r_{x1} & r_{x2} & r_{x3} & dx \\ r_{y1} & r_{y2} & r_{y3} & dy \\ r_{z1} & r_{z2} & r_{z3} & dz \\ 0 & 0 & 0 & 1 \end{bmatrix} \begin{bmatrix} x \\ y \\ z \\ 1 \end{bmatrix} \tag{7.2}$$

The global transformation can be either rigid or affine. The rigid transformation does not change the distance and the angle between every pair of points during the registration. It consists of a rotation and a translation. There are three parameters need to be estimated for 2D rigid registration and six for 3D. The rigid transformation is usually represented by the following equation

$$T_{global} = \begin{bmatrix} x' \\ y' \\ z' \\ 1 \end{bmatrix} = \begin{bmatrix} R & Dis \\ 0 & 1 \end{bmatrix} \begin{bmatrix} x \\ y \\ z \\ 1 \end{bmatrix} \tag{7.3}$$

where R is the rotation matrix and Dis is a vector giving the translation of the origin. The rotation matrix R is determined by the rotation angles α, β, χ about axes x, y and z

$$R = R_x R_y R_z \tag{7.4}$$

$$R_x = \begin{bmatrix} 1 & 0 & 0 \\ 0 & \cos(a) & -\sin(\alpha) \\ 0 & \sin(\alpha) & \cos(\alpha) \end{bmatrix} \tag{7.5}$$

$$R_y = \begin{bmatrix} \cos(\beta) & 0 & -\sin(\beta) \\ 0 & 1 & 0 \\ \sin(\beta) & 0 & \cos(\beta) \end{bmatrix} \tag{7.6}$$

$$R_z = \begin{bmatrix} \cos(\chi) & -\sin(\chi) & 0 \\ \sin(\chi) & \cos(\chi) & 0 \\ 0 & 0 & 1 \end{bmatrix} \tag{7.7}$$

Affine registration

Affine registration is one of the most commonly used methods in registering two images. Although only linear, it models a combination of effects stemming from four simple transformations: translating, rotating, scaling and shearing. An affine registration corrects some global distortions in the image to be registered. The affine registration can be expressed by the general expression of global transformation in Eq. (7.2). In this matrix, the scaling and shearing information is included. In affine registration, there are 12 parameters that need to be estimated, 3 for rotation, 3 for translation, 3 for shearing and 3 for scaling.

As we choose the ADAM heart as reference and the CCBM heart as the moving image, we use the landmark-based affine registration to align the CCBM heart to the ADAM heart. More details about landmark-based registrations can be found in [Rohr *et al.*, 2001]. The landmarks can be anatomical or geometrical points, such as visible morphological features. The landmark-based registration consists in determining one transformation of these features: any features of the moving image are mapped onto the corresponding features of the fixed image. More precisely, if A and B are two images to be registered. Assuming that $F(A, j)$ and $F(B, j)$ are the given features of the images A and B, with $j = 1,2,3...m$ where m designates the number of features involved. The transformation T of a landmark-based registration can be expressed by:

$$F(A,j)=T[F(B,j)] \quad j=1,2,3...m \tag{7.8}$$

In our case, T is restricted to one affine transformation. We choose manually four pairs of features (landmarks) according to the heart anatomical structures. These four features are respectively the left ventricle center, the two connection points of left and right ventricles along the axial direction (up and down), and the apex. The registration is realized by the ITK applications of LandmarkBasedTransformInitializer. The affine registration result is illustrated in Fig. 7.5.

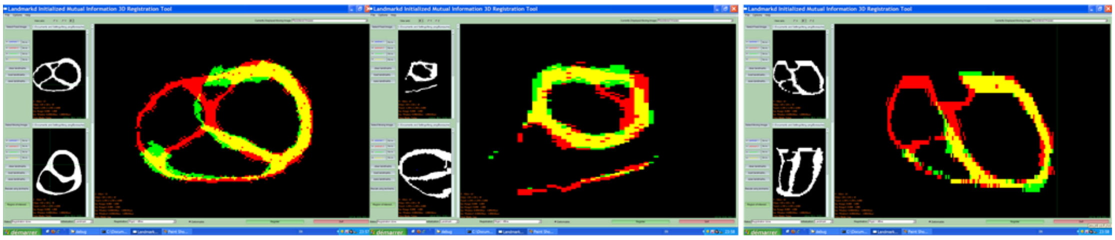

Axial Coronal Sagittal

Fig. 7.5 Register the CCBM heart to the ADAM heart using landmark-based affine transformation.

It can be observed that the two images are not perfectly matched. This is because, as we mentioned, only global registration is permitted in order to avoid destroying the cardiac fiber arrangement of the CCBM heart. To accurately match cardiac motion information of the ADAM heart onto the CCBM heart, registration of the ADAM heart to the intermediate image should further be performed. As the rigid registration is unable to match them perfectly, further non-rigid deformation is required.

Non-rigid registration

Transformations used in non-rigid registration ranges from smooth regional variation described by a small number of parameters to dense displacement fields defined at each voxel. There are numerous models about the non-rigid transformation. According to the constraint conditions, they can be divided into two main categories: non-parametric and parametric registrations.

Non-parametric non-rigid registration

Among the non-parametric registrations, we can cite the elastic registration [Broit, 1981; Christensen *et al.*, 2001; Ashburner, 2007], in which the image under deformation is modeled by an elastic object, under the influence of intra- and extra-forces the image is deformed until these two forces cancel out. In general, the elastic registration is only limited to small deformations. To cope with larger deformations, the viscous fluid registration was proposed [Christensen *et al.*, 1996; D’Agostino *et al.*, 2003; Crum *et al.*, 2005] that models the image transformation as a viscous fluid and the deformation is governed by the Navier-Stokes equation. This method evolves the fluid velocity field with time according to the deformation, and therefore it allows the moving image deforming smoothly into the fixed image even when large deformations are encountered. Computing efficiency is an issue of viscous fluid models and is the most important reason that they are not widely used as other popular non-rigid registration methods. In order to reduce the computing time, the demons registration algorithm was proposed by Thirion [Thirion, 1998]. It calculates the transformation field based on the image edge forces, and using Gaussian kernels to regularize the transformation field to make it smooth. Strictly speaking, demons is a registration framework rather than a method, because a lot of methods were derived from it, such as the diffeomorphic demons registration [Vercauteren *et al.*, 2009], spherical demons [Yeo *et al.*, 2010], and multi-modality demons [Lu *et al.*, 2010]. Because of the high registration accuracy, the demons methods are widely used in medical image registration.

Parametric non-rigid registration

Unlike non-parametric non-rigid registrations, in which the transformations do not require some special parameters for the calculation of the deformation, the parametric non-rigid methods describe the space transformation in terms of a finite number of parameters, such as the image intensities or features. The most important parametric registration method is based on the basis function, especially the splines, such as thin plate spline (TPS) [Rohr, 2001], B-spline [Szeliski *et al.*, 1997] and free form deformation (FFD) [Rueckert, 1999; Holden, 2008].

In our application of registering the ADAM heart to our deformed CCBM heart, to guarantee the registration accuracy, we use the diffeomorphic demons transformation method [Lenglet *et al.*, 2005; Lu, 2010] to deform the heart motion. The registration result is shown in Fig. 7.6.

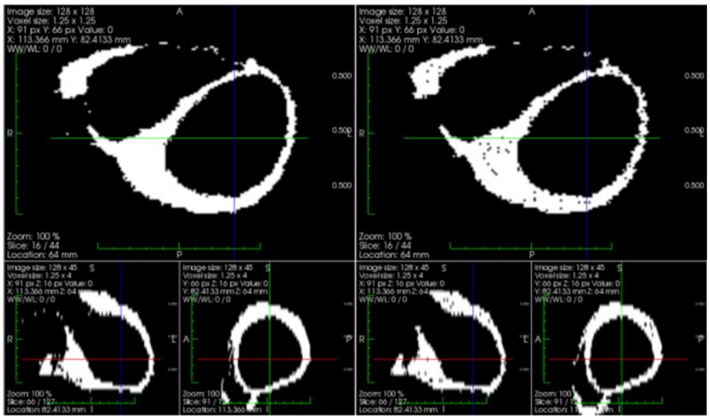

Fig. 7.6 Register the ADAM heart to the deformed CCBM heart to derive heart motion information. Left: the deformed ADAM heart (moving image). Right: the intermediate CCBM heart (fixed image).

The interpolation method used in this registration is B-spline. According to the transformation matrix, new heart motion for each voxel of the deformed ADAM heart is calculated that conforms to our deformed CCBM heart structure.

7.3.2 Modeling *in vivo* cardiac fiber structure with FFD

Once the motion field is obtained, we use the free form deformation (FFD) to vary the cardiac fiber architecture and orientations at different cardiac cycle moments.

FFD is an important tool for modeling dynamic geometries, which deforms the objects by deforming the space in which the object is embedded. The space is usually divided into a series of control points, whose displacements determine the object shape variations. Fig. 7.7 shows the principle of FFD. To describe the FFD, a new spatial space $\Omega(s,t,u)$ should be first defined. Here, we align the axes s,t,u to the Cartesian coordinates x,y,z. For a point in the regular region whose Cartesian coordinates are (x,y,z), the corresponding locations in the coordinates (s,t,u) are defined as:

$$s = (\frac{x - x\min}{x\max - x\min}) \tag{7.9}$$

$$t = (\frac{y - y\min}{y\max - y\min}) \tag{7.10}$$

$$u = (\frac{z - z\min}{z\max - z\min}) \tag{7.11}$$

Along these axes, the number of control points is $l,\ m,\ n$ respectively. If we define the position of the control points as $P_{i,j,k}(0 < i < l, 0 < j < m, 0 < k < n)$, then the object points position P_{obj} can be expressed by these control points using the Bernstein polynomial equation:

$$P_{obj}(s,t,u) = \sum_{i=0}^{l}\sum_{j=0}^{m}\sum_{k=0}^{n} B_i^l(s)B_j^m(t)B_k^n(u)P_{i,j,k} \tag{7.12}$$

where the Bernstein polynomial are defined by:

$$B_i^l = \binom{l}{i}(1-s)^{l-i}s^i \tag{7.13}$$

$$B_j^m = \binom{m}{j}(1-t)^{m-j}t^j \tag{7.14}$$

$$B_k^n = \binom{n}{k}(1-u)^{n-k}t^k \tag{7.15}$$

From Eq.(7.12), it can be seen that if the control points move, the position of object points will change subsequently and therefore vary the object shape.

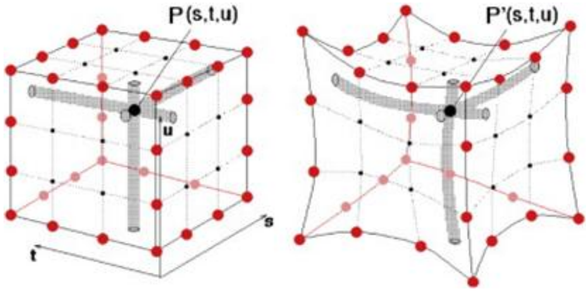

Fig. 7.7 Principle of FFD. The red points represent the control points, and the big black point indicates one point of object. On the left, the object and the control points experience no deformation. On the right, object deforms with the displacement of control points.

For cardiac fibers, the FFD model changes not only the cardiac fiber position but also the local cardiac fiber orientation. The cardiac fiber position is determined by the spatial resolution and the voxel position and the fiber orientation is given by the CCBM dataset. Based on the cardiac fiber modeling method elaborated in chapter 5, when the heart is in a static state, the cardiac fiber is modeled by one oriented cylinder with radius r of 7 µm and length l of 100 µm. If the cardiac fiber position pos and the orientation dir are respectively expressed by the vectors of $[posx, posy, posz]$ and $[dirx, diry, dirz]$. After the FFD transformation, they become $[posx', posy', posz']$ and $[dirx', diry', dirz']$. The former determines the imaging position and the latter gives the new fiber orientation and provides the new cardiac fiber length and radius. In our modeling, we assume that the volume of a cardiac fiber does not change. Thus the new length l' and radius r' are

$$l' = \|dir'\| l \tag{7.16}$$

$$r' = \sqrt{r^2 l / l'} \tag{7.17}$$

According to the work of Haddad [Haddad, 2007], the heart displacement can reach up to 20 mm. Therefore, the cardiac motion not only changes the fiber orientation but also varies the imaging voxel locations, which implies that, different heart regions may be « seen » by the same voxel at different times. For this reason, in order to distinguish the signal attenuation caused by motion from that induced by local variation in cardiac fiber orientation, the diffusion weighted images for different moments are simulated using our dMRI simulator and the corresponding diffusion image properties are calculated. From the diffusion images, the relationships between the heart motion, fiber orientation variation and image intensity are analyzed.

7.4 dMRI simulation results for *in vivo* cardiac fiber model

Based on the analysis in the last chapter about the effects of imaging parameters on image properties, the following imaging parameters are chosen for the dMRI simulation of in vivo cardiac fibers:

- Diffusion time: 200 ms;
- Diffusion gradient strength : 85.51 mT/m;
- Gradient duration : 2 ms;
- Gradient ramp time: 0.5 ms;
- q-value : 12.6 mm^{-1} ;
- b-value: 1267 s/mm^{2} ;
- Diffusion gradient directions: the direction file is given by the Siemens MRI scanner and the number of diffusion direction is 12.

Simulated diffusion weighted images

The dMRI simulation is performed in 3D with a spatial resolution of 1.25 × 1.25 × 4 mm^3. For illustration, Fig. 7.8 gives only the DW images of one sagittal slice simulated at different cardiac cycle phases. There are 14 phases totally and the time interval between each phase is

64 ms. The instant T1 corresponds to the phase of the end-diastole, T2 to T6 are phases of systole, T7 to T14 are in diastole. It can be seen that, in the middle of the left ventricle, the wall thickness changes significantly with cardiac motion. According to the research of [Englund, 2011], the cardiac motion introduces the movement of cardiac myocytes and the heart extension may result from the increased diameter of myocyte. The increase in myocyte diameter due to myocyte shortening could contribute at most about 20% of the local wall thickening [LeGrice *et al.*, 1995]. Contrarily, during the heart dilation, the wall thinning may be caused by the decrease of the cardiac myocyte diameter and the lengthening of the cardiac fiber.

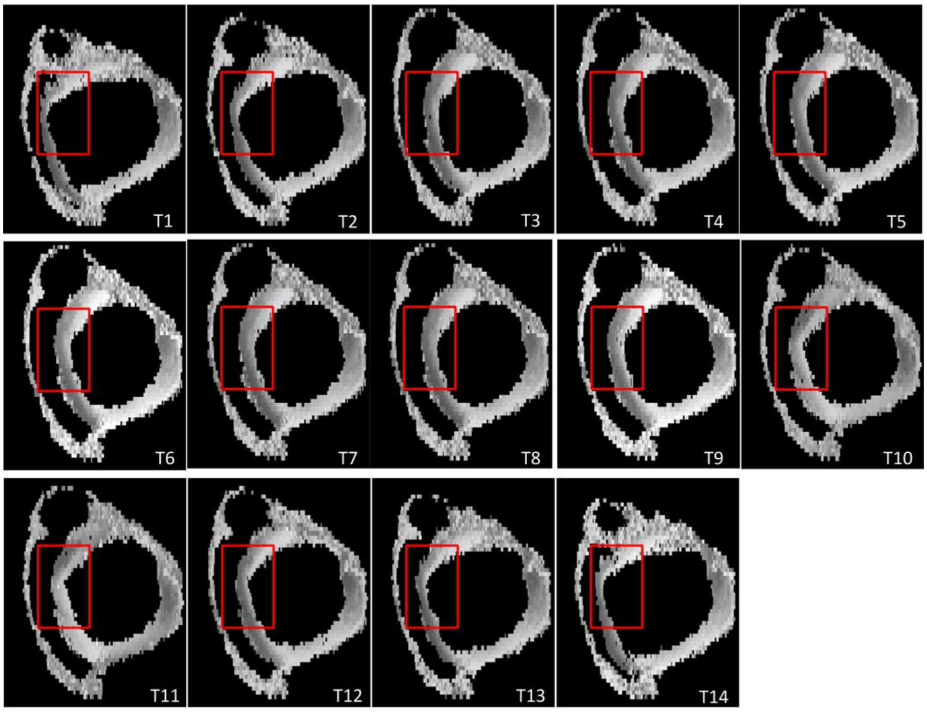

Fig. 7.8 Simulated DW images (diffusion gradient is applied along z direction) for different cardiac cycle instants along the coronal direction.

To better investigate the variation of cardiac fiber properties with cardiac motion, we select a region of interest (ROI) of size 20 × 40 in the above sagittal slice, inside the red square as shown in Fig. 7.8. The variations of the cardiac fiber length and radius with heart motion in this region are illustrated in Fig. 7.9 and Fig. 7.10. Note that during the cardiac dilation, from the time points T10 to T14, the decrease in radius of myocytes is visible. In the simulation, we assumed that the myocyte volume does not change which leads to the increase of the cardiac myocyte length, as can be observed in Fig. 7.10. Comparing the corresponding DW images from T10 to T14, we can conclude that the decrease in cardiac myocyte radius really results in the wall thinning, which conforms to the previous conjectures. Similarly, at the beginning of the systole, from the instant T1 to T3, the radius of the myocyte increases and accordingly leads to the wall thickening. However, form T4 to T8, the wall thickness experiences tiny variations because the cardiac fiber shape does not change too much.

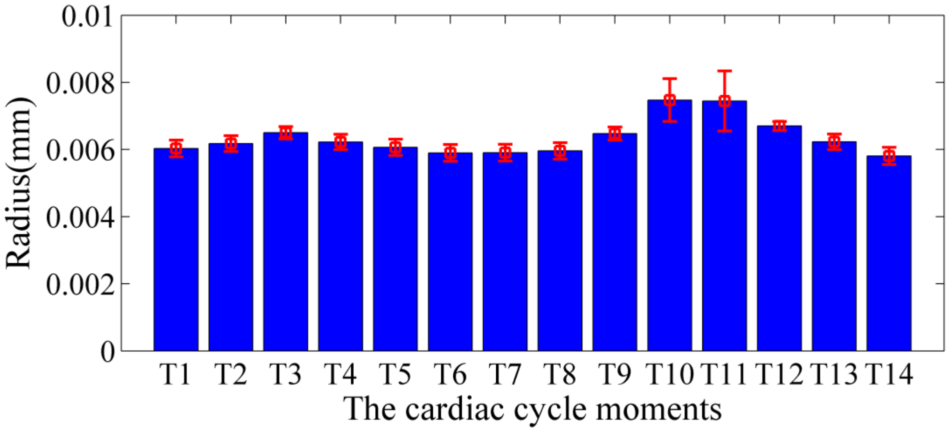

Fig. 7.9 Cardiac fiber radius distribution as a function of cardiac cycle moments for the selected ROI

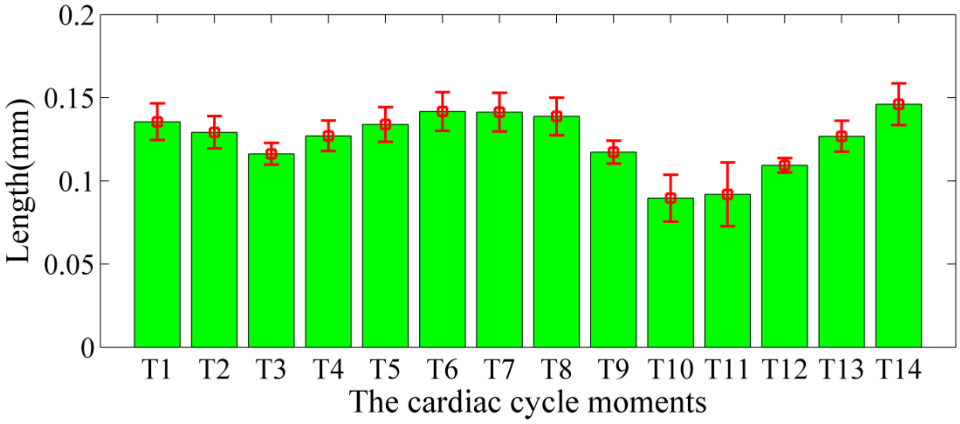

Fig. 7.10 Cardiac fiber length distribution as a function of cardiac cycle moments for the selected ROI

Fiber orientation

In the simulation, no additional signal attenuation due to motion was present. Therefore, the variation in intensity of the simulated DW images is only due to the change in structure of myocardium. As a result, this intensity variation allows us to reveal the cardiac fiber structure changes. By combining heart motion and fiber orientations at the static state, the relationship between the cardiac motion and the fiber orientation can then be quantitatively analyzed. Fig. 7.11 shows the cardiac fiber orientations of the selected myocardial ROI simulated at different cardiac cycle moments.

Because the motion information used in the simulation is derived from the MRI measurement that was obtained after registration, it presents some errors. In addition, when registering the cardiac motion from the ADAM heart to the CCBM heart, the motion estimation error is further amplified. In order to quantitatively analyze the influence of motion and to avoid motion error effects, all the following analysis and conclusion are based on the "a priori known motion" that has been used in the simulation. In the selected ROI, at the beginning there are 1096 cardiac fibers. Their motion information is shown in Fig. 7.12. The red one designates the displacement along x direction, and the green and blue ones represent the displacement along y and z directions respectively. The bar value signifies the mean value of the displacement and the length of the line segment indicates the displacement variance. It can be observed that, in this region, the motions along z and y directions are more obvious than along x direction.

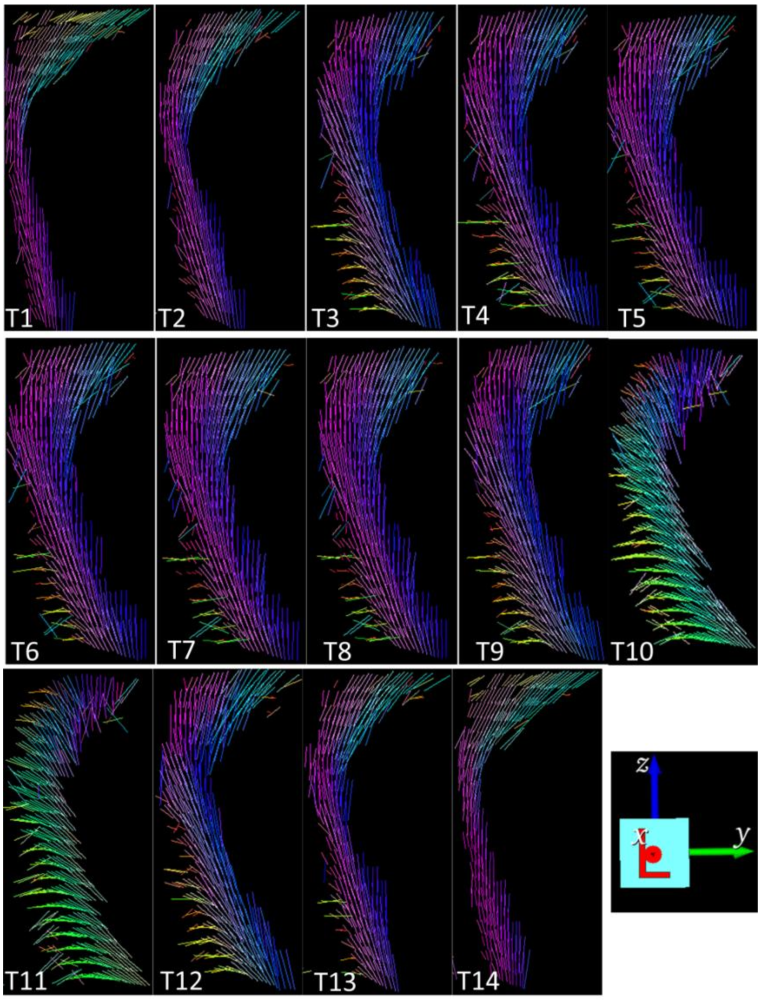

Fig. 7.11 Variation of cardiac fiber orientations of selected ROI as a function of cardiac motion.

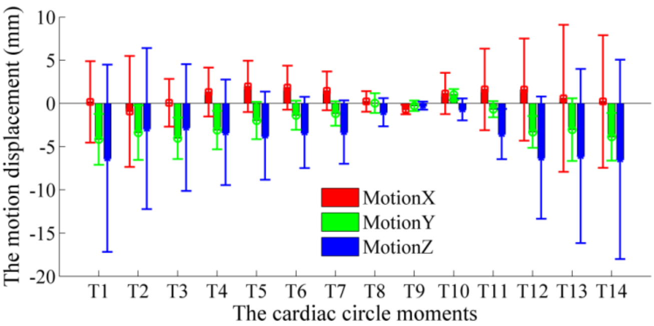

Fig. 7.12 Cardiac motion at different cardiac cycle moments for the chosen ROI.

Comparing Fig. 7.11 with Fig. 7.12, the motion along z direction makes the cardiac fiber orientation incline to the z direction, especially during the dilation, from the instants T11 to T14. It can be seen that during the cardiac systole, from instant T2 to T7, the fiber orientation experiences a relative big variation, which leads also to the wall thickening. However, during the dilation, for instance from T10 to T14, the orientations of myocytes in this zone becomes more coherent which results in a thinner wall thickness.

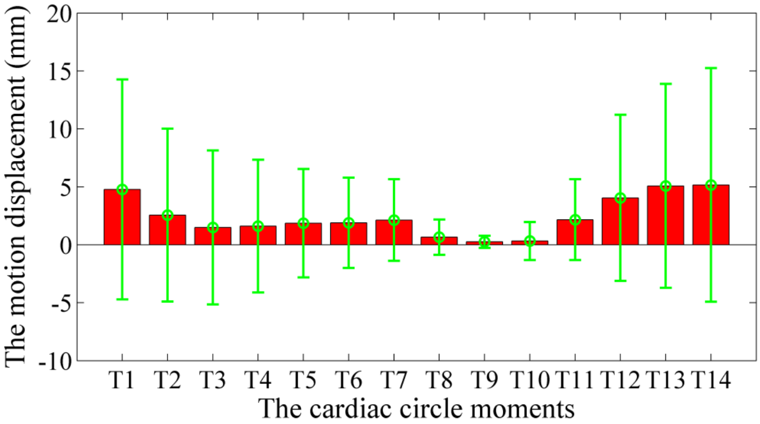

Fig. 7.13 Motion displacements projected along the cardiac fiber orientations.

With respect to the absolute motion information, the relative motion displacement along the cardiac fiber orientation is given in Fig. 7.13. Note that, during the cardiac dilation, from T10 to T14, the relative cardiac motion increases gradually, which will definitely extend the myocyte lengths as shown in Fig. 7.10.

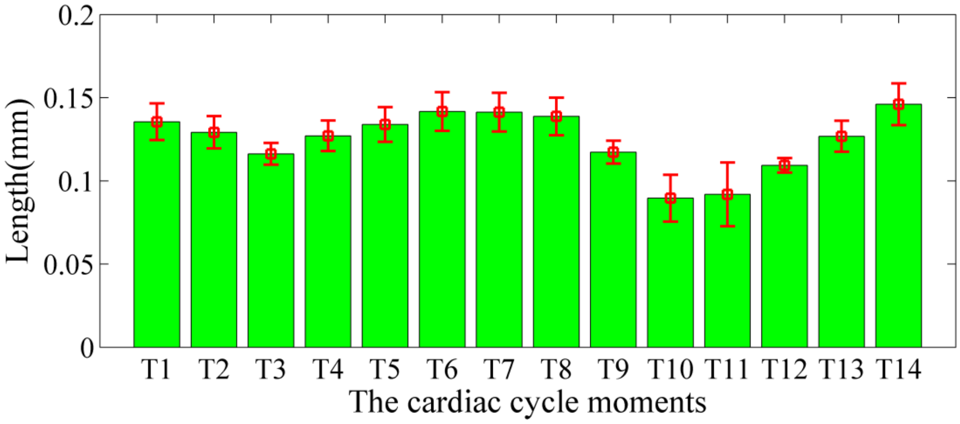

FA and MD

FA and MD values are the most important indices to describe cardiac fiber properties. FA reflects the hindrance level along the different directions, and MD the average hindrance for the water molecular diffusion. Fig. 7.14 and Fig. 7.15 illustrate the variation of FA and MD values as a function of cardiac motion. As we demonstrated above, the cardiac motion changes the radius and length of myocytes. The variation of FA and MD value can then be explained by the change in shape of cardiac myocytes.

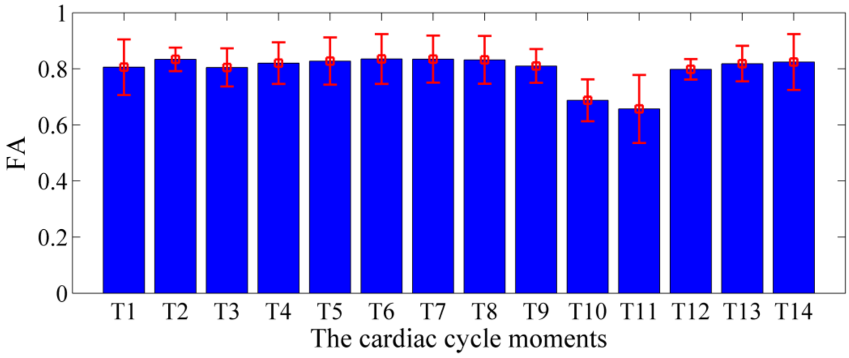

Fig. 7.14 FA values of the selected ROI

Comparing Fig. 7.14 with Fig. 7.9 and Fig. 7.10, it can be seen that as the myocyte radius decreases, FA increases (cardiac dilatation, from T11 to T14) and that the variance of FA is proportional to the myocyte length-to-radius ratio. From the time moments T4 to T8, the variation of FA values is not significant since the cardiac myocyte radius does not change too much.

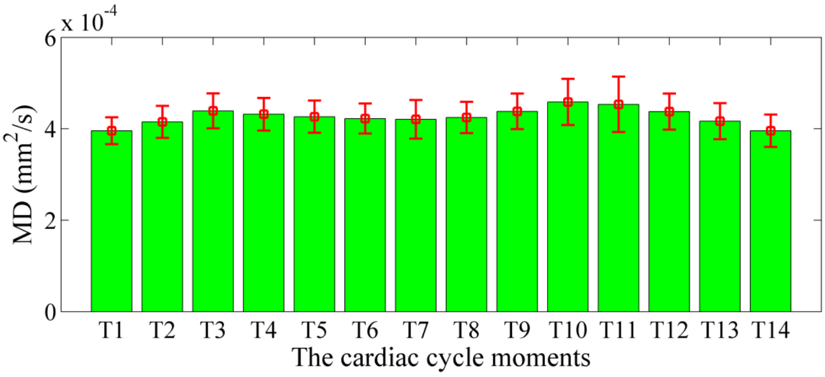

Fig. 7.15 MD values of the selected ROI

As to MD, the decrease of cardiac myocyte radius reduces its value (cardiac dilatation, from T11 to T14). MD is determined by both diffusion coefficient used in the simulation and the radius of cardiac myocytes. In our simulation, the diffusion coefficient is chosen as 0.001 mm^2/s, which results in a maximum diffusion displacement of 35 μm during the diffusion time of 200 ms. In the cardiac myocyte, along the radius direction, the restriction of water diffusion is predominant. With decreasing of the myocyte radius, more water molecules are involved in the restricted diffusion and therefore reduce the MD values.

7.5 Conclusion

In this chapter, we have performed the first attempt of simulating dMRI of in vivo cardiac fibers using in vivo modeling based on registration and FFD and dMRI simulator. According to the cardiac motion information extracted from registered motion fields, we have used the free form deformation method in order to mimic *in vivo* cardiac fiber structures, in which the cardiac myocyte volume keeps constant. After the in vivo modeling, the DW images and diffusion tensor images for different cardiac cycle phases have been simulated using our dMRI simulator. The variations of myocardial wall thickness, fiber orientation, FA and MD values in an ROI were analyzed as a function of cardiac motion. The results show that the thinning of the myocardial wall is mainly caused by the decrease of the cardiac myocyte diameters. The variation of the cardiac fiber orientations and the decrease of blood also contribute to the thinning of myocardial wall. The change in shape of cardiac myocytes also leads to the variation of FA and MD values. FA increases and MD decreases with the decreasing of myocyte diameters.

Since the motion in our study does not cause additional attenuation of diffusion signals, but changes the arrangement of myocytes, this change in myocyte arrangement is the only factor causing the variation in intensity of DW images and the variation of diffusion properties. Consequently, the proposed method allows us, to some extent, overcome the sensibility of dMRI to the heart motion, which suggests that, if the cardiac motion information is introduced appropriately, the proposed simulation approach will allow providing a new way for correcting the influence of the heart motion in practically acquired DW images. In addition, the combination of motion information and fiber structure, which may be obtained from different imaging modalities, provides us a valuable tool for *in vivo* cardiac fiber imaging applications.

The proposed first in vivo simulations are limited by the lack of accurate 3D motion information or even ground-truth. Further study in the future should be carried out to investigate how more accurate motion fields will change the in vivo dMRI data and how well the thus obtained results fit the reality.

PART III

General Conclusion

Chapter 8

Conclusions and perspectives

8.1 Conclusions

Le thème central de cette thèse était de simuler les images d'IRM de diffusion des fibres cardiaques à la fois *ex vivo* et *in vivo* afin de mieux comprendre la relation entre les structures microscopiques des fibres et les propriétés macroscopiques des images de diffusion, et d'interpréter ou prédire dans un but ultime les pathologies du cœur. Afin d'atteindre cet objectif, des simulateurs de l'IRM de diffusion pour les fibres cardiaques ont été développés en s'appuyant sur la méthode de Monte-Carlo (MC). Plus précisément, des structures virtuelles des fibres cardiaques (VCFS) *ex vivo* et *in vivo* ont été modélisées en intégrant des données provenant des modalités d'imagerie différentes. Ensuite, le comportement de la diffusion des molécules d'eau dans ces VCFS a été simulé à l'aide de l'algorithme de MC. Enfin, selon le déplacement des molécules d'eau, le signal d'IRM de diffusion a été calculé et l'image de diffusion a été obtenue.

Afin de mieux présenter le contexte et les fondements de ce travail de thèse, nous avons tout d'abord brièvement présenté l'organisation architecturale du cœur humain en multi-échelles, puis décrit en détail les principes de l'imagerie par résonance magnétique de diffusion et de l'imagerie en lumière polarisée (PLI), et enfin résumé l'état de l'art sur les modélisations et les simulations de l'IRM de diffusion. Basés sur cette étude bibliographique, des simulateurs de l'IRM de diffusion ont été proposés pour des fibres cardiaques à la fois *ex vivo* et *in vivo* issues de la modélisation géométrique et de l'imagerie PLI. À l'aide de ces simulateurs, la relation entre les propriétés des images de diffusion et les structures microscopiques des fibres cardiaques a été étudiée.

Nos contributions principales se situent dans les domaines suivants:

- Un simulateur de l'IRM de diffusion permettant d'étudier l'influence des caractéristiques physiques et structurelles des fibres cardiaques sur les propriétés des images de diffusion

  Nous avons modélisé les architectures des fibres cardiaques avec un modèle géométrique assez simple, et introduit l'algorithme de Monte-Carlo pour réaliser la simulation des images de diffusion des fibres cardiaques. Deux VCFS ont été modélisées qui permettent d'analyser l'influence des caractéristiques physiques et structurelles des fibres cardiaques sur les propriétés de diffusion. D'une part, le fait de représenter le myocyte cardiaque par la combinaison d'une série d'hexagones nous a permis de changer aisément la forme de l'espace intra- et extracellulaires et d'analyser l'influence du contenu des molécules d'eau et de la perméabilité de leur membrane sur l'anisotropie de diffusion. Les résultats obtenus montrent que l'augmentation de la contenue de l'eau dans l'espace intracellulaire et la diminution de la perméabilité de la membrane se traduisent par une plus grande valeur de FA. D'autre part, la modélisation par cylindres des myocytes nous a permis de varier de manière souple l'orientation et la disposition des fibres, ce qui a rendu possible la simulation des images de diffusion en multi-échelles ainsi que l'estimation de l'influences de l'arrangement des myocytes, de la dimension des myocytes et de l'échelle d'observation sur l'anisotropie fractionnelle. Les résultats suggèrent que le simulateur proposé peut être utilisé pour analyser la relation entre l'hétérogénéité des structures microscopiques et les mesures macroscopiques.

- La simulation de l'IRM de diffusion à multi-échelles pour un modèle réaliste des fibres cardiaques basé sur l'intégration des données multimodales

En combinant l'imagerie de PLI et l'IRM de diffusion simulée, nous avons pu pour la première fois simuler des images de diffusion réalistes et à multi-échelles des fibres cardiaques, qui peuvent être utilisées à différentes fins. Évaluer les algorithmes de traitement d'images et élaborer la relation entre la structure microscopique et les propriétés de diffusion macroscopiques en sont deux exemples immédiats. Pour les mêmes structures, FA diminue et MD augmente avec l'augmentation de l'échelle d'observation. En outre, en modifiant les paramètres du modèle des fibres, nous étions capables de simuler des images pondérées en diffusion ainsi que les indices de diffusion correspondants très variées, ce qui permet d'étudier l'influence de l'hétérogénéité des orientations des fibres et des dimensions des myocytes sur FA et MD, ouvrant ainsi la possibilité d'élucider d'éventuelles corrélations entre des maladies cardiaques et les propriétés des images de diffusion.

- L'influence des paramètres d'imagerie par résonance magnétique sur les propriétés des images de diffusion

En simulant les effets des paramètres du gradient de diffusion (y compris le temps de diffusion, l'amplitude et la durée du gradient) sur les propriétés des images de diffusion, nous avons pu démontrer que le simulateur de l'IRM de diffusion proposé peut être utilisé pour optimiser les paramètres du gradient de diffusion selon la structure des fibres cardiaques en question. Se plaçant dans des situations plus réalistes quant au gradient de diffusion, l'amélioration de la théorie de calcul des signaux de diffusion a permis d'analyser les effets du temps de diffusion, de la durée et du temps de rampe sur les propriétés des images, et de ce fait d'envisager la possibilité de trouver un compromis raisonnable entre les différents paramètres (amplitude du gradient, la durée, le temps de rampe et la valeur de b) pour des imageries à hautes valeurs de b. Ainsi, ensemble avec les résultats sur l'étude de l'influence des gradients d'imagerie comprenant les gradients de sélection de coupe, de codage de phase et de lecture, le modèle de simulation proposé permet d'analyser l'influence de tous les paramètres d'imagerie sur l'estimation des propriétés des fibres cardiaques, et de déterminer un jeu de paramètres optimal pour une problématique donnée.

- La simulation de l’IRM de diffusion des fibres cardiaques *in vivo*

En combinant, via des prétraitements de segmentation et de recalage, le mouvement et la structure des fibres, nous avons démontré qu’il est possible de modéliser l’architecture des fibres cardiaques *in vivo*. Plus précisément, suivant l'information du mouvement cardiaque, nous avons modélisé la structure des fibres cardiaques *in vivo* en utilisant la méthode de déformation libre, dans laquelle le volume des myocytes cardiaques est maintenu constant. Après la modélisation, les images de diffusion aux instants différents d’un cycle cardiaque sont simulées au moyen de notre simulateur. La variation de l'épaisseur de la paroi, de l’orientation des fibres, des valeurs FA et MD dans une région d’intérêt (ROI) présentant le mouvement a été analysée quantitativement. Les résultats montrent que, l'amincissement de l'épaisseur de la paroi pendant la diastole est principalement causé par la diminution des diamètres des myocytes cardiaques et la moins variation d’orientation des fibres. La modification de la forme des myocytes cardiaques conduit également à la variation des valeurs FA et MD. FA augmente et MD diminue avec le rétrécissement du diamètre des myocytes.

Dans notre étude, nous avons supposé que le mouvement cardiaque est connu à l'avance. Ce mouvement change l'architecture des fibres cardiaques et ce changement de structure modifie les images de diffusion et les propriétés de diffusion correspondantes. Par conséquent, nous avons pu supprimer la sensibilité de l'IRM de diffusion au mouvement du cœur car, avec une telle simulation, le mouvement du cœur n’a changé que la structure des fibres au lieu de provoquer l'atténuation du signal de diffusion supplémentaire. Ainsi, si l'information de mouvement cardiaque est introduite de façon appropriée, l’approche de simulation proposée est capable de fournir un critère pour corriger l'influence du mouvement cardiaque sur les intensités de l’image de diffusion acquise, ce qui est très intéressant pour envisager des méthodes permettant d’évaluer la qualité des imageries *in vivo* des fibres cardiaque.

8.1 Perspectives

Dans cette thèse, nous avons développé un simulateur de l’IRM de diffusion pour les fibres cardiaques à la fois *ex vivo* et *in vivo*. Ces travaux nous ont donné des moyens efficaces pour évaluer et valider la relation entre les propriétés de diffusion et les structures des fibres cardiaques ; ils nous fournissent également un outil utile pour optimiser les paramètres d’imagerie et pour étudier l’imagerie par résonance magnétique *in vivo*.

Comme nos images simulées sont des images de diffusion sans bruit ni artéfacts, il serait intéressant dans le futur de les utiliser comme images de référence (vérité-terrain) pour évaluer les algorithmes de traitement (débruitage, reconstruction, interpolation, réduction des arttéfacts, etc.) des images classiques (niveaux de gris) ou modernes (champs de tenseurs, champs de vecteurs, tractographies de fibres, etc.).

Une autre perspective de nos travaux serait de fournir une aide à la conception de séquences d’IRM de diffusion. Dans notre simulation, nous avons analysé l’influence des paramètres d’imagerie sur la qualité des images en utilisant la séquence d’écho de spin. Appliquer le simulateur aux autres séquences pourrait être un autre sujet de recherche dans le futur.

La simulation de l’IRM de diffusion des fibres cardiaques *in vivo* constitue un premier travail préliminaire, et l’information de mouvement utilisée provient de l’IRM. Intégrer les mouvements en provenance d’autres séquences IRM ou modalités d’imagerie serait intéressant. Cela nous permettrait d’analyser la déformation des fibres cardiaques *in vivo* avec plusieurs modalités.

Bien que le simulateur proposé ait été ciblés sur des fibres cardiaques, ils pourraient être appliqués à d’autres tissus vivants, par exemple le cerveau. Il s’agit d’un simulateur générique.

8.2 Author’s publications

- Lihui Wang, Yue-Min Zhu, Hongying Li, Wanyu Liu and Isabelle E. Magnin, Simulation of Diffusion Anisotropy in DTI for Virtual Cardiac Fiber Structure, FIMH 2011, LNCS 6666: 95-104, 2011.

- L. H. Wang, Y. M. Zhu, H. Y. Li, W. Y. Liu, and I. E. Magnin, Multi-Scale Modeling and Simulation of the Cardiac Fiber Architecture for DMRI, IEEE Trans. Biomedical Engineering, 59:16-19, 2012.

- Lihui Wang, Sorina Camarasu-Pop, Tristan Glatard, Yue-Min Zhu, Isabelle E. Magnin. Diffusion MRI simulation with the Virtual Imaging Platform. *Journées scientifiques mésocentres et France Grilles,* 2012.

Appendix

Calculation of $\vec{F}(t)$ and b-value:

Comparing Eq. (6.13) and Eq. (6.35), note that $\vec{F}(t)$ and $\vec{q}(t)$ have the same definition, thus in the following calculation, Q represents F. Because $\vec{q}(t)$ can be decomposed into three components along slice selection, phase encoding, and readout directions, we calculate them respectively. All the following results are calculated with Mathmatica.

Along the phase-encoding direction, the q-value ($\vec{F}(t)$) definitions:

$$\begin{gathered}\text{Q1}=\gamma*\text{Simplify}\left[\text{Integrate}\left[g_p*\left(T-\left(\tau_s+\epsilon\right)/2\right),\left\{T,\left(\tau_s+\epsilon\right)/2,t\right\}\right]\right]/.\left\{g_p\to G_p/\epsilon\right\}\\ \text{f1}=\text{Simplify}\left[\text{Q1}/.t\to\left(\tau_s+\epsilon\right)/2+\epsilon\right]\end{gathered}\tag{A.18}$$

$$\begin{gathered}\text{Q2}=\text{Simplify}\left[\text{f1}+\gamma*\text{Integrate}\left[G_p,\left\{T,\left(\tau_s+\epsilon\right)/2+\epsilon,t\right\}\right]\right]\\ \text{f2}=\text{Simplify}\left[\text{Q2}/.t\to\left(\tau_s+\epsilon\right)/2+\tau_p\right]\end{gathered}\tag{A.19}$$

$$\begin{gathered}\text{Q3}=\text{Simplify}\left[\begin{array}{l}\text{f2}+\gamma*\text{Integrate}\left[-g_p*\left(T-\left(\tau_s+\epsilon\right)/2-\tau_p-\epsilon\right),\left\{T,\left(\tau_s+\epsilon\right)/2+\tau_p,t\right\}\right]\\ /.\left\{g_p\to G_p/\epsilon\right\}\end{array}\right]\\ \text{f3}=\text{Simplify}\left[\text{Q3}/.t\to\left(\tau_s+\epsilon\right)/2+\tau_p+\epsilon\right]\end{gathered}\tag{A.20}$$

$$\begin{gathered}\text{Q4}=\text{Simplify}\left[\begin{array}{l}\text{f3}+\gamma*\text{Integrate}\left[g_{\text{dp}}*(T-\text{t1}),\{T,\text{t1},t\}\right]/.\\ \left\{g_{\text{dp}}\to G_{\text{dp}}/\epsilon,\text{t1-\$}>\text{\$}\tau\text{-}\Delta/2\text{-}\epsilon/2\text{-}\delta/2\right\}\end{array}\right]\\ \text{f4}=\text{Simplify}[\text{Q4}/.t\to\tau-\Delta/2+\epsilon/2-\delta/2]\end{gathered}\tag{A.21}$$

$$\begin{gathered}\text{Q5}=\text{Simplify}\left[\text{f4}+\gamma*\text{Integrate}\left[G_{\text{dp}},\{T,\tau-\Delta/2+\epsilon/2-\delta/2,t\}\right]\right]\\ \text{f5}=\text{Simplify}[\text{Q5}/.t\to\tau-\Delta/2-\epsilon/2+\delta/2]\end{gathered}\tag{A.22}$$

$$\begin{gathered}\text{Q6}=\text{Simplify}\left[\begin{array}{l}\text{f5}+\gamma*\text{Integrate}\left[-g_{\text{dp}}*(T-\text{t1}-\delta-\epsilon),\{T,\text{t1}+\delta,t\}\right]\\ /.\left\{g_{\text{dp}}\to G_{\text{dp}}/\epsilon,\text{t1-\$}>\text{\$}\tau\text{-}\Delta/2\text{-}\epsilon/2\text{-}\delta/2\right\}\end{array}\right]\\ \text{f6}=\text{Simplify}[\text{Q6}/.t\to\tau-\Delta/2+\epsilon/2+\delta/2]\end{gathered}\tag{A.23}$$

$$\begin{gathered}\text{Q7}=\text{Simplify}[\text{f6}]\\ \text{f7}=\text{Q7}\end{gathered}\tag{A.24}$$

$$\begin{gathered}\text{Q8}=-\text{Q7}\\ \text{f8}=\text{Q8}\end{gathered}\tag{A.25}$$

$$\begin{aligned}
&\text{Q9} = \text{Simplify}\left[\begin{array}{l}\text{f8} + \gamma * \text{Integrate}\left[g_{\text{dp}} * (T - \text{t3}), \{T, \text{t3}, t\}\right] \\ /.\left\{g_{\text{dp}} \to G_{\text{dp}} / \epsilon, \text{t3-\$} > \$(\tau\text{+}\Delta\text{/2-}\delta\text{/2-}\epsilon\text{/2)}\right\}\end{array}\right] \\
&\text{f9} = \text{Simplify}[\text{Q9}/.t \to \tau + \Delta / 2 - \delta / 2 + \epsilon / 2]
\end{aligned} \tag{A.26}$$

$$\begin{aligned}
&\text{Q10} = \text{Simplify}\left[\text{f9} + \gamma * \text{Integrate}\left[G_{\text{dp}}, \{T, \tau + \Delta / 2 - \delta / 2 + \epsilon / 2, t\}\right]\right] \\
&\text{f10} = \text{Simplify}[\text{Q10}/.t \to (\tau + \Delta / 2 + \delta / 2 - \epsilon / 2)]
\end{aligned} \tag{A.27}$$

$$\begin{aligned}
&\text{Q11} = \text{Simplify}\left[\begin{array}{l}\text{f10} + \gamma * \text{Integrate}\left[-g_{\text{dp}} * (T - \text{t3} - \delta - \epsilon), \{T, \text{t3} + \delta, t\}\right] \\ /.\left\{g_{\text{dp}} \to G_{\text{dp}} / \epsilon, \text{t3-\$} > \$(\tau\text{+}\Delta\text{/2-}\delta\text{/2-}\epsilon\text{/2)}\right\}\end{array}\right] \\
&\text{f11} = \text{Simplify}[\text{Q11}/.t \to (\tau + \Delta / 2 + \delta / 2 + \epsilon / 2)]
\end{aligned} \tag{A.28}$$

$$\text{Q12} = \text{Simplify}[\ \text{f11}] \tag{A.29}$$

b-value along phase-encoding direction is :

$$\begin{aligned}
\text{Bpp} = \text{Simplify}\Big[&\text{Integrate}\left[(\text{Q1})\hat{}2, \left\{t, \left(\tau_s + \epsilon\right) / 2, \left(\tau_s + \epsilon\right) / 2 + \epsilon\right\}\right] \\
&+\text{Integrate}\left[(\text{Q2})\hat{}2, \left\{t, \left(\tau_s + \epsilon\right) / 2 + \epsilon, \left(\tau_s + \epsilon\right) / 2 + \tau_p\right\}\right] \\
&+\text{Integrate}\left[(\text{Q3})\hat{}2, \left\{t, \left(\tau_s + \epsilon\right) / 2 + \tau_p, \left(\tau_s + \epsilon\right) / 2 + \tau_p + \epsilon\right\}\right] \\
&+\text{Integrate}[(\text{Q4})\hat{}2, \{t, \tau - \Delta / 2 - \epsilon / 2 - \delta / 2, \tau - \Delta / 2 + \epsilon / 2 - \delta / 2\}] \\
&+\text{Integrate}[(\text{Q5})\hat{}2, \{t, \tau - \Delta / 2 + \epsilon / 2 - \delta / 2, \tau - \Delta / 2 - \epsilon / 2 + \delta / 2\}] \\
&+\text{Integrate}[(\text{Q6})\hat{}2, \{t, \tau - \Delta / 2 - \epsilon / 2 + \delta / 2, \tau - \Delta / 2 + \epsilon / 2 + \delta / 2\}] \\
&+\text{Integrate}[(\text{Q7})\hat{}2, \{t, \tau - \Delta / 2 + \epsilon / 2 + \delta / 2, \tau\}] \\
&+\text{Integrate}[(\text{Q8})\hat{}2, \{t, \tau, \tau + \Delta / 2 - \epsilon / 2 - \delta / 2\}] \\
&+\text{Integrate}[(\text{Q9})\hat{}2, \{t, \tau + \Delta / 2 - \epsilon / 2 - \delta / 2, \tau + \Delta / 2 + \epsilon / 2 - \delta / 2\}] \\
&+\text{Integrate}[(\text{Q10})\hat{}2, \{t, \tau + \Delta / 2 + \epsilon / 2 - \delta / 2, \tau + \Delta / 2 - \epsilon / 2 + \delta / 2\}] \\
&+\text{Integrate}[(\text{Q11})\hat{}2, \{t, \tau + \Delta / 2 - \epsilon / 2 + \delta / 2, \tau + \Delta / 2 + \epsilon / 2 + \delta / 2\}] \\
&+\text{Integrate}[(\text{Q12})\hat{}2, \{t, \tau + \Delta / 2 + \epsilon / 2 + \delta / 2, 2 * \tau\}]]
\end{aligned} \tag{A.30}$$

Along the frequency-encoding direction, q-value is calculated by:

$$\begin{aligned}
&\text{Q1} = \text{Simplify}\left[\gamma * \text{Integrate}\left[g_{\text{df}} * (T - \text{t1}), \{T, \text{t1}, t\}\right] /.\left\{g_{\text{df}} \to \text{G}_{\text{df}} /\epsilon, \text{t1} \to \tau\text{-}\Delta\text{/2-}\epsilon\text{/2-}\delta\text{/2}\right\}\right] \\
&\text{f1} = \text{Simplify}[\text{Q1}/.t \to \tau - \Delta / 2 + \epsilon / 2 - \delta / 2]
\end{aligned} \tag{A.31}$$

$$\begin{aligned}
&\text{Q2} = \text{Simplify}\left[\text{f1} + \gamma * \text{Integrate}\left[G_{\text{df}}, \{T, \text{t1} + \epsilon, t\}\right] /.\left\{g_{\text{df}} \to G_{\text{df}} / \epsilon, \text{t1} \to \tau\text{-}\Delta\text{/2-}\epsilon\text{/2-}\delta\text{/2}\right\}\right] \\
&\text{f2} = \text{Simplify}[\text{Q2}/.t \to (\tau - \Delta / 2 - \epsilon / 2 + \delta / 2)]
\end{aligned} \tag{A.32}$$

$$\begin{aligned}
&\text{Q3} = \text{Simplify}\left[\begin{array}{l}\text{f2} + \gamma * \text{Integrate}\left[-g_{\text{df}} * (T - \text{t1} - \delta - \epsilon), \{T, \text{t1} + \delta, t\}\right] \\ /.\left\{g_{\text{df}} \to G_{\text{df}} / \epsilon, \text{t1} \to \tau\text{-}\Delta\text{/2-}\epsilon\text{/2-}\delta\text{/2}\right\}\end{array}\right] \\
&\text{f3} = \text{Simplify}[\text{Q3}/.t \to (\tau - \Delta / 2 + \epsilon / 2 + \delta / 2)]
\end{aligned} \tag{A.33}$$

$$\begin{aligned}
&\text{Q4} = \text{Simplify}[\text{f3}] \\
&\text{f4} = \text{Q4}
\end{aligned} \tag{A.34}$$

$$\begin{aligned}&\mathrm{Q5}=-\mathrm{f4}\\&\mathrm{f5}=\mathrm{Q5}\end{aligned}\tag{A.35}$$

$$\begin{aligned}&\mathrm{Q6}=\mathrm{Simplify}\left[\begin{array}{l}\mathrm{f5}+\gamma*\mathrm{Integrate}\left[g_{\mathrm{df}}*(T-\mathrm{t3}),\{T,\mathrm{t3},t\}\right]\\ /.\left\{g_{\mathrm{df}}\rightarrow G_{\mathrm{df}}/\epsilon,\mathrm{t3}\rightarrow(\tau\text{+}\Delta\text{/2-}\delta\text{/2-}\epsilon\text{/2})\right\}\end{array}\right]\\&\mathrm{f6}=\mathrm{Simplify}[\mathrm{Q6}/.\{t\rightarrow\tau+\Delta/2-\delta/2+\epsilon/2\}]\end{aligned}\tag{A.36}$$

$$\begin{aligned}&\mathrm{Q7}=\mathrm{Simplify}\left[\mathrm{f6}+\ \gamma*\mathrm{Integrate}\left[G_{\mathrm{df}},\{T,(\tau+\Delta/2-\delta/2+\epsilon/2),t\}\right]/.\left\{g_{\mathrm{df}}\rightarrow G_{\mathrm{df}}/\epsilon\right\}\right]\\&\mathrm{f7}=\mathrm{Simplify}[\mathrm{Q7}/.t\rightarrow(\tau+\Delta/2+\delta/2-\epsilon/2)]\end{aligned}\tag{A.37}$$

$$\begin{aligned}&\mathrm{Q8}=\mathrm{Simplify}\left[\begin{array}{l}\mathrm{f7}+\gamma*\mathrm{Integrate}\left[-g_{\mathrm{df}}*(T-(\tau+\Delta/2+\delta/2+\epsilon/2)),\{T,(\tau+\Delta/2+\delta/2-\epsilon/2),t\}\right]\\ /.\left\{g_{\mathrm{df}}\rightarrow G_{\mathrm{df}}/\epsilon\right\}\end{array}\right]\\&\mathrm{f8}=\mathrm{Simplify}[\mathrm{Q8}/.t\rightarrow(\tau+\Delta/2+\delta/2+\epsilon/2)]\end{aligned}\tag{A.38}$$

$$\begin{aligned}&\mathrm{Q9}=\mathrm{Simplify}[\mathrm{f8}]\\&\mathrm{f9}=\mathrm{Q9}\end{aligned}\tag{A.39}$$

$$\begin{aligned}&\mathrm{Q10}=\mathrm{Simplify}\left[\mathrm{f9}+\gamma*\mathrm{Integrate}\left[-g_f*(T-\mathrm{t4}),\{T,\mathrm{t4},t\}\right]/.\left\{g_f\rightarrow G_r/\epsilon,\mathrm{t4}\rightarrow\left(2\text{*}\tau\text{-3*}\epsilon\text{/2-}\tau_{\mathrm{r}}\right)\right\}\right]\\&\mathrm{f10}=\mathrm{Simplify}\left[\mathrm{Q10}/.t\rightarrow\left(2*\tau-\epsilon/2-\tau_r\right)\right]\end{aligned}\tag{A.40}$$

$$\begin{aligned}&\mathrm{Q11}=\mathrm{Simplify}\left[\mathrm{f10}+\gamma*\mathrm{Integrate}\left[-G_r,\{T,\mathrm{t4}+\epsilon,t\}\right]/.\left\{\mathrm{t4}\rightarrow\left(2\text{*}\tau\text{-3*}\epsilon\text{/2-}\tau_{\mathrm{r}}\right)\right\}\right]\\&\mathrm{f11}=\mathrm{Simplify}\left[\mathrm{Q11}/.t\rightarrow\left(2*\tau-3*\epsilon/2-\tau_r/2\right)\right]\end{aligned}\tag{A.41}$$

$$\begin{aligned}&\mathrm{Q12}=\mathrm{Simplify}\left[\begin{array}{l}\mathrm{f11}+\gamma*\mathrm{Integrate}\left[g_f*\left(T-\mathrm{t4}-\tau_r/2\right),\left\{T,\mathrm{t4}+\tau_r/2,t\right\}\right]\\ /.\left\{g_f\rightarrow G_r/\epsilon,\mathrm{t4}\rightarrow\left(2\text{*}\tau\text{-3*}\epsilon\text{/2-}\tau_{\mathrm{r}}\right)\right\}\end{array}\right]\\&\mathrm{f12}=\mathrm{Simplify}\left[\mathrm{Q12}/.t\rightarrow\left(2*\tau-\epsilon/2-\tau_r/2\right)\right]\end{aligned}\tag{A.42}$$

$$\begin{aligned}&\mathrm{Q13}=\mathrm{Simplify}\left[\begin{array}{l}\mathrm{f12}+\gamma*\mathrm{Integrate}\left[g_r*\left(T-\mathrm{t4}-\tau_r/2-\epsilon\right),\left\{T,\mathrm{t4}+\tau_r/2+\epsilon,t\right\}\right]\\ /.\left\{g_r\rightarrow G_r/\epsilon,\mathrm{t4}\rightarrow\left(2\text{*}\tau\text{-3*}\epsilon\text{/2-}\tau_{\mathrm{r}}\right)\right\}\end{array}\right]\\&\mathrm{f13}=\mathrm{Simplify}\left[\mathrm{Q13}/.t\rightarrow\left(2*\tau-\tau_r/2+\epsilon/2\right)\right]\end{aligned}\tag{A.43}$$

$$\begin{aligned}&\mathrm{Q14}=\mathrm{Simplify}\left[\mathrm{f13}+\gamma*\mathrm{Integrate}\left[G_r,\left\{T,2*\tau-\tau_r/2+\epsilon/2,t\right\}\right]\right]\\&\mathrm{f14}=\mathrm{Simplify}[\mathrm{Q14}/.t\rightarrow(2*\tau)]\end{aligned}\tag{A.44}$$

The b-value along the frequency-encoding direction is:

$$\begin{aligned}
\text{Bff} = {} & \text{Simplify[Integrate[(Q1)}{}^\wedge 2,\{t,\tau-\Delta/2-\epsilon/2-\delta/2,\tau-\Delta/2+\epsilon/2-\delta/2\}] \\
& +\text{Integrate[(Q2)}{}^\wedge 2,\{t,\tau-\Delta/2+\epsilon/2-\delta/2,\tau-\Delta/2-\epsilon/2+\delta/2\}] \\
& +\text{Integrate[(Q3)}{}^\wedge 2,\{t,\tau-\Delta/2-\epsilon/2+\delta/2,\tau-\Delta/2+\epsilon/2+\delta/2\}] \\
& +\text{Integrate[(Q4)}{}^\wedge 2,\{t,\tau-\Delta/2+\epsilon/2+\delta/2,\tau\}] \\
& +\text{Integrate[(Q5)}{}^\wedge 2,\{t,\tau,\tau+\Delta/2-\epsilon/2-\delta/2\}] \\
& +\text{Integrate[(Q6)}{}^\wedge 2,\{t,\tau+\Delta/2-\delta/2-\epsilon/2,\tau+\Delta/2-\delta/2+\epsilon/2\}] \\
& +\text{Integrate[(Q7)}{}^\wedge 2,\{t,\tau+\Delta/2-\delta/2+\epsilon/2,\tau+\Delta/2-\epsilon/2+\delta/2\}] \\
& +\text{Integrate[(Q8)}{}^\wedge 2,\{t,\tau+\Delta/2-\epsilon/2+\delta/2,\tau+\Delta/2+\epsilon/2+\delta/2\}] \\
& +\text{Integrate}\left[\text{(Q9)}{}^\wedge 2,\left\{t,\tau+\Delta/2+\epsilon/2+\delta/2,2*\tau-3*\epsilon/2-\tau_r\right\}\right] \\
& +\text{Integrate}\left[\text{(Q10)}{}^\wedge 2,\left\{t,2*\tau-3*\epsilon/2-\tau_r,2*\tau-\epsilon/2-\tau_r\right\}\right] \\
& +\text{Integrate}\left[\text{(Q11)}{}^\wedge 2,\left\{t,2*\tau-\epsilon/2-\tau_r,2*\tau-3*\epsilon/2-\tau_r/2\right\}\right] \\
& +\text{Integrate}\left[\text{(Q12)}{}^\wedge 2,\left\{t,2*\tau-3*\epsilon/2-\tau_r/2,2*\tau-\epsilon/2-\tau_r/2\right\}\right] \\
& +\text{Integrate}\left[\text{(Q13)}{}^\wedge 2,\left\{t,2*\tau-\epsilon/2-\tau_r/2,2*\tau+\epsilon/2-\tau_r/2\right\}\right] \\
& +\text{Integrate}\left[\text{(Q14)}{}^\wedge 2,\left\{t,2*\tau+\epsilon/2-\tau_r/2,2*\tau\right\}\right]]
\end{aligned} \tag{A.45}$$

The q-value along the slice selection gradient direction is:

$$\begin{aligned}
& \text{Q1} = \gamma*\text{Simplify}\left[\text{Integrate}\left[G_s,\{T,0,t\}\right]\right] \\
& \text{f1} = \text{Q1}/.t \to \left(\tau_\text{s}\text{-}\epsilon\right)/2
\end{aligned} \tag{A.46}$$

$$\begin{aligned}
& \text{Q2} = \text{Simplify}\left[\text{f1}+\gamma*\text{Integrate}\left[-g_s*\left(T-\left(\tau_s+\epsilon\right)/2\right),\left\{T,\left(\tau_s-\epsilon\right)/2,t\right\}\right]/.g_s \to \text{G}_\text{s}/\epsilon\right] \\
& \text{f2} = \text{Simplify}\left[\text{Q2}/.t \to \left(\tau_s+\epsilon\right)/2\right]
\end{aligned} \tag{A.47}$$

$$\begin{aligned}
& \text{Q3} = \text{Simplify}\left[\text{f2}+\gamma*\text{Integrate}\left[-g_s*\left(T-\left(\tau_s+\epsilon\right)/2\right),\left\{T,\left(\tau_s+\epsilon\right)/2,t\right\}\right]/.g_s \to \text{G}_\text{s}/\epsilon\right] \\
& \text{f3} = \text{Simplify}\left[\text{Q3}/.t \to \tau_s/2+3*\epsilon/2\right]
\end{aligned} \tag{A.48}$$

$$\begin{aligned}
& \text{Q4} = \text{Simplify}\left[\text{f3}+\gamma*\text{Integrate}\left[-G_s,\left\{T,\tau_s/2+3*\epsilon/2,t\right\}\right]\right] \\
& \text{f4} = \text{Simplify}\left[\text{Q4}/.t \to \tau_s+\epsilon/2\right]
\end{aligned} \tag{A.49}$$

$$\begin{aligned}
& \text{Q5} = \text{Simplify}\left[\text{f4}+\gamma*\text{Integrate}\left[g_s*\left(T-\tau_s-3*\epsilon/2\right),\left\{T,\tau_s+\epsilon/2,t\right\}\right]/.g_s \to \text{G}_\text{s}/\epsilon\right] \\
& \text{f5} = \text{Simplify}\left[\text{Q5}/.t \to \tau_\text{s}\text{+3*}\epsilon\text{/2}\right]
\end{aligned} \tag{A.50}$$

$$\begin{aligned}
& \text{Q6} = \text{Simplify}\left[\text{f5}+\gamma*\text{Integrate}\left[g_\text{ds}*(T-\text{t1}),\{T,\text{t1},t\}\right]/.\left\{\text{t1} \to \tau\text{-}\Delta\text{/2-}\epsilon\text{/2-}\delta\text{/2},\text{g}_\text{ds} \to \text{G}_\text{ds}/\epsilon\right\}\right] \\
& \text{f6} = \text{Simplify}[\text{Q6}/.t \to \tau-\Delta/2+\epsilon/2-\delta/2]
\end{aligned} \tag{A.51}$$

$$\begin{aligned}
& \text{Q7} = \text{Simplify}\left[\text{f6}+\gamma*\text{Integrate}\left[G_\text{ds},\{T,\text{t1}+\epsilon,t\}\right]/.\text{t1} \to \text{-}\Delta\text{/2-}\epsilon\text{/2-}\delta\text{/2}\right] \\
& \text{f7} = \text{Simplify}[\text{Q7}/.t \to \tau-\Delta/2-\epsilon/2+\delta/2]
\end{aligned} \tag{A.52}$$

$$\begin{aligned}&\mathrm{Q8}=\mathrm{Simplify}\left[\begin{array}{l}\mathrm{f7}+\gamma*\mathrm{Integrate}\left[-g_{\mathrm{ds}}*(T-\mathrm{t1}-\delta-\epsilon),\{T,\mathrm{t1}+\delta,t\}\right]\\ /.\left\{\mathrm{t1}\to\tau\text{-}\Delta/2\text{-}\epsilon/2\text{-}\delta/2,\mathrm{g}_{\mathrm{ds}}\to\mathrm{G}_{\mathrm{ds}}/\epsilon\right\}\end{array}\right]\\&\mathrm{f8}=\mathrm{Simplify}[\mathrm{Q8}/.t\to(\tau-\Delta/2+\epsilon/2+\delta/2)]\end{aligned}\tag{A.53}$$

$$\begin{aligned}&\mathrm{Q9} = \mathrm{Simplify}[\ \mathrm{f8}]\\&\mathrm{f9} = \mathrm{Q9}\end{aligned}\tag{A.54}$$

$$\begin{aligned}&\mathrm{Q10}=\mathrm{Simplify}\left[\mathrm{f9}+\gamma*\mathrm{Integrate}\left[g_s*(T-\mathrm{t2}),\{T,\mathrm{t2},t\}\right]\right]/.\left\{g_s\to\mathrm{G_s}/\epsilon,\mathrm{t2}\to\text{-}\epsilon/4\text{-}\tau_{\mathrm{s}}/2\right\}\\&\mathrm{f10}=\mathrm{Simplify}\left[\mathrm{Q10}/.t\to\left(\tau-\tau_s/2+\epsilon/4\right)\right]\end{aligned}\tag{A.55}$$

$$\begin{aligned}&\mathrm{Q11}=\mathrm{Simplify}\left[\mathrm{f10}+\gamma*\mathrm{Integrate}\left[G_s/2,\left\{T,\tau-\tau_s/2+\epsilon/4,t\right\}\right]\right]\\&\mathrm{f11}=\mathrm{Simplify}[\mathrm{Q11}/.t\to\tau]\end{aligned}\tag{A.56}$$

$$\begin{aligned}&\mathrm{Q12}=\mathrm{Simplify}\left[-\mathrm{f11}+\gamma*\mathrm{Integrate}\left[G_s/2,\{T,\tau,t\}\right]\right]\\&\mathrm{f12}=\mathrm{Simplify}\left[\mathrm{Q12}/.t\to\left(\tau-\epsilon/4+\tau_s/2\right)\right]\end{aligned}\tag{A.57}$$

$$\begin{aligned}&\mathrm{Q13}=\mathrm{Simplify}\left[\begin{array}{l}\mathrm{f12}+\gamma*\mathrm{Integrate}\left[-g_s*\left(T-\tau-\tau_s/2-\epsilon/4\right),\left\{T,\tau-\epsilon/4+\tau_s/2,t\right\}\right]\\ /.g_s\to\mathrm{G_s}/\epsilon\end{array}\right]\\&\mathrm{f13}=\mathrm{Simplify}\left[\mathrm{Q13}/.t\to\left(\tau+\epsilon/4+\tau_s/2\right)\right]\end{aligned}\tag{A.58}$$

$$\begin{aligned}&\mathrm{Q14}=\mathrm{Simplify}[\mathrm{f13}]\\&\mathrm{f14}=\mathrm{Q14}\end{aligned}\tag{A.59}$$

$$\begin{aligned}&\mathrm{Q15}=\mathrm{Simplify}\left[\mathrm{f14}+\gamma*\mathrm{Integrate}\left[g_{\mathrm{ds}}*(T-\mathrm{t3}),\{T,\mathrm{t3},t\}\right]/.\left\{\mathrm{t3}\to(\tau\text{+}\Delta/2\text{-}\delta/2\text{-}\epsilon/2),\mathrm{g}_{\mathrm{ds}}\to\mathrm{G}_{\mathrm{ds}}/\epsilon\right\}\right]\\&\mathrm{f15}=\mathrm{Simplify}[\mathrm{Q15}/.t\to\tau+\Delta/2-\delta/2+\epsilon/2]\end{aligned}\tag{A.60}$$

$$\begin{aligned}&\mathrm{Q16}=\mathrm{Simplify}\left[\mathrm{f15}+\gamma*\mathrm{Integrate}\left[G_{\mathrm{ds}},\{T,\tau+\Delta/2-\delta/2+\epsilon/2,t\}\right]\right]\\&\mathrm{f16}=\quad\mathrm{Simplify}[\mathrm{Q16}/.t\to(\tau+\Delta/2+\delta/2-\epsilon/2)]\end{aligned}\tag{A.61}$$

$$\begin{aligned}&\mathrm{Q17}=\mathrm{Simplify}\left[\begin{array}{l}\mathrm{f16}+\gamma*\mathrm{Integrate}\left[-g_{\mathrm{ds}}*(T-(\tau+\Delta/2+\delta/2+\epsilon/2)),\{T,\tau+\Delta/2+\delta/2-\epsilon/2,t\}\right]\\ /.g_{\mathrm{ds}}\to\mathrm{G}_{\mathrm{ds}}/\epsilon\end{array}\right]\\&\mathrm{f17}=\mathrm{Simplify}[\mathrm{Q17}/.t\to(\tau+\Delta/2+\delta/2+\epsilon/2)]\end{aligned}\tag{A.62}$$

$$\mathrm{Q18} = \mathrm{Simplify}[\mathrm{f17}]\tag{A.63}$$

The b-value along the slice selection gradient direction is defined as:

$$
\begin{aligned}
\mathrm{Bss}=\mathrm{Simplify}\Big[&\mathrm{Integrate}\left[(\mathrm{Q1})\hat{}2,\left\{t,0,\left(\tau_s-\epsilon\right)/2\right\}\right]\\
&+\mathrm{Integrate}\left[(\mathrm{Q2})\hat{}2,\left\{t,\left(\tau_s-\epsilon\right)/2,t,\left(\tau_s+\epsilon\right)/2\right\}\right]\\
&+\mathrm{Integrate}\left[(\mathrm{Q3})\hat{}2,\left\{t,\left(\tau_s+\epsilon\right)/2,\left(\tau_s+3*\epsilon\right)/2\right\}\right]\\
&+\mathrm{Integrate}\left[(\mathrm{Q4})\hat{}2,\left\{t,\left(\tau_s+3*\epsilon\right)/2,\tau_s+\epsilon/2\right\}\right]\\
&+\mathrm{Integrate}\left[(\mathrm{Q5})\hat{}2,\left\{t,\tau_s+\epsilon/2,3*\epsilon/2+\tau_s\right\}\right]\\
&+\mathrm{Integrate}[(\mathrm{Q6})\hat{}2,\{t,\tau-\Delta/2-\epsilon/2-\delta/2,\tau-\Delta/2+\epsilon/2-\delta/2\}]\\
&+\mathrm{Integrate}[(\mathrm{Q7})\hat{}2,\{t,\tau-\Delta/2+\epsilon/2-\delta/2,\tau-\Delta/2-\epsilon/2+\delta/2\}]\\
&+\mathrm{Integrate}[(\mathrm{Q8})\hat{}2,\{t,\tau-\Delta/2-\epsilon/2+\delta/2,\tau-\Delta/2+\epsilon/2+\delta/2\}]\\
&+\mathrm{Integrate}\left[(\mathrm{Q9})\hat{}2,\left\{t,\tau-\Delta/2+\epsilon/2+\delta/2,\tau-\epsilon/4-\tau_s/2\right\}\right]\\
&+\mathrm{Integrate}\left[(\mathrm{Q10})\hat{}2,\left\{t,\tau-\epsilon/4-\tau_s/2,\tau+\epsilon/4-\tau_s/2\right\}\right]\\
&+\mathrm{Integrate}\left[(\mathrm{Q11})\hat{}2,\left\{t,\tau+\epsilon/4-\tau_s/2,\tau\right\}\right]\\
&+\mathrm{Integrate}\left[(\mathrm{Q12})\hat{}2,\left\{t,\tau,\tau-\epsilon/4+\tau_s/2\right\}\right]\\
&+\mathrm{Integrate}\left[(\mathrm{Q13})\hat{}2,\left\{t,\tau-\epsilon/4+\tau_s/2,\tau+\epsilon/4+\tau_s/2\right\}\right]\\
&+\mathrm{Integrate}\left[(\mathrm{Q14})\hat{}2,\left\{t,\tau+\epsilon/4+\tau_s/2,\tau+\Delta/2-\epsilon/2-\delta/2\right\}\right]\\
&+\mathrm{Integrate}[(\mathrm{Q15})\hat{}2,\{t,\tau+\Delta/2-\epsilon/2-\delta/2,\tau+\Delta/2+\epsilon/2-\delta/2\}]\\
&+\mathrm{Integrate}[(\mathrm{Q16})\hat{}2,\{t,\tau+\Delta/2+\epsilon/2-\delta/2,\tau+\Delta/2-\epsilon/2+\delta/2\}]\\
&+\mathrm{Integrate}[(\mathrm{Q17})\hat{}2,\{t,\tau+\Delta/2-\epsilon/2+\delta/2,\tau+\Delta/2+\epsilon/2+\delta/2\}]\\
&+\mathrm{Integrate}[(\mathrm{Q18})\hat{}2,\{t,\tau+\Delta/2+\epsilon/2+\delta/2,2*\tau\}]\Big]
\end{aligned}
\tag{A.64}
$$

The cross items bsf of b-value:

Where Qs1 to Qs18 is same with definition of Qs, for Qf1 to Qf14 is the selected Qf.

$$
\begin{aligned}
&\mathrm{Qf1}=\mathrm{Simplify}\left[\gamma*\mathrm{Integrate}\left[g_{\mathrm{df}}*(T-\mathrm{t1}),\{T,\mathrm{t1},t\}\right]/.\left\{g_{\mathrm{df}}\to \mathrm{G}_{\mathrm{df}}/\epsilon,\mathrm{t1}\to\tau\text{-}\Delta/2\text{-}\epsilon/2\text{-}\delta/2\right\}\right]\\
&\mathrm{ff1}=\mathrm{Simplify}[\mathrm{Qf1}/.t\to\tau-\Delta/2+\epsilon/2-\delta/2]
\end{aligned}
\tag{A.65}
$$

$$
\begin{aligned}
&\mathrm{Qf2}=\mathrm{Simplify}\left[\mathrm{ff1}+\gamma*\mathrm{Integrate}\left[G_{\mathrm{df}},\{T,\mathrm{t1}+\epsilon,t\}\right]/.\left\{g_{\mathrm{df}}\to G_{\mathrm{df}}/\epsilon,\mathrm{t1}\to\tau\text{-}\Delta/2\text{-}\epsilon/2\text{-}\delta/2\right\}\right]\\
&\mathrm{ff2}=\mathrm{Simplify}[\mathrm{Qf2}/.t\to(\tau-\Delta/2-\epsilon/2+\delta/2)]
\end{aligned}
\tag{A.66}
$$

$$
\begin{aligned}
&\mathrm{Qf3}=\mathrm{Simplify}\left[\begin{array}{l}\mathrm{ff2}+\gamma*\mathrm{Integrate}\left[-g_{\mathrm{df}}*(T-\mathrm{t1}-\delta-\epsilon),\{T,\mathrm{t1}+\delta,t\}\right]\\ /.\left\{g_{\mathrm{df}}\to G_{\mathrm{df}}/\epsilon,\mathrm{t1}\to\tau\text{-}\Delta/2\text{-}\epsilon/2\text{-}\delta/2\right\}\end{array}\right]\\
&\mathrm{ff3}=\mathrm{Simplify}[\mathrm{Qf3}/.t\to(\tau-\Delta/2+\epsilon/2+\delta/2)]
\end{aligned}
\tag{A.67}
$$

$$
\begin{aligned}
&\mathrm{Qf4}=\mathrm{Simplify}[\mathrm{ff3}]\\
&\mathrm{ff4}=\mathrm{Qf4}
\end{aligned}
\tag{A.68}
$$

$$
\begin{aligned}
&\mathrm{Qf5}=-\mathrm{ff4}\\
&\mathrm{ff5}=\mathrm{Qf5}
\end{aligned}
\tag{A.69}
$$

$$\begin{aligned}
&\mathrm{Qf6} = \mathrm{Simplify}\left[\mathrm{ff5} + \gamma * \mathrm{Integrate}\left[g_{\mathrm{df}} * (T - \mathrm{t3}), \{T, \mathrm{t3}, t\}\right] /. \left\{g_{\mathrm{df}} \to G_{\mathrm{df}} / \epsilon, \mathrm{t3} \to (\tau\text{+}\Delta\text{/2-}\delta\text{/2-}\epsilon\text{/2})\right\}\right] \\
&\mathrm{ff6} = \mathrm{Simplify}[\mathrm{Qf6}/.\{t \to \tau + \Delta/2 - \delta/2 + \epsilon/2\}]
\end{aligned} \tag{A.70}$$

$$\begin{aligned}
&\mathrm{Qf7} = \mathrm{Simplify}\left[\mathrm{ff6} + \ \gamma * \mathrm{Integrate}\left[G_{\mathrm{df}}, \{T, (\tau + \Delta/2 - \delta/2 + \epsilon/2), t\}\right] /. \left\{g_{\mathrm{df}} \to G_{\mathrm{df}} / \epsilon\right\}\right] \\
&\mathrm{ff7} = \mathrm{Simplify}[\mathrm{Qf7}/.t \to (\tau + \Delta/2 + \delta/2 - \epsilon/2)]
\end{aligned} \tag{A.71}$$

$$\begin{aligned}
&\mathrm{Qf8} = \mathrm{Simplify}\left[\begin{array}{l} \mathrm{ff7} + \gamma * \mathrm{Integrate}\left[-g_{\mathrm{df}} * (T - (\tau + \Delta/2 + \delta/2 + \epsilon/2)), \{T, (\tau + \Delta/2 + \delta/2 - \epsilon/2), t\}\right] \\ /.\left\{g_{\mathrm{df}} \to G_{\mathrm{df}} / \epsilon\right\} \end{array}\right] \\
&\mathrm{ff8} = \mathrm{Simplify}[\mathrm{Qf8}/.t \to (\tau + \Delta/2 + \delta/2 + \epsilon/2)]
\end{aligned} \tag{A.72}$$

$$\begin{aligned}
&\mathrm{Qf9} = \mathrm{Simplify}[\mathrm{ff8}] \\
&\mathrm{ff9} = \mathrm{Qf9}
\end{aligned} \tag{A.73}$$

$$\begin{aligned}
&\mathrm{Qf10} = \mathrm{Simplify}\left[\mathrm{ff9} + \gamma * \mathrm{Integrate}\left[-g_f * (T - \mathrm{t4}), \{T, \mathrm{t4}, t\}\right] /. \left\{g_f \to G_r / \epsilon, \mathrm{t4} \to \left(2\text{*}\tau\text{-3*}\epsilon\text{/2-}\tau_{\mathrm{r}}\right)\right\}\right] \\
&\mathrm{ff10} = \mathrm{Simplify}\left[\mathrm{Qf10}/.t \to \left(2 * \tau - \epsilon/2 - \tau_r\right)\right]
\end{aligned} \tag{A.74}$$

$$\begin{aligned}
&\mathrm{Qf11} = \mathrm{Simplify}\left[\mathrm{ff10} + \gamma * \mathrm{Integrate}\left[-G_r, \{T, \mathrm{t4} + \epsilon, t\}\right] /. \left\{\mathrm{t4} \to \left(2\text{*}\tau\text{-3*}\epsilon\text{/2-}\tau_{\mathrm{r}}\right)\right\}\right] \\
&\mathrm{ff11} = \mathrm{Simplify}\left[\mathrm{Qf11}/.t \to \left(2 * \tau - 3 * \epsilon/2 - \tau_r/2\right)\right]
\end{aligned} \tag{A.75}$$

$$\begin{aligned}
&\mathrm{Qf12} = \mathrm{Simplify}\left[\begin{array}{l} \mathrm{ff11} + \gamma * \mathrm{Integrate}\left[g_f * \left(T - \mathrm{t4} - \tau_r/2\right), \left\{T, \mathrm{t4} + \tau_r/2, t\right\}\right] \\ /.\left\{g_f \to G_r / \epsilon, \mathrm{t4} \to \left(2\text{*}\tau\text{-3*}\epsilon\text{/2-}\tau_{\mathrm{r}}\right)\right\} \end{array}\right] \\
&\mathrm{ff12} = \mathrm{Simplify}\left[\mathrm{Qf12}/.t \to \left(2 * \tau - \epsilon/2 - \tau_r/2\right)\right]
\end{aligned} \tag{A.76}$$

$$\begin{aligned}
&\mathrm{Qf13} = \mathrm{Simplify}\left[\begin{array}{l} \mathrm{ff12} + \gamma * \mathrm{Integrate}\left[g_r * \left(T - \mathrm{t4} - \tau_r/2 - \epsilon\right), \left\{T, \mathrm{t4} + \tau_r/2 + \epsilon, t\right\}\right] \\ /.\left\{g_r \to G_r / \epsilon, \mathrm{t4} \to \left(2\text{*}\tau\text{-3*}\epsilon\text{/2-}\tau_{\mathrm{r}}\right)\right\} \end{array}\right] \\
&\mathrm{ff13} = \mathrm{Simplify}\left[\mathrm{Qf13}/.t \to \left(2 * \tau - \tau_r/2 + \epsilon/2\right)\right]
\end{aligned} \tag{A.77}$$

$$\begin{aligned}
&\mathrm{Qf14} = \mathrm{Simplify}\left[\mathrm{ff13} + \gamma * \mathrm{Integrate}\left[G_r, \left\{T, 2 * \tau - \tau_r/2 + \epsilon/2, t\right\}\right]\right] \\
&\mathrm{ff14} = \mathrm{Simplify}[\mathrm{Qf14}/.t \to (2 * \tau)]
\end{aligned} \tag{A.78}$$

$$
\begin{aligned}
\mathrm{bsf} = {} & \mathrm{FullSimplify}[(\mathrm{Integrate}[\mathrm{Qf1}*\mathrm{Qs6},\{t,\mathrm{t1},\mathrm{t1}+\epsilon\}] \\
& ++\mathrm{Integrate}[\mathrm{Qf2}*\mathrm{Qs7},\{t,\mathrm{t1}+\epsilon,\mathrm{t1}+\delta\}] \\
& +\mathrm{Integrate}[\mathrm{Qf3}*\mathrm{Qs8},\{t,\mathrm{t1}+\delta,\mathrm{t1}+\delta+\epsilon\}] \\
& +\mathrm{Integrate}[\mathrm{Qf4}*\mathrm{Qs9},\{t,\mathrm{t1}+\delta+\epsilon,\mathrm{t2}\}] \\
& +\mathrm{Integrate}\left[\mathrm{Qf4}*\mathrm{Qs10},\left\{t,\mathrm{t2},\tau-\tau_s/2+\epsilon/4\right\}\right] \\
& +\mathrm{Integrate}\left[\mathrm{Qf4}*\mathrm{Qs11},\left\{t,\tau-\tau_s/2+\epsilon/4,\tau\right\}\right] \\
& +\mathrm{Integrate}\left[\mathrm{Qf5}*\mathrm{Qs12},\left\{t,\tau,\tau-\epsilon/4+\tau_s/2\right\}\right] \\
& +\mathrm{Integrate}\left[\mathrm{Qf5}*\mathrm{Qs13},\left\{t,\tau-\epsilon/4+\tau_s/2,\tau+\epsilon/4+\tau_s/2\right\}\right] \\
& +\mathrm{Integrate}\left[\mathrm{Qf5}*\mathrm{Qs14},\left\{t,\tau+\epsilon/4+\tau_s/2,\mathrm{t3}\right\}\right] \\
& +\mathrm{Integrate}[\mathrm{Qf6}*\mathrm{Qs15},\{t,\mathrm{t3},\mathrm{t3}+\epsilon\}] \\
& +\mathrm{Integrate}[\mathrm{Qf7}*\mathrm{Qs16},\{t,\mathrm{t3}+\epsilon,\mathrm{t3}+\delta\}] \\
& +\mathrm{Integrate}[\mathrm{Qf8}*\mathrm{Qs17},\{t,\mathrm{t3}+\delta,\mathrm{t3}+\delta+\epsilon\}] \\
& +\mathrm{Integrate}[\mathrm{Qf9}*\mathrm{Qs18},\{t,\mathrm{t3}+\delta+\epsilon,\mathrm{t3}+\delta+2*\epsilon\}] \\
& +\mathrm{Integrate}\left[\mathrm{Qf10}*\mathrm{Qs18},\left\{t,\mathrm{t3}+\delta+2*\epsilon,2*\tau-\epsilon/2-\tau_r\right\}\right] \\
& +\mathrm{Integrate}\left[\mathrm{Qf11}*\mathrm{Qs18},\left\{t,2*\tau-\epsilon/2-\tau_r,2*\tau-3*\epsilon/2-\tau_r/2\right\}\right] \\
& +\mathrm{Integrate}\left[\mathrm{Qf12}*\mathrm{Qs18},\left\{t,2*\tau-3*\epsilon/2-\tau_r/2,2*\tau-\epsilon/2-\tau_r/2\right\}\right] \\
& +\mathrm{Integrate}\left[\mathrm{Qf13}*\mathrm{Qs18},\left\{t,2*\tau-\epsilon/2-\tau_r/2,2*\tau-\tau_r/2+\epsilon/2\right\}\right] \\
& +\mathrm{Integrate}\left[\mathrm{Qf14}*\mathrm{Qs18},\left\{t,2*\tau-\tau_r/2+\epsilon/2,2*\tau\right\}\right]\Big) \\
& /.\left\{\mathrm{t1}\to\tau\text{-}\Delta/2\text{-}\epsilon/2\text{-}\delta/2,\mathrm{t3}\to\tau\text{+}\Delta/2\text{-}\epsilon/2\text{-}\delta/2,\mathrm{t2}\to\tau\text{-}\epsilon/4\text{-}\tau_s/2\right\}]
\end{aligned}
\tag{A.79}
$$

The cross items bfp of b-value: here Q1~Q12 represent the q-value along the phase encoding direction.

$$
\begin{aligned}
\mathrm{bfp} = {} & \mathrm{Simplify}[(\mathrm{Integrate}[\mathrm{Q4}*\mathrm{Qf1},\{t,\tau-\Delta/2-\epsilon/2-\delta/2,\tau-\Delta/2+\epsilon/2-\delta/2\}] \\
& +\mathrm{Integrate}[\mathrm{Q5}*\mathrm{Qf2},\{t,\tau-\Delta/2+\epsilon/2-\delta/2,\tau-\Delta/2-\epsilon/2+\delta/2\}] \\
& +\mathrm{Integrate}[\mathrm{Q6}*\mathrm{Qf3},\{t,\tau-\Delta/2-\epsilon/2+\delta/2,\tau-\Delta/2+\epsilon/2+\delta/2\}] \\
& +\mathrm{Integrate}[\mathrm{Q7}*\mathrm{Qf4},\{t,\tau-\Delta/2+\epsilon/2+\delta/2,\tau\}] \\
& +\mathrm{Integrate}[\mathrm{Q8}*\mathrm{Qf5},\{t,\tau,\tau+\Delta/2-\delta/2-\epsilon/2\}] \\
& +\mathrm{Integrate}[\mathrm{Q9}*\mathrm{Qf6},\{t,\tau+\Delta/2-\delta/2-\epsilon/2,\tau+\Delta/2-\delta/2+\epsilon/2\}] \\
& +\mathrm{Integrate}[\mathrm{Q10}*\mathrm{Qf7},\{t,\tau+\Delta/2-\delta/2+\epsilon/2,\tau+\Delta/2+\delta/2-\epsilon/2\}] \\
& +\mathrm{Integrate}[\mathrm{Q11}*\mathrm{Qf8},\{t,\tau+\Delta/2+\delta/2-\epsilon/2,\tau+\Delta/2+\delta/2+\epsilon/2\}] \\
& +\mathrm{Integrate}\left[\mathrm{Q12}*\mathrm{Qf9},\left\{t,\tau+\Delta/2+\delta/2+\epsilon/2,2*\tau-3*\epsilon/2-\tau_r\right\}\right] \\
& +\mathrm{Integrate}\left[\mathrm{Q12}*\mathrm{Qf10},\left\{t,2*\tau-3*\epsilon/2-\tau_r,2*\tau-\epsilon/2-\tau_r\right\}\right] \\
& +\mathrm{Integrate}\left[\mathrm{Q12}*\mathrm{Qf11},\left\{t,2*\tau-\epsilon/2-\tau_r,2*\tau-3*\epsilon/2-\tau_r/2\right\}\right] \\
& +\mathrm{Integrate}\left[\mathrm{Q12}*\mathrm{Qf12},\left\{t,2*\tau-3*\epsilon/2-\tau_r/2,2*\tau-\epsilon/2-\tau_r/2\right\}\right] \\
& +\mathrm{Integrate}\left[\mathrm{Q12}*\mathrm{Qf13},\left\{t,2*\tau-\epsilon/2-\tau_r/2,2*\tau-\tau_r/2+\epsilon/2\right\}\right] \\
& +\mathrm{Integrate}\left[\mathrm{Q12}*\mathrm{Qf14},\left\{t,2*\tau-\tau_r/2+\epsilon/2,2*\tau\right\}\right])]
\end{aligned}
\tag{A.80}
$$

The cross item bsp of b-value:

$$
\begin{aligned}
\mathrm{bsp} = \mathrm{FullSimplify}\Big[\Big(&\mathrm{Integrate}\big[\mathrm{Qs3}*\mathrm{Q1},\{t,(\tau_s+\epsilon)/2,\tau_s/2+3*\epsilon/2\}\big]\\
&+\mathrm{Integrate}\big[\mathrm{Qs4}*\mathrm{Q2},\{t,\tau_s/2+3*\epsilon/2,\tau_s+\epsilon/2\}\big]\\
&+\mathrm{Integrate}\big[\mathrm{Qs5}*\mathrm{Q3},\{t,\tau_s+\epsilon/2,\tau_s+3*\epsilon/2\}\big]\\
&+\mathrm{Integrate}\big[\mathrm{Qs6}*\mathrm{Q4},\{t,\tau_s+3*\epsilon/2,\tau_s+5*\epsilon/2\}\big]\\
&+\mathrm{Integrate}\big[\mathrm{Qs7}*\mathrm{Q5},\{t,\tau_s+5*\epsilon/2,\tau_s+3*\epsilon/2+\delta\}\big]\\
&+\mathrm{Integrate}\big[\mathrm{Qs8}*\mathrm{Q6},\{t,\tau_s+3*\epsilon/2+\delta,\tau_s+5*\epsilon/2+\delta\}\big]\\
&+\mathrm{Integrate}\big[\mathrm{Qs9}*\mathrm{Q7},\{t,\tau_s+5*\epsilon/2+\delta,\Delta/2+\delta/2+\tau_s/2+7*\epsilon/4\}\big]\\
&+\mathrm{Integrate}\big[\mathrm{Qs10}*\mathrm{Q7},\{t,\Delta/2+\delta/2+\tau_s/2+7*\epsilon/4,\Delta/2+\delta/2+\tau_s/2+9*\epsilon/4\}\big]\\
&+\mathrm{Integrate}\big[\mathrm{Qs11}*\mathrm{Q7},\{t,\Delta/2+\delta/2+\tau_s/2+9*\epsilon/4,\Delta/2+\delta/2+\tau_s+2*\epsilon\}\big]\\
&+\mathrm{Integrate}\big[\mathrm{Qs12}*\mathrm{Q8},\{t,\Delta/2+\delta/2+\tau_s+2*\epsilon,\Delta/2+\delta/2+7*\epsilon/4+3*\tau_s/2\}\big]\\
&+\mathrm{Integrate}\big[\mathrm{Qs13}*\mathrm{Q8},\{t,\Delta/2+\delta/2+7*\epsilon/4+3*\tau_s/2,\Delta/2+\delta/2+9*\epsilon/4+3*\tau_s/2\}\big]\\
&+\mathrm{Integrate}\big[\mathrm{Qs14}*\mathrm{Q8},\{t,\Delta/2+\delta/2+9*\epsilon/4+3*\tau_s/2,\tau_s+3*\epsilon/2+\Delta\}\big]\\
&+\mathrm{Integrate}\big[\mathrm{Qs15}*\mathrm{Q9},\{t,\tau_s+3*\epsilon/2+\Delta,\tau_s+5*\epsilon/2+\Delta\}\big]\\
&+\mathrm{Integrate}\big[\mathrm{Qs16}*\mathrm{Q10},\{t,\tau_s+5*\epsilon/2+\Delta,\tau_s+3*\epsilon/2+\Delta+\delta\}\big]\\
&+\mathrm{Integrate}\big[\mathrm{Qs17}*\mathrm{Q11},\{t,\tau_s+3*\epsilon/2+\Delta+\delta,\tau_s+5*\epsilon/2+\Delta+\delta\}\big]\\
&+\mathrm{Integrate}\big[\mathrm{Qs18}*\mathrm{Q12},\{t,\tau_s+5*\epsilon/2+\Delta+\delta,\Delta+\delta+2*\tau_s+4*\epsilon\}\big])]
\end{aligned}
\tag{A.81}
$$

Bibliographies

[Aganj *et al.*, 2009] AGANJ, LENGLET C., SAPIRO G., *et al.* Multiple Q-shell ODF Reconstruction in Q-ball Imaging. In: YANG, HAWKES David J., RUECKERT Daniel., *et al.* Eds. Proc. of the *12th Ed.* conf. on *Medical Image Computing and Computer-Assisted Intervention: MICCAI*, Sep.2009, London, England. 2009, pp. 423–431.

[Aletras *et al.*, 1999] ALETRAS, BALABAN R. S., WEN H. High-resolution Strain Analysis of the Human Heart with fast-DENSE. *Journal of Magnetic Resonance*, 1999, vol. 140, no. 1, pp. 41–57.

[Allender *et al.*, 2008] ALLENDER, SCARBOROUGH P., PETO V. European Cardiovascular Disease Statistics, Brussels: European Heart Network AISBL, 2008, 112 p.

[Ashburner, 2007] ASHBURNER. A Fast Diffeomorphic Image Registration Algorithm. *NeuroImage*, 2007, vol. 38, no. 1, pp. 95–113.

[Assaf *et al.*, 2008a] ASSAF, BAR-SHIR A., COHEN Y., *et al.* Three-dimensional Water Diffusion in Impermeable Cylindrical Tubes: Theory Versus Experiments. *NMR in Biomedicine*, 2008, vol. 21, no. 8, pp. 888–898.

[Assaf *et al.*, 2005] ASSAF, BASSER P. J. Composite Hindered and Restricted Model of Diffusion (CHARMED) MR Imaging of the Human Brain. *NeuroImage*, 2005, vol. 27, no. 1, pp. 48–58.

[Assaf *et al.*, 2008b] ASSAF, BLUMENFELD-KATZIR T., YOVEL Y., *et al.* AxCaliber: a Method for Measuring Axon Diameter Distribution from Diffusion MRI. *Magnetic Resonance in Medicine*, 2008, vol. 59, no. 6, pp. 1347–1354.

[Assaf *et al.*, 2008c] ASSAF, PASTERNAK O. Diffusion Tensor Imaging (DTI)-based White Matter Mapping in Brain Research: a Review. *Journal of Molecular Neuroscience*, 2008, vol. 34, no. 1, pp. 51–61.

[Assemlal *et al.*, 2011] ASSEMLAL, TSCHUMPERLÉ D., BRUN L., *et al.* Recent Advances in Diffusion MRI Modeling: Angular and Radial Reconstruction. *Medical Image Analysis*, 2011, vol. 15, no. 4, pp. 369–396.

[Avram *et al.*, 2004] AVRAM, ASSAF Y., COHEN Y. The Effect of Rotational Angle and Experimental Parameters on the Diffraction Patterns and Micro-structural Information Obtained from Q-space Diffusion NMR: Implication for Diffusion in White Matter Fibers. *Journal of Magnetic Resonance*, 2004, vol. 169, no. 1, pp. 30–38.

[Awojoyogbe *et al.*, 2009] AWOJOYOGBE, BOUBAKER K. A Solution to Bloch NMR Flow Equations for the Analysis of Hemodynamic Functions of Blood Flow System Using m-Boubaker Polynomials. *Current Applied Physics*, 2009, vol. 9, no. 1, pp. 278–283.

[Axer *et al.*, 2011a] AXER, AMUNTS K., GRÄSSEL D., *et al.* A Novel Approach to the Human Connectome: Ultra-high Resolution Mapping of Fiber Tracts in the Brain. *NeuroImage*, 2011, vol. 54, no. 2, pp. 1091–1101.

[Axer *et al.*, 2011b] AXER, GRÄSSEL D., KLEINER M., *et al.* High-resolution Fiber Tract Reconstruction in the Human Brain by Means of Three-dimensional Polarized Light Imaging. *Frontiers in Neuroinformatics*, 2011, vol. 5, no. December, p. 34.

[Balac *et al.*, 2008] BALAC, CHUPIN L. Fast Approximate Solution of Bloch Equation for Simulation of RF Artifacts in Magnetic Resonance Imaging. *Mathematical and Computer Modelling*, 2008, vol. 48, no. 11–12, pp. 1901–1913.

[Bar-Shir *et al.*, 2008] BAR-SHIR, AVRAM L., OZARSLAN E., *et al.* The Effect of the Diffusion Time and Pulse Gradient Duration Ratio on the Diffraction Pattern and the Structural Information

Estimated from Q-space Diffusion MR: Experiments and Simulations. *Journal of Magnetic Resonance*, 2008, vol. 194, no. 2, pp. 230–236.

[Basser, 1995] BASSER. Inferring Microstructural Features and the Physiological. *NMR in Biomedicine*, 1995, vol. 8, pp. 333–344.

[Basser *et al.*, 1994a] BASSER, MATTIELLO J., LE BIHAN D. Estimation of the Effective Self-diffusion Tensor from NMR Spin Echo. *Journal of Magnetic Resonance*, 1994, vol. B 103, pp. 247–254.

[Basser *et al.*, 1994b] BASSER, MATTIELLO J., LEBIHAN D. MR Diffusion Tensor Spectroscopy and Imaging. *Biophysical Journal*, 1994, vol. 66, no. 1, pp. 259–267.

[Beaulieu, 2002] BEAULIEU. The Basis of Anisotropic Water Diffusion in the Nervous System - a Technical Review. *NMR in Biomedicine*, 2002, vol. 15, no. 7–8, pp. 435–455.

[Benoit-Cattin *et al.*, 2005] BENOIT-CATTIN, COLLEWET G., BELAROUSSI B., *et al.* The SIMRI Project: a Versatile and Interactive MRI Simulator. *Journal of Magnetic Resonance*, 2005, vol. 173, no. 1, pp. 97–115.

[Bernstein *et al.*, 2004] BERNSTEIN, KING K. F., ZHOU X. J. Handbook of MRI Pulse Sequences. Burlington: Elsevier Academic Press, 2004, 1040 p. ISBN 0120928612.

[Bloch F, 1946] BLOCH F. Nuclear Induction. *Physical Review*, 1946, vol. 70, no. 7, pp. 460–474.

[Broit, 1981] BROIT. Optimal Registration of Deformed Images. University of Pennsylvania, 1981.

[Brown, 1866] BROWN. A Brief Account of Microscopical Observations Made on the Particles Contained in the Pollen of Plants - Wikisource, the Free Online Library. *Philosophical Magazine*, 1866, vol. 4, pp. 161–173.

[Cai *et al.*, 2005] CAI, CHEN Z., CAI S., *et al.* Propagator Formalism and Computer Simulation of Restricted Diffusion Behaviors of Inter-molecular Multiple-quantum Coherences. *Physica B: Condensed Matter*, 2005, vol. 366, no. 1–4, pp. 127–137.

[P Callaghan, 1994] CALLAGHAN P. Principles of Nuclear Magnetic Resonance Microscopy. USA: Oxford University Press, 1994, 516 p. ISBN 0198539975.

[PT Callaghan *et al.*, 1999] CALLAGHAN P. T., CODD S. L., SEYMOUR J. D. Spatial Coherence Phenomena Arising from Translational Spin Motion in Gradient Spin Echo Experiments. *Concepts in Magnetic Resonance*, 1999, vol. 11, no. 4, pp. 181–202.

[Canales-Rodríguez *et al.*, 2009] CANALES-RODRÍGUEZ, MELIE-GARCÍA L., ITURRIA-MEDINA Y. Mathematical Description of Q-space in Spherical Coordinates: Exact Q-ball Imaging. *Magnetic Resonance in Medicine*, 2009, vol. 61, no. 6, pp. 1350–1367.

[Chen *et al.*, 2003] CHEN, SONG S.-K., LIU W., *et al.* Remodeling of Cardiac Fiber Structure After Infarction in Rats Quantified with Diffusion Tensor MRI. *American Journal of Physiology. Heart and Circulatory Physiology*, 2003, vol. 285, no. 3, pp. H946–954.

[Cheng *et al.*, 2011] CHENG, MERLET S., CARUYER E., *et al.* Compressive Sensing Ensemble Average Propagator Estimation via L1 Spherical Polar Fourier Imaging. *MICCAI Workshop on Computational Diffusion MRI - CDMRI'11*, Sep.2011. 2011, pp. 1–11.

[Cho *et al.*, 2008] CHO, YEH C.-H., TOURNIER J.-D., *et al.* Evaluation of the Accuracy and Angular Resolution of Q-ball Imaging. *NeuroImage*, 2008, vol. 42, no. 1, pp. 262–271.

[Chou *et al.*, 2012] CHOU, KAO E.-F., MORI S. Effects of B-value and Echo Time on MR-DTI Derived Axial,radial, Mean Diffusivity, Fractional Anisotropy and Principal Eigenvector at 1.5T a Voxel Wise Study. *J.Med.Biol.Eng.*, 2012, vol. In presse.

[Christensen *et al.*, 2001] CHRISTENSEN, JOHNSON H. J. Consistent Image Registration. *IEEE Transactions on Medical Imaging*, 2001, vol. 20, no. 7, pp. 568–582.

[Christensen *et al.*, 1996] CHRISTENSEN, RABBITT R. D., MILLER M. I. Deformable Templates Using Large Deformation Kinematics. *IEEE Transactions on Image Processing*, 1996, vol. 5, no. 10, pp. 1435–1447.

[Collin *et al.*, 2006] COLLIN, TRACQUI P., STEPHANOU A., *et al.* Spatiotemporal Dynamics of Actin-rich Adhesion Microdomains: Influence of Substrate Flexibility. *Journal of Cell Science*, 2006, vol. 119, no. Pt 9, pp. 1914–1925.

[Corno *et al.*, 2006] CORNO, KOCICA M. J., TORRENT-GUASP F. The Helical Ventricular Myocardial Band of Torrent-Guasp: Potential Implications in Congenital Heart Defects. *European Journal of Cardio-thoracic Surgery*, 2006, vol. 29 Suppl 1, pp. S61–68.

[Cory *et al.*, 1990] CORY, GARROWAY A. N. Measurement of Translational Displacement Probabilities by NMR: An Indicator of Compartmentation. *Magnetic Resonance in Medicine*, 1990, vol. 14, no. 3, pp. 435–444.

[Crum *et al.*, 2005] CRUM, TANNER C., HAWKES D. J. Anisotropic Multi-scale Fluid Registration: Evaluation in Magnetic Resonance Breast Imaging. *Physics in Medicine and Biology*, 2005, vol. 50, no. 21, pp. 5153–5174.

[Dammers *et al.*, 2010] DAMMERS, AXER M., GRÄSSEL D., *et al.* Signal Enhancement in Polarized Light Imaging by Means of Independent Component Analysis. *NeuroImage*, 2010, vol. 49, no. 2, pp. 1241–1248.

[Dammers *et al.*, 2012] DAMMERS, BREUER L., AXER M., *et al.* Automatic Identification of Gray and White Matter Components in Polarized Light Imaging. *NeuroImage*, 2012, vol. 59, no. 2, pp. 1338–1347.

[Delattre *et al.*, 2012] DELATTRE, VIALLON M., WEI H., *et al.* In Vivo Cardiac Diffusion-weighted Magnetic Resonance Imaging: Quantification of Normal Perfusion and Diffusion Coefficients with Intravoxel Incoherent Motion Imaging. *Investigative Radiology*, 2012, vol. 47, no. 11, pp. 662–70.

[Delon *et al.*, 2006] DELON, USSON Y., DEROUARD J., *et al.* Continuous Photobleaching in Vesicles and Living Cells: a Measure of Diffusion and Compartmentation. *Biophysical Journal*, 2006, vol. 90, no. 7, pp. 2548–2562.

[Deriche *et al.*, 2004] DERICHE, TSCHUMPERL D. Dt-mri Estimation, Regularization and Fiber Tractography. 2004, pp. 9–12.

[Descoteaux *et al.*, 2007] DESCOTEAUX, ANGELINO E., FITZGIBBONS S., *et al.* Regularized, Fast, and Robust Analytical Q-ball Imaging. *Magnetic Resonance in Medicine*, 2007, vol. 58, no. 3, pp. 497–510.

[Descoteaux *et al.*, 2009] DESCOTEAUX, DERICHE R. Diffusion Propagator Imaging: Using Laplace's Equation and Multiple Shell Acquisitions to Reconstruct the Diffusion Propagator. In: PRINCE, PHAM Dzung L, MYERS Kyle J Eds. Proc. of the *21st Ed.* conf. on *Information Processing in Medical Imaging*, Jul.2009, Williamsburg: USA. 2009, pp. 1–13.

[Descoteaux *et al.*, 2011] DESCOTEAUX, DERICHE R., LE BIHAN D., *et al.* Multiple Q-shell Diffusion Propagator Imaging. *Medical Image Analysis*, 2011, vol. 15, no. 4, pp. 603–621.

[Dou *et al.*, 2003] DOU, TSENG W.-Y. I., REESE T. G., *et al.* Combined Diffusion and Strain MRI Reveals Structure and Function of Human Myocardial Laminar Sheets in Vivo. *Magnetic Resonance in Medicine*, 2003, vol. 50, no. 1, pp. 107–113.

[Douaud *et al.*, 2011] DOUAUD, JBABDI S., BEHRENS T. E. J., *et al.* DTI Measures in Crossing-fibre Areas: Increased Diffusion Anisotropy Reveals Early White Matter Alteration in MCI and Mild Alzheimer's Disease. *NeuroImage*, 2011, vol. 55, no. 3, pp. 880–890.

[Duh *et al.*, 2001] DUH, MOHORIC A., STEPISNIK J. Computer Simulation of the Spin-echo Spatial Distribution in the Case of Restricted Self-diffusion. *Journal of Magnetic Resonance*, 2001, vol. 148, no. 2, pp. 257–266.

[D'Agostino *et al.*, 2003] D'AGOSTINO, MAES F., VANDERMEULEN D., *et al.* A Viscous Fluid Model for Multimodal Non-rigid Image Registration Using Mutual Information. *Medical Image Analysis*, 2003, vol. 7, no. 4, pp. 565–575.

[Einstein, 1956] EINSTEIN. Investigations on the Theory Brownian Movement. 1956, 1–19 p. .

[Englund *et al.*, 2011] ENGLUND, ELDER C. P., XU Q., *et al.* Combined Diffusion and Strain Tensor MRI Reveals a Heterogeneous, Planar Pattern of Strain Development During Isometric Muscle Contraction. *American Journal of Physiology. Regulatory, Integrative and Comparative Physiology*, 2011, vol. 300, no. 5, pp. R1079–1090.

[Farnell *et al.*, 2004] FARNELL, GIBSON W. G. Monte Carlo Simulation of Diffusion in a Spatially Nonhomogeneous Medium: Correction to the Gaussian Steplength. *Journal of Computational Physics*, 2004, vol. 198, no. 1, pp. 65–79.

[Fieremans *et al.*, 2008] FIEREMANS, DE DEENE Y., DELPUTTE S., *et al.* Simulation and Experimental Verification of the Diffusion in an Anisotropic Fiber Phantom. *Journal of Magnetic Resonance*, 2008, vol. 190, no. 2, pp. 189–199.

[Fieremans *et al.*, 2010] FIEREMANS, NOVIKOV D. Monte Carlo Study of a Two-• compartment Exchange Model of Diffusion. *NMR in Biomedicine*, 2010, vol. 23, no. 7, pp. 711–724.

[Frindel *et al.*, 2010] FRINDEL, ROBINI M., SCHAERER J., *et al.* A Graph-based Approach for Automatic Cardiac Tractography. *Magnetic Resonance in Medicine*, 2010, vol. 64, no. 4, pp. 1215–1229.

[Gamper *et al.*, 2007] GAMPER, BOESIGER P., KOZERKE S. Diffusion Imaging of the in Vivo Heart Using Spin Echoes--considerations on Bulk Motion Sensitivity. *Magnetic Resonance in Medicine*, 2007, vol. 57, no. 2, pp. 331–337.

[Gerdes *et al.*, 1995] GERDES, CAPASSO J. M. Structural Remodeling and Mechanical Dysfunction of Cardiac Myocytes in Heart Failure. *Journal of Molecular and Cellular Cardiology*, 1995, vol. 27, no. 3, pp. 849–856.

[Goel *et al.*, 1974] GOEL, RICHTER-DYN N. Stochastic Models in Biology. NewYork: Academic Press, 1974, 284 p. ISBN 193066592X.

[Goh *et al.*, 2009] GOH, LENGLET C., THOMPSON P. M., *et al.* Estimating Orientation Distribution Functions with Probability Density Constraints and Spatial Regularity. In: YANG G, HAWKES D J, RUECKERT D Eds. Proc. of the *12th Ed.* conf. on *Medical Image Computing and Computer-assisted Intervention : MICCAI,* Sep.2009, London, England. 2009, pp. 877–885.

[Goldman M, 2004] GOLDMAN M. Histoire De La RMN. *L'actualité Chimique*, 2004, vol. 273, pp. 57–60.

[Grebenkov, 2007] GREBENKOV. NMR Survey of the Reflected Brownian Motion. *Reviews of Modern Physics*, 2007, vol. 79, no. 3, pp. 1077–1137.

[Groot *et al.*, 1962] GROOT, MAZUR P. Non-equilibrium Thermodynamics,. Amsterdam: Dover Publications, 1962, 528 p. ISBN 0486647412.

[Gullmar *et al.*, 2005] GULLMAR, HAUEISEN J., REICHENBACH J. R. Analysis Ofb-value Calculations in Diffusion Weighted and Diffusion Tensor Imaging. *Concepts in Magnetic Resonance Part A*, 2005, vol. 25A, no. 1, pp. 53–66.

[Haddad, 2007] HADDAD. Un Modèle Numérique Anthropomorphique Et Dynamique Du Thorax Respirant Et Du Cœur Battant. Lyon: INSA-LYON, 2007, 172 p.

[Hahn, 1950] HAHN. Spin Echoes. *Physical Review*, 1950, vol. 80, no. 4, pp. 580–594.

[Hall *et al.*, 2009] HALL, ALEXANDER D. C. Convergence and Parameter Choice for Monte-Carlo Simulations of Diffusion MRI. *IEEE Transactions on Medical Imaging*, 2009, vol. 28, no. 9, pp. 1354–1364.

[Healy *et al.*, 2011] HEALY, JIANG Y., HSU E. W. Quantitative Comparison of Myocardial Fiber Structure Between Mice, Rabbit, and Sheep Using Diffusion Tensor Cardiovascular Magnetic Resonance. *Journal of Cardiovascular Magnetic Resonance*, 2011, vol. 13, no. 74, pp. 1–8.

[Hecht, 1998] HECHT. Optics. 3rd ed. Addison Wesley Publishing Company, 1998, 694 p. ISBN 0201838877.

[Helm, 2005] HELM. A Novel Technique for Quantifying Variability of Cardiac Anatomy : Application to the Dyssynchronous Failing Heart. Johns Hopkins University, 2005.

[Helm *et al.*, 2005] HELM, TSENG H.-J., YOUNES L., *et al.* Ex Vivo 3D Diffusion Tensor Imaging and Quantification of Cardiac Laminar Structure. *Magnetic Resonance in Medicine,* 2005, vol. 54, no. 4, pp. 850–859.

[Hess *et al.*, 2006] HESS, MUKHERJEE P., HAN E. T., *et al.* Q-ball Reconstruction of Multimodal Fiber Orientations Using the Spherical Harmonic Basis. *Magnetic Resonance in Medicine*, 2006, vol. 56, no. 1, pp. 104–117.

[Holden, 2008] HOLDEN. A Review of Geometric Transformations for Nonrigid Body Registration. *IEEE Transactions on Medical Imaging*, 2008, vol. 27, no. 1, pp. 111–128.

[Hoyert *et al.*, 2009] HOYERT, HERON M., MURPHY S., *et al.* Deaths: Final Data for 2003. *National Vital Statistics Reports*, 2009, vol. 57, no. 14, p. 135.

[Hsu *et al.*, 2001] HSU, HENRIQUEZ C. S. Myocardial Fiber Orientation Mapping Using Reduced Encoding Diffusion Tensor Imaging. *Journal of Cardiovascular Magnetic Resonance*, 2001, vol. 3, no. 4, pp. 339–347.

[Hwang *et al.*, 2003] HWANG, CHIN C.-L., WEHRLI F. W., *et al.* An Image-based Finite Difference Model for Simulating Restricted Diffusion. *Magnetic Resonance in Medicine*, 2003, vol. 50, no. 2, pp. 373–382.

[Hüppi *et al.*, 2006] HÜPPI, DUBOIS J. Diffusion Tensor Imaging of Brain Development. *Seminars in Fetal & Neonatal Medicine*, 2006, vol. 11, no. 6, pp. 489–497.

[Iaizzo, 2009] IAIZZO. Handbook of Cardiac Anatomy, Physiology, and Devices. 2nd Ed. Humana Press Inc., 2009, 710 p. ISBN 1603273719.

[Imae *et al.*, 2009] IMAE, SHINOHARA H., SEKINO M., *et al.* Estimation of Cell Membrane Permeability and Intracellular Diffusion Coefficient of Human Gray Matter. *Magnetic Resonance in Medical Sciences*, 2009, vol. 8, no. 1, pp. 1–7.

[Jefferies *et al.*, 2010] JEFFERIES, TOWBIN J. a. Dilated Cardiomyopathy. *Lancet*, 2010, vol. 375, no. 9716, pp. 752–762.

[Jochimsen *et al.*, 2006] JOCHIMSEN, SCHÄFER A., BAMMER R., *et al.* Efficient Simulation of Magnetic Resonance Imaging with Bloch-Torrey Equations Using Intra-voxel Magnetization Gradients. *Journal of Magnetic Resonance*, 2006, vol. 180, no. 1, pp. 29–38.

[Johansen-Berg *et al.*, 2009] JOHANSEN-BERG, EJ B. T. Diffusion MRI. 1st Ed. Academic Press, 2009, 504 p. ISBN 9780123747099.

[Jones, 1941] JONES. A New Calculus for the Treatment of Optical Systems. *Journal of the Optical Society of America*, 1941, vol. 31, no. 7, p. 488.

[Jouk *et al.*, 2007] JOUK, MOURAD A., MILISIC V., *et al.* Analysis of the Fiber Architecture of the Heart by Quantitative Polarized Light Microscopy. Accuracy, Limitations and Contribution to the Study of the Fiber Architecture of the Ventricles During Fetal and Neonatal Life. *European Journal of Cardio-thoracic Surgery*, 2007, vol. 31, no. 5, pp. 915–921.

[Jouk *et al.*, 1995] JOUK, USSON Y., MICHALOWICZ G., *et al.* Mapping of the Orientation of Myocardial Cells by Means of Polarized Light and Confocal Scanning Laser Microscopy. *Microscopy Research and Technique*, 1995, vol. 30, no. 6, pp. 480–490.

[Kanai *et al.*, 1995] KANAI, SALAMA G. Optical Mapping Reveals That Repolarization Spreads Anisotropically and Is Guided by Fiber Orientation in Guinea Pig Hearts. *Circulation Research*, 1995, vol. 77, no. 4, pp. 784–802.

[Kezele *et al.*, 2010] KEZELE, DESCOTEAUX M., POUPON C., *et al.* Spherical Wavelet Transform for ODF Sharpening. *Medical Image Analysis*, 2010, vol. 14, no. 3, pp. 332–342.

[Kim *et al.*, 2000] KIM, DALAL S. S., YOUNG E., *et al.* Disruption of the Myocardial Extracellular Matrix Leads to Cardiac Dysfunction. *The Journal of Clinical Investigation*, 2000, vol. 106, no. 7, pp. 857–866.

[Kingsley, 2006a] KINGSLEY. Introduction to Diffusion Tensor Imaging Mathematics: Part II. Anisotropy, Diffusion • weighting Factors, and Gradient Encoding Schemes. *Concepts in Magnetic Resonance Part A*, 2006, vol. 28A, no. 2, pp. 123–154.

[Kingsley, 2006b] KINGSLEY. Introduction to Diffusion Tensor Imaging Mathematics: Part I. Tensors, Rotations, and Eigenvectors. *Concepts in Magnetic Resonance Part A*, 2006, vol. 28A, no. 2, pp. 101–122.

[Kingsley, 2006c] KINGSLEY. Introduction to Diffusion Tensor Imaging Mathematics : Part III . Tensor Calculation , Noise , Simulations , And. *Concepts in Magnetic Resonance Part A*, 2006, vol. 28A, no. 2, pp. 155–179.

[Kushwaha *et al.*, 1997] KUSHWAHA, FALLON J. T., FUSTER V. Restrictive Cardiomyopathy. *N Engl J Med*, 1997, vol. 336, pp. 267–276.

[Köpf *et al.*, 1996] KÖPF, CORINTH C., HAFERKAMP O., *et al.* Anomalous Diffusion of Water in Biological Tissues. *Biophysical Journal*, 1996, vol. 70, no. 6, pp. 2950–2958.

[LAKS *et al.*, 1970] LAKS, MORADY F., ADOMIAN G. . E. ., *et al.* Presence of Widened and Multiple Intercalated Discs in the Hypertrophied Canine Heart. *Circulation Research*, 1970, vol. 27, pp. 391–402.

[Langlet, 2006] LANGLET. Geometric and Variational Methods for Diffusion Tensor MRI Processing | Diffusion Magnetic Resonance Imaging INRIA-ARC, 2006. [Online]. Available: http://www-sop.inria.fr/odyssee/contracts/arcDMRI2007/node/64. [Accessed: 28-Aug-2012].

[Larsen *et al.*, 2007] LARSEN, GRIFFIN L. Polarized Light Imaging of White Matter Architecture. *Microscopy Research and Technique*, 2007, vol. 70, pp. 851–863.

[Larsson, 2008] LARSSON. Introductionto phaseencodinginMRI, 2008, 18 p.

[Latta *et al.*, 2010] LATTA, GRUWEL M. L. H., JELLÚS V., *et al.* Bloch Simulations with Intra-voxel Spin Dephasing. *Journal of Magnetic Resonance*, 2010, vol. 203, no. 1, pp. 44–51.

[Layton, 2006] LAYTON. Modeling Water Transport Across Elastic Boundaries Using an Explicit Jump Method. 2006.

[Le Bihan, 2003] LE BIHAN. Looking into the Functional Architecture of the Brain with Diffusion MRI. *Nature Reviews. Neuroscience*, 2003, vol. 4, no. 6, pp. 469–480.

[Le Bihan, 2007] LE BIHAN. The ‘Wet Mind’: Water and Functional Neuroimaging. *Physics in Medicine and Biology*, 2007, vol. 52, no. 7, pp. R57–90.

[Le Bihan *et al.*, 1985] LE BIHAN, BRETON E. Imagerie De Diffusion In-vivo Par Résonance Magnétique Nucléaire. *C R Acad Sci*, 1985, vol. 301, no. 15, pp. 1109–1112.

[Le Bihan *et al.*, 2001] LE BIHAN, MANGIN J. F., POUPON C., *et al.* Diffusion Tensor Imaging: Concepts and Applications. *Journal of Magnetic Resonance Imaging : JMRI*, 2001, vol. 13, no. 4, pp. 534–546.

[Le Bihan *et al.*, 2006] LE BIHAN, POUPON C., AMADON A., *et al.* Artifacts and Pitfalls in Diffusion MRI. *Journal of Magnetic Resonance Imaging*, 2006, vol. 24, no. 3, pp. 478–488.

[LeBihan *et al.*, 1986] LEBIHAN, BRETON E., LALLEMAND D., *et al.* MR Imaging of Intravoxel Incoherent Motions: Application to Diffusion and Perfusion in Neurologic Disorders. *Radiology*, 1986, vol. 161, no. 2, pp. 401–407.

[Legrice *et al.*, 1997] LEGRICE, HUNTER P. J., SMAILL B. H. Laminar Structure of the Heart: a Mathematical Model. *Am J Physiol Heart Circ Physiol*, 1997, vol. 272, no. 5, pp. H2466–2476.

[Legrice *et al.*, 1995] LEGRICE, SMAILL B. H., CHAI L. Z., *et al.* Laminar Structure of the Heart: Ventricular Myocyte Arrangement and Connective Tissue Architecture in the Dog. *Am J Physiol Heart Circ Physiol*, 1995, vol. 269, no. 2, pp. H571–582.

[LeGrice *et al.*, 1995] LEGRICE, TAKAYAMA Y., COVELL J. W. Transverse Shear Along Myocardial Cleavage Planes Provides a Mechanism for Normal Systolic Wall Thickening. *Circulation Research*, 1995, vol. 77, no. 1, pp. 182–193.

[Lenglet *et al.*, 2009] LENGLET, CAMPBELL J. S. ., DESCOTEAUX M., *et al.* Mathematical Methods for Diffusion MRI Processing. *NeuroImage*, 2009, vol. 45, no. 1 Suppl, pp. S111–122.

[Lenglet *et al.*, 2005] LENGLET, FAUGERAS O., PAPADOPOULO T., *et al.* Diffeomorphic Matching of Symmetric Positive Definite Matrix Field. Proc. of the *2nd Ed.* conf. on *Congrès National De Mathématiques Appliquées Et Industrielles*, May.2005, Evian : France. 2005.

[Levitt, 2002] LEVITT. Spin Dynamics: Basics of Nuclear Magnetic Resonance. 2nd Ed. Wiley, 2002, 744 p. ISBN 0470511176.

[Lin *et al.*, 2001] LIN, TSENG W. Y., CHENG H. C., *et al.* Validation of Diffusion Tensor Magnetic Resonance Axonal Fiber Imaging with Registered Manganese-enhanced Optic Tracts. *NeuroImage*, 2001, vol. 14, no. 5, pp. 1035–1047.

[Liu *et al.*, 2001] LIU, LI F., TATLISUMAK T., *et al.* Regional Variations in the Apparent Diffusion Coefficient and the Intracellular Distribution of Water in Rat Brain During Acute Focal Ischemia. *Stroke*, 2001, vol. 32, no. 8, pp. 1897–1905.

[Lu *et al.*, 2010] LU, REYES M., SERIFOVIC A., *et al.* Multi-modal Diffeomorphic Demons Registration Based on Point-wise Mutual Information. Proc. of the *7th Ed.* conf. on *2010 IEEE International Symposium on Biomedical Imaging: From Nano to Macro*, Apr.2010, Rotterdam: Netherlands. 2010, pp. 372–375.

[Malcolm *et al.*, 2010] MALCOLM, MICHAILOVICH O., BOUIX S., *et al.* A Filtered Approach to Neural Tractography Using the Watson Directional Function. *Medical Image Analysis*, 2010, vol. 14, no. 1, pp. 58–69.

[Markl *et al.*, 2002] MARKL, SCHNEIDER B., HENNIG J. Fast Phase Contrast Cardiac Magnetic Resonance Imaging: Improved Assessment and Analysis of Left Ventricular Wall Motion. *Journal of Magnetic Resonance Imaging : JMRI*, 2002, vol. 15, no. 6, pp. 642–653.

[Maron, 1997] MARON. Hypertrophic Cardiomyopathy. *Lancet*, 1997, vol. 350, no. 9071, pp. 127–133.

[Masood *et al.*, 2001] MASOOD, YANG G. Macroscopic Structure and Physiology of the Normal and Diseased Heart, Imperial College of Science, 2001, 32 p.

[Mattiello *et al.*, 1997] MATTIELLO, BASSER P. J., LE BIHAN D. The b Matrix in Diffusion Tensor Echo-planar Imaging. *Magnetic Resonance in Medicine*, 1997, vol. 37, no. 2, pp. 292–300.

[Mekkaoui *et al.*, 2012] MEKKAOUI, NIELLES-VALLESPIN S., GATEHOUSE P., *et al.* Diffusion MRI Tractography of the Human Heart In Vivo at End-diastole and End-systole. *Journal of Cardiovascular Magnetic Resonance*, 2012, vol. 14, no. Suppl 1, p. O49.

[Merboldt *et al.*, 1985] MERBOLDT, HANICKE W., FRAHM J. Self-diffusion NMR Imaging Using Stimulated Echoes. *Journal of Magnetic Resonance (1969)*, 1985, vol. 64, no. 3, pp. 479–486.

[Michailovich *et al.*, 2010a] MICHAILOVICH, RATHI Y. On Approximation of Orientation Distributions by Means of Spherical Ridgelets. *IEEE Transactions on Image Processing*, 2010, vol. 19, no. 2, pp. 461–477.

[Michailovich *et al.*, 2010b] MICHAILOVICH, RATHI Y. Spatially Regularized Q-ball Imaging Using Spherical Ridgelets. Proc. of the *7th Ed.* conf. on *International Symposium on Biomedical Imaging: From Nano to Macro*, Apr.2010, Rotterdam: Netherlands. 2010, pp. 1181–1184.

[Michailovich *et al.*, 2010c] MICHAILOVICH, RATHI Y., DOLUI S. Spatially Regularized Compressed Sensing of Diffusion MRI Data, *arXiv preprint arXiv:1009.1889*, vol. 1. p. 38, 2010.

[Milica *et al.*, 2005] MILICA, VUNJAK-NOVAKOVI G. Cardiac Tissue Engineering. *J. Serb. Chem. Soc.*, 2005, vol. 70, no. 3, pp. 541–556.

[Moratal *et al.*, 2008] MORATAL, VALLÉS-LUCH a, MARTÍ-BONMATÍ L., *et al.* k-Space Tutorial: An MRI Educational Tool for a Better Understanding of K-space. *Biomedical Imaging and Intervention Journal*, 2008, vol. 4, no. 1, p. e15.

[Mori *et al.*, 1999] MORI, BARKER P. B. Diffusion Magnetic Resonance Imaging : Its Principle and Applications. *The Anatomical Record.*, 1999, vol. 257, pp. 102–109.

[Mori *et al.*, 2002] MORI, VAN ZIJL P. C. M. Fiber Tracking: Principles and Strategies - a Technical Review. *NMR in Biomedicine*, 2002, vol. 15, no. 7–8, pp. 468–480.

[Moseley *et al.*, 1990] MOSELEY, COHEN Y., MINTOROVITCH J., *et al.* Early Detection of Regional Cerebral Ischemia in Cats: Comparison of Diffusion- and T2-weighted MRI and Spectroscopy. *Magnetic Resonance in Medicine*, 1990, vol. 14, no. 2, pp. 330–346.

[Nezamzadeh, 2012] NEZAMZADEH. Diffusion Time Dependence of Magnetic Resonance Diffusion Signal Decays: An Investigation of Water Exchange in Human Brain in Vivo. *Magn Reson Mater Phy*, 2012, vol. 25, no. 4, pp. 285–296.

[Nichols *et al.*, 2012] NICHOLS, TOWNSEND N., SCARBOROUGH P., *et al.* European Cardiovascular Disease Statistics, Brussels: European Heart Network AISBL, 2012, 129 p.

[Nielles-Vallespin *et al.*, 2012] NIELLES-VALLESPIN, MEKKAOUI C., GATEHOUSE P., *et al.* In Vivo Diffusion Tensor MRI of the Human Heart: Reproducibility of Breath-hold and Navigator-based Approaches. *Magnetic Resonance in Medicine*, 2012.

[Nilsson *et al.*, 2009] NILSSON, LÄTT J., NORDH E., *et al.* On the Effects of a Varied Diffusion Time in Vivo: Is the Diffusion in White Matter Restricted? *Magnetic Resonance Imaging*, 2009, vol. 27, no. 2, pp. 176–187.

[Nossin-Manor *et al.*, 2005] NOSSIN-MANOR, DUVDEVANI R., COHEN Y. Effect of Experimental Parameters on Highb-valueq-space MR Images of Excised Rat Spinal Cord. *Magnetic Resonance in Medicine*, 2005, vol. 54, no. 1, pp. 96–104.

[Ogura *et al.*, 2002] OGURA, IMANISHI S., SHIBAMOTO T. Osmometric and Water-transporting Properties of Guinea Pig Cardiac Myocytes. *The Japanese Journal of Physiology*, 2002, vol. 52, no. 4, pp. 333–342.

[Ozarslan *et al.*, 2006] OZARSLAN, SHEPHERD T. M., VEMURI B. C., *et al.* Resolution of Complex Tissue Microarchitecture Using the Diffusion Orientation Transform (DOT). *NeuroImage*, 2006, vol. 31, no. 3, pp. 1086–1103.

[Pai *et al.*, 2006] PAI, AXEL L. Advances in MRI Tagging Techniques for Determining Regional Myocardial Strain. *Current Cardiology Reports*, 2006, vol. 8, no. 1, pp. 53–58.

[Palm *et al.*, 2010] PALM, AXER M., GRÄSSE D., *et al.* Towards Ultra-High Resolution Fibre Tract Mapping of the Human Brain - Registration of Polarised Light Images and Reorientation of Fibre Vectors. *Frontiers in Human Neuroscience*, 2010, vol. 4, pp. 1–16.

[Pasternak *et al.*, 2008] PASTERNAK, ASSAF Y., INTRATOR N., *et al.* Variational Multiple-tensor Fitting of Fiber-ambiguous Diffusion-weighted Magnetic Resonance Imaging Voxels. *Magnetic Resonance Imaging*, 2008, vol. 26, no. 8, pp. 1133–1144.

[Petitjean *et al.*, 2005] PETITJEAN, ROUGON N., CLUZEL P. Assessment of Myocardial Function: a Review of Quantification Methods and Results Using Tagged MRI. *Journal of Cardiovascular Magnetic Resonance : Official Journal of the Society for Cardiovascular Magnetic Resonance*, 2005, vol. 7, no. 2, pp. 501–516.

[Pfeuffer *et al.*, 2000] PFEUFFER, TKAC I., GRUETTER R. Extracllular-Intracelluar Distribution of Glocose and Lactate in the Rat Bain Assessed Noninvasively by Diffusion-weighted 1H Nuclear Magnetic Resonance Spectroscopy in Vivo.pdf. *Journal of Cerebral Blood Flow and Metabolism*, 2000, vol. 20, pp. 736–746.

[Pierpaoli *et al.*, 1996] PIERPAOLI, BASSER P. J. Toward a Quantitative Assessment of Diffusion Anisotropy. *Magnetic Resonance in Medicine*, 1996, vol. 36, no. 6, pp. 893–906.

[Polimeni, 1974] POLIMENI. Extracellular Space and Ionic Distribution in Rat Ventricle. *Am J Physiol -- Legacy Content*, 1974, vol. 227, no. 3, pp. 676–683.

[Price, 1997] PRICE. Pulsed-field Gradient Nuclear Magnetic Resonance as a Tool for Studying Translational Diffusion: Part 1. Basic Theory. *Concepts in Magnetic Resonance*, 1997, vol. 9, no. 5, pp. 299–336.

[Price *et al.*, 1998] PRICE, PRICE W. S. Pulsed-field Gradient Nuclear Magnetic Resonance as a Tool for Studying Translational Diffusion. Part 2. Experimental Aspects. *Concepts in Magnetic Resonance*, 1998, vol. 10, no. 4, pp. 197–237.

[Rapacchi *et al.*, 2009] RAPACCHI, CROISILLE P., VIALLON M., *et al.* In Vivo Cardiac NMR Diffusion Weighted Imaging (DWI) for the Human Heart : Tackling Motion Issue with Temporal Maximum Intensity Projection (tMIP) -DWI and First Results in Humans. *Proc. Intl. Soc. Mag. Reson. Med.*, 2009, Hawaii, USA. 2009, p. 4718.

[Rapacchi *et al.*, 2011] RAPACCHI, WEN H., VIALLON M., *et al.* Low B-value Diffusion-weighted Cardiac Magnetic Resonance Imaging: Initial Results in Humans Using an Optimal Time-window Imaging Approach. *Investigative Radiology*, 2011, vol. 46, no. 12, pp. 751–758.

[Reese *et al.*, 1996] REESE, WEDEEN V., WEISSKOFF R. Measuring Diffusion in the Presence of Material Strain. *Journal of Magnetic Resonance. Series B*, 1996, vol. 112, no. 3, pp. 253–258.

[Rhomer *et al.*, 2006] RHOMER, GULLBERG G. T. A Bloch-Torrey Equation for Diffusion in a Deforming Media. Lawrence Berkeley National Laboratory, p. 20, 2006.

[Roger *et al.*, 2011] ROGER, GO A. S., LLOYD-JONES D. M., *et al.* Heart Disease and Stroke Statistics--2011 Update: a Report from the American Heart Association. *Circulation*, 2011, vol. 123, no. 4, pp. e18–e209.

[Rohr *et al.*, 2001] ROHR, STIEHL H. S., SPRENGEL R., *et al.* Landmark-based Elastic Registration Using Approximating Thin-plate Splines. *IEEE Transactions on Medical Imaging*, 2001, vol. 20, no. 6, pp. 526–534.

[Ross *et al.*, 1979] ROSS, STREETER D. Myocardial Fiber Disarray. *Circulation*, 1979, vol. 60, no. 6, pp. 1425–1426.

[Rueckert *et al.*, 1999] RUECKERT, SONODA L. I., HAYES C., *et al.* Nonrigid Registration Using Free-form Deformations: Application to Breast MR Images. *IEEE Transactions on Medical Imaging*, 1999, vol. 18, no. 8, pp. 712–721.

[Salat *et al.*, 2010] SALAT, TUCH D. S., VAN DER KOUWE a J. W., *et al.* White Matter Pathology Isolates the Hippocampal Formation in Alzheimer's Disease. *Neurobiology of Aging*, 2010, vol. 31, no. 2, pp. 244–256.

[Savadjiev *et al.*, 2008] SAVADJIEV, CAMPBELL J. S. W., DESCOTEAUX M., *et al.* Labeling of Ambiguous Subvoxel Fibre Bundle Configurations in High Angular Resolution Diffusion MRI. *NeuroImage*, 2008, vol. 41, no. 1, pp. 58–68.

[Schaefer *et al.*, 2003] SCHAEFER, GROSS W., PREUSS M., *et al.* Monitoring of Water Content and Water Distribution in Ischemic Hearts. *Bioelectrochemistry*, 2003, vol. 61, no. 1–2, pp. 85–92.

[Schmitt *et al.*, 2012] SCHMITT, YEH C., LEBOIS A., *et al.* Project SIMUDMRI Task 3 : Development of a Monte-Carlo Simulator Diffusion of Water Molecules in Brain Tissues, 2012.

[Sehy *et al.*, 2002] SEHY, BANKS A. a, ACKERMAN J. J. H., *et al.* Importance of Intracellular Water Apparent Diffusion to the Measurement of Membrane Permeability. *Biophysical Journal*, 2002, vol. 83, no. 5, pp. 2856–2863.

[Severs, 2000] SEVERS. The Cardiac Muscle Cell. *BioEssays : News and Reviews in Molecular, Cellular and Developmental Biology*, 2000, vol. 22, no. 2, pp. 188–199.

[Shehata *et al.*, 2009] SHEHATA, CHENG S., OSMAN N. F., *et al.* Myocardial Tissue Tagging with Cardiovascular Magnetic Resonance. *Journal of Cardiovascular Magnetic Resonance*, 2009, vol. 11, no. 55, pp. 1–12.

[Shemesh *et al.*, 2009] SHEMESH, OZARSLAN E., BASSER P. J., *et al.* Measuring Small Compartmental Dimensions with Low-q Angular double-PGSE NMR: The Effect of Experimental Parameters on Signal Decay. *Journal of Magnetic Resonance*, 2009, vol. 198, no. 1, pp. 15–23.

[Shemesh *et al.*, 2012] SHEMESH, ÖZARSLAN E., BASSER P. J., *et al.* Accurate Noninvasive Measurement of Cell Size and Compartment Shape Anisotropy in Yeast Cells Using Double-pulsed Field Gradient MR. *NMR in Biomedicine*, 2012, vol. 25, no. 2, pp. 236–246.

[Sosnovik *et al.*, 2009a] SOSNOVIK, WANG R., DAI G., *et al.* Diffusion MR Tractography of the Heart. *Journal of Cardiovascular Magnetic Resonance*, 2009, vol. 11, no. 47, pp. 1–15.

[Sosnovik *et al.*, 2009b] SOSNOVIK, WANG R., DAI G., *et al.* Diffusion Spectrum MRI Tractography Reveals the Presence of a Complex Network of Residual Myofibers in Infarcted Myocardium. *Circulation. Cardiovascular Imaging*, 2009, vol. 2, no. 3, pp. 206–212.

[Stejskal, 1965] STEJSKAL. Use of Spin Echoes in a Pulsed Magnetic-Field Gradient to Study Anisotropic, Restricted Diffusion and Flow. *The Journal of Chemical Physics*, 1965, vol. 43, no. 10, pp. 3597–3603.

[Stejskal *et al.*, 1965] STEJSKAL, TANNER J. E. Spin Diffusion Measurements: Spin Echoes in the Presence of a Time-Dependent Field Gradient. *The Journal of Chemical Physics*, 1965, vol. 42, no. 1, pp. 288–293.

[Streeter, 1979] STREETER. Gross Morphology and Fiber Geometry of the Heart, in *In handbook of physiology:The cardiovascular system*, vol. 1, USA: Oxford University Press, 1979, pp. 61 – 112.

[Stylianopoulos *et al.*, 2010] STYLIANOPOULOS, DIOP-FRIMPONG B., MUNN L. L., *et al.* Diffusion Anisotropy in Collagen Gels and Tumors: The Effect of Fiber Network Orientation. *Biophysical Journal*, 2010, vol. 99, no. 10, pp. 3119–3128.

[Sukstanskii *et al.*, 2004] SUKSTANSKII, YABLONSKIY D. a, ACKERMAN J. J. H. Effects of Permeable Boundaries on the Diffusion-attenuated MR Signal: Insights from a One-dimensional Model. *Journal of Magnetic Resonance*, 2004, vol. 170, no. 1, pp. 56–66.

[Szeliski *et al.*, 1997] SZELISKI, COUGHLAN J. Spline-based Image Registration. *International Journal of Computer Vision*, 1997, vol. 22, no. 3, pp. 199–218.

[Taylor *et al.*, 1985] TAYLOR, BUSHELL M. C. The Spatial Mapping of Translational Diffusion Coefficients by the NMR Imaging Technique. *Physics in Medicine and Biology*, 1985, vol. 30, no. 4, pp. 345–349.

[Thirion, 1998] THIRION. Image Matching as a Diffusion Process: An Analogy with Maxwell's Demons. *Medical Image Analysis*, 1998, vol. 2, no. 3, pp. 243–260.

[Torrent-Guasp, 1973] TORRENT-GUASP. The Cardiac Muscle. Madrid: Guadarrama, 1973, 15:134 p. .

[Torrent-Guasp *et al.*, 2001a] TORRENT-GUASP, BALLESTER M., BUCKBERG G. D., *et al.* Spatial Orientation of the Ventricular Muscle Band: Physiologic Contribution and Surgical Implications. *J. Thorac. Cardiovasc. Surg.*, 2001, vol. 122, no. 2, pp. 389–392.

[Torrent-Guasp *et al.*, 2001b] TORRENT-GUASP, BUCKBERG G. D., CLEMENTE C., *et al.* The Structure and Function of the Helical Heart and Its Buttress Wrapping. I. The Normal Macroscopic Structure of the Heart. *Seminars in Thoracic and Cardiovascular Surgery*, Oct.2001. 2001, pp. 301–319.

[Torrey, 1956] TORREY. Bloch Equations with Diffusion Terms. *Physical Review*, 1956, vol. 104, no. 3, pp. 563–565.

[Tournier *et al.*, 2004] TOURNIER, CALAMANTE F., GADIAN D. G., *et al.* Direct Estimation of the Fiber Orientation Density Function from Diffusion-weighted MRI Data Using Spherical Deconvolution. *NeuroImage*, 2004, vol. 23, no. 3, pp. 1176–1185.

[Toussaint *et al.*, 2010] TOUSSAINT, SERMESANT M., STOECK C. T., *et al.* In Vivo Human 3D Cardiac Fibre Architecture: Reconstruction Using Curvilinear Interpolation of Diffusion Tensor Images. In: JIANG, NAVAB N, PLUIM J.P.W, *et al.* Eds. Proc. of the *13th Ed.* conf. on *Medical Image Computing and Computer-assisted Intervention : MICCAI*, Sep.2010, Beijing: China. 2010, pp. 418–425.

[Tristán-Vega *et al.*, 2009] TRISTÁN-VEGA, WESTIN C.-F., AJA-FERNÁNDEZ S. Estimation of Fiber Orientation Probability Density Functions in High Angular Resolution Diffusion Imaging. *NeuroImage*, 2009, vol. 47, no. 2, pp. 638–650.

[Tristán-Vega *et al.*, 2010] TRISTÁN-VEGA, WESTIN C.-F., AJA-FERNÁNDEZ S. A New Methodology for the Estimation of Fiber Populations in the White Matter of the Brain with the Funk-Radon Transform. *NeuroImage*, 2010, vol. 49, no. 2, pp. 1301–1315.

[Tuch, 2002] TUCH. Diffusion MRI of Complex Tissue Structure. PhD thesis of Philosophy in Biomedical Imaging. Massachusetts : MIT, 2002, 220 p.

[Tuch, 2004] TUCH. Q-ball Imaging. *Magnetic Resonance in Medicine*, 2004, vol. 52, no. 6, pp. 1358–1372.

[Tuch *et al.*, 2002] TUCH, REESE T. G., WIEGELL M. R., *et al.* High Angular Resolution Diffusion Imaging Reveals Intravoxel White Matter Fiber Heterogeneity. *Magnetic Resonance in Medicine*, 2002, vol. 48, no. 4, pp. 577–82.

[Vercauteren *et al.*, 2009] VERCAUTEREN, PENNEC X., PERCHANT A., *et al.* Diffeomorphic Demons: Efficient Non-parametric Image Registration. *NeuroImage*, 2009, vol. 45, no. 1 Suppl, pp. S61–72.

[Villarreal, 2004] VILLARREAL. Interstitial Fibrosis in Heart Failure. Springer-Verlag, 2004, 373 p. ISBN 0387228241.

[Walker *et al.*, 1999] WALKER, SPINALE F. G. The Structure and Function of the Cardiac Myoycte: a Review of Fundamental Concepts. *J. Thorac. Cardiovasc. Surg.*, 1999, vol. 118, no. 2, pp. 375–382.

[H Wang *et al.*, 2012] WANG H., AMINI A. A. Cardiac Motion and Deformation Recovery from MRI: a Review. *IEEE Transactions on Medical Imaging*, 2012, vol. 31, no. 2, pp. 487–503.

[H Wang *et al.*, 2011] WANG H., BLACK A. J., ZHU J., *et al.* Reconstructing Micrometer-scale Fiber Pathways in the Brain: Multi-contrast Optical Coherence Tomography Based Tractography. *NeuroImage*, 2011, vol. 58, no. 4, pp. 984–992.

[V Wang *et al.*, 2009] WANG V., LAM H. I., ENNIS D. B., *et al.* Modelling Passive Diastolic Mechanics with Quantitative MRI of Cardiac Structure and Function. *Medical Image Analysis*, 2009, vol. 13, no. 5, pp. 773–784.

[V Wedeen *et al.*, 2005] WEDEEN V., HAGMANN P. Mapping Complex Tissue Architecture with Diffusion Spectrum Magnetic Resonance Imaging. *Magnetic Resonance in Medicine*, 2005, vol. 54, pp. 1377–1386.

[VJ Wedeen *et al.*, 2008] WEDEEN V. J., WANG R. P., SCHMAHMANN J. D., *et al.* Diffusion Spectrum Magnetic Resonance Imaging (DSI) Tractography of Crossing Fibers. *NeuroImage*, 2008, vol. 41, no. 4, pp. 1267–1277.

[Weiss *et al.*, 2007] WEISS, KELLER D. U. J., SEEMANN G., *et al.* The Influence of Fibre Orientation, Extracted from Different Segments of the Human Left Ventricle, on the Activation and Repolarization Sequence: a Simulation Study. *Europace*, 2007, vol. 9 Suppl 6, pp. vi96–104.

[Weisstein WEISSTEIN. Fresnel Equations -- from Eric Weisstein’s World of Physics. [Online]. Available: http://scienceworld.wolfram.com/physics/FresnelEquations.html. [Accessed: 29-Aug-2012].

[Westbrook *et al.*, 2011] WESTBROOK, ROTH C. K., TALBOT J. MRI in Practice, 4th Ed. 4th Ed. Wiley-Blackwell, 2011, 456 p. ISBN 1444337432.

[M-T Wu *et al.*, 2006] WU M.-T., TSENG W.-Y. I., SU M.-Y. M., *et al.* Diffusion Tensor Magnetic Resonance Imaging Mapping the Fiber Architecture Remodeling in Human Myocardium After Infarction: Correlation with Viability and Wall Motion. *Circulation*, 2006, vol. 114, no. 10, pp. 1036–1045.

[Y-C Wu *et al.*, 2007] WU Y.-C., ALEXANDER A. L. Hybrid Diffusion Imaging. *NeuroImage*, 2007, vol. 36, no. 3, pp. 617–629.

[Xu *et al.*, 2007] XU, DOES M. D., GORE J. C. Numerical Study of Water Diffusion in Biological Tissues Using an Improved Finite Difference Method. *Physics in Medicine and Biology*, 2007, vol. 52, no. 7, pp. N111–126.

[F Yang *et al.*, 2012] YANG F., ZHU Y.-M., MAGNIN I. E., *et al.* Feature-based Interpolation of Diffusion Tensor Fields and Application to Human Cardiac DT-MRI. *Medical Image Analysis*, 2012, vol. 16, no. 2, pp. 459–481.

[Yassine *et al.*, 2006] YASSINE, YOUSSEF A. M., KADAH Y. M. Novel Multi-Tensor Estimation for High-Resolution Diffusion Tensor Magnetic Resonance Imaging. Proc. of the *23rd Ed.* conf. on *National Radio Science Conference :NRSC*, Mar.2006, Menouf: Egypt. 2006, pp. 1–12.

[Yeh *et al.*, 2011] YEH, KEZELE I., ALEXANDER D., *et al.* Evaluation of Fiber Radius Mapping Using Diffusion MRI Under Clinical System Constraints. 2011, p. 2017.

[Yeh *et al.*, 2010] YEH, TOURNIER J., CHO K., *et al.* The Effect of Finite Diffusion Gradient Pulse Duration on Fibre Orientation Estimation in Diffusion MRI. *Neuroimage*, 2010, vol. 51, no. 2, pp. 743–751.

[Yeo *et al.*, 2010] YEO, SABUNCU M. R., VERCAUTEREN T., *et al.* Spherical Demons: Fast Diffeomorphic Landmark-free Surface Registration. *IEEE Transactions on Medical Imaging*, 2010, vol. 29, no. 3, pp. 650–668.

[Zerhouni *et al.*, 1988] ZERHOUNI, PARISH D. M., ROGERS W. J., *et al.* Human Heart: Tagging with MR Imaging--a Method for Noninvasive Assessment of Myocardial Motion. *Radiology*, 1988, vol. 169, no. 1, pp. 59–63.

[Zhang *et al.*, 2010] ZHANG, CROW J. A., YANG X., *et al.* The Correlation of 3D DT-MRI Fiber Disruption with Structural and Mechanical Degeneration in Porcine Myocardium. *Annals of Biomedical Engineering*, 2010, vol. 38, no. 10, pp. 3084–3095.

[Zheng, 2009] ZHENG. Rapid Diffusion in the Brain Extracellular Space-biophysical Constraints and Physiological Implications. Thesis of PhD. University College London, 2009, 118 p.

[Zhukov *et al.*, 2003] ZHUKOV, BARR A. H. Heart-muscle Fiber Reconstruction from Diffusion Tensor MRI. Proc. of the *14th Ed.* conf. on *IEEE Visualization Conference*, Oct.2003, Washington. 2003, pp. 597–602.

FOLIO ADMINISTRATIF

THESE SOUTENUE DEVANT L'INSTITUT NATIONAL DES SCIENCES APPLIQUEES DE LYON

NOM : WANG **DATE de SOUTENANCE :** 21/01/2013

Prénoms : Lihui

TITRE : Modélisation et Simulation de l’IRM de Diffusion des Fibres Myocardiques

NATURE : Doctorat **Numéro d'ordre :** 2013-ISAL-0004

École doctorale : École Doctorale Électronique, Électrotechnique, Automatique

Spécialité : Image et System

RESUME :

L’imagerie par résonance magnétique de diffusion (l’IRMd) est actuellement la seule technique non-invasive pour étudier l’architecture tridimensionnelle des fibres myocardiques du cœur humain à la fois *ex vivo* et *in vivo*. Cependant, il est difficile de savoir comment les caractéristiques de diffusion calculées à partir des images de diffusion reflètent les propriétés des microstructures du myocarde à cause de l’absence de la vérité-terrain sans parler de l’influence de divers facteurs tels que la résolution spatiale, le bruit et les artéfacts. L'objectif principal de cette thèse est donc de développer des simulateurs de l’IRM de diffusion basés sur des modèles réalistes afin de simuler, en intégrant différentes modalités d'imagerie, les images pondérées en diffusion des fibres myocardiques à la fois *ex vivo* et *in vivo*, et de proposer un outil générique permettant d’évaluer la qualité de l’imagerie et les algorithmes de traitement d’images.

Pour atteindre cet objectif, le présent travail se focalise sur quatre parties principales. La première partie concerne la formulation de la théorie de simulation IRMd pour la génération d’images de diffusion et pour les applications sur les modèles simples de fibres cardiaques chez l’homme, et essaie de comprendre la relation sous-jacente entre les propriétés mesurées de la diffusion et les caractéristiques à la fois physiques et structurelles des fibres cardiaques. La seconde partie porte sur la simulation des images de résonance magnétique de diffusion à différentes échelles en s’appuyant sur des données du cœur humain issues de l'imagerie par lumière polarisée. En comparant les propriétés de diffusion à différentes échelles, la relation entre la variation de la microstructure et les propriétés de diffusion observée à l'échelle macroscopique est étudiée. La troisième partie consacre à l’analyse de l'influence des paramètres d'imagerie sur les propriétés de diffusion en utilisant une théorie de simulation améliorée. La dernière partie a pour objectif de modéliser la structure des fibres cardiaques *in vivo* et de simuler les images de diffusion correspondantes en combinant la structure des fibres cardiaques et le mouvement cardiaque connu a priori.

Les simulateurs proposés nous fournissent un outil générique pour générer des images de diffusion simulées qui peuvent être utilisées pour évaluer les algorithmes de traitement d’images, pour optimiser le choix des paramètres d’IRM pour les fibres cardiaque aussi bien ex vivo que in vivo, et pour étudier la relation entre la structure de fibres microscopique et les propriétés de diffusion macroscopiques.

MOTS-CLES :

Modélisation des fibres cardiaques ; IRM de diffusion ; L’imagerie de lumière polarisée ; La simulation de Monte-Carlo, L’anisotrope fractionnelle; La diffusivité moyenne ; L’orientation de fibre ; L’IRM de diffusion *in vivo*

Laboratoire (s) de recherche :

Creatis (CNRS UMR 5520, INSERM U1044)

Directeur de thèse : Isabelle Magnin

Président de jury : Jean-Philippe Thiran

Composition du jury : Rachid DERICHE, Cyril POUPON, Jean-Philippe THIRAN, Leon AXEL, Pierre CROISILLE, Isabelle E. MAGNIN, Yue-Min ZHU, Wan-Yu LIU